Cosmic-Ray Neutron Sensing and its Applications to Soil and Land Surface Hydrology

On neutron physics, method development, and soil moisture estimation across scales

Martin Schrön

DISSERTATION, 2017

Published online at the
Institutional Repository of the University of Potsdam:
URN urn:nbn:de:kobv:517-opus4-395433
http://nbn-resolving.de/urn:nbn:de:kobv:517-opus4-395433

Institut für Erd- und Umweltwissenschaften
Arbeitsgruppe "Wasser- und Stofftransport in Landschaften"

Cosmic-Ray Neutron Sensing and its Applications to Soil and Land Surface Hydrology

DISSERTATION

zur Erlangung des akademischen Grades
"doctor rerum naturalium" (Dr. rer. nat.)

in der Wissenschaftsdisziplin
"Geoökologie/Hydrogeologie"

eingereicht an der
Mathematisch-Naturwissenschaftlichen Fakultät
der Universität Potsdam

von

Martin Schrön

Potsdam, den 27.06.2016

Reviewers:

Prof. Dr. Sascha E. Oswald (Institute of Earth and Environmental Science, University of Potsdam),

Prof. Dr. Peter Dietrich (Dep. Monitoring and Exploration Technologies, UFZ),

Prof. Dr. Kurt Roth (Institute of Environmental Physics, Heidelberg University).

Thesis Committee:

Prof. Dr. Axel Bronstert (Institute of Earth and Environmental Science, University of Potsdam),

Prof. Dr. Philipp Richter (Institute of Physics and Astronomy, University of Potsdam).

Additional Supervision:

Dr. Steffen Zacharias (Dep. Monitoring and Exploration Technologies, UFZ),

Dr. Luis E. Samaniego (Dep. Computational Hydrosystems, UFZ).

The dissertation was submitted on June 27th, 2016, and defended on February 22nd, 2017.
Research was conducted at the Helmholtz Centre for Environmental Research GmbH – UFZ, Leipzig. It was supported by the Helmholtz Impulse and Networking Fund through the Helmholtz Interdisciplinary School for Environmental Research (HIGRADE), and by Terrestrial Environmental Observatories (TERENO).
This document was written in `Markdown`, and typeset using `pandoc`, `perl`, and `pdflatex`.

Für Opa Gerhard

Contents

List of Figures

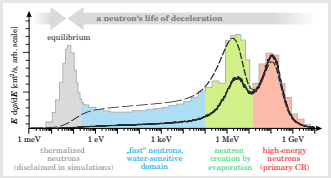

Fig. 3.1: A typical neutron energy spectrum at the surface.

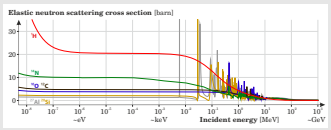

Fig. 3.2: Elastic neutron cross sections of relevant elements.

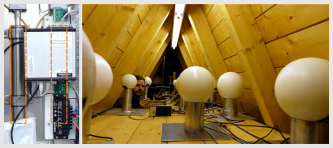

Fig. 3.3: Detector shielding for CRS1000 and Bonner spheres.

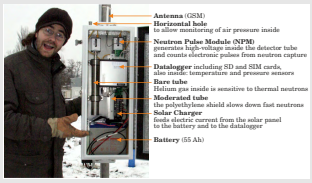

Fig. 3.4: Components inside the Cosmic-Ray Neutron Sensor.

Fig. 3.5: Components of the CRNS rover.

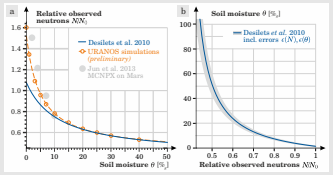

Fig. 3.6: From neutrons to soil moisture and back.

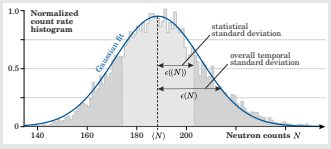

Fig. 3.7: Statistical distribution of neutron counts.

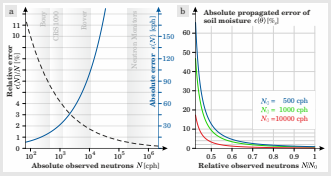

Fig. 3.8: Count rate errors and their propagation to soil moisture estimations.

Fig. 4: Temporary installation of ten Cosmic-Ray Neutron Sensors at the *Schmetterlingswiese*, UFZ area.

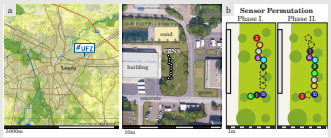

Fig. 4.1: Experimental site *Schmetterlingswiese* to compare 9 CRNS detectors.

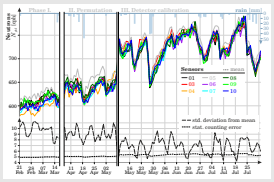

Fig. 4.2: Time series of 9 CRNS detectors during intercomparison phases I–III.

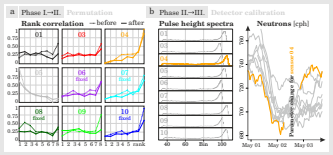

Fig. 4.3: Rank correlation and PHS of 9 CRNS probes.

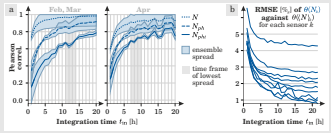

Fig. 4.4: Influence of integration time to sensor correlation and soil moisture performance.

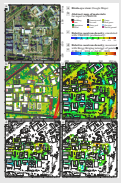

Fig. 4.5: Neutron environment of the urban test site at UFZ.

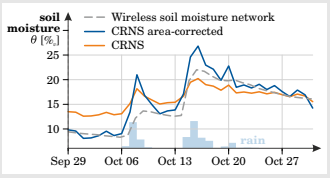

Fig. 4.6: Area correction of CRNS signal in the *Schmetterlingswiese*.

Fig. 5: Installation of the "cosmic buoy" at *Seelhauser See*, with the help of K. Rahn and M. Wieprecht (UFZ Magdeburg).

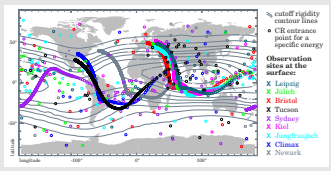

Fig. 5.1: Cutoff rigidity and incoming directions of cosmic ray neutrons.

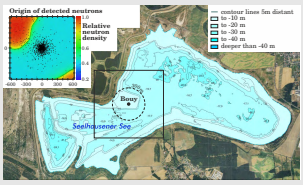

Fig. 5.2: Location of the CRNS buoy detector at lake *Seelhausener See*.

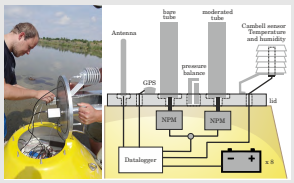

Fig. 5.3: Detector system housing inside the buoy.

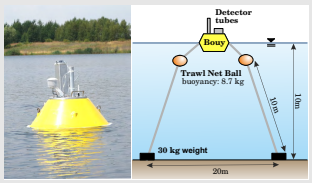

Fig. 5.4: Anchorage of the stationary buoy in the lake.

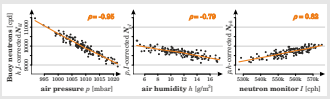

Fig. 5.5: Correlations of buoy neutrons to air pressure, humidity, and incoming radiation.

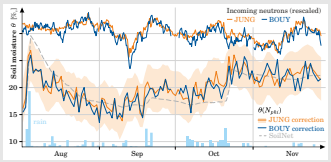

Fig. 5.6: Performance of the buoy incoming correction for soil moisture estimation.

Fig. 6: Thorough investigation of neutron physics, simulations, and tape rules led to new insights about the CRNS footprint (Köhli et al. 2015).

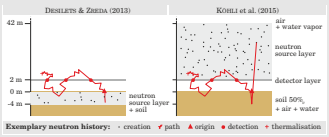

Fig. 6.1: Model setup of the conventional and the revised simulations.

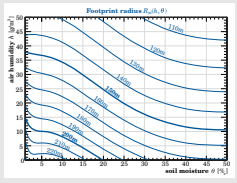

Fig. 6.2: Footprint radius as a function of h and θ.

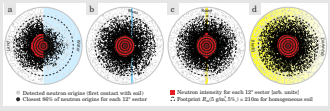

Fig. 6.3: Anisotropy of detected neutrons in complex terrain.

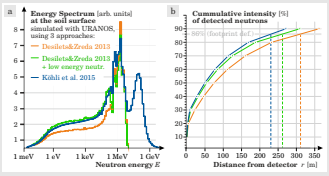

Fig. 6.4: Input spectrum for simulations and their influence on the footprint.

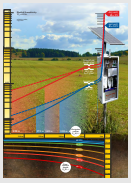

Fig. 7: Visualization of the footprint weighting function $W_r(h,\theta)$ and penetration depth $D_{86}(\theta,r)$, which are beneficial for averaging point data.

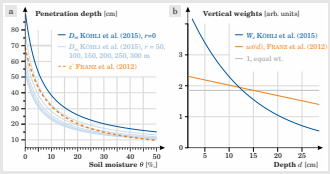

Fig. 7.1: Revised footprint depth and vertical weighting.

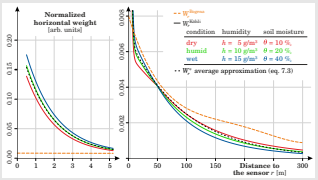

Fig. 7.2: Horizontal weighting functions compared.

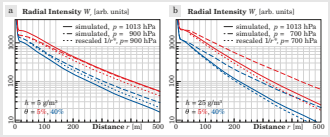

Fig. 7.3: Pressure dependence of the weighting function.

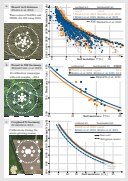

Fig. 7.4: Three example sites that show the importance of weighted averages.

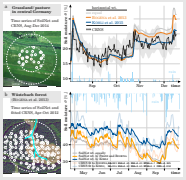

Fig. 7.5: Time series in *Großes Bruch* and *Wüstebach* using a weighted average.

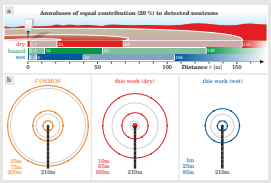

Fig. 7.6: Regions of equal contribution to the neutron signal and sampling schemes.

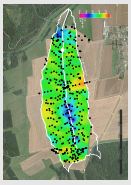

Fig. 8: Volumetric water content in the *Schäfertal* estimated by the CRNS rover on Aug 11th, 2015. *Credit: background from Google Maps*

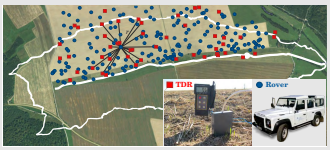

Fig. 8.1: Calibration of the rover with TDR in the *Schäfertal*.

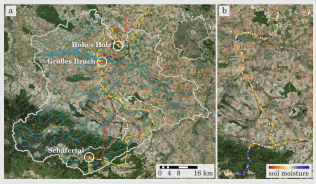

Fig. 8.2: Map of the CRNS rover tracks in the *Bode* and *Selke* river catchments.

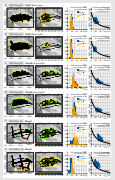

Fig. 8.3: Comparison of rover and TDR on six campaign days.

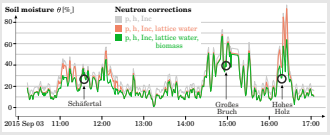

Fig. 8.4: Time series of a rover campaign on Sep 03, 2015.

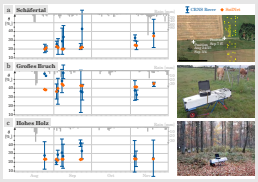

Fig. 8.5: Validation of eleven rover campaigns and three SoilNet sites.

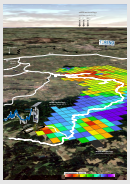

Fig. 9: Illustration of parts of the *Selke* basin modeled with mHM: mean θ (color) and neutron data in the *Schäfertal* subbasin (left).

Credit: backgr. from Google Earth

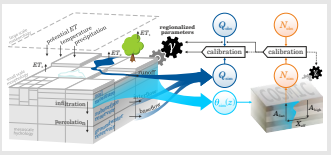

Fig. 9.1: Schematic of processes in mHM and the calibration workflow.

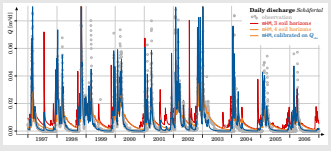

Fig. 9.2: Discharge in the *Schäfertal* modeled with mHM.

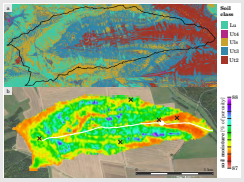

Fig. 9.3: Soil moisture estimation in the *Schäfertal* by mHM.

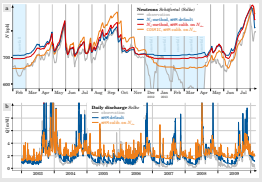

Fig. 9.4: Effect of neutron calibration in the *Selke* basin.

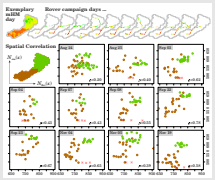

Fig. 9.5: Comparing rover transects and mHM neutrons in the *Selke*.

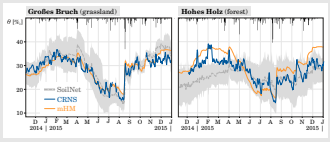

Fig. 9.6: mHM soil moisture prediction in pasture land and forests.

Fig. 10: Gyrocopters carrying the double-tube CRS1000 neutron detector. *Credit: Photos by L. Bannehr. Second gyrocopter (sky) inserted by own montage.*

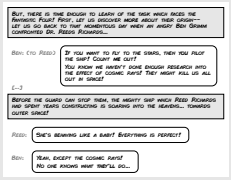

Fig. 10.1: The *Fantastic Four* meet airborne cosmic rays.

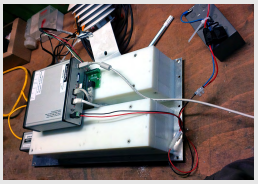

Fig. 10.2: Double-tube detector system assembled from two CRS1000.

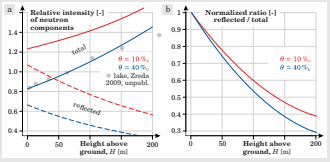

Fig. 10.3: Variation of neutron counts with height above ground H.

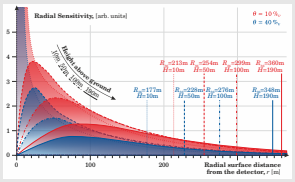

Fig. 10.4: Footprint and sensitivity increase with height above ground.

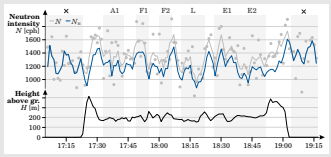

Fig. 10.5: Time series of the gyrocopter campaign including height above ground.

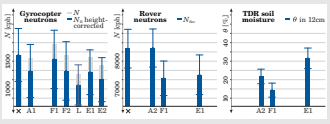

Fig. 10.6: Gyrocopter, rover, and TDR measurements compared.

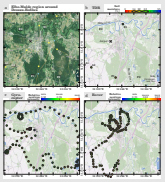

Fig. 10.7: Measurements of TDR, gyrocopter and rover around Dessau-Roßlau.

Fig. 11: Surveying spatial patterns of neutrons (inside rover) and natural gamma rays (trailing sled) in the *Schäfertal*.

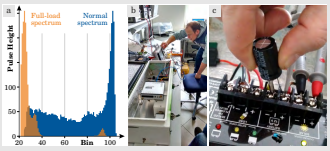

Fig. B.1: Abnormal pulse height spectra during full-load periods.

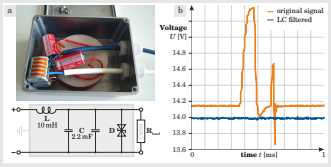

Fig. B.2: A low-pass filter can deal with full-load voltage.

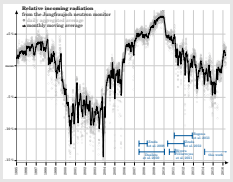

Fig. C.1: Periods of high incoming CR variation and uncertainty.

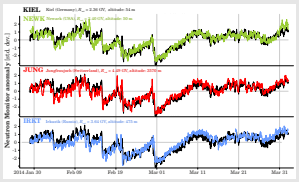

Fig. C.2: Comparison of four neutron monitors.

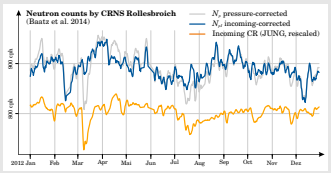

Fig. C.3: Remaining features after incoming correction.

179

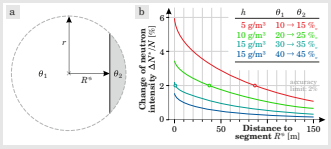

Fig. E.1: Alternative footprint definition and consequences.

186

Picture Credits

Cover image, parts of Figs. 3 and 7: own montage, using:
starry sky: http://bisceglie24.it/discorso-sul-mito,
landscape and sensor: own photographs,
soil: http://foxsilver.deviantart.com/art/Soil-and-Grass-114597279,
rain drops: https://www.pexels.com/photo/droplets-50677.

Fig. 2: own montage, using:
Crab Nebula: https://commons.wikimedia.org/w/index.php?curid=516106,
galaxy: http://www.photosforclass.com/download/14559318362,
planets: https://pixabay.com/en/solar-system-planet-planetary-system-11111,
aurora: https://pixabay.com/en/satellite-iss-northern-lights-1030780,
glacier: https://pixabay.com/en/glacier-argentina-south-america-583419.

Fig. 3: own montage, greyscale image by M. Köhli.

List of Tables

Abstract

Water scarcity, adaption on climate change, and risk assessment of droughts and floods are critical topics for science and society these days. Monitoring and modeling of the hydrological cycle are a prerequisite to understand and predict the consequences for weather and agriculture. As soil water storage plays a key role for partitioning of water fluxes between the atmosphere, biosphere, and lithosphere, measurement techniques are required to estimate soil moisture states from small to large scales.

The method of cosmic-ray neutron sensing (CRNS) promises to close the gap between point-scale and remote-sensing observations, as its footprint was reported to be $\sim$ 30 ha. However, the methodology is rather young and requires highly interdisciplinary research to understand and interpret the response of neutrons to soil moisture. In this work, the signal of nine detectors has been systematically compared, and correction approaches have been revised to account for meteorological and geomagnetic variations. Neutron transport simulations have been consulted to precisely characterize the sensitive footprint area, which turned out to be $\sim$ 6–18 ha, highly local, and temporally dynamic. These results have been experimentally confirmed by the significant influence of water bodies and dry roads. Furthermore, mobile measurements on agricultural fields and across different land use types were able to accurately capture the various soil moisture states. It has been further demonstrated that the corresponding spatial and temporal neutron data can be beneficial for mesoscale hydrological modeling. Finally, first tests with a gyrocopter have proven the concept of airborne neutron sensing, where increased footprints are able to overcome local effects.

This dissertation not only bridges the gap between scales of soil moisture measurements. It also establishes a close connection between the two worlds of observers and modelers, and further aims to combine the disciplines of particle physics, geophysics, and soil hydrology to thoroughly explore the potential and limits of the CRNS method.

Zusammenfassung

Wasserknappheit, Anpassung an Klimaveränderungen, und Gefahrenabschätzungen von Dürren und Fluten sind heutzutage dringende Themen für Forschung und Gesellschaft. Vorallem um die Auswirkungen auf Wetter und Landwirtschaft zu verstehen und vorherzusagen, ist es wichtig, den Wasserkreislauf der Erde zu beobachten und zu simulieren. In diesem System spielt Bodenfeuchte eine Schlüsselrolle, welche den Wasseraustausch zwischen Boden, Luft, und Pflanzen bestimmt. Daher sind ausgeklügelte Messtechnologien erforderlich, welche Bodenfeuchte von kleinen Ackerschlägen bis hin zu großen Gebieten erfassen können.

Die neuartige Methode, Neutronen aus kosmischer Strahlung zu messen (CRNS), ist eine vielversprechende Technologie um die Lücke zwischen Punktmessungen und Fernerkundungen zu schließen, da der Einflussbereich des Sensors bei ca. 30 ha liegen soll. Allerdings ist intensive interdisziplinäre Forschung nötig, um die Beziehung zwischen Neutronen und Bodefeuchte zu verstehen. In dieser Arbeit wurden erstmals verschiedene Sensoren systematisch miteinander verglichen, und die bisherigen Korrekturen für meteorologische und geomagnetische Einflüsse näher untersucht. Darüber hinaus wurden Simulationen der Neutronenphysik herangezogen, um den Einflussbereich des Sensors genauestens zu charakterisieren. Demnach ist der Sensor je nach Umgebungsfeuchte hauptsächlich in der Fläche von ca. 6–18 ha, sowie besonders im Nahbereich, sensitiv. Diese Resultate konnten durch Experimente nahe Gewässern und Straßen bestätigt werden. Dennoch ist die Methode nachwievor sehr gut in der Lage, die Bodenfeuchte in Ackerflächen, Grasland und auch Wäldern zu erfassen. Zudem wurde gezeigt, dass sich die räumlichen und zeitlichen Neutronen-Daten gut für die hydrologische Modellierung eignen. Abschließend wurde eine neue Möglichkeit untersucht, um Neutronen aus der Luft mit einem Traghubschrauber in noch größeren Gebieten zu messen.

Diese Dissertation untersucht die CRNS-Methode auf verschiedenen Skalen, und verknüpft dabei Beobachtung mit Modellierung. Außerdem verbindet diese Arbeit die verschiedenen Disziplinen der Teilchenphysik, Geophysik, und Bodenhydrologie, um das Potential und die Grenzen der Methode ganzheitlich zu beurteilen.

Fig. 1:
Water ponds on clay soil during a summer drought in the *Schäfertal*.

1.

Water & Soils

The role of subsurface water in the environment

Near-surface water content is a remarkable variable in environmental sciences, as it controls plant growth, water infiltration, and the regional climate. For example, soil moisture is a key quantity that decides between flood or drought, effective or absent groundwater recharge, and finally, fruitful agricultural yield or hunger crisis.

Computer models have been developed in all fields of research to deal with water scarcity and weather prediction. The level of precision is often crucial for hazard warnings or risk management. However, validation with real-time observations is strongly needed in order to improve the prediction performance.

In the course of the last decade, creative methods have been developed to efficiently measure soil moisture at various spatial scales. Unfortunately, near-surface water is highly heterogeneous, so point-scale measurements are not representative enough to support hydrological models at the regional scale. Remote-sensing observations are the method of choice for larger scales, however, they only account for water in the first 0–5 cm below the surface.

Since 2008, environmental scientists have investigated a new measurement method using reflected neutron counts above the soil as a proxy for subsurface water content. The so-called cosmic-ray neutron sensor (CRNS) is a detector which operates non-invasively, passively, and requires low maintenance. These advantages have led to major investments in the last years, resulting in hundreds of sensors around the globe.

1.1. The water cycle in a changing world

The life cycle on Earth is naturally related to the water cycle (Budds et al. 2014). Animals, plants, and humans usually settle close to water reservoirs, as constant availability of drinkable water is highly appreciated. The water bodies further set along topographical gradients by forming streams that can cross hundreds of miles through countries and continents, and finally discharge into the ocean. Meanwhile, a fraction of water can escape into the atmosphere and form clouds at various heights above ground. Those accumulations of water drops may travel even longer distances, thereby exchanging water with different regions across the globe. Clouds typically spend most of their time preventing terrestrial heat from escaping into space and solar radiation from entering the atmosphere. However, sometimes clouds rearrange to form awful hurricanes, or condense to gently release their droplets above thirsty lifeforms. While strong rain events are able to quickly revive arid regions, they can also cause highly destructive floods elsewhere. Finally, precipitation and snowfall lead to refilling of the groundwater and surface reservoirs, thereby nourishing life and starting the cycle all over again.

The rising number of people on Earth will increase the demands on food and freshwater resources, and further increase the reliance on groundwater (Mekonnen and Hoekstra 2011). As approximately 40% of the global food production come from irrigated agriculture, the problems of water scarcity can be directly connected to food security, especially in arid regions (Postel et al. 1996; Mekonnen and Hoekstra 2011). According to Mueller and Zhang (2015), anthropogenic processes are suspected to be responsible for longer periods without precipitation, such that droughts are becoming one of the major global risks for water availability and food security in the next decades (World Economic Forum 2016).

Therefore, effective water resource management is one of the major challenges for humanity, which can be supported by monitoring, modeling, and forecasting of the hydrological cycle (Wood et al. 2011; Beven and Cloke 2012). Similar to other countries, Germany is highly vulnerable to climate change with regards to the high agricultural dependence on water availability, strong coupling between shallow groundwater and the root zone, expected decrease of summer precipitation, and consequently, risk of summer droughts (Samaniego et al. 2013; Zink et al. 2016), and flooding (Petrow and Merz 2009).

1.2. The role of soil moisture

Interestingly, soil plays an important role in this intriguing game, as it stores and retains water from immediate infiltration. The storage in the subsurface layer appears like a memory of precipitation and works as a spongy reservoir, from which water and heat is made accessible to plants and the atmosphere. Consequently, soil moisture governs the partitioning of water into surface runoff, infiltration, evaporation, and groundwater recharge. As water is a great conductor for heat and solute, it further supports atmospheric cooling and the diffusion of chemicals or radioactive gases (Iskandar et al. 2004). In agricultural management, soil moisture is an important information to estimate the accessibility of fields with heavy equipment, and for real-time estimation of water deficit of crops (Smith et al. 2002) and consequent

optimization of irrigation rates in water scarce regions (Vereecken et al. 2008).

In the light of land surface hydrology, soil moisture controls the efficiency of water exchange with the atmosphere, groundwater, and rivers (Brutsaert 2005). Accurate description of both, energy balance as well as water balance of regional catchments are a prerequisite for reliable hydrological predictions, in which soil water storage plays a key role. If soil moisture states were known, direct implications could be drawn for flood risk assessment (Norbiato et al. 2008), real-time estimation of water deficit in agriculture (Smith et al. 2002), or drought forecasting and analysis (Sheffield 2004; Samaniego et al. 2013; Ceppi et al. 2014; Zink et al. 2016). Consequently, there is a huge demand for such information from models that describe hydrological discharge (Brocca et al. 2012; Kumar et al. 2013b), land-surface energies and fluxes (Jung et al. 2010), and atmospheric circulations (Koster et al. 2004). However, there is a lack of soil moisture observations at the scales from 100 m to kilometers, at which most models operate (see section 1.7), such that validation and calibration of these models remain one of the key challenges in hydrology and climate science (Vereecken et al. 2007).

Moreover, soil moisture states are actually able to influence the regional weather. In fact, Findell and Eltahir (1997) found lagged correlation between soil saturation and precipitation patterns in Illinois. The water in soil from earlier precipitation can be made accessible to the atmosphere by evaporation and transpiration processes. This "recylcing" feature can drive subsequent precipitation events, modify downwind structures, and generate large scale circulations (Taylor 2015). As a consequence, knowledge of the soil moisture state in late spring can support flood or drought prediction in the summer months (Findell and Eltahir 1997; Koster et al. 2004). The so-called *feedback mechanism* between soil moisture and precipitation is now generally accepted (Tuttle and Salvucci 2016), however, its characteristics greatly depend on the spatial scale (Taylor et al. 2013).

1.3. Intensive monitoring networks

With improved infrastructure for environmental monitoring, the causation mechanisms of soil moisture and the impact of climate and land use change could be studied. In this regard, the Terrestrial Environmental Observatories (TERENO) have been set up in four specific parts of Germany (Zacharias et al. 2011), to understand and predict the behavior of the environment in response to changing climatic conditions, to support decisions for environmental management, and to provide data for early warning systems.

Also other interdisciplinary research groups around the globe developed long-term monitoring strategies and established intensive research sites at large scales, e.g., the Mesonet in Oklahoma (Illston et al. 2008), or research sites supported by the International Soil Moisture Network Initiative (ISMNI, Dorigo et al. 2011). However, interpretation and interpolation of soil moisture data across scales must be taken with care. Gruber et al. (2013) concluded from analysis of ISMNI data that there is a strong need to find representative sites and sensors for reliable large-scale measurements (see also Ochsner et al. 2013).

The most relevant methods to estimate soil moisture across scales are described in section 1.7.

1.4. Flow and transport from soil physics to hydrology

The previous sections have introduced water and soil moisture as important factors for climate and society. But what causes changes of water storage in the environment? How and why does water move in soils?

Flow mechanisms usual follow the concept of the *flux* ϕ, which depicts the amount of mass passing a certain area in a certain amount of time (Landau and Lifshitz 1966). Under static conditions, however, continuous gases or liquids obey the law of inertia and have little motivation to move through imaginary interfaces. Still, air molecules in the atmosphere as well as water in the ocean or underground seem to be permanently on the move. In order to set water in motion, external forces $F \propto \nabla p$ are required, which tell the water molecules to move along a certain pressure gradient ∇p. This generates the flux $\phi = -K \cdot \nabla p$ towards the downhill direction of that gradient, which further depends on the conductivity K of the medium passed. Typical macro-scale pressure gradients occur due to gravitation along the vertical axis, $p_{\text{grav}} = \varrho g \cdot z$, while micro-scale gradients are typically related to capillary forces, $p_{\text{cap}} \propto 1/r_{\text{pore}}$, where r_{pore} is the radius of the pore volume. Other processes like drainage or evapotranspiration can also induce pressure gradients, forcing soil water to either move downward or upward (Or et al. 2013).

In contrast to saturated zones (e.g., groundwater), unsaturated pores are not completely filled up, such that $p(\theta)$ and $K(\theta)$ become dependent on the fraction of available water, the so-called *soil moisture* θ. Following the logical principles of mass conservation, water content in the pores changes if the transporting net fluxes $\phi_{\text{in}} - \phi_{\text{out}}$ through the considered volume changed, $\partial_t \theta = -\nabla \phi$. This leads to the famous *Richards equation* (Richardson 1922; Richards 1931), describing the dynamics of soil moisture in the pores:

$$\text{Richards:} \quad \partial_t \theta = \nabla \big[K(\theta) \, \nabla p(\theta) \big] \, . \tag{1.1}$$

Unfortunately, the relations for K and p are highly non-linear in θ, while those quantities further depend on the complex and heterogeneous distribution of grain size and other soil properties (Rudiyanto et al. 2015, and references therein). The elaborated equations are thus only valid at the centimeter to meter scale. Vereecken et al. (2007) presents a wide range of approaches to extend the applicability of those equations to larger scales, which often tend to result in the determination of *effective parameters* K_{eff}, Θ_{eff} (porosity), among others. According to Vereecken, identification of those parameters is highly scale-dependent, and their validation is almost impossible due to the lack of data at the required scales. Samaniego et al. (2010) presented a regionalization scheme to design effective parameters at any scale, which is described in more detail in chapter 9.

Considering *average* water fluxes in a hydrological unit (e.g., a grid cell), a *scale-independent* formulation of soil moisture dynamics can be given, which is inofficially known as the *law of hydrology* or *water balance equation*:

$$\underset{\substack{\text{soil water}\\ \text{dynamics}}}{\partial_t \theta} = \underset{\text{precipitation}}{P} - \underset{\text{evapotranspiration}}{ET} - \underset{\text{infiltration}}{I} - \underset{\substack{\text{discharge}\\ \text{runoff, interflow}}}{Q} \, . \tag{1.2}$$

Similar to eq. 1.1, the formulation above is based on the conservation of mass and

fluxes in a domain, and any hydrological model is well advised to obey (see Coron et al. 2014, for a critical perspective). The main processes involved in the water partitioning at the land surface are

1. precipitation (or rain) as the main input of water into the system,
2. evapotranspiration, which removes water from soil (evaporation) or plants (transpiration) depending on solar radiation, wind speed, among others,
3. infiltration and percolation of soil water into deeper reservoirs (e.g., groundwater),
4. discharge, including (1) surface runoff when the soil water capacity is reached, (2) lateral interflow when the infiltration is hindered by dense soil or bedrock, or the capacities are reached, and (3) groundwater flow.

The water balance equation can also be used, for instance, to "do hydrology backwards". Brocca et al. (2013) infers rainfall from soil moisture variations, where θ is non-linearly related to P under several assumptions. However, the approach fails when rain events overwhelm the field capacity of soil layers.

1.5. Patterns and controls

Primary physical controls for soil moisture are precipitation, soil properties, vegetation, and topography (Grayson et al. 1997; Western et al. 2004). According to Gaur and Mohanty (2013), soil texture is one of the dominant controls for moisture patterns at the field scale, which can be confirmed by hydrological modeling in chapter 9, and which is also observed at even larger scales (Cosh and Brutsaert 1999; Jawson and Niemann 2007). Vegetation is particularly important under dry conditions, while topography controls patterns under wet conditions when the conductivity $K(\theta)$ is highest (section 1.4). As topography is further related to hill slopes, the corresponding exposition to sunlight may support evaporation processes. At the larger scales > 1 km, soil moisture patterns are driven by precipitation pattern which in turn may exhibit remarkable heterogeneity. Interestingly, Famiglietti et al. (2008) found that soil moisture variability even follows a fractal power law across spatial extents from meters to kilometers.

Geology is a controlling factor that can be important in catchments with irregular bedrock formation below the surface. For example, Fig. 1 shows contact springs in the *Schäfertal* catchment, where the groundwater table becomes shallow enough to permanently saturate the surface layer even under drought conditions. Moreover, vegetation can have a strong dynamic impact on the vertical flow of water in the soil system, and thus determines partitioning between infiltration, evaporation and runoff. Leaves can also intercept precipitation water which evaporates before it reaches the soil. Especially forests can thereby dampen the groundwater recharge efficiency of rain or snow events. All those processes strongly depend on the type of vegetation, strength of the roots, size of the leaves, etc. (see e.g., Mohanty et al. 2000)

The temporal stability of patterns is typically governed by precipitation events, or by variations of evapotranspiration due to temperature, wind, sunlight, and other weather conditions (see e.g., Allen et al. 1998; Or et al. 2013).

1.6. Soil properties

As water fills the pore space of the soil, the subsequent dynamics are related to soil properties (e.g. bulk density, texture, porosity, among others). Those quantities are an important information in agriculture, for instance, as the grain size distribution determines the capillary pressure and thus the wilting point for plants. Hydrological applications rely on knowledge about the pore space to estimate partitioning between infiltration and runoff. And knowledge about the bulk density is of particular importance to translate gravimetric measurements of water content (e.g., with neutrons) to a quantity related to pore saturation.

The bulk soil material usually consists of SiO_2 and Al_2O_3, aggregated to grains of a variety of sizes. Macroscopic accumulation of grains of certain size are classified under the term *soil texture*, which encompasses *sand*, *silt*, *clay*, and their mixtures (FitzPatrick 1980). Further classifications are commonly used that account for the relationship between soil types, soil genesis, and suitability for particular applications (IUSS Working Group 2014). Fig. 1.1 shows measurements of soil properties in the *Schäfertal* catchment, which were used for sensor calibration and hydrological modeling (chapter 9).

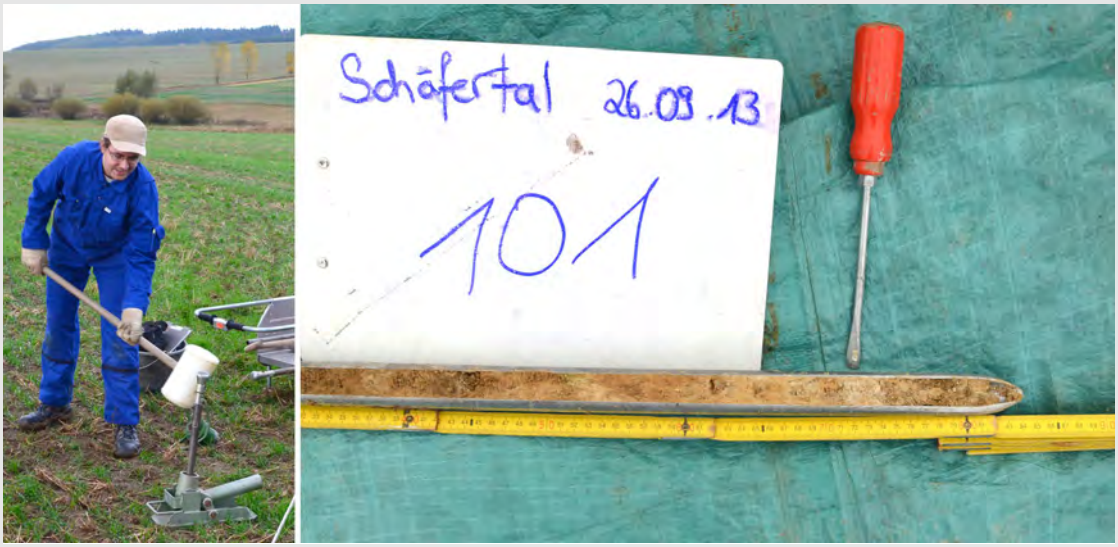

Fig. 1.1: One of 30 locations during a soil sampling campaign in the *Schäfertal*. An auger is pushed up to 80 cm into the soil and subsequently pulled out. The soil colors and texture reveal insights into the composition of the vertical soil profile.

The *bulk density* ϱ_{bulk} is expressed in units grams of oven-dry soil per cubic centimeter of soil material (Klute et al. 1986). Typical values range from from about 1.0 g/cm^3 (fine-textured soils) to 1.4 or 1.7 g/cm^3 (coarse-textured soils). Tillage or humus can reduce the bulk density, while cows or vehicles contribute to compaction (Brady and Weil 1996).

$$\text{bulk density} \quad \varrho_{\text{bulk}} = \left.\frac{m_{\text{bulk}}}{V_{\text{soil}}}\right|_{\text{dry}} .$$

The *particle density* describes the solid part of the soil that excludes the pore space. As the mineral content of typical soil particles does not vary significantly, the quantity can be approximated with the density of quartz (2.65 g/cm^3), which is the dominant mineral in most soils (Brady and Weil 1996),

$$\text{particle density} \quad \varrho_\text{p} = \left.\frac{m_\text{bulk}}{V_\text{bulk}}\right|_\text{dry} \approx 2.65\,\text{g/cm}^3\,.$$

Consequently, the *porosity* Θ expresses the relative amount of pore space in the soil. It can either be determined from laborious saturation experiments, or from the particle density and bulk density information (which in turn is easily determined by oven-drying and weighting of soil samples):

$$\text{porosity} \quad \Theta = 1 - \frac{\varrho_\text{bulk}}{\varrho_\text{p}} = 1 - \frac{V_\text{bulk}}{V_\text{soil}}\,.$$

Following the concepts above, soil moisture is usually measured in percent of the volumetric water capacity, $V_\text{water}/V_\text{soil}$ [$\%_v \equiv \text{m}^3/\text{m}^3$] or percent of the gravimetric weight, $m_\text{water}/m_\text{soil}$ [$\%_g \equiv \text{kg/kg}$].

1.7. Experimental methods to estimate soil moisture

The remarkable horizontal heterogeneity of soil patterns requires highly resolved measurements at the meter-scale, while areal coverage of hundreds of meters is necessary for regional modeling and agricultural applications. Additionally, soil moisture profiles can be highly stratified, such that detailed examination of the vertical distribution is necessary to support predictions for evaporation, infiltration, and root-water uptake. With regards to those requirements, Western and Blöschl (1999) and Famiglietti et al. (2008) conclude that single measurements at the local scale (cm to m) are usually not representative and unusable for large-scale applications. Schelle et al. (2013) investigated this problem theoretically in a virtual environment and had to conclude with the following withering assessment:

> “Our results showed that measurements, particularly those of water contents, varied strongly with measuring position. [...] As a consequence, the correct calculation of the water balance is rather a lucky coincidence than the rule.”

On the other hand, remote-sensing techniques have evolved in the last decade that promised to deliver soil moisture at much larger scales and to solve the problem of representativeness. However, shallow integration depth (0–5 cm) and too coarse resolution (0.1–40 km) are the major disadvantages of satellite and airborne products (Fang and Lakshmi 2014). Under these circumstances, Robinson et al. (2008) gave the following statement about the current status of the observation methods:

> “There is currently a gap in our ability to routinely measure soil moisture at intermediate scales (subwatershed or catchment or vegetation stands) for hydrological, ecohydrological, and biogeochemical studies.”

Robinson further argued that this gap has historical reasons, as soil moisture measurements where either used for small-scale agriculture, or large scale understanding of soil-atmosphere interactions. One of the solutions to bring the local measurements towards larger extents are the Soil Moisture Monitoring Networks (Bogena et al. 2010), although a huge number of devices is required to cover large areas (Pan and Peters-Lidard 2008). A different perspective has been elaborated by Dong et al. (2016), who suggested to use *distributed temperature sensing* (DTS) with long cables as a proxy to upscale local soil moisture measurements. Moreover, new instruments have been developed in the last years that promise to fill the gap by providing an average signal over larger radii, e.g., gravimetry (> 100 m), GPS (30 m), or cosmic-ray neutron sensing (CRNS) which covers radii of 150–240 m on its own and can be extended towards areas of ~ 100 km^2 in a mobile mode.

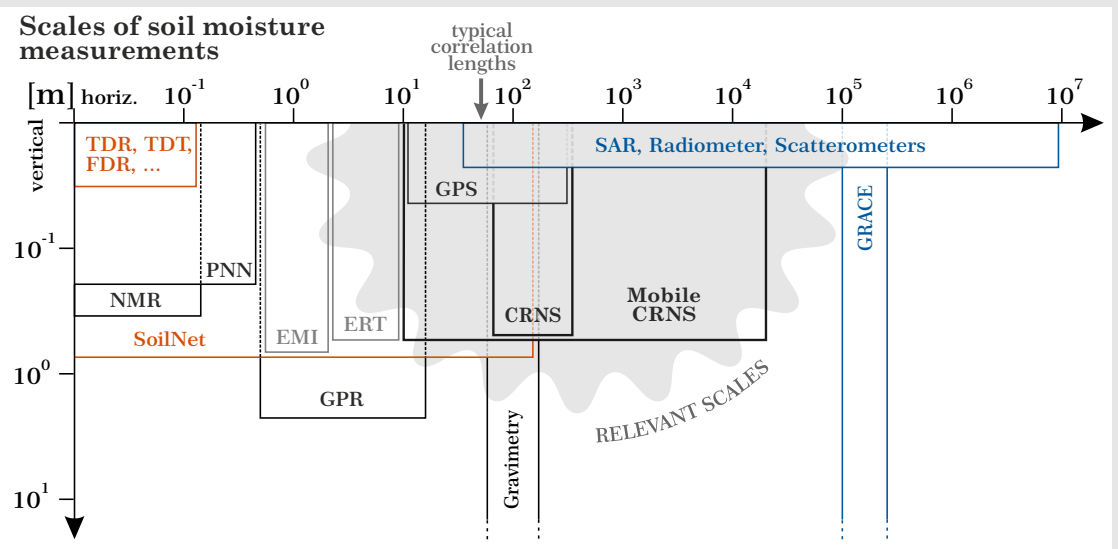

Fig. 1.2: Scales of soil moisture measurements covering invasive (brown), non-invasive (black), and remote-sensing (blue) methods. The CRNS technology promises to fill the scale gap (gray) which is relevant to agricultural, hydrological, and modeling applications. Typical correlation lengths of soil moisture patterns reported by Western et al. (2004) are indicated.

1.7.1 Remote Sensing

In general, remote-sensing techniques rely on the electromagnetic interaction of photons with the ground medium. Depending on their frequency (or wavelength), photons may get absorbed or scattered by specific electrons and shell configurations in all kinds of atoms or molecules. One advantage of this principle is that different properties of the material can be examined by different photon frequencies (e.g., photosynthesis of plants or reflectivity of rocks). However, since atomic envelopes (or at least the area of influence) fill up almost the whole space between densely packed atoms, the photons typically may not penetrate dense soil material much deeper than a few centimeters. Lower frequencies (longer wavelengths) may increase the

penetration depth, but they are typically accompanied by lower signal strength and increasing noise.

Apart from the high costs, low temporal resolution, interfering cloud coverage, and significant influence of surface conditions, the shallow penetration is the major disadvantage of remote-sensing products (Entekhabi et al. 2004; Wagner et al. 2007; Chang and Hong 2012). Current research focuses on extrapolations down to deeper soil layers (e.g., Ford et al. 2014), however, with rather poor statistical success.

For applications where surface moisture is relevant, remote-sensing products became a widely accepted and well-established data basis. One of the first satellite missions for soil moisture estimation was the passive microwave imaging radiometer SMOS (Kerr et al. 2001; Kerr 2007), with spatial resolutions of about 40 km and full coverage of the globe at least twice every three days. Later, the SMAP satellite mission was launched with revised technology that is able to observe the microwave domain passively and actively at resolutions down to 10 km (Entekhabi et al. 2010). New hope has been set to the upcoming Tandem-L satellite, which promises to deliver changes of soil moisture at resolutions of only a few tens of meters (Moreira et al. 2015). In contrast to satellite techniques, airborne remote-sensing can achieve much higher spatial resolution and is thus able to use longer wavelengths for deeper soil penetration. For example, Tabatabaeenejad et al. (2015) evaluated first results from AirMOSS surveys to estimate root-zone soil moisture with the help of sophisticated extrapolation strategies. Although this technology is promising to estimate soil moisture in the first decimeters (Cuenca et al. 2013), airborne campaigns are usually expensive and are not conducted at a regular basis.

As a general remark, the lack of comparable data at the surface complicates the analysis and validation of remote-sensing products. While first validation approaches were tested using large-scale precipitation patterns (Tuttle and Salvucci 2014) or distributed soil moisture networks (Jackson et al. 2012), the method of mobile cosmic-ray neutron sensing could serve as a promising tool to validate remotely sensed soil moisture in the future (Chrisman and Zreda 2013), see also chapter 10.

1.7.2 Local measurements

Soil sampling, gravimetry, EMI/ERT, gamma-rays, NMR, and GPS

The most direct method to measure soil moisture in the field uses destructive soil sampling, where parts of the soil can be weighted in a laboratory before and after oven-drying, to determine the soil water content that escaped during that process. Although this method appears to be highly accurate, it can be exhausting for larger fields, unfeasible for deep horizons, and unreliable for stony soils (Western et al. 2002; Bogena et al. 2010).

The "local" method of *gravimetry* is a modern relative to gravimetric sampling (Kazama and Okubo 2009) and very similar to the (highly non-local) GRACE satellite technique that is used for groundwater and surface water applications (Jiang et al. 2014). A gravimeter measures the variations of the Earth's gravitational field due the change of mass (e.g, change of water) in an integrative volume. The footprint extents beyond a few hundred meters, because the whole mass below (and slightly besides) the device is considered in the integrated domain (Creutzfeldt et al. 2010). However, since researchers aim to detect tiniest gravitational changes with this instrument,

the device uses super-conducting material that demands enormous cooling efforts.

It is further believed that soil moisture can also be estimated from measurements of electrical properties of the soil, either by *electromagnetic induction* (EMI) or *electrical resistivity tomography* (ERT), for water is a good conductor. However, under field conditions the signal intensity and its spatial sensitivity are complex variables that depend on porosity, soil texture, and other conducting materials (Callegary et al. 2007). The method of soil moisture estimation by *gamma ray attenuation* exhibits similar limits with regards to soil texture, as the detected photon signal depends on the soil density. However, the number of radioactive photon emitters (e.g., uranium, thorium, potassium) is usually site-specific, such that temporal variations at a single location could be related to soil moisture dynamics in the first few centimeters (Schmugge et al. 1980).

The method of *nuclear magnetic resonance* (NMR) is a modern technology that is able to perform non-invasive measurements at the point scale (Walsh et al. 2011, 2013). The instrument generates external magnetic fields that motivate the spins of hydrogen nuclei to align and relax, thereby leaving specific signatures in the measured field attenuation. The resonance signal's amplitude is directly proportional to water content, while the spin relaxation time is proportional to the pore size. The sensor is thus able to directly provide volumetric water content without lithology calibration, and even to distinguish between mobile and immobile water. Although the footprint is only a few tens of centimeters, specific soil horizons can be sampled directly depending on the frequency of the magnetic fields.

Another promising method relates soil moisture to ground-reflections of signals from the *global positioning system* (GPS) (Chew et al. 2016). The modern technology is able to cover representative areas of a few tens of meters and a few centimeters in depth (Larson et al. 2008), while advances in vegetation corrections are on their way (Small et al. 2016). Compared to the other "local measurements" presented here, the GPS method ventures a promising step from point observations towards more representative, areal averages.

Permittivity sensed by TDR, TDT, FDR, GPR, and SoilNet

As soil and water molecules tend to align their dipols along external electromagnetic fields, the generation and propagation of such fields is affected depending on the medium's dielectric *permittivity* ε (where $\varepsilon_{\text{water}} \gg \varepsilon_{\text{soil}}$). This principle is exploited by many geophysical methods, e.g., *time-domain reflectrometry* (TDR), *frequency-domain reflectrometry* (FDR), *time-domain transmissometry* (TDT), or ring oscillators (see Romano 2014, for a review). Those devices send electromagnetic pulses through metallic sticks/rings, and measure the travel time of the reflected/transmitted pulse (TDR/TDT), or the according frequency change (FDR). As the sticks are inserted into the soil, the pulse propagation depends on the permittivity of the surrounding medium (Topp et al. 1980). A non-invasive alternative is the *ground-penetrating radar* (GPR), which transmits microwave pulses several meters deep into the ground (Huisman et al. 2003). The method can visualize spatial changes of permittivity by the reflected signal, but its performance varies across soil types (see Dobriyal et al. 2012, and references therein). Nevertheless, recent studies conclusively demonstrated the value of GPR measurements for soil water estimation in the horizontal (Qin et al.

2013) and vertical dimension (Schmelzbach et al. 2012).

The measured permittivity in the field, ε, is actually a compound quantity of the individual media ε_i and their volumetric fraction f_i (Brovelli and Cassiani 2008):

$$\varepsilon^\kappa = \sum_i f_i \, \varepsilon_i^\kappa \, ,$$

where κ is a structural parameter of the porous medium. For soil with porosity Θ, volumetric soil moisture θ_v, and randomly aligned microscopic structures, $\kappa = 0.5$, this relation reveals the individual soil compartments: the bulk soil matrix, water, and air.

$$\sqrt{\varepsilon} = (1-\Theta)\sqrt{\varepsilon_{\text{soil}}} + \theta_v\sqrt{\varepsilon_{\text{water}}} + (\Theta-\theta_v)\sqrt{\varepsilon_{\text{air}}} \, ,$$

$$\text{where} \quad \varepsilon_{\text{soil}} \approx 4.6 \, (\text{quartz}) \, , \quad \varepsilon_{\text{water}}(T) \approx 78.35 \cdot e^{-(T-25)/220} \, , \quad \varepsilon_{\text{air}} \approx 1 \, , \quad [\text{F/m}].$$

If ε, Θ, and water temperature T were measured in the field, the volumetric soil moisture θ_v could be deduced. This so-called *CRIM formula* is based on a complex refractive index model (Roth et al. 1990), which is applicable to all kinds of geophysical instruments that determine electrical permittivity. The official measurement uncertainty of ring oscillators and TDRs, 1–2 $\%_v$, can vary from wet to dry conditions and is highly dependent on proper calibration against water and soil. Kögler et al. (2013) recommends a sensor-specific calibration procedure against reference media of well-known electrical permittivity (e.g., glass beads and ethylene glycol).

TDR measurements are a quick and easy way to assess integral soil moisture the first soil layers (depending on stick length). They were used in chapter 8 to conduct surveys in the *Schäfertal*, and in chapter 10 for ground-truthing of the neutron gyrocopter.

The distribution of multiple permittivity sensors in an area of a few tens to hundreds of meters is called a *soil moisture monitoring network* (SoilNet, Bogena et al. (2010)). SoilNets are intended for permanent use and typically consist of several ring oscillators ("spades") sampling the soil profile (Hübner et al. 2009), and an above-ground device to store and transmit the data. Three of those networks are operated in the `TERENO` research sites *Schäfertal*, *Großes Bruch*, and *Hohes Holz*, which were consulted in chapters 5, 7, 8, and 9. Variants of this system were developed by Mollenhauer et al. (2015) and Bumberger et al. (2015), to allow for more flexible and mobile applications. The so-called *Wireless Soil Moisture Networks* use spades of type `Truebner SMT100` and require less installation and technical efforts. Chapter 4 utilizes the system for a short-term application.

Active neutron sources

Neutrons can be used estimate water content in the field due to their extraordinarily high sensitivity to hydrogen (see chapter 3). During the last decades, researchers successfully applied the technology of active neutron generation ($\sim 10^5$/sec at $\sim$ 14 MeV) with radioactive sources like Americium and Beryllium (*Troxler Model 3440*). The ratio of detected to emitted neutrons mostly depends on the amount of effective neutron moderators in the soil (e.g., hydrogen), while being almost insensitive to soil texture. Active neutron probes have been used in a wide range of applications, e.g.,

for the detection of water flow in rocks (Hall 2013), soil contamination by petroleum (Mercer et al. 2007), or landmine detection (Obhođaš et al. 2004; Masoudi and Ghashami 2014), while Monte-Carlo simulations have supported those research activities (Pazirandeh et al. 2006).

IAEA (2008) concluded that active neutron probes are the most accurate method to estimate soil moisture profiles in the field and as such exhibit unique capabilities to provide water balance information for agricultural and irrigation management (see also Hignett and Evett 2002). However, the main disadvantages of active neutron sources constitute (1) high radioactivity, (2) soil destruction (invasiveness), and (3) footprints of less than a few decimeters in soil.

1.7.3 Cosmic-Ray Neutron Sensing (CRNS)

Cosmic radiation is permanent and omnipresent on Earth and has attracted attention to researchers since the beginning of the 20th century. Besides the charged and ionizing component, measurements of *neutrons* have become a promising tool to examine atmospheric and solar processes (see Dorman and Dorman 2014, for a historical review). After Hendrick and Edge (1966) considered near-surface water a nuisance for cosmic-ray neutron observations, Kodama (1980) discovered a relation of snow water equivalent to neutrons below ground. In a subsequent study with below-ground neutron detectors, Kodama et al. (1985) was even able to relate the measured cosmic radiation to soil water content. Then, space satellites discovered water on Mars with reflected cosmic-ray neutrons (Mitrofanov et al. 2002) which led Dorman (2004) to suggest to use albedo neutrons for soil water estimation also in environmental sciences. Soon afterwards, Zreda et al. (2005) and Desilets et al. (2007) jointly presented first measurements and simulations at two international conferences, where they tried to relate water content to neutron observations above the ground. By their first publication, Zreda et al. (2008) initiated a new field of research at the interface between hydrological and geophysical sciences.

The method of cosmic-ray neutron sensing above the ground is based on the extraordinary sensitivity to hydrogen nuclei, while most of the atoms appear almost invisible for fast neutron moderation (see section 3.2 for details). As a consequence, the fast moving particles carry their information almost unhindered along their path, which manifests itself in two most-exciting advantages compared to other techniques:

1. detected neutrons penetrated the soil down to 90 cm depth, and
2. detected neutrons diffused quickly in air across distances of hundreds of meters,

as was shown by Köhli et al. (2015) using Monte Carlo simulations (chapter 6). A single cosmic-ray neutron detector, installed just 1–2 m above ground, can sample the largely homogeneous neutron density at one location, thereby providing an area-average soil moisture signal of tens of hectares and tens of decimeters depth. Admittedly, hydrogen sources that are unrelated to soil moisture are visible in the integral CRNS signal, too. Most of them can be easily identified with additional, independent measurements (e.g., Baroni and Oswald 2015), while correction approaches exist to further address static and meteorological influences (sections 3.5 and 3.6).

Since the research field is still rather young, the question of sensor comparability has not been studied yet (chapter 4), while some of the correction approaches may need further improvement (chapter 5) or additional experimental verification (chapters 7, 8). Moreover, advances in detector technology (chapter 10) are logical steps to improve the method even further. Nevertheless, cosmic-ray neutron sensing has become a well-established alternative to non-representative point measurements (Franz et al. 2012a; Pang et al. 2016), with increased accuracy under dry conditions (see also Figures 3.6b, 3.8b).

The "global coverage" of such monitoring stations started with the COSMOS network in the United States (Zreda et al. 2012), and since then further networks have been evolved all over the world (Fig. 1.3 and Table 1.1). As many studies already have indicated, the CRNS method could be most beneficial in future applications linked to agricultural management (e.g., Rivera Villarreyes et al. 2011; Coopersmith et al. 2014; Franz et al. 2016, among others) and hydrological/land-surface modeling (see chapter 9 and references therein).

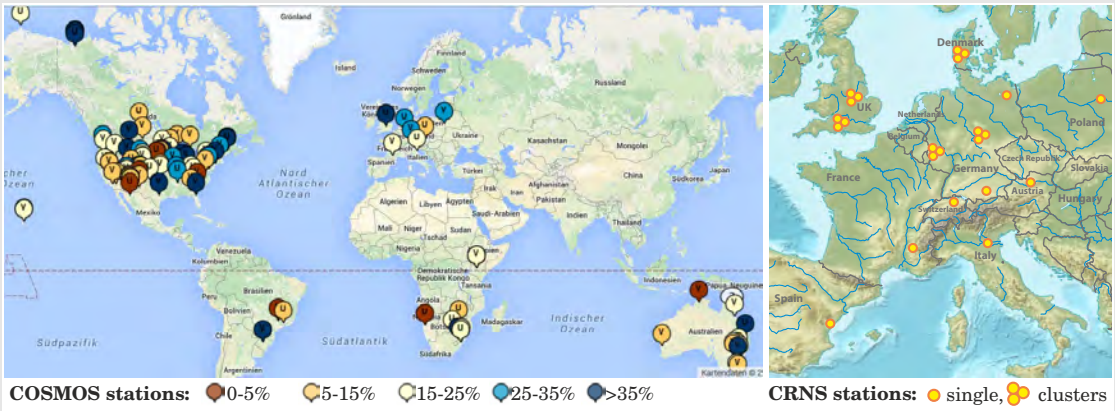

Fig. 1.3: Existing CRNS stations around the world: (left) stations listed in the COSMOS online platform[1], (right) European stations and clusters (> 2 stations).

Table 1.1: List of large networks for soil moisture monitoring with cosmic-ray neutron sensors.

Network	Country	Reference	Website
COSMOS	USA	Zreda et al. (2012)	cosmos.hwr.arizona.edu
TERENO	Germany	Zacharias et al. (2011)	teodoor.icg.kfa-juelich.de
COSMOS-UK	UK	Fry et al. (2014)	cosmos.ceh.ac.uk
CosmOz	Australia	Hawdon et al. (2014)	cosmoz.csiro.au

[1] cosmos.hwr.arizona.edu

Fig. 2:
An artist's view of galactic, solar, and atmospheric cosmic rays. *Credit: Own montage using images from pixabay.com, PhotosForClass.com, NASA/ESA*

2.

Messengers from Space

Origins and Impact of Cosmic-Rays

As early as 1054, people on Earth witnessed a supernova event by its intensive luminosity at the night sky. Then in 1912, Victor Hess discovered cosmic radiation for the first time and was awarded the Nobel Prize in physics. Since that time, scientists have been curious about the origins of cosmic radiation and have conducted measurement campaigns from the deepest caves of the Antarctic to the farthest places of the solar system.

To understand the cosmic-ray signal at the Earth's surface, it is beneficial to know about the paths it took all the way down. Knowledge about incident energies as well as spatial and temporal variations has been collected over the years, and it is astonishing to see to what extent cosmic radiation has determined and still determines our everyday life.

Astrophysicists, space scientists, and radiologists have laid a profound basis in the last decades, and it is now for us to make use of this knowledge on behalf of hydrology, environmental science, and society.

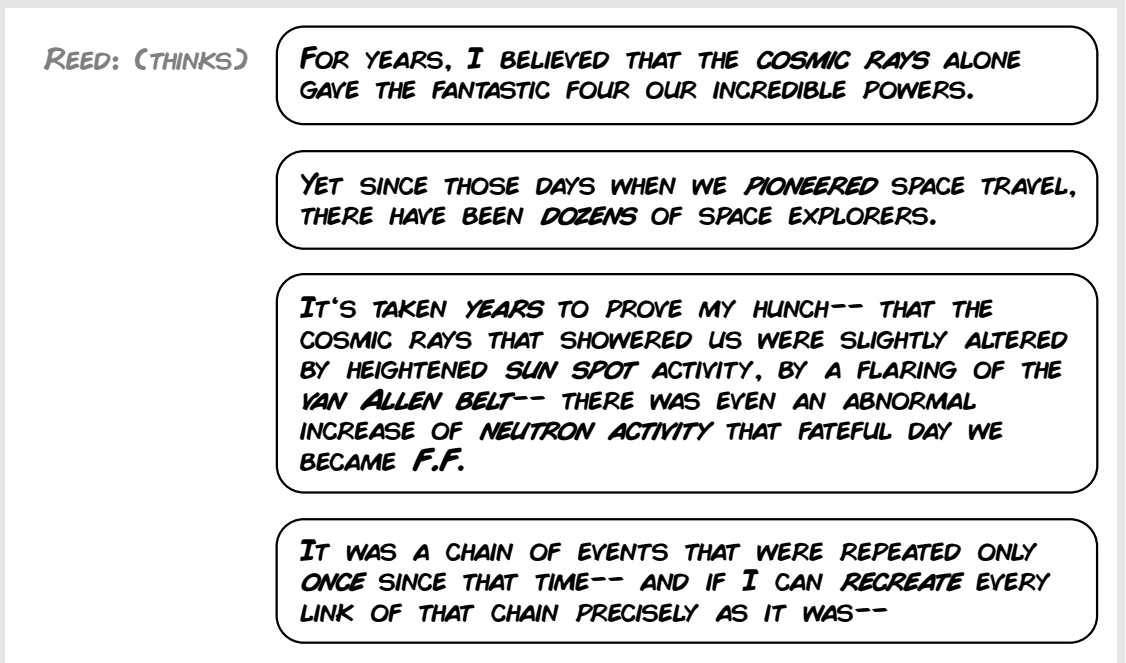

Fig. 2.1: Cosmic rays gave the *Fantastic Four* their power due to abnormally high neutron activity; quoted from "Fantastic Four" Vol. 1, by S. Lee, J. Kirby, G. Klein, and C. Rule (1961), ISSN: 0274-5291, Marvel Comics. (Lee et al. 1961).

2.1. Mechanisms in outer space

2.1.1 Senile stars give birth to cosmic rays

Due to their high gravitational pressure, stars are able to induce fission reactions in their inner shells, thereby generating deuterium, carbon, oxygen, and all the other elements below the atomic mass of $A = 56$ in the universe. However, fission is energetically unlikely for heavier elements. Nuclei of lead, uranium, or gold, for instance, were produced under inconceivable pressures that typically occur during a *supernova*: the final event in the life of a star, after gravitation has turned to dominate over the outward radiative pressure. In a blink of an eye (at time scales of solar evolution) all the massive layers of a star collapse to the center, where nuclei merge with larger nuclei, and even protons merge with electrons. The rapidly increasing density of the core abruptly repels the collapsing material, which turns to an outward directed, super-fast shock front.

Fig. 2 shows a photograph of such supernova remnants in the top right corner (credit: NASA/ESA, J. Hester). The so-called *Crab Nebula* has the size of $5–6 \cdot 10^{16}$ m and is still extending. The historic supernova event was witnessed by humans in the year 1054, as the star imploded and blew out high-energy gamma radiation and charged particles, as well as its shell full of hydrogen, oxygen, and other elements. A compact neutron star was left behind, spinning so fast that it ejects additional

charged particles into the interstellar medium and forms a strong rotating magnetic field. The latter interacts with the galactic magnetic fields of the interstellar medium, and both become tightly bonded in shock regions of the supernova remnants. The strong density gradients therein introduce immensely steep magnetic gradients that motivate passing charged particles to accelerate to energies of several hundreds of GeV, allowing them to leave local structures, to cross the galaxy, and to finally end up at our beloved solar system.

2.1.2 Cosmic rays require tremendous acceleration

Vink et al. (2006), among others, suggested that supernova remnants could be efficient cosmic-ray accelerators, because they exhibit regions of extremely dense matter, dense magnetic fields, and high temperature. And in fact, these "origins of cosmic rays" have been recently confirmed with two independent observational approaches (Ackermann et al. 2013; Nikolić et al. 2013).

The main acceleration processes of cosmic rays take place in so-called *diffusive shocks* (Blandford and Ostriker 1978; Malkov and Drury 2001), which usually occur in supernova remnants (Hillas 2005). As thermal cosmic-rays pass the dense shock region, the strong magnetic gradient forces them to spin around the shock multiple times. Each turn accelerates the particle further until enough energy is reached to leave the structure. Therefore properties of the shock determine the exponent of the cosmic-ray energy spectrum (Blasi 2013), which has been observed to peak at about 1 GeV and quickly decreases logarithmically (Fig. 2.2). As this peak energy is too low for intergalactic distances, most cosmic rays are expected to originate in our galaxy. The fraction of particles with energies beyond 10^{15} eV must have extragalactic origins, where long-living jets and outflows from active galactic centers can contribute to post-acceleration of cosmic-rays (Dorfi and Breitschwerdt 2012). Those shock-forming winds can also be generated in our galaxy by heavy stars, while outflows generated during star formation are rather unlikely to meet the criteria of sharp and well-heated shock fronts (e.g., Federrath et al. 2014). Just recently, Abramowski et al. (2016) showed that high-energy cosmic-rays can also be accelerated by gravitational forces in the vicinity of black holes at the heart of our galaxy.

2.1.3 Cosmic rays are mostly positive

As observed by Lacki et al. (2010), the ratio between protons and electrons is estimated to 10:1, where significant uncertainties must be taken into account as a result of measurements at the far-infrared end of the radio spectrum. Protons not only portray the majority of cosmic-ray particles, they also carry most of the corresponding energy (as protons are much more massive than electrons).

As a result the net charge of cosmic rays on Earth appears to be highly positive, although no discrimination of charges is made in shock regions or outflows. Sources of cosmic-rays are therefore generating a neutral net amount of protons, electrons, and positrons. However, on their way through the galaxy cosmic-rays interact with the microwave background by the so-called *inverse Compton scattering* (Sarazin and Lieu 1998). This effect transfers energy from particles to photons, which is most

efficient for low-mass particles and thus leads to under-representation of galactic electrons and positrons in our solar system.

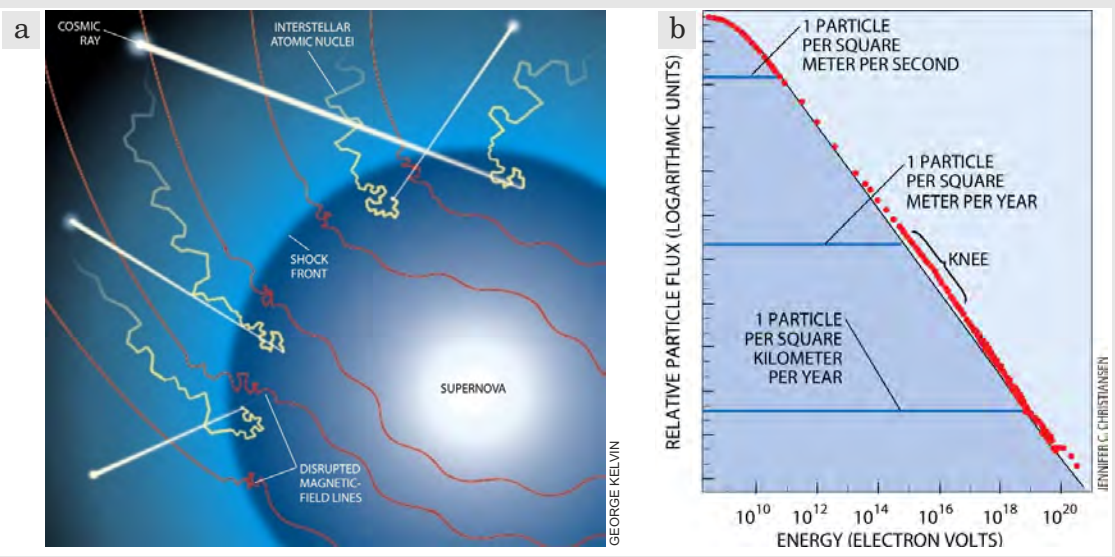

Fig. 2.2: Galactic cosmic rays: a particle acceleration by disturbed magnetic fields in dense shock regions of supernova remnants, b energy spectrum of observed cosmic rays with typical energies of 1 GeV, and an indication of extra-galactic processes beyond the "knee". *Credit: both figures from* Cronin *et al. (1997).*

2.1.4 Cosmic rays are almost isotropic

Cosmic radiation undergoes several non-linear processes and scattering effects, preventing it from streaming freely through the interstellar medium (see Breitschwerdt et al. 2002; Zweibel 2013). Furthermore, the charged particles are deflected by magnetic fields, which are omnipresent in space. The motion can be described as "random walk", which is governed by the laws of diffusion. However, diffusion along magnetic field lines requires energy-dependent diffusion coefficients, making accurate prediction of their pathways a complex challenge for theoretical physicists. Simulations suggest that this diffusion process is almost isotropic on the scale of the *Milkyway* (Strong et al. 2007). Although supernovae happen only every few decades in our galaxy, the time scale of particle diffusion through the magnetic field structures is of the order of thousands of years. Therefore, the incoming radiation in the solar system is almost uniform and isotropic with intensity variations of less than $\approx 0.1\,\%$.

2.1.5 Our sun as a protector and perpetrator

The solar magnetic field contributes to deflection and spatial smoothing of incoming *galactic cosmic rays* (GCR). For example, in periods of high solar activity, its stronger magnetic field reduces the GCR intensity to a minimum (see Fig. C.1). The sun also produces *solar cosmic rays* (SCR) itself, which usually have minor influence on Earth

due to their low energy (see section 2.1.2). However, large solar-plasma releases, so-called *coronal mass ejections* (CME), are able to reach the Earth and to cause *ground level enhancements* (GLE) of cosmic ray intensity (Moraal and McCracken 2012). Alternatively, CMEs can strengthen the solar magnetic field for a short time, which translates to GCR reduction from a few hours to days. These so-called *Forbush decreases* (FD) were investigated by Belov (2008), among others, and are also visible to CRNS data (Mar 2012 in Fig. C.3, and Sep 2014 in Fig. 5.6). During periods of high solar activity, CMEs can occur three times per day, while only occuring every fifth day in quiet periods.

2.1.6 Periodicity

The most prominent temporal variation of incoming cosmic radiation is the 11-year oscillation of the solar magnetic field, which periodically prevents more or less galactic cosmic rays from entering the solar system. To be accurate, our sun reverses its magnetic polarity every 11 years, resulting in a full cycle period of actually 22 years.

Daily, monthly, and seasonal oscillations can be observed in various energy bands of the incoming signal (Rühm et al. 2012). For example, the famous 27-days cycle can be explained by the sun's rotation around its own axis, while the corresponding amplitudes may increase due to the growth of the atmosphere as it gets warmer (Dorman 2004). In fact, a manifold of other periodicities (e.g., 9 days, 154 days, 1.7 years, among others) were found using wavelet analysis (Zarrouk and Bennaceur 2009; Mavromichalaki et al. 2003), and indicate more complex mechanisms in outer space ranging from solar activity to planetary interactions (see Kudela 2012, and references therein).

2.2. Mechanisms on Earth

2.2.1 Deflection by the magnetic field

In contrast to the complex magnetic field of the sun, the Earth's magnetic field exhibits a simple dipole structure and spreads cosmic rays slightly anisotropically across the atmosphere. This shape, combined with its slight shift of the magnetic angle compared to the Earth's rotational axis, is able to effectively shadow or favor individual particle trajectories depending on their charge and energy. Consequently, incident cosmic rays exhibit a slight day-night effect, while arriving at the Earth's atmosphere from different directions. According to Cooke et al. (1991), the viewing directions on Earth can be classified as (1) a cone of allowed incident angles, (2) a cone of forbidden angles, and (3) a *Penumbra* region where incident particles are possible depending on their energy. For example, positively charged particles from the eastward direction exhibit much higher cutoff rigidities, which manifests itself in the so-called *East-West effect*, given the fact that the *allowed cone* is aligned to the West at any place on Earth (Jacklyn and Fenton 1957).

Since most of the primary cosmic rays are charged particles, their paths are governed by the Lorentz force $F_L = q\vec{v} \times \vec{B}$, which strongly depends on local magnetic field conditions $\vec{B}$, and the inclination angle $\measuredangle(\vec{B}, \vec{v})$ between $\vec{B}$ and the incident particle velocity $\vec{v}$. The related quantity is called *rigidity*, $R_{\text{mag}} = m/q \cdot \vec{v}/\vec{B}$ (also

known as P or r), its connection to the particle energy is given by $E = \vec{p}^2/m$, where $\vec{p} = m\vec{v}$. The rigidity can also be interpreted as the spinning radius of a particle around the magnetic field line. The higher the rigidity, the more likely is the deflection of the cosmic ray. As a consequence, particles that arrive orthogonally onto the Earth, $\vec{v} \perp$ surface, are more likely to be rejected at the equator, where $\vec{B} \parallel$ surface $\Rightarrow \measuredangle(\vec{B}, \vec{v}) = 1$ (maximal rejection force F_L). On the other hand, the dipole field is almost orthogonal to the surface at the poles, leading to $\vec{B} \perp$ surface $\Rightarrow \measuredangle(\vec{B}, \vec{v}) = 0$ (no rejection) and thus allowing more primary cosmic rays to arrive on Earth at low latitudes. This concept is energy-dependent, where particles above a certain *cutoff rigidity* R_cut are rejected, depending on the shape of $\vec{B}$ and the particle's momentum $\vec{p}$ (see also contour lines in Fig. 5.1). In other words, the intensity of cosmic rays that made it through the magnetic field can be estimated with:

$$N(R > R_\mathrm{cut}) = \int_{R_\mathrm{cut}}^{\infty} \frac{dN}{dR} dR\,.$$

The term $-dN/dR$ is the *differential response function* (DRF), which is proportional to the primary cosmic ray intensity $I_\mathrm{prim}(R, t)$ and the local yield function $Y(R, z_\mathrm{atm})$. The DRF can be estimated by latitude surveys or by comparing signals of multiple neutron monitors (Krüger et al. 2008). Based on this concept, Dorman et al. (1970) developed an approximate function for the DRF in order to relate incoming neutron radiation depending on the vertical cutoff rigidity R_cut:

$$N = N_\mathrm{base}\left(1 - e^{-\alpha R_\mathrm{cut}^{-k}}\right),$$

where $N_\mathrm{base} \approx 5.17 \cdot 10^4$ cph, $\alpha \approx 9.0212$, and $k \approx 1.05$ are sufficient fitting parameters to neutron monitor data (Usoskin et al. 1999). Following this approach, the base neutron intensity can drop below 50 % at the equator, while the location of Leipzig ($R_\mathrm{cut} \approx 3.06$ GV) suffers from a reduction of neutron radiation by ≈ 7 %.

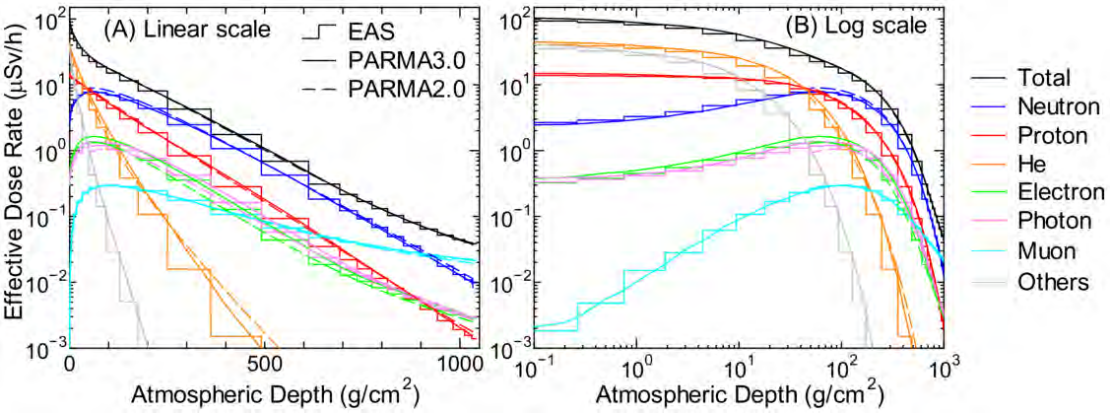

Fig. 2.3: Dose rate over altitude for various cosmic-ray particles. Neutrons (blue) show a maximum at $z_\mathrm{atm} = 50$–100 g/cm^2 atmospheric depths (Pfotzer 1936), and decrease towards sea level (≈ 1020 g/cm^2). *Credit: Figure taken from* Sato *(2015), Fig. 20.*

2.2.2 Reactions in the atmosphere

Hess et al. (1961) has laid the basis for research on incoming cosmic-ray neutrons and further explored their tendency to form isotopes in the atmosphere or to leak out and decay. As soon as primary cosmic rays touch the first layers of the Earth's atmosphere, their reactions with the molecules start to generate particles like neutrons, among others, that reach a maximum intensity at $z_{\mathrm{atm}} = 50$–$100\,\mathrm{g/cm^2}$ atmospheric depths (Pfotzer (1936), see also Fig. 2.3). To be accurate, the charged particles collide with air nuclei, generating *hadrons* (i.e., neutrons, protons, pions, kaons) that induce additional hadronic showers until they reach the surface (compare Fig. 2). The following processes and particles are involved:

- neutral pions π^0 decay into photons that can induce electron-positron showers,
- charged pions $\pi^\pm$ decay into neutrinos ν and charged muons $\mu^\pm$,
- also charged kaons $K^\pm$ can be involved in the generation of muons and pions,
- charged muons $\mu^\pm$ are able to penetrate the Earth's surface up to several tens of meters and can be detected with scintillators or cameras,
- hadrons ($\pi^\pm$, p^+, n^0) collide with air nuclei and create additional showers.

Especially the collision of hadrons with nuclei leads to a wide spreading of neutrons and muons. A single interaction can therefore cover a large surface area with secondary particles.

2.2.3 Creation of cosmogenic nuclides

Since the Earth has formed, cosmic rays bear the major responsibility for nuclear transformations (i.e., isotope generation and radioactivity) in the Earth's atmosphere, hydrosphere, and lithosphere (Lal 1991). The corresponding products are widely used for dating (age determination) in environmental sciences (Phillips et al. 2016). One of such isotopes is tritium, which has been applied in oceanic research as a tracer for ocean circulation and ventilation (Doney et al. 1997). The following list shows the most famous isotopic products of cosmic-ray interactions with air molecules, depicted in the isotopic notation of elements containing a number of protons p and neutrons n: ${}^{n+p}_{p}\mathrm{element}$.

$$\begin{aligned}
\text{Tritium } {}^{3}\mathrm{H}\text{, created by} \quad & {}^{14}_{7}\mathrm{N} + \mathrm{n} \xrightarrow{\text{spallation}} {}^{12}_{6}\mathrm{C} + {}^{3}_{1}\mathrm{H}\,, \\
\text{Beryllium } {}^{10}\mathrm{Be}\text{, created by} \quad & {}^{14}_{7}\mathrm{N} + \mathrm{n} \xrightarrow{\text{spallation}} {}^{10}_{4}\mathrm{Be} + {}^{4}_{2}\alpha + \mathrm{p}\,, \\
\text{Carbon } {}^{14}\mathrm{C}\text{, created by} \quad & {}^{14}_{7}\mathrm{N} + \mathrm{n} \xrightarrow{\text{activation}} {}^{14}_{6}\mathrm{C} + \mathrm{p}\,,
\end{aligned}$$

The radio nucleids ${}^{14}\mathrm{C}$ and ${}^{10}\mathrm{Be}$ were produced from collisions of cosmic rays with atmospheric nitrogen and oxygen (Masarik and Beer 2009). ${}^{14}\mathrm{C}$ then combines to $\mathrm{CO_2}$ and enters the global carbon cycle, where it falls out in tree rings or other organic material that contributes to $\mathrm{CO_2}$ exchange. On the other hand, ${}^{10}\mathrm{Be}$ attaches to aerosols and with them is removed very quickly from the atmosphere, falling out in polar ice sheets, for instance (cmp. Fig. 2).

From analysis of these "natural neutron monitors", Steinhilber et al. (2012) were able to identify historic cosmic-ray modulation of the past 9 400 years. In the

light of this enormous time series it can be concluded that the current intensity N of cosmic-rays on Earth has reached its global minimum since 7390 B.C.. The corresponding solar maximum generates significant temporal variations, while the relative measurement error $\sqrt{1/N}$ (section 3.7) of cosmic-ray neutrons contributes to maximum uncertainty for any measurement on Earth (see also Appendix C).

It is thus venturesome to do research of neutron radiation in such a late period of the Quaternary, and it will be a challenge to conduct scientific experiments that allow for accurate conclusions on soil moisture despite all the other sources of errors involved.

2.2.4 Neutron Monitors

Since a few decades, scientists examine the temporal variation of primary cosmic-ray showers with so-called *neutron monitors* (NM), large helium detectors surrounded by lead in order to extent its sensitivity towards primary protons (Mavromichalaki et al. 2011). More than 60 stations exist around the globe, out of which Table 2.1 lists the most relevant for this work, with special regards to chapter 5 and Appendix C.

Table 2.1: Neutron monitor stations that are geomagnetically close to Leipzig (cutoff rigidity around $R_{\text{cut}} \approx 3.06\,\text{GV}$).

station	location	altitude	R_{cut}
KIEL	Kiel (Germany)	54 m	2.36 GV
NEWK	Newark (USA)	50 m	2.40 GV
JUNG	Jungfraujoch (Switzerland)	3570 m	4.49 GV
IRKT	Irkustk (Russia)	475 m	3.64 GV

2.2.5 Mostly harmless?

Neutrons can actually do have impact on organic materials by kicking hydrogen out of a molecule (e.g., DNA), or by being captured, exciting the target nucleus, and forcing it to perform spallation or to release highly energetic protons. Following this argumentation, Astbury (2005) discovered that cancer mortality and cosmic-ray dose share similar geographical dependence. Juckett (2007) also found a relation between cancer deaths and cosmic radiation by analyzing historical datasets. Their measurements (e.g., ^{10}Be) demonstrated remarkable correlation not only to temporal variations from solar activity, but also to the geomagnetic cutoff rigidity (i.e., to latitude).

However, the corresponding molecular alteration must not necessarily lead to significant damage. On the contrary, those reactions also contributed to biological mutation, and finally to evolution on Earth (Erlykin and Wolfendale 2010; Atri and Melott 2014). Moreover, cosmic radiation is even suspected of influencing tree growth by biological interactions at the molecular scale (Sax 1963) or by altering available sunlight due to aerosol formation (Dengel et al. 2009), which is however still under critical discussion (Kulmala et al. 2009).

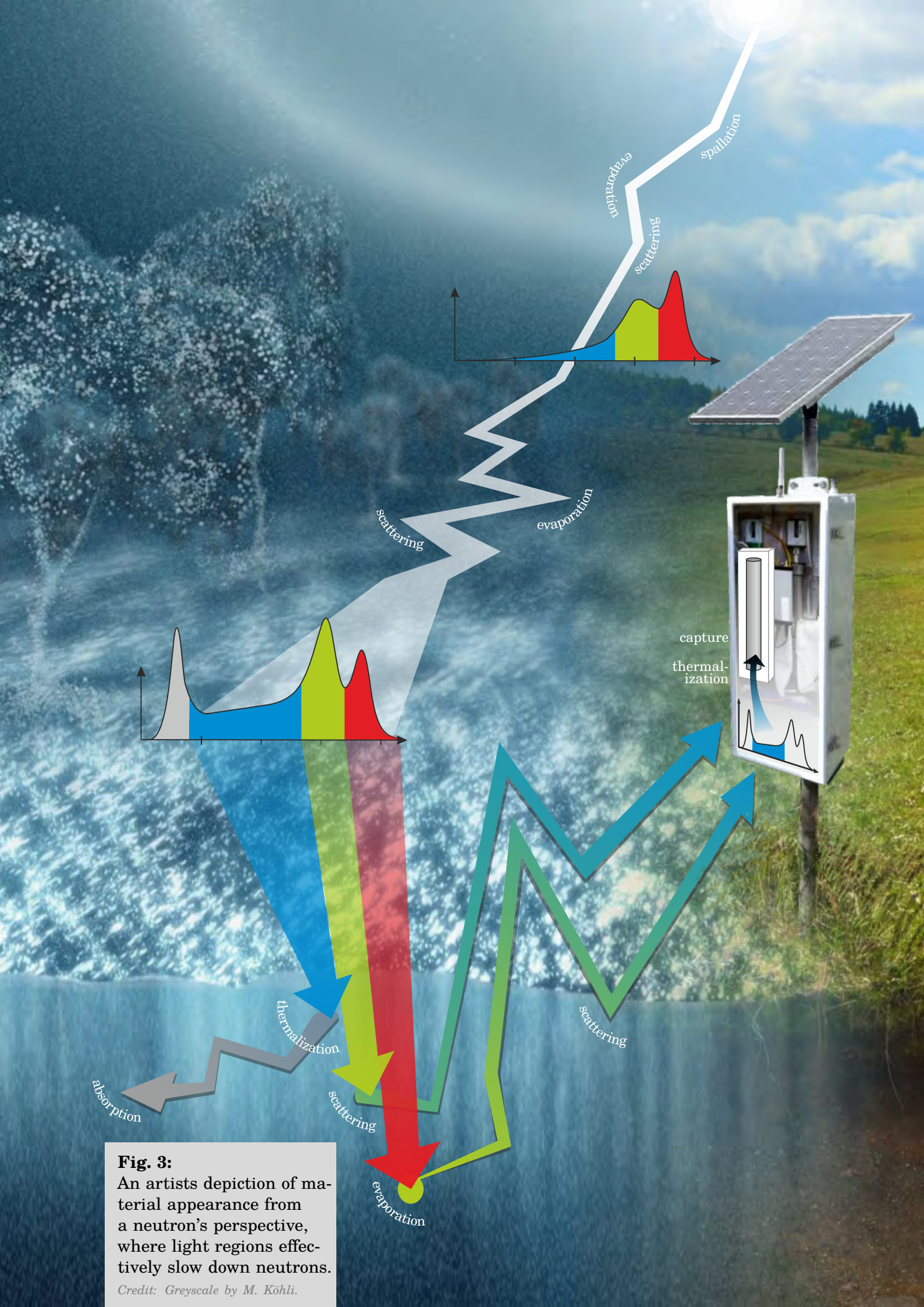

Fig. 3:
An artists depiction of material appearance from a neutron's perspective, where light regions effectively slow down neutrons.

Credit: Greyscale by M. Köhli.

3.

The Moderate Life of a Neutron

Physics from generation to detection

This chapter discusses the unique properties of neutrons, introduces the CRNS detector system, and presents the transfer functions for soil moisture. Following the generation of high-energy neutrons in the atmosphere (chapter 2), their journey towards the Earth's surface, through the soil, and into the detector, is accompanied by progressive energy loss (i.e., moderation). The following short story outlines the relevant processes from a personal, metaphoric point of view:

> "Unlike most particles, a neutron is born with a maximum motivation and spends its life to get rid of it. To make a long story short, its ever-positively thinking brother is especially good at dragging the neutron down. Every interaction, every rebuff turns poor neutron down even more. Before it ends up slam-dancing in a troubled graveyard. This is the only place where short-term euphoria can occur.
>
> But watch out, there are dark shapes lingering around the tombs, which are hungering for these depressive little neutrons. In a fraction of a second, poor neutron gets bound to a group of excited nucleons. But eventually some day, an accidental collision, a senile decay, or divine external force may induce its reincarnation. Great to have you back, little pilot, reborn with whatever motivation the prior event has left.
>
> There are stories about a neutron that grew lonely by the absence of interaction, vanished within a few minutes, and has never been seen ever since. Some scientists say that it managed to divest its negative ego and turned to something more cheerful, sprightly enjoying the rest of its life until the end of the universe.
>
> But this is *not* the story about protons."

3.1. Birth and decay

It is very unlikely to generate neutrons out of nothing just from quantum foam. *Heisenberg's uncertainty principle*, $\Delta E\,\Delta t \geq \hbar/2$, offers to loan neutrons, $E = m_\mathrm{n}\,c^2$, for less than 10^{-22} seconds, which is just too short for most applications, particularly for environmental monitoring (Brocca et al. 2010, 2012).

Fortunately, most neutrons evolve from precursors like protons, p^+, either by radioactive decay inside heavy nuclei, or by external pressure during the *Big Bang* or *super novae*, where electrons and protons can merge to form the neutral particle:

$$\mathrm{p} \xrightarrow{\text{decay}} \mathrm{n} + \mathrm{e}^+ + \nu_e \quad \text{(inside a nucleus)}$$
$$\mathrm{e}^- + \mathrm{p} \xrightarrow{\text{capture}} \mathrm{n} + \nu_e \quad \text{(under high pressure)}$$
$$\mathrm{n} \xrightarrow{\text{decay}} \mathrm{p} + \mathrm{e}^- + \bar{\nu}_e \quad \text{(free)}$$

Free neutrons in vacuum decay with a halflife of ≈ 10 min (Christensen et al. 1972) to protons, electrons, and neutrinos. Once decayed, the resulting free protons have never been observed to decay before 10^{35} years (which is a matter of speculation).

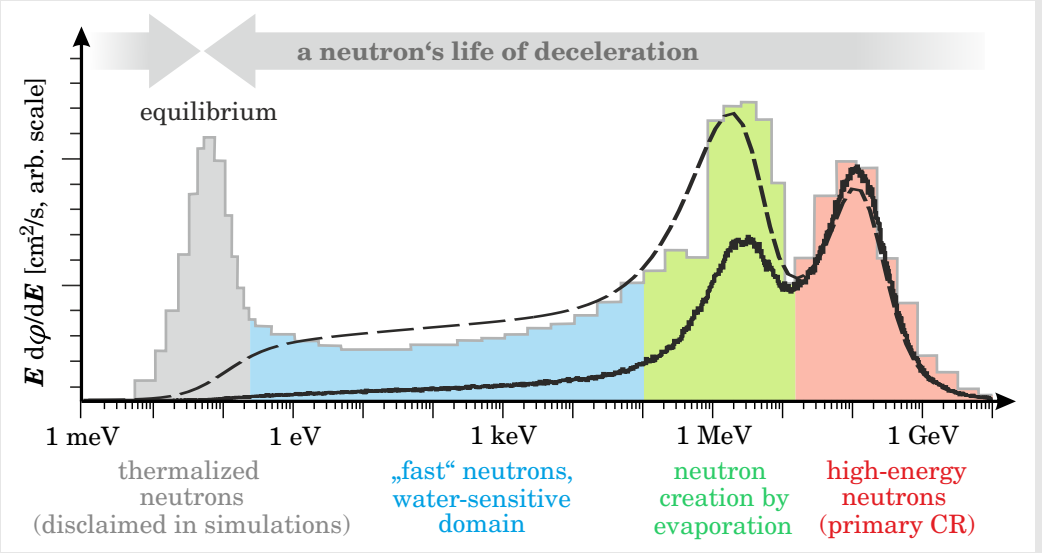

Fig. 3.1: Typical neutron energy spectra at the surface represent incident and reflected neutrons. The figure shows; measurements by Goldhagen et al. (2002) (grey line), simulations by Sato and Niita (2006) (dashed), and pure incoming component by Köhli et al. (2015) (black line) which is used as the source spectrum in URANOS (chapter 6). Colors illustrate initial high-energy neutrons (red), which interacted with heavy atoms and turned to evaporation neutrons (green), which in turn collided elastically with light atoms in the detector-sensitive regime (blue), and finally thermalized (light grey). *Credit: Figure adapted from Köhli et al. (2015)*

3.2. Processes down the path of energy loss

Neutrons have an electrical charge of the factor 10^{-22} smaller than that of an electron, and can thus be considered as entirely neutral with regards to the measurement uncertainties (Olive and Particle Data Group 2014). As a consequence, there is no interaction with electrons or atom shells, which fill up a factor of $\approx 10^{15}$ more volume of space than a single nucleus. In strong contrast to experiments in chemistry or optics, for instance, neutron interactions are extremely rare compared to the number of particles present, and are thus hard to detect.

However, the constituent quark particles do have electrical charge, individual spins, and are orbiting the potential well of the strong force. Thereby creating a total spin $s = 1/2$ and angular momentum $S \propto \sqrt{s(s+1)}$ of the neutron, and consequently provoking a tiny magnetic moment $\mu \propto S \cdot q/m$ (Beane et al. 2014). However, electromagnetic interactions are negligible in environmental situations, where (quantum-)mechanical collisions are the main process for neutron interaction.

Chapter 2 explained that primary cosmic-rays of energies around 1 GeV induce secondary showers of high-energy neutrons in the atmosphere at ≈ 100 MeV. The responsible reactions often lead to *spallation* and incorporate pre-equilibrium processes and intranuclear cascades, as the *deBroglie wavelength* $\lambda_{\mathrm{dB}} = h/\sqrt{2mE}$ of the incident projectile is short enough to interact with individual nucleons inside the nucleus (see Gudima et al. 1983, and references therein).

The resulting high-energy neutrons (red in Fig. 3.1) may further collide with atoms in air or soil. As the captured neutron hesitantly "jumps down" in the nuclear energy shells, the excited nucleus releases gamma rays or decides for radioactive decay or spallation. The latter processes may release neutrons around 1–2 MeV, as this is the average binding energy in nuclei. The process is also called *evaporation* and manifests itself at the green peak in Fig. 3.1.

The processes described above can be interpreted as *inelastic collisions*, while the sub-MeV regime is governed by *elastic collisions* (blue in Fig. 3.1). Neutrons in this regime are typically referred to as *fast neutrons*, and their energy loss is roughly correlated with the mass of the target nucleus (eq. 3.1). Following the principles from classical mechanics, hydrogen as the lightest atom is most suited for neutron moderation in this regime, and thus responsible for the success of the cosmic-ray neutron sensing (CRNS). However, this rule does not set along, because neutrons belong to the group of fermions, just like electrons, which prefer to pair up. The best neutron absorbers are therefore isotopes that need just one neutron to fill their nuclear energy shells. Good examples are ^{3}He, ^{6}Li, and ^{10}B, which are consequently used to design neutron detectors (see section 3.3.2).

Depending on the moderation potential of the environment (e.g., the number of hydrogen atoms), fast neutrons slow down below the elastic regime, which was detectable by moderated counters (see section 3.3), and enter the *thermal equilibrium* with the environment (grey in Fig. 3.1). Here, the atoms of the surrounding material exhibit similar energies as the neutron, which is $E_{\mathrm{th}} = k_{\mathrm{B}}\, T \approx 25$ meV at 25 °C, and the corresponding collisions contribute to permanent acceleration and deceleration around the average energy.

The benefit of thermal neutrons for CRNS research and hydrology has never been elaborated consistently in literature. However, hints to other research fields like earthquake detection have been published (e.g., Alekseenko et al. 2009; Salikhov et al. 2013). The accepted theory is that earthquakes open up fissures in the Earth's crust, through which radioactive gases can escape and quickly decay to α particles and neutrons. Moreover, variations of the thermal neutron signal may highly depend on individual site conditions, as many elements in the subsurface are efficient absorbers for thermal neutrons, e.g., Cl, Fe, Gd, Mn, or Ti. As chlorine is highly abundant in most soils, a *chlorine-equivalent* is often determined in planetary science to assess soil composition (e.g., Litvak et al. 2014; Mitrofanov et al. 2014).

3.2.1 Interaction probability (cross sections)

The probability of a neutron interaction with a target can be expressed by the term *cross section*, σ [b, barn]. Just like the target disk in archery, the unit $1\,\mathrm{b} = 10^{-28}\,\mathrm{m}^2$ can be interpreted as the geometrical area of the target particle with regards to the *deBroglie wavelength* $\lambda_{\mathrm{dB}} = h/\sqrt{2mE}$ of the incident neutron. As such, $\sigma(E)$ is a function of neutron energy and depends on the target composition, for which the circular geometry is a rather ragged picture.

Cross sections published in the *Evaluated Nuclear Data File* (ENDF, www.nndc.bnl.gov) were determined either experimentally or by complex calculations. Unfortunately, experiments with high-energy neutrons exhibit uncertainties of up to 50% and are usually extrapolated with theoretical models, however, progress has been made to narrow the results (Salvatores et al. 1994; Palmiotti et al. 2007). In order to minimize the issues with high-energy interactions in neutron transport simulations, Köhli et al. (2015) recommend to use verified near-surface spectra as model input.

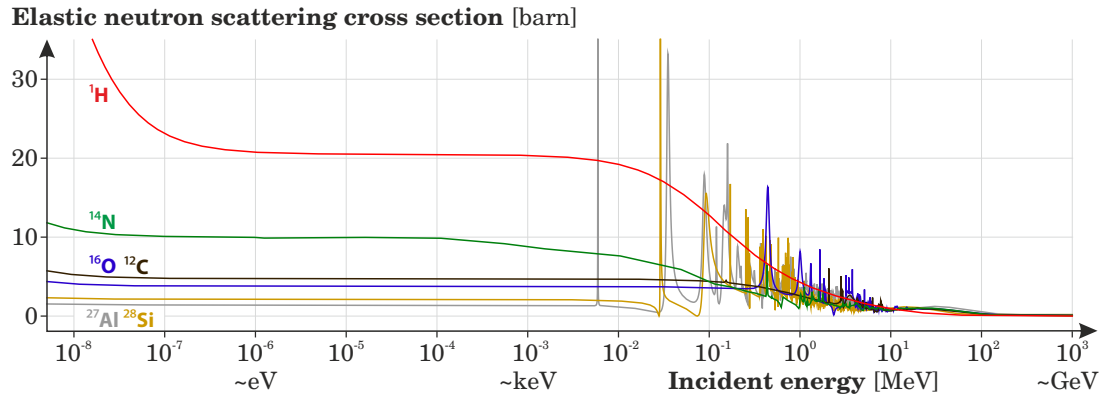

Fig. 3.2: Comparison of elastic neutron cross sections of hydrogen (red), nitrogen (green), oxygen (blue), carbon (black), silicon (ocher), and aluminum (grey) for kinetic energies between 5 meV and 1000 MeV, data taken from JENDL/HE-2007 (Shibata et al. 2011). *Credit: Figure and caption from Köhli et al. (2015).*

Different (microscopic) processes can be arranged in different cross sectional categories. For example, the *scattering cross section* σ_{sct} of a target quantifies its probability to scatter incident neutrons, either inelastically or elastically. On the other hand, the *absorption cross section* σ_{abs} denotes the probability to perform neutron capture (absorption). There are nuclei that are talented in both, for example hydrogen. For applications of the CRNS technology, scattering cross sections are most relevant, as they determine the efficiency with which a material (e.g., soil or water) moderates fast neutrons, i.e., removes neutrons from the detectable energy regime. Fig. 3.2 shows elastic/scattering cross sections of the six most relevant elements in everyday life. While the exceptional position of hydrogen is evident, decreasing probability and resonances occur for most elements at higher energies.

3.2.2 Practical quantities for neutron moderation

With the help of the *microscopic* cross sections σ_{sct} and σ_{abs} of individual elements, the *macroscopic* response to neutrons can be derived for certain materials. The *macroscopic cross section* $\Sigma = \sigma \cdot \varrho$ denotes the interaction probability of a material with neutrons, where ϱ is the number density (elements per volume) therein. For example, the cross section for Gadolinium is many orders of magnitude higher than that of hydrogen, however, its abundance in soil is so low that neutrons still exhibit a higher macroscopic cross section for soil water.

Moreover, the *mean logarithmic reduction of the neutron energy E per collision*, ξ, is an important quantity in slow down theory that describes the rate of energy loss per interaction in the elastic scattering regime (Dobrzynski and Blinowski 1994):

$$\xi := \ln \frac{E_0}{E} = 1 + \frac{(A-1)^2}{2A} \ln\left(\frac{A-1}{A+1}\right) \approx \frac{2}{A+1}\,, \tag{3.1}$$

where A is the atomic mass number of the considered element. It can be directly linked to the *number of collisions* n_{coll} necessary to slow a neutron of energy E_0 down to E_1: $n_{\text{coll}} = \ln(E_0/E_1)/\xi$.

Following these equations, it can be estimated that fast neutrons ($\approx 10^6$ eV) need ≈ 18 collisions with hydrogen to get thermalized below 10^{-5} eV, whereas collisions with large nuclei like iron take more than 500 collisions. This is the reason why the effect of metallic cases is negligible, as the CRNS detector is often used in cars and aircrafts (chapters 8 and 10).

The energy loss per collision and the macroscopic cross section both constitute the *stopping power* $\Xi_{\text{pow}} = \xi \cdot \Sigma_{\text{sct}}$ of a material. Zreda et al. (2012) exhaustively uses this quantity to argue that hydrogen has by far the highest stopping power in soils, thus its impact on fast neutrons is most dominant among relevant elements.

Finally, the so-called *moderating efficiency* $\Xi_{\text{eff}} = \xi \cdot \Sigma_{\text{sct}}/\Sigma_{\text{abs}}$ incorporates the material's capabilities to absorb neutrons. For example, Stacey (2007) explains that heavy water, D_2O, needs twice as much collisions to thermalize a neutron compared to light water, H_2O. However, hydrogen is also a much better absorber than deuterium, such that the moderating efficiency of heavy water becomes larger by a factor of 80. This property to moderate, but not to absorb neutrons is highly appreciated for root water experiments using neutron tomography (Oswald et al. 2008), or in nuclear reactors.

Depending on the macroscopic cross section, the *mean free path* $\lambda = 1/\Sigma$ through a material describes the distance a neutron can travel without an interaction (e.g., collision). Consequently, fast neutrons may travel hundreds of meters in air between collisions, while they cannot freely pass the soil in more than a few tens of centimeters. This is the reason why the proper choice of the neutron source is important to calculate the CRNS footprint (chapter 6), as fast neutrons released *in* the soil will have completely different trajectories (towards their way out) than fast neutrons *entering* the soil.

3.2.3 Spatial neutron transport

As illustrated in Fig. 3, neutrons that arrived from the atmosphere penetrate the soil in different depths. Due to the high bulk density ϱ_{bulk} of the ground, the macroscopic cross section Σ is large, and thus the penetration depth, $\sim \lambda$, is just a few decimeters. High-energy neutrons can travel longer distances into the soil (red in Fig. 3), because they come upon lower cross sections (Fig. 3.2). Their interaction with heavy nuclei leads to isotropic *evaporation*, and some of the resulting fast neutrons may find their way back to the surface.

One of the major advantages of the CRNS technology is the huge representative footprint, within which neutrons of different origins have elaborated an almost homogeneous density. Why do neutrons mix like a gas in the air, and what is the reason for its "footprint length"? The following mono-energetic approximation can provide first insights, which is described in more detail in famous textbooks like Glasstone and Edlund (1952) or Williams (1966).

Thermal neutrons are a rewarding source for first-order estimations, because their average energy $\langle E_{\text{th}} \rangle \approx 25\,\text{meV}$ at 25 °C is in equilibrium with the environment and thus does not change during collisions. The neutron density $N(\vec{x})$ at a location $\vec{x}$ is then determined by the production rate P (e.g., from moderated fast neutrons), the absorption rate $= Nv/\lambda^{\text{abs}}$ (e.g., due to hydrogen), and the leakage by diffusion, $-D\nabla^2 N$. Here, the diffusion coefficient $D = \frac{1}{3} v \lambda^{\text{sct}}$ is determined by the average neutron velocity v and λ^{sct} is the *mean free path* for neutron transport (e.g., scattering processes).

$$\underset{\substack{\text{neutron}\\\text{dynamics}}}{\partial_t N} = \underset{\text{production}}{P} \underset{\text{absorption}}{- Nv/\lambda^{\text{abs}}} \underset{\text{leakage}}{+ D\nabla^2 N} \tag{3.2}$$

Considering the steady state, $\partial_t N = 0$, the solution of this equation provides the neutron density at the distance r from a point source. Famous textbook examples further expand this to an infinite plane source, e.g., the Earth's surface:

$$\text{point source:} \quad N(r) \propto \frac{P}{\lambda^{\text{sct}}} \cdot \frac{1}{r} \cdot e^{-r/L}\,, \quad \text{plane source:} \quad N(r) \propto \frac{PL}{\lambda^{\text{sct}}} \cdot e^{-r/L}\,. \tag{3.3}$$

where $L \propto \sqrt{\lambda^{\text{sct}} \lambda^{\text{abs}}}$ is called the *diffusion length* of neutrons in a specific material. In the case of an infinite planar source, L equals the distance r at which the neutron density was reduced by $1/e$. Desilets and Zreda (2013) found $L \approx 150\,\text{m}$ for fast neutrons in air, and defined the footprint cutoff radius as $R = 2L$, within which $1 - e^{-2} \approx 86.5\,\%$ of detected neutrons originated.

As argued in Köhli et al. (2015), actual neutron transport in the environment is way more complex, as (1) a whole spectrum of different neutron energies $E \propto v^2$ are involved, (2) mean free paths $\lambda(E)$ depend on neutron energies, (3) the neutron source is on top of the atmosphere, (4) soil and air have different densities and introduce interface effects, and (5) more inelastic and resonance effects occur, depending on energy. One of the major challenges is, that neutrons loose energy with every collision during diffusion. The *Fermi age* theory (e.g., applied by Barkov et al. 1957) offers a first-order approach to that problem, by letting neutrons *diffuse* also in the *energy space*. Finally, Monte-Carlo codes (e.g., `MCNP` or `URANOS`, chapter 6) are the only way to account for all the mentioned issues involved in the process of neutron transport through a complex environment.

3.3. Detection and counts

Due to the absence of electrical charge, neutrons can only be detected "the hard way", through nuclear reactions. As most natural abundant elements exhibit highest interaction cross-sections in the thermal energy regime of neutrons (Fig. 3.2), it is preferred to slow down fast neutrons beforehand, and then to detect their nuclear interaction process.

3.3.1 Shielding

As fast neutrons are the quantity of interest, but only thermal neutrons can be efficiently detected, moderator materials were introduced to surround the bare detector tubes. *Polyethylene* (PE) is a famous plastic and solid material which is sensitive to fast neutrons due to the chemical composition $(C_2H_4)_n$. Simultanuously, PE shields thermal neutrons from entering the tube, which turns the moderated detector tube to be sensitive only to fast neutrons. The popular CRNS probes delivered by `Hydroinnova` come with a 1 inch PE shield. Although this thickness was known to be insufficient to completely exclude thermal neutrons (Desilets and Zreda 2008; McJannet et al. 2014), it has been a good compromise between efficient moderation and low absorption probability.

Another famous detector shield is lead, which can be used to protect the detector from high-energy photons. This is especially useful when active neutron measurements are performed, e.g., in DAN campaigns on Mars (Litvak et al. 2014). Neutron monitors also use lead as a surrounding material, although for different reasons. Lead is able to support multiplicity, i.e., the generation of multiple neutrons from one incident neutron or proton, and thus is able to increase the probability to detect hadronic radiation. The use of lead batteries for CRNS stations might introduce such effects, too, which should be kept in mind when data is interpreted (especially on a lake where tubes are all alone with eight batteries, chapter 5).

Other detectors on Mars use cadmium enclosure with 1 mm thickness in order to absorb thermal neutrons, while it can also help to reduce X-ray contamination. On Earth, cadmium shielding is not recommended for environmental research, because the material is highly toxic. Still, experiments under strict control were performed by Andreasen et al. (2017) in forests in order to learn about thermal contribution on moderated CRNS detectors.

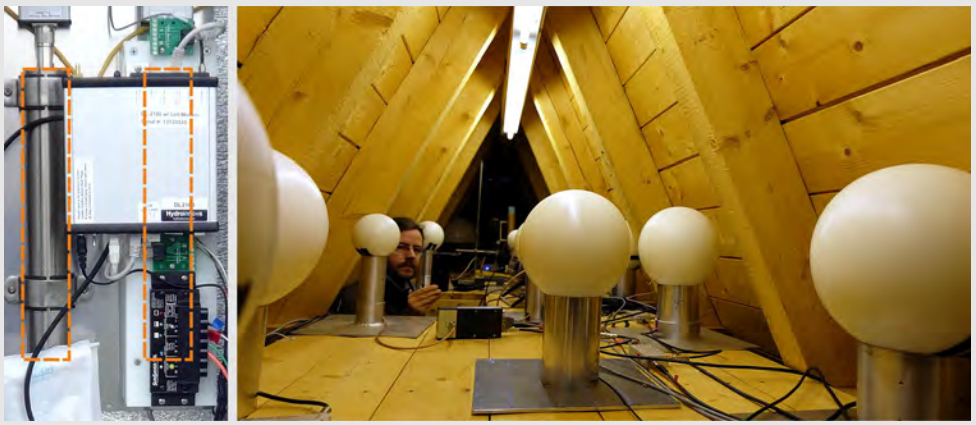

Fig. 3.3: Left: The CRS1000 detector houses a bare and a shielded tube of 1 inch thickness. Right: Bonner spheres at the *Schneefernerhaus* exhibit various thicknesses of shielding. In November 2015, one sensor CRS07 was added to their "Kugel-Alm" in order to learn more about the energy sensitivity of the CRNS detector system.

3.3.2 Popular detector gases

An appropriate detector gas should (1) have a large cross section, (2) its reaction product should lead to an easily detectable signal, and (3) the signal should be distinguishable from other radiation sources.

The lighter isotope of **helium** is highly sensitive to thermal neutrons due to its large cross-section of $\approx 5330\,\mathrm{b}$, while a captured neutron induces the reaction $\mathrm{n} + {}^{3}\mathrm{He} \longrightarrow {}^{3}\mathrm{H} + \mathrm{p} + E$. The released energy of $E \approx 764\,\mathrm{keV}$ is distributed between the tritium nucleus (*triton*, 191 keV) and a proton (573 keV) as indicated by their inverse masses. To be accurate, the ${}^{3}\mathrm{He}$ nucleus has an additional option to turn into the stable element ${}^{4}\mathrm{He}$. However, creation of pure helium is very unlikely with thermal neutrons, because its lowest energy state is at $\approx 20\,\mathrm{MeV}$.

Many other materials exhibit high cross sections for thermal neutron capture, one of such popular elements is the **boron** isotope ${}^{10}\mathrm{B}$. Its cross section for thermal neutrons is about 4000 b and drops rapidly with $1/E$. The corresponding reaction follows ${}^{10}\mathrm{B} + \mathrm{n} \longrightarrow {}^{7}_{3}\mathrm{Li} + \alpha + \mathrm{E}$, where $E = 2.8\,\mathrm{MeV}$ is the released kinetic energy, which can be also $E = 2.3\,\mathrm{MeV}$ if Litium got excited (94 % probability). The detector gas ${}^{10}\mathrm{BF}_3$ is widely used in proportional counters, because it is highly ionizable by bypassing charged particles if operated at pressures from 0.5 to 1 bar. In contrast to helium reactions, the heavy α particle is usually not able to loose its entire energy before reaching the wall. Thus, ${}^{10}\mathrm{BF}_3$ tubes have to have large physical dimensions to be efficient (see section 3.3.3). The toxic fill gas further degrades quickly, resulting in significant changes of performance after 10^{10}–10^{11} neutron interactions, depending on the detector configuration (Pellegrin et al. 2010).

As one of the lightest elements, **litium** is also well suited for neutron capture. However, only ^{6}Li has appropriate cross sections of $\approx 940\,\mathrm{b}$, while cross sections for ^{7}Li are less by a factor of $\approx 5 \cdot 10^{-5}$. Unfortunately, the separation effort for both abundant isotopes limits the feasibility of litium detectors.

Appendix A addresses the question whether detectors containing the toxic gas BF_3 are suited for applications in Germany, and concludes that its concentration exceeds the minimal allowed limit by a factor of 10^3. Due to the planned activities using mobile neutron detectors in cars and aircrafts (chapters 8 and 10) as well as on lakes (chapter 5), the decision was made in favor of the more expensive but less problematic helium gas.

3.3.3 Counting gas collisions with a Pulse Height Spectrum (PHS)

Common to all considered detector gases, the primary reaction product ionizes the surrounding gas as it passes the tube, thereby releasing electron showers that follow the applied electrical gradient. Without such an external voltage ($\approx 1000\,\mathrm{V}$), the charged particles would not show any endeavor to reach the detector wall. However, accumulation of charge in the wall is the only indication of the antecedent reaction with the neutron. As the reaction products and showers reach the electrode (wall), a small measurable current is invoked which is directly related to the number of charges received. As the energy of the reaction product is well known, a characteristic current (or *bin* number) can be expected and translates to a prominent peak in a so-called *pulse height spectrum* (PHS), see for example Figures 4.3 and B.1. However, sometimes the reaction product reaches the wall of the tube before it had the chance to completely release all of its energy into electronic pulses. The so-called *wall effect* is then visible in the PHS as a number of pulses at smaller bins. As such, the typical shape of the pulse height spectrum is independent of the neutron energy, it is rather a function of the reaction kinematics and the amplifier used in the detector (Crane and Baker 1991).

Finally, gamma rays can also induce pulses in the instrument which are mainly located in the lower end of the PHS. As the PHS is integrated to give the total number of neutrons counted, most detectors introduce a cutoff parameter to discriminate for gamma rays. Such radiation is often related to other hydro-meteorological effects (Balabin et al. 2013) or neutron interactions with cadmium. Thus, special care is recommended to exclude this information from the neutron count rate, for example by reducing the discriminator at the cost of efficiency (Appendix B), or by choosing modern detector designs (e.g., Chandra et al. 2010).

An irregular PHS can have multiple reasons, for example collapsing voltage supply, gas leakage, or impurity in the detector tube, while variations at the lower end are an indication for electronic noise. Some of those effects were observed in pulse height spectra of CRNS stations in the *Schäfertal*, and efforts have been presented in Appendix B to resolve these issues.

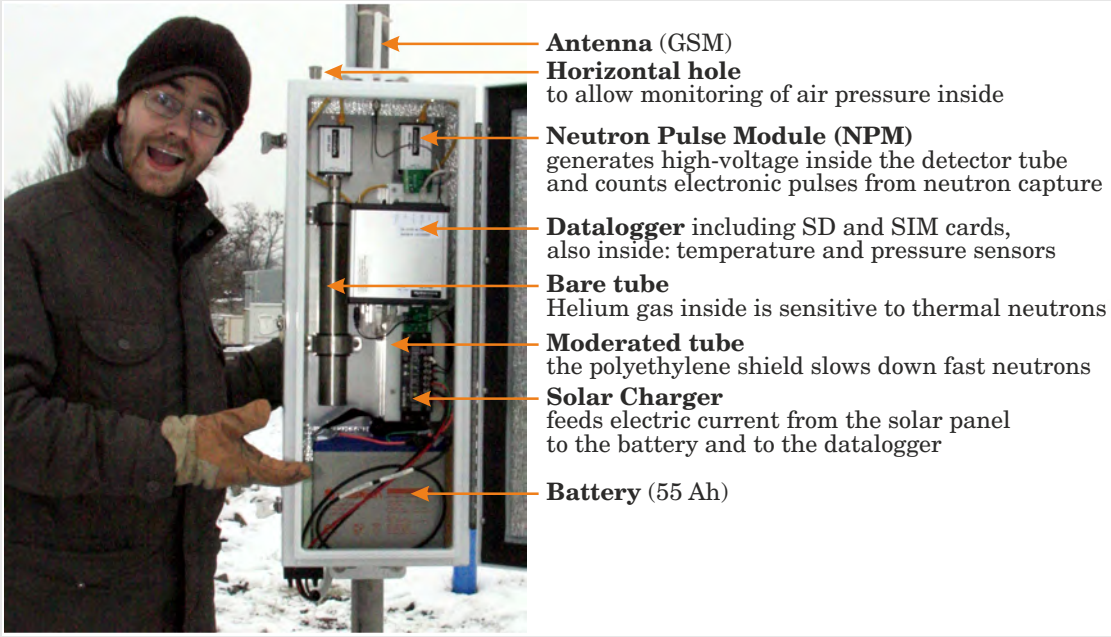

Fig. 3.4: Description of the components inside the cosmic-ray neutron sensor (here: the first sensor installed at UFZ in Jan 2014).

3.4. The CRNS probe CRS1000 and the rover system

Modern neutron detector devices were tailored to the needs of hydrologists and environmental scientists by the company Hydroinnova (Albuquerque, New Mexico) and the manufacturer of the tubes, Quaesta Instruments (Tucson, Arizona). Fig. 3.4 describes the main components of sensor system housing, hermetically sealed in a robust metal case. The data logger is able to receive SDI-12 information from two *neutron pulse modules* (NPM), which generate the high voltage while communicating with the detector tubes. For experimental reasons, standard CRS1000 systems exhibit one bare and one moderated tube, as the benefit of thermal neutrons is expected to crystallize in the near future. The logger additionally handles digital I/O signals from the Campbell CS215 temperature/humidity sensor, rain gauges, GPS, among others. The attached antenna is able to transmit data via the GSM network to FTP servers or email accounts. On top of the mounting stick a 100 W solar panel ensures permanent power supply even during three weeks of snow coverage. By the way, the slight inclination of the panel politely motivates any snow accumulation to slip off after a little while.

The CRNS rover system is constructed in a very similar manner, although data logger and battery were encased separately from the NPMs and tubes. In contrast to the stationary probes, the rover system exhibits two moderated counters in order to achieve highest count rates possible for fast neutrons. The temperature sensor is recommended to be placed outside of the car to sample actual conditions in the field. Power supply is given by using a 12 V connector to the car cigarette lighter.

Fig. 3.5: Components of the CRNS rover system. Inside view (orange) of the two moderated tubes (PE cover removed). *Credit: original photos by Mandy Kasner*

3.5. Temporal meteorological variations

The magnitude of detected near-surface neutrons N_{raw} is primarily driven by the number of incoming cosmic-ray neutrons from above. As introduced in chapter 2 and discussed in chapter 5, this quantity varies considerably over time t and consequently obscures the variable of interest, $N(\theta, t)$. The three most dominant factors are air humidity h, air pressure p, and variations of incoming cosmic rays at the upper atmosphere, I. The accepted approaches assume proportional and thus cumulative influence of the so-called *correction functions*, C_h, C_p, and C_I, on the raw detected neutron signal, N_{raw} (Zreda et al. 2012; Rosolem et al. 2013a). Fig. 5.5 illustrates how those meteorological variations correlate with the semi-corrected neutron counts from a detector buoy.

$$N_{phI} = N_{\text{raw}} \cdot C_p \cdot C_h \cdot C_I \,, \tag{3.4}$$

where N_{phI} denotes the fully corrected neutron count rate. Neutron measurements in the following chapters are denoted as N by omitting the correction indication, as they were already fully corrected if not otherwise explicitly stated.

3.5.1 Atmospheric water vapor

The detected neutron abundance at the surface is influenced by atmospheric water content in two ways. Firstly, the incoming radiation was moderated by the integral water content (IWC) in the whole air column above the neutron detector. Secondly, the soil-albedo component N_{refl} is reduced by the presence of near-surface water vapor in the sensor's footprint. Rosolem et al. (2013a) implicitly assumes that the latter effect on N_{refl} is negligible and suggests the following correction function for

IWC:

$$C_{\mathrm{IWC}} = 1 + \alpha_{\mathrm{IWC}}\,(\mathrm{IWC} - \mathrm{IWC}_{\mathrm{ref}})\,, \quad \alpha_{\mathrm{IWC}} = 0.0143\,.$$

In most cases, measurements of the whole atmospheric water profile are not available, if no microwave radiometer or GNOME satellite is nearby (the study in section 5.3.1 made use of such a situation). As typical CRNS stations are equipped with sensors of temperature T (in °C) and relative humidity h_{rel} (in %), the corresponding *absolute humidity* h (in g/m^3) could be inferred as a proxy for IWC. The correction relation has been elaborated by Rosolem et al. (2013a) based on neutron transport simulations:

$$C_h = 1 + \alpha\,(h - h_{\mathrm{ref}})\,, \quad \alpha = 0.0054\,, \tag{3.5}$$

$$\text{where} \quad h(h_{\mathrm{rel}}, T) = 6.112 \cdot \frac{2.1674 \cdot h_{\mathrm{rel}}}{273.15 + T} \cdot e^{\frac{17.67 \cdot T}{243.5 + T}}\,.$$

This work universally applies the reference value $h(50\,\%, 25°\mathrm{C}) = 12\,\mathrm{g/m^3}$. Using a buoy detector on a lake, chapter 5 tests the real-life performance of the α parameters.

3.5.2 Air mass correction by pressure

Air is highly contributing to the number of neutrons for multiple reasons. Firstly, incoming neutrons from space are attenuated by air molecules in the atmosphere. Consequently, the number of surface neutrons changes when air mass or atmospheric stratification changes. For this reason correction is needed for the mass in the atmosphere, for which near-surface air pressure p is a great proxy.

$$C_p = e^{\beta(p - p_{\mathrm{ref}})}\,,$$

where β denotes the *barometric attenuation coefficient*, which is inversely related to the *atmospheric attenuation length* $L \propto \beta^{-1}$. In this work, $p_{\mathrm{ref}} = 1013.25\,\mathrm{hPa}$ is applied universally, and $L = 131.6\,\mathrm{hPa}$ for Germany (Desilets et al. 2006). However, $L = 138.7\,\mathrm{hPa}$ is used by operators of the neutron monitor station in Kiel as well as the Bonner sphere station at the *Schneefernerhaus*. Chapter 5 will discuss the various approaches to determine β, as well as its dependencies on space, time, and detector device (section 5.2.3). Bütikofer (1999) further suggests to apply a pressure correction based on the *Bernoulli effect* during strong winds, $\Delta p \propto \varrho_{\mathrm{air}}\, v^2_{\mathrm{wind}}$. As most of the present work has been conducted in German low-lands, only minor effect on the soil moisture prediction below 1 % was expected and consequently neglected. However, chapter 10 revisits this effect in the scope of fast moving screws on an aircraft.

3.5.3 Incoming cosmic-ray intensity

The incoming radiation $I(t)$ penetrates the upper atmosphere and varies due to solar activity and other more complex temporal effects (see chapter 2). Fortunately, independent measurements exist to quantify $I(t)$ using so-called *neutron monitors* (NM). Although these devices effectively measure the high-energy proton component $> 20\,\mathrm{MeV}$, the accepted correction approach assumes similarity to incident neutron dynamics (Zreda et al. 2012). A worldwide network of NM stations provides online

access[1] to their data in real-time. Under the assumption that incoming radiation is almost similar along the rigidity lines (section 2.2.1), a nearby NM should be able to provide representative data for other locations on Earth with similar R_{cut}. The local cutoff rigidity can be estimated for individual CRNS stations with the help of an online tool[2] provided by the University of Arizona, or more modern approaches following Bütikofer et al. (2007).

Since every detector comes with an individual efficiency, the value $I(t)$ is normalized with a constant reference I_{ref}, which is chosen to be ≈ 150 cps for the *Jungfraujoch* neutron monitor in this work. The following correction approach was introduced by Zreda et al. (2012) using $\gamma = 1$, while other approaches to scale the corresponding anomalies will be discussed in section 5.2.3.

$$C_I = 1 + \gamma \left(\frac{I_{\text{ref}}}{I} - 1 \right) .$$

3.6. From neutrons to soil moisture

Neutron detectors receive two components of neutron radiation: incoming neutrons from the atmosphere that have not had contact with the soil, N_{inc}, and reflected neutrons N_{refl} that scattered in soil and air before entering the detector almost isotropically (see e.g., Schrön et al. 2015, Fig. 3). Most of the time, the incoming component is rather low, depending on detector geometry and local site conditions.

$$\begin{aligned} N_{phI} \equiv N &= N_{\text{inc}} + N_{\text{refl}}(\theta) \\ &= a_{\text{inc}} \cdot N_{\text{base}} + a_{\text{refl}}(\theta) \cdot N_{\text{base}} . \end{aligned} \tag{3.6}$$

N_{base} (or *calibration parameter* N_0) is an arbitrary baseline which can be interpreted as the potential count rate over ideally dry soil, which implicitly accounts for local structures. Following this framework, the results from Desilets et al. (2010) can be interpreted as an inverse relation between N_{refl} and gravimetric soil moisture θ_g,

$$a_{\text{refl}}(\theta) = \frac{a_0}{a_2 + \theta_g} , \quad a_{\text{inc}} \equiv a_1 , \tag{3.7}$$

where $a_{0,1,2} = (0.0808, 0.372, 0.115)$ were fitted semi-empirically (see also Fig. 3.6). These parameters correspond to a signal partitioning of $a_{\text{inc}} \approx 37\,\%$ and $a_{\text{refl}} \approx 63\,\%$ for dry soil, $\theta = 1.4\,\%_g$. As Rivera Villarreyes et al. (2011) noted, individual site conditions may exhibit important features which cannot be tracked by N_0 alone. In fact, Lv et al. (2014) and Iwema et al. (2015) demonstrated that site-specific optimization can lead to different parameters, e.g., for the latter: $a_{\text{inc}} = 34$–$42\,\%$ (cmp. b_1/N_0 in their Table 4). On the other hand, Heidbüchel et al. (2016) found that the incoming offset $a_{\text{inc}} < 1\,\%$ is almost negligible in forests, where tree canopies may thermalize neutrons before detection. The various approaches to calibrate $a_{0,1,2}$ show that the eq. 3.7 together with parameters from Desilets et al. (2010) are not a universal representation of relevant processes. However, it will be accepted as a well-validated standard approach as long as the "arbitrary statistical optimization"

[1] previ.obspm.fr
[2] cosmos.hwr.arizona.edu/Util/rigidity.php

of $a_{0,1,2}$ has not been related to physical reasons. It was further possible to estimate a relationship for $N_{\text{refl}}(\theta, h)$ with the URANOS neutron transport code (section 3.8) by integrating the radial sensitivity $\int_{r=0}^{\infty} W_r(\theta, h)\,\mathrm{d}r$ (Köhli et al. 2015). However, preliminary results presented in Fig. 3.6 are work in progress and their potential to compete with eq. 3.7 needs to be assessed in future studies.

Apart from those approaches, Franz et al. (2013a) presents a *Universal Calibration Function*, where H_{mol} is the molecular fraction of all hydrogen atoms:

$$N(H_{\text{mol}}) = N_{\text{water}} \cdot \left[4.486 \cdot e^{-48.1 \cdot H_{\text{mol}}} + 4.195 \cdot e^{-6.181 \cdot H_{\text{mol}}}\right] .$$

However, the improved performance of this method has not been confirmed (McJannet et al. 2014). Moreover, chapter 9 presents an analytical model COSMIC (Shuttleworth et al. 2013), which is able to predict neutron counts by numerically integrating soil moisture profiles. In a systematic study Baatz et al. (2014) compared those methods mentioned above and found acceptable agreement for all of them.

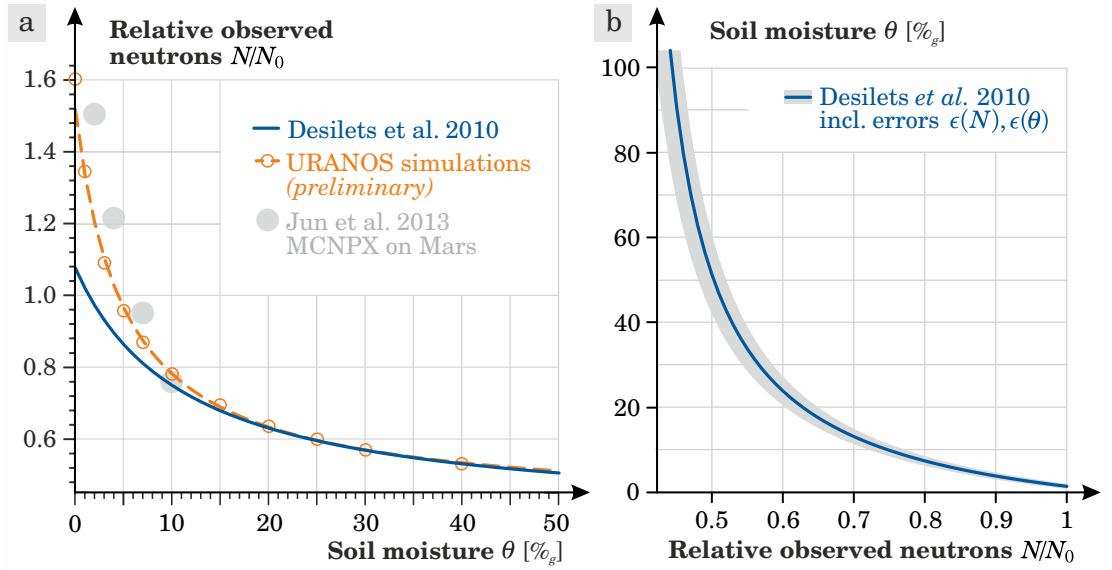

Fig. 3.6: From neutrons to soil moisture and back. a Two different approaches, Desilets et al. (2010) and simulations with URANOS (by M. Köhli, private communication), both normalised to $\frac{1}{2}N_0$ at 50 $\%_g$, and compared with approaches from space science (Jun et al. 2013). b Soil moisture as a function of neutron counts, including an error band for signal uncertainty $\epsilon(N)$ and propagated uncertainty $\epsilon(\theta)$ (see section 3.7.2).

Correction of static effects in the footprint

Neutrons are most effectively moderated by materials that contain a noticeable amount of hydrogen. Thus, the quantity θ_g in eq. 3.7 not only comprises mobile accessible water in the soil, θ_{mob}, but also bound lattice water θ_{lw}, and the water equivalent of organic soils, θ_{org}. Bogena et al. (2013) suggested that these quantities

simply add up to:

$$\theta_g = \theta_{\text{mob}} + \theta_{\text{lw}} + \theta_{\text{org}} \,, \tag{3.8}$$

where usually θ_{mob} denotes *soil moisture*, the quantity of interest for most applications.

Other sources of hydrogen are expected to be implicitly accounted for by the calibration parameter N_0. For example, Baatz et al. (2015) and Franz et al. (2015) found linear relationships to *biomass water equivalent* (BWE),

$$N_0(\text{BWE}) = N_0 - s \cdot \text{BWE} \,, \tag{3.9}$$

which have been applied to mobile measurements in chapter 8. Naturally, snow is also an efficient moderator for neutrons, as has been shown theoretically by Zweck et al. (2013) in the scope of cosmogenic nuclide dating applications. However, a simple linear relation between neutrons N and *snow water equivalent* (SWE) was found empirically by Sigouin and Si (2016), without the functional relationships in eqs. 3.7 and 3.9.

Apart from additional hydrogen sources, site-specific geometrical or structural conditions could be addressed implicitly by calibrating N_0. The study presented in section 4.3.5 elaborated a new, more sophisticated *areal correction* approach based on Köhli et al. (2015), to rescale the damping effect induced by dry, static ground in the footprint.

3.7. Statistical and propagated errors

Neutron detectors collect discrete numbers of samples and thus obey the Poissonian law of counting statistics. For a large number of counts, $\langle N \rangle > 30$, the Poissonian distribution turns into the Gaussian distribution, and the corresponding standard deviation can be approximated as $\epsilon(N) = \sqrt{N}$. In this dissertation, ϵ denotes *standard deviations*, as the otherwise conventional symbol σ is reserved for *cross sections* (section 3.2.1).

Poissonian statistics also helps in practical situations, for example when the CRNS technology is demonstrated to an audience or its proper functioning needs to be checked. From looking at the NPM (Fig. 3.4) it is possible to witness the detection of neutrons from a flashing LED. However, the function check is semi-decidable: a dark LED can stay for long, leaving you wonder whether the detector actually works or not. In these situations it could be helpful to know about the Poissonian probability $P(\mu\,, r)$ of witnessing zero counts ($N = 0$).

$$\text{Poissonian probability:} \quad P(\mu = \langle N \rangle\,, r = N) = \frac{1}{r!}\mu^r \cdot e^{-\mu}$$

For example, taking a quick look for $t = 3\,\text{sec}$ at a typical CRNS detector with average count rates of about $\langle N \rangle \approx t \cdot 830\,\text{cph}$, the chance to miss any neutron detection is 50 %. Certainly, starring at the LED for $t = 20\,\text{sec}$ is almost guaranteed to see it flashing at least once with a 99 % success rate.

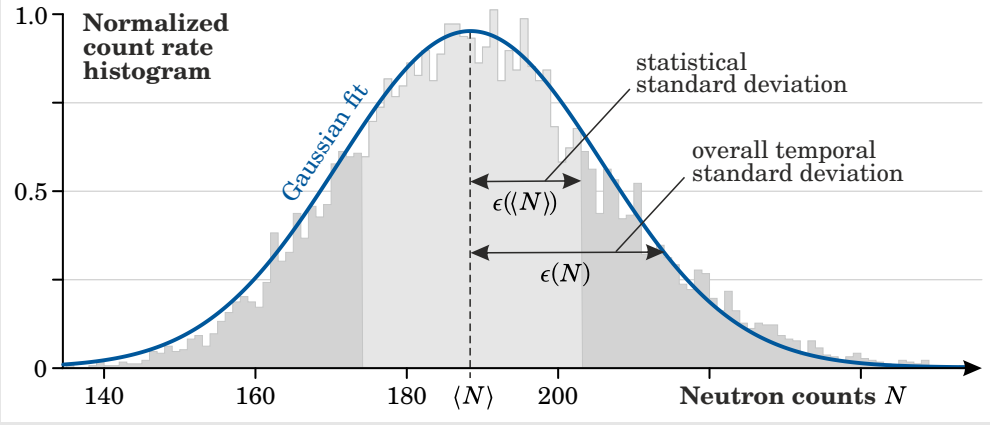

Fig. 3.7: Statistical distribution of observed neutron counts over a period of 6 months. The gaussian statistical standard deviation $\epsilon(\langle N \rangle)$ is explained by the mean value $\langle N \rangle$. On the other hand, the temporal standard deviation is much broader and asymmetric, as demonstrated with the gaussian fit, due to the significantly varying conditions in the measurement period.

3.7.1 Error of time series data

During analysis of neutron time series, the statistical error can be modified by aggregation and averaging procedures. It is therefore necessary to clarify how errors change, which are often neglected when scientific results are presented.

Observed neutrons N always come with a corresponding statistical error of $\epsilon(N) = \sqrt{N}$. Usually, the measured integration time of CRNS sensors is $\tau = 15\,\text{min}$, while, by convention, analysis is usually performed with hourly values in units of [cph]. During this aggregation with *time factor* $a = 4$ (as $4 \cdot 15\,\text{min} = 1\,\text{h}$) the data appears as follows:

$$\tau_a = a \cdot \tau \,, \quad N_a = \sum_1^a N \approx a \cdot \langle N \rangle \,, \quad \epsilon(N_a) = \sqrt{\sum_1^a \epsilon(N)^2} \approx \sqrt{a} \cdot \langle \epsilon(N) \rangle \,.$$

By scaling the neutron counts by the factor a, the absolute error only increases with $\sqrt{a}$. For example, aggregating the 15 min observations to hourly values ($a = 4$), the original error scales by the factor of 2. Often 6-hourly or daily values are plotted to reduce the visible noise, while keeping their units in [cph]. To achieve this, neutron counts within a time window a are aggregated and devided by a:

$$\tau_a = a \cdot \tau \,, \quad N_a = \frac{1}{a} \sum_1^a N \approx \langle N \rangle \,, \quad \epsilon(N_a) = \frac{1}{a} \sqrt{\sum_1^a \epsilon(N)^2} \approx \frac{1}{\sqrt{a}} \cdot \langle \epsilon(N) \rangle \,. \quad (3.10)$$

For example, averaging hourly data to daily values reduces the error band by almost a factor of $1/\sqrt{24} \approx 5$.

What count rate is needed to achieve a specific accuracy?

For site and investment planning, it is handy to estimate the necessary size of a neutron detector to achieve a certain level of accuracy. Often, a relative error of $\epsilon(N)/N \approx 2\,\%$ is demanded, e.g., for accurate irrigation management or to detect certain features of changing water pools in the environment. Let ϵ_{rel} be a general relative error (or *accuracy*), then

$$\epsilon_{\text{rel}} = \frac{\epsilon(N)}{N} = \frac{1}{\sqrt{N}} \quad \Leftrightarrow \quad N = \epsilon_{\text{rel}}^{-2}\,.$$

So N neutrons within an integration time of τ are needed to achieve an accuracy of ϵ_{rel}. Sometimes it is an option to increase the integration time by a factor a if the measured quantity is not expected to change on a longer time scale. Then,

$$\epsilon_{\text{rel}} = \frac{\epsilon(N_a)}{N_a} = \frac{1}{\sqrt{a}} \cdot \frac{\epsilon(N)}{N} \quad \Rightarrow \quad N = \frac{1}{a} \cdot \epsilon_{\text{rel}}^{-2}\,.$$

For example, 2500 cph are needed to significantly detect a 2 % change on hourly time scales. 417 cph will be sufficient to detect these changes on a 6-hourly average.

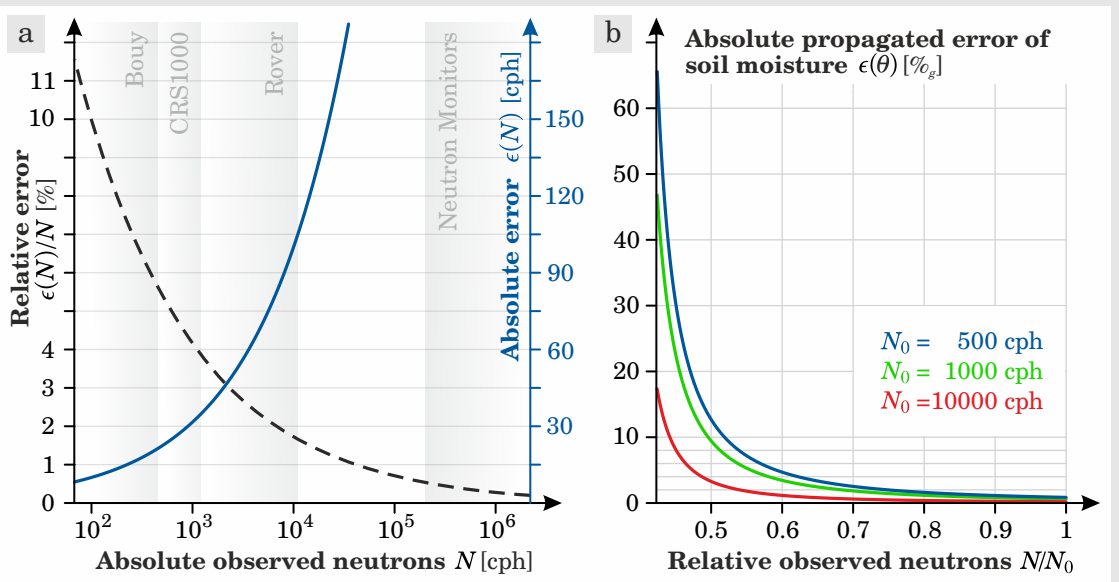

Fig. 3.8: Errors of neutron count rates and their propagation to soil moisture estimations. a Absolute error $\epsilon(N) = \sqrt{N}$ (blue) of neutron count rates for different detector types. The corresponding relative error $\epsilon(N)/N = 1/\sqrt{N}$ (dashed) decreases with detection rate. b Absolute error of soil moisture $\epsilon(\theta)$ which propagated from $\epsilon(N)$ through eqs. 3.11 (or equivalently eq. 3.7).

3.7.2 Error propagation towards soil moisture

As elaborated in section 3.7, the counting error for neutrons is Poissonian and its absolute error is defined as $\epsilon(N) = \sqrt{N}$. Since the quantity of interest in hydrology is *soil moisture* θ, the question is raised how the rather large errors of N propagate through eq. 3.7:

$$\theta(N) = \frac{a_0}{N/N_0 - a_2} - a_1 \,. \tag{3.11}$$

To address this question, the *Taylor expansion* is applied to eq. 3.11, which requires calculation of the i^{th} derivative by N:

$$\theta(N + \epsilon(N)) = \sum_{i=0}^{\infty} \frac{1}{i!} \partial_N^{(i)} \theta(N) \cdot \epsilon(N)^i \,.$$

Usually, expansions up to the *first* order ($i = 1$) provide sufficient accuracy for most applications. However, significant overestimation of errors was recognized under wet conditions by using the first-order approach in this work. Due to the oscillating nature of polynomials, at least 3 orders were found to be necessary for adequate error quantification:

$$\begin{aligned} \epsilon(\theta) &= \theta(N + \epsilon(N)) - \theta(N) \\ &\approx -\frac{a_0 N_0}{(a_2 N_0 - N)^2} N^{1/2} - \frac{a_0 N_0}{(a_2 N_0 - N)^3} N - \frac{a_0 N_0}{(a_2 N_0 - N)^4} N^{3/2} \,. \end{aligned} \tag{3.12}$$

These propagated errors are shown in Fig. 3.8b as a function of wetness condition N/N_0 for three typical N_0 values (buoy, stationary, rover). Interestingly, accuracies of $\approx 2\,\%_g$ are easily achievable with the CRNS method under certain conditions. In low-count regions like forests (Bogena et al. 2013; Heidbüchel et al. 2016), high-precision measurements are only possible under dry conditions, $N/N_0 > 0.8$, whereas sensors under standard field conditions at sea level exhibit low uncertainty already at $N/N_0 > 0.7$. The rover can accurately predict soil moisture even under wet conditions, $N/N_0 > 0.55$. Although almost unrecognized in the CRNS community these days, those error estimations have been implicitly applied in this work.

3.7.3 Statistical data analysis

In order to remove high-frequency noise in the neutron data, time series can be smoothed over several integration intervals. In this work, either rigorous aggregation or box-model moving averages were applied to smooth out those statistical fluctuations. In future studies, more sophisticated approaches could be adapted from Orford (2000), who developed methods based on classical and bayesian statistics that can be used for pattern recognition, burst identification, and periodicity. Orford tailored these methods for the pure cosmic-ray community, and great potential is supposed for improving also CRNS analysis.

3.8. The neutron transport simulator URANOS

The present chapter has elaborated the complex theory of neutron transport and has shown that interaction processes are highly sensitive to the neutron energy and the nuclear composition of the passed medium. It is therefore not feasible to find deterministic, analytical solutions under realistic conditions. Statistical and computational approaches are the only way to take all relevant physical interactions into account. In the so-called *Monte-Carlo codes* millions of particles can be summoned with randomly sampled initial conditions, while their paths can be tracked and their interactions with nuclei obey the laws of physics. Finally, the summary statistics of those neutrons can reveal insights into their collective behavior.

In the last decades, the Monte-Carlo code MCNP (Pelowitz 2005) was often consulted to study the behavior of neutrons near the surface (e.g., Desilets et al. 2006; Zreda et al. 2008; Franz et al. 2013c; Zweck et al. 2013). However, the model accounts punctiliously for all kinds of particles and various interactions such that the computational efficiency suffers, and the complex user interface hampers flexibility. As an alternative, M. Köhli developed the Monte-Carlo code URANOS (Ultra Rapid Adaptable Neutron-Only Simulation) which was specifically tailored to address the open questions of the CRNS community (Köhli et al. 2015). As the model has been developed further, it also proved to be useful for neutron spin echo detectors in other research fields (Köhli et al. 2016). URANOS is very flexible, as the developer has direct access to the code and is able to adapt input and output routines to the needs of a specific scientific question. Furthermore, URANOS is very efficient, as it only accounts for the most relevant neutron interaction processes, namely elastic collisions, inelastic collisions, absorption, and evaporation. As has been explained in section 3.2.1, cross sections of various elements determine the magnitude of those effects. It is therefore important to consult the newest updates of official cross section databases, namely ENDF/B-VII.1 (Chadwick et al. 2011) and JENDL/HE-2007 (Shibata et al. 2011). The latter especially accounts for precise cross section models in the high-energy domain > 20 MeV, where the corresponding uncertainties are highest.

The capabilities of URANOS and its developer have been consulted multiple times throughout this dissertation to support theories, ideas, and experiments. The main model features are:

- tracking of particle histories from creation to detection,
- detector representation as layers or geometric shapes,
- automatic model and material setup based on color codes in 2D bitmap images (applied in chapters 4 and 5).

Using ENDF and JENDL, the model refers to the same physics database as other particle transport codes. Thus, adequate representation of reality can be expected from URANOS. Nevertheless, additional model comparisons with MCNPX have been conducted for a specific case (section 6.4), and a variety of experiments have confirmed the model results (see e.g., chapters 4, 7, 10, or section 4.6 in Köhli et al. (2015)).

Fig. 4:
Temporary installation of ten Cosmic-Ray Neutron Sensors at the *Schmetterlingswiese*, UFZ area.

4.

Intercomparison in an Urban Environment

Lessons learned from nine neighboring sensors

Upon the arrival of ten stations for cosmic-ray neutron sensing (CRNS) a short period was scheduled to confirm individual sensor comparability before deploying them at remote research sites. While the integrated supplementary sensors of air pressure, humidity, and temperature exhibited acceptable agreement, surprising variability has been observed in the time series of all neutron detectors.

By permutation of sensor positions, calibrating detector parameters, and surveying neutron density in the surrounding area, evidence has been found that neighboring CRNS stations deliver different observations under the same conditions. In order to ensure comparability, sensors need to be calibrated in advance, and their common temporal integration window needs to be of the order of half a day. Moreover, this work proposes a new areal correction function to account for complex terrain, while remarkable heterogeneity of neutrons has been revealed within the CRNS footprint.

The presented arrangement at the small urban meadow *Schmetterlingswiese* (Fig. 4) offers a unique opportunity to test individual sensor performances – a strategy that improved the understanding of the instrument.

4.1. Introduction

Sensor comparability studies are an important step towards joint usage of multiple sensors for a single application or global calibration strategies, e.g., assimilating multiple stations to a hydrological model (chapter 9) or using them as anchor points for mobile surveys with a rover (chapter 8).

Intercomparison studies for soil moisture sensors are a preferable way to correct for sensor-specific biases, e.g., applied to point sensors (Walker et al. 2004) or to remote sensing instruments (Su et al. 2013). For example, Kögler et al. (2013) developed strategies to intercalibrate TDR and SoilNet sensors in order to achieve comparable results. Intercalibration is also one of the main goals for the worldwide neutron monitor network (Bachelet et al. 1965; Moraal et al. 2001; Krüger et al. 2008). For example, observations of the same event measured with neutron monitors on three continents revealed clear longitudinal discrepancies (Chiba et al. 1975). Moreover, Oh et al. (2013) compared data from 15 neutron monitors in the same period and concluded that individual detrending correction factors were needed for coherent prediction performance. After the results of this intercomparison study were presented at the 4th COSMOS Workshop 2014, Baatz et al. (2015) were the first to publish sensor-specific *efficiency* values for some of their cosmic-ray neutron sensors, ranging from 10 to 20 %.

Apart from that, detectors for cosmic-ray neutron sensing (CRNS) might be a promising instrument to estimate representative urban water content (see also Cassis and Schreiner-McGraw 2014), which is otherwise hard to measure with conventional instruments. It is the goal for this chapter to assess the sensor-to-sensor variability and to test the performance of CRNS in complex urban terrain.

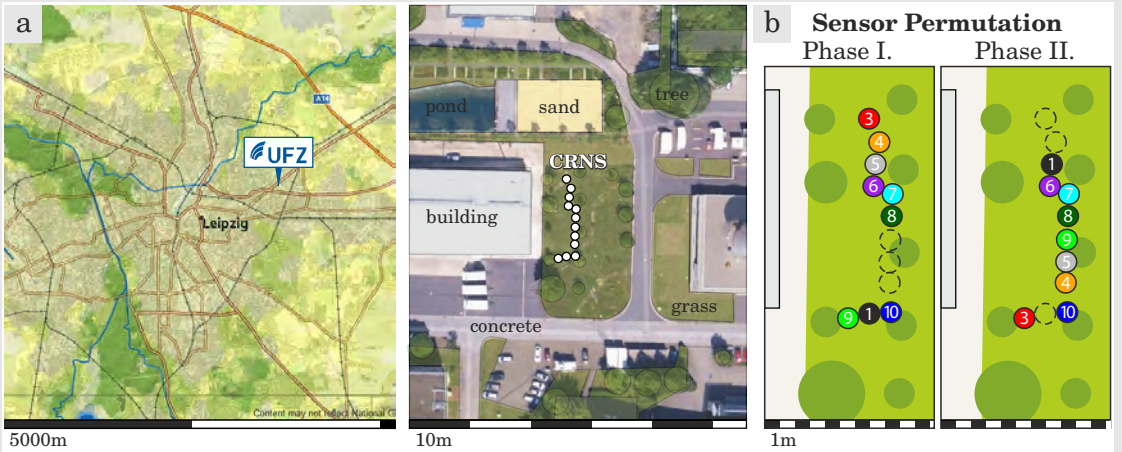

Fig. 4.1: Intercomparison of 9 CRNS detectors deployed at a small meadow in the UFZ area. By the end of March, positions of some sensors were switched to test a hypothetic positional effect. *Credit: (left) own montage from OpenStreetMap tiles, (mid) Google Maps*

4.2. Methods

Ten cosmic-ray neutron sensors were deployed at a small grassland site *Schmetterlingswiese* in the UFZ area, Leipzig, Germany. Shortly after installation, sensor CRS02 has been removed and disassembled for later use as a "COSMOS buoy" on a lake (chapter 5). The other stations were equipped with sensors for air pressure, air temperature, and relative humidity, and the according averages were shared to correct the individual neutron count rates $N_{\text{raw}} \mapsto N_{phI}$ (section 3.5).

As the grouped ensemble of nine sensors is a unique opportunity to frame the concept of a "super-detector", the combined signal will exhibit higher count rates and thus lower statistical noise. The average count rate $\langle N \rangle$ and its propagated uncertainty of each i^{th} sensor are given as:

$$\langle N \rangle = \frac{1}{9} \sum N_i \,, \quad \epsilon(\langle N \rangle) = \frac{1}{9} \sqrt{\sum \epsilon(N_i)^2} \,.$$

Under the assumption that $N_i \approx N_j \;\forall i, j \in (1, .., 9)$, their corresponding counting statistics will be similar as well:

$$\epsilon(N_i) \approx \langle \epsilon(N_i) \rangle \;\forall i \,, \quad \Rightarrow \quad \epsilon(\langle N \rangle) \approx \frac{1}{9} \sqrt{9 \cdot \langle \epsilon(N_i) \rangle^2} = \frac{1}{3} \langle \epsilon(N_i) \rangle \approx \frac{1}{3} \sqrt{\langle N \rangle} \,.$$

Since the individual statistical errors are given as $\epsilon(N_i) = \sqrt{N_i}$, the average statistical error for $\langle N \rangle$ can be reduced to 33 % when nine sensors are combined. Following eq. 3.10, the average statistical error at the daily aggregated time scale is given as $\epsilon(\langle N \rangle) = \sqrt{\langle N \rangle / 24}$.

4.2.1 Measures

Generally, deviation measures can be expressed as an average of the individual vector p-norms (not to confuse with air pressure p) of all nine sensors:

$$\epsilon^p(N) = \left(\frac{1}{9} \sum_i |N_i - \langle N \rangle|^p \right)^{\frac{1}{p}} \,, \quad \text{where} \quad \langle N \rangle = \frac{1}{9} \sum_i N_i \,. \tag{4.1}$$

The *standard deviation*, $\epsilon^{p=2}(N)$, is used in Fig. 4.2 to measure the spread of individual sensors around their average $\langle N \rangle$. If not explicitly indicated, $\epsilon \equiv \epsilon^{p=2}$. For two time series $N_1(t)$ and $N_2(t)$ with standard deviations ϵ_1 and ϵ_2, the *Pearson correlation coefficient* is defined as:

$$\rho(N_1, N_2) = \frac{\text{Cov}(N_1, N_2)}{\epsilon_1 \, \epsilon_2} = \frac{\big\langle (N_1 - \langle N_1 \rangle) \cdot (N_2 - \langle N_2 \rangle) \big\rangle}{\epsilon_1 \, \epsilon_2} \,.$$

For example, $\rho = 0.7$ depicts that N_1 and N_2 can explain $0.7^2 \approx 50\,\%$ of their respective variance. If those two variables N_1 and N_2 were ranked depending on the order of their magnitude, $N_i \mapsto \text{Rank}(N_i)$, the *Pearson correlation* turns to the

so-called *Spearman rank correlation*:

$$\rho_s(N_1\,,\,N_2) = 1 - 6\frac{\sum_t \Big(\mathrm{Rank}(N_1) - \mathrm{Rank}(N_2)\Big)^2}{n(n^2-1)}\,,$$

where n is the number of days and $t \in (1\,,\,..\,,\,n)$. This quantity can be used to identify events that changed the rank of specific sensors.

4.2.2 Validation with independent soil moisture measurements

In order to validate and calibrate the sensors against real soil water content in the *Schmetterlingswiese*, two independent measurement methods were consulted to quantify soil moisture profiles: volumetric soil samples (once), and *Wireless Soil Moisture Network* (WSN, continuous). Since SoilNet installations are usually laborious and permanent, the WSN technology has been developed specifically for short-term applications (Mollenhauer et al. 2015; Bumberger et al. 2015). The measurements were taken in different depths at two locations near sensor `CRS08` (north) and `CRS10` (south). The corresponding soil parameters (Table 4.1) and time series (Fig. 4.6) have been used to calibrate the neutron signal on soil moisture. The sensors used for WSN are of type `Truebner SMT100` and exhibit the following uncertainties:

- uncertainty of the WSN device itself, $\epsilon_1(\theta_{\mathrm{WSN}}) \approx 2\,\%_v$,
- uncertainty about the correct electrical permitivity for rocks below the quartz standard of $\varepsilon_r = 4.6$ (section 1.7.2), $\epsilon_2(\theta_{\mathrm{WSN}}) \approx 3\,\%_v$,
- large heterogeneity in soil properties and composition within and between the profiles, $\epsilon_3(\theta_{\mathrm{WSN}}) \approx 8\,\%_v$,.

which leads to a total uncertainty of $\epsilon(\theta_{\mathrm{WSN}}) = \sqrt{\sum_i \epsilon_i^2} \approx 8.8\,\%_v$ for soil moisture estimation with WSN at the *Schmetterlingswiese*.

Table 4.1: Two soil profiles in the *Schmetterlingswiese* sampled nearby the corresponding Wireless Sensor Boxes on Jan 14th, 2016, 13:30 CEST. Samples were taken with *Stechzylinder* at three depths, oven-dried, and weighted (following section 1.6).

profile	depth	ϱ_{bulk}	porosity Θ	moisture θ
South	7–12 cm	1.62 g/cm^3	38 $\%_v$	18 $\%_v$
South	15–20 cm	1.52 g/cm^3	42 $\%_v$	15 $\%_v$
South	25–30 cm	1.58 g/cm^3	40 $\%_v$	18 $\%_v$
North	5–10 cm	1.60 g/cm^3	40 $\%_v$	32 $\%_v$
North	15–20 cm	1.93 g/cm^3	27 $\%_v$	19 $\%_v$
North	25–30 cm	1.96 g/cm^3	26 $\%_v$	28 $\%_v$

4.3. Results & Discussion

In the course of the first weeks after sensor installation, statistical significant variability and offsets have been observed by comparing the nine detector signals. For example, Fig. 4.2 shows prominent offsets for sensors `04` and `05`, while standard deviations from the mean for all sensors exceeded the daily statistical error $\epsilon(N) \approx \sqrt{600/24} = 5$ by a factor of 2. Since the sensor locations were spread to an extent of 15 m, a positional effect has been hypothesized.

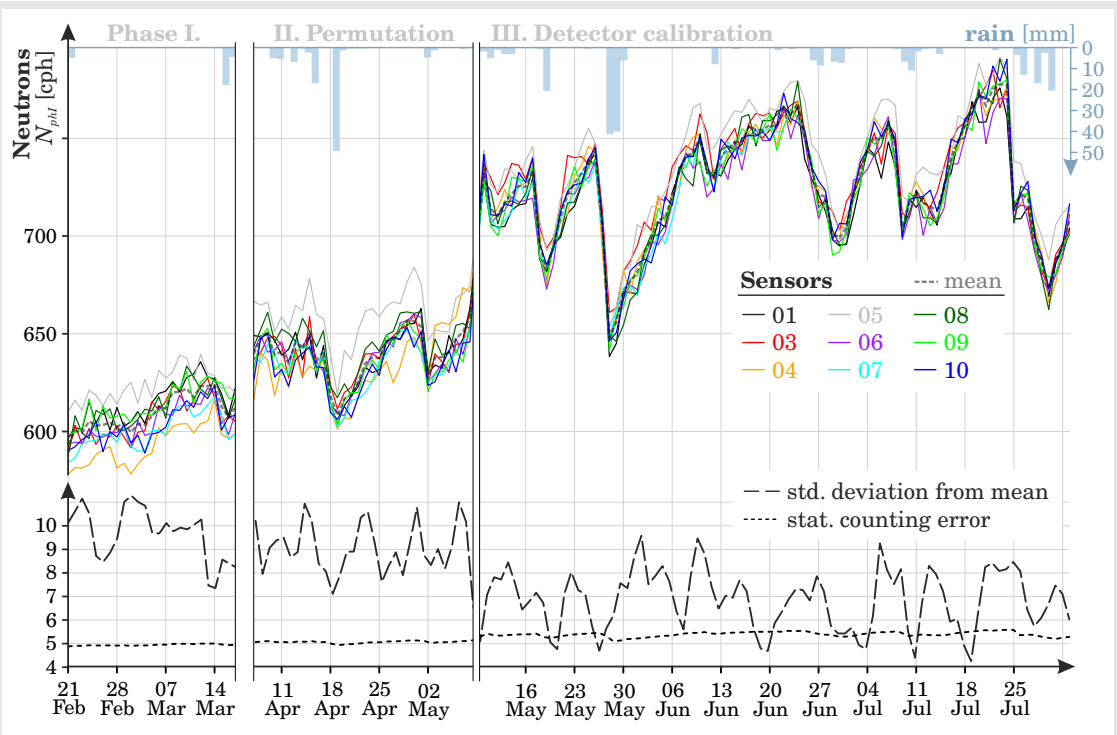

Fig. 4.2: Time series of nine sensors covering phases I (installation), II (permutation) and III (calibration). By removing detector-specific effects in Phase III, the standard deviation of the sensor ensemble from their mean could be reduced down to the statistical error, $\sqrt{N/24} \approx 5$.

4.3.1 Small-scale positioning has minor effect

In a second phase, some sensors have been moved to different locations, while others remained fixed (see Fig. 4.1b). In order to assess the effect on their individual offsets, *Spearman rank correlations* have been applied and visualized in Fig. 4.3a. This quantity explains the probability with which a sensor's count rate was assigned to an ordered rank among the ensemble. The data shows, for instance, that the favored rank (or offset) of sensors `04` and `05` remained to be at the high or low end, respectively. Furthermore, the standard deviation of the sensor signals did not change significantly between Phase I and II (Fig. 4.2). Following this argumentation,

it can be concluded that the small-scale positioning has not been the root cause of the individual deviations.

4.3.2 Detector calibration reduces the offset

Phase III was then dedicated to the *pulse height spectra* (PHS) of the detectors. As `Hydroinnova` has noted, this supplementary data can be helpful to find and explain irregularities in the detection signal (see also Appendix B). Section 3.3.3 already explained the physics behind these spectra and concluded that their shape determines the efficiency with which neutrons and gamma rays were detected. Consistent positioning of all peaks (e.g., bin 100) and of all discriminators (e.g., bin 25) are prerequisites to assure that the same type of particles are counted by all detectors. Fig. 4.3b shows that this requirement was absent before Phase III. However, `Hydroinnova` provided users with access to the *neutron pulse module* (NPM), in order to adjust its parameters accordingly:

1. **high-voltage** in the typical range of 1000–1200 V.
2. **amplifier gain** in the typical range of 1.0–3.0 .
3. **lower discriminator** below the wall-effect shelf around bin 24–26.

The impact is demonstrated in Fig. 4.3b for sensor `04`, where the PHS peak has been shifted and the average count rate went up. After manual adjustment of the parameters for all sensors, the individual offsets almost vanished and the standard deviation from the mean, $\epsilon^{p=2}(N)$, has been reduced by 50 % down to the order of the statistical error (Fig. 4.2). Moreover, the average absolute deviation, $\epsilon^{p=1}(N)$ (not shown), was reduced even below the statistical error $\epsilon(N) = \sqrt{N/24}$ of the daily aggregated time series.

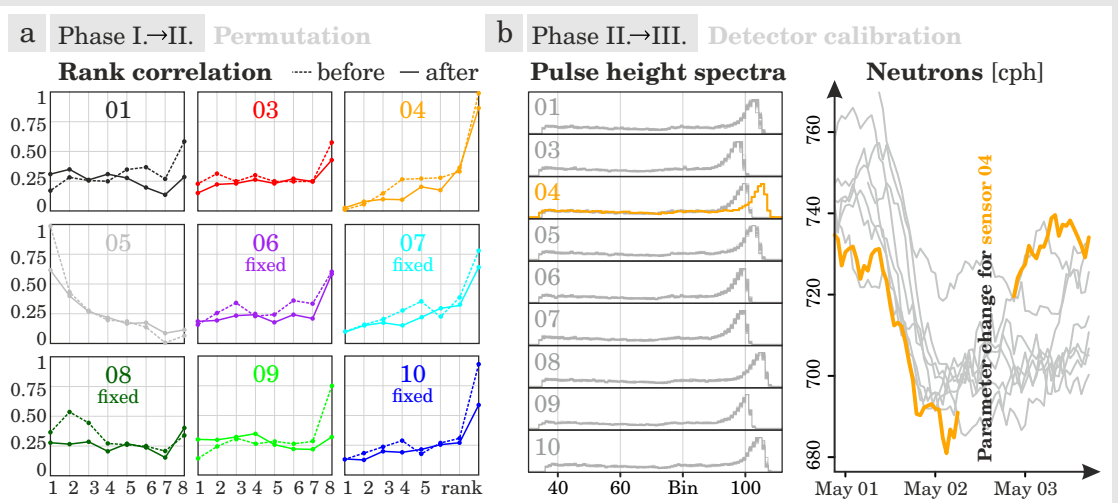

Fig. 4.3: a Rank correlations of CRNS detector signals before and after permutation did not show significant change. b Calibration of the pulse height spectrum from `CRS04` (orange) and its impact on the count rate.

4.3.3 Minimum temporal resolution

While Bogena et al. (2013) was able to assess the appropriate temporal resolution of CRNS observations theoretically, the present arrangement provides a unique opportunity to test the approach with multiple sensors. The sensor-to-sensor variability must be an effect of statistical noise if all sensors were exposed to similar meteorological forcings and were sensitive to similar areas in the footprint. Whether these assumptions hold or not is further investigated in section 4.3.4 and chapters 5–6. In this section, only the statistical effect of the time-integration interval is to be discussed.

Fig. 4.4a depicts the changes of sensor-to-sensor correlations by four effects. Firstly, correlations are typically higher under dryer conditions (Apr), as wet periods typically implicate increased counting uncertainty (Feb–Mar). Secondly, the correlation decreases as meteorological correction approaches were applied, which is expected since common temporal modulations were removed from the time series of all sensors. Thirdly, the correlation increases with integration time, as additional smoothing typically removes random noise around the mean. And lastly, the ensemble spread is lowest for integration intervals of 8–14 hours, as further smoothing may exaggerate linear biases between the signals.

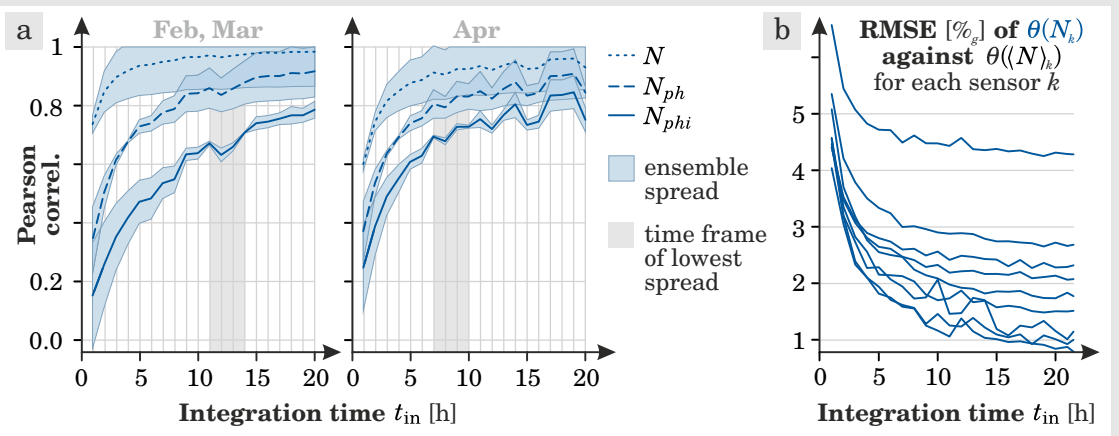

Fig. 4.4: Influence of integration time to correlations among a 9 sensor ensemble and soil moisture performance. a Pearson correlations for uncorrected and corrected neutron counts during a wet and a dry period. As expected, correlations decrease as common dependencies were removed (pressure, humidity, and incoming radiation, see section 3.5). The lowest ensemble spread is achieved for 8–12 hours integration time. b Root mean square error of converted soil moisture prediction against converted soil moisture of the ensemble mean $\langle N \rangle$. Accuracy below 2 % is achieved for t_{in} = 5–12 hours. However, individual sensor signals are shifted due to the sensor-specific detection parameters (section 4.3.2).

In Fig. 4.4b the aggregation effect is propagated to the individual soil moisture products $\theta(N_i)$, where their *root-mean-square-errors* to the ensemble mean $\theta(\langle N \rangle_i)$ is plotted. Although this analysis has been performed before sensor permutation, the relative decrease with integration interval is hardly influenced by NPM parameters

(section 4.3.2). For all sensors, RMSEs were reduced by 50-70 %, which fell below the typical accuracy limit of 2 $\%_g$ after 10 hours of integration time. These findings agree quantitatively with theoretical calculations by Bogena et al. (2013), as well as similar experiments using Bonner spheres (Rühm et al. 2009, Fig. 8–9).

4.3.4 Spatial heterogeneity in the footprint

To assess the influence of complex terrain in the urban area, the authors conducted two spatial surveys with the mobile CRNS rover and neutron transport simulations with URANOS (see also chapter 8 and section 3.8, respectively).

The two campaigns in May 2014 and July 2015 cover different wetness conditions that were only visible in the non-paved areas (Fig. 4.5d,e). Although the applied Kriging interpolation is invidious for such low numbers of measurement points, both campaign data agree well in terms of the north-south gradient and the influence of a water pool P. The urban scene has been re-enacted with the Monte-Carlo code URANOS v0.7, using 2D images of different depths $(-5, -0.3, 0, 0.1, 10, 20)$ m that define the different material compositions on the basis of their color code. Fig. 4.5b shows a combined image of the layers which were used as model input.

The neutron density calculated by the simulation (Fig. 4.5c, preliminary) confirms that the observed north-south gradient is a permanent geometrical or structural effect. However, differences between simulated and observed patterns may be directly related to urban water content, as grassland areas in URANOS were set up homogeneously with $\theta = 10\,\%_v$.

Both experimental and theoretical results clearly demonstrate that a significant neutron heterogeneity can occur within the CRNS footprint under conditions of complex terrain. Moreover, slight variability is evident in the *Schmetterlingswiese*, where trees and structures might influence the neutron density at the scale of a few meters. This could serve as an explanation for some position-related variability observed in the course of this study (see also chapters 6–7).

4.3.5 Areal correction for partly paved ground

The CRNS footprint is reported to be as large as 30 ha (Desilets and Zreda 2013) and thus covers a much larger area than the *Schmetterlingswiese* (0.1 ha) in which the sensors were located. Even if the revised footprint area of $6 - 18$ ha is considered (Köhli et al. 2015), the question remains whether the paved ground beyond the meadow might bias the soil moisture signal due to its inability to store water. This section applies the radial sensitivity function W_r published by Köhli et al. (2015) to calculate the number of detected neutrons N from certain ring elements at distances r (compare also chapters 6–7):

$$N = \int_0^\infty W_r(h\,,\theta) \cdot \mathrm{d}r\,.$$

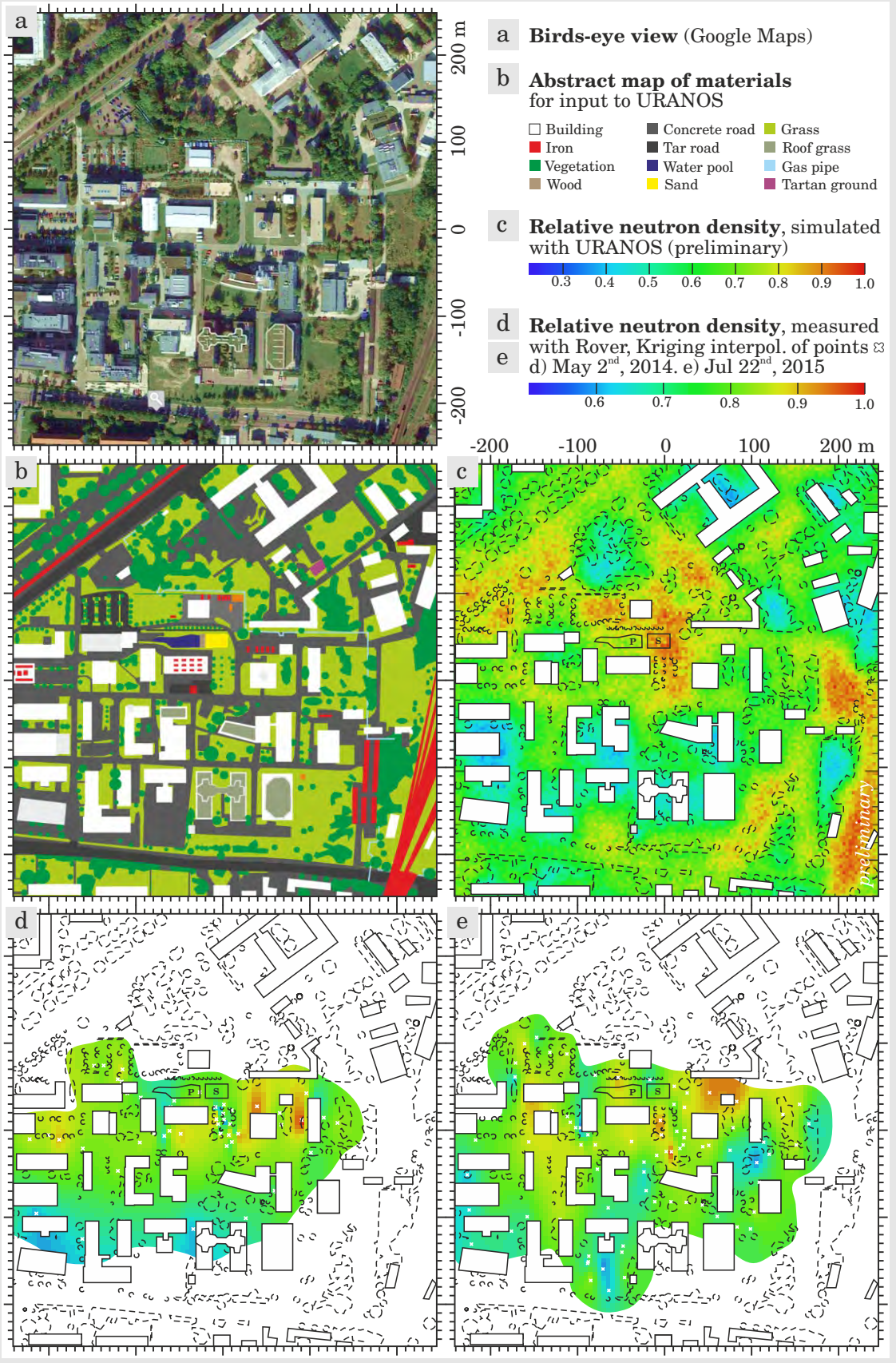

Fig. 4.5: Neutron environment of the urban CRNS test site (centered). Modeled and measured neutrons show significant heterogeneity in the 0.1 ha installation area at (0,0), as well as in the 25 ha footprint of the 10 sensors (whole domain).

Thus, a circular section of angle φ which is confined between radii r_1 and r_2 contributes the following fraction of neutrons n:

$$n(r_1, r_2, \varphi) = \int_0^{\varphi} \int_{r_1}^{r_2} W_r(h, \theta) \cdot \mathrm{d}r \cdot \mathrm{d}\varphi = \frac{\varphi}{2\pi} \int_{r_1}^{r_2} W_r(h, \theta) \cdot \mathrm{d}r \,. \tag{4.2}$$

The contributing area of the *Schmetterlingswiese* and surrounding patches is roughly equivalent to a circle of radius $r_2 \approx 20\,\mathrm{m}$. Hence, the portion of measured neutrons from this area is $n(0, r_2) \approx 41 \pm 2\,\%$, depending on h and θ.

Pursueing this idea even further, we suggest a new scaling method for CRNS measurements covering both a variable and a constant area in their footprint. At the *Schmetterlingswiese* test site only 0.1 ha of the footprint contains soil, beyond which everything else are either concrete materials or buildings. Thus, the neutron dynamics is significantly damped as only a small fraction $n(r_1, r_2, \varphi)$ of the total neutrons is connected to soil moisture variability. In order to compare these measurements with independent soil moisture sensors, we introduce an

$$\text{areal correction:} \quad N' = C_{\mathrm{area}}(N) = \frac{N - \langle N \rangle}{n(r_1, r_2, \varphi)} + \langle N \rangle \;, \tag{4.3}$$

that essentially scales the anomaly of neutrons by the inverse fraction of the contributing area. Using an exemplary sensor, `CRS08`, and the average soil moisture from a mobile soil moisture network, Fig 4.6 demonstrates that this scaling approach can help to interpret CRNS data with confined areal coverage. Apart from the improved match of soil moisture dynamics in drying periods, the areal correction generates much too high peaks during rain events. Eventually, the whole footprint should be considered during those periods, because precipitation water still ponds on paved ground before it evaporates. As a consequence, the areal correction reveals interception processes during precipitation and results in more realistic response of the CRNS signal (not shown).

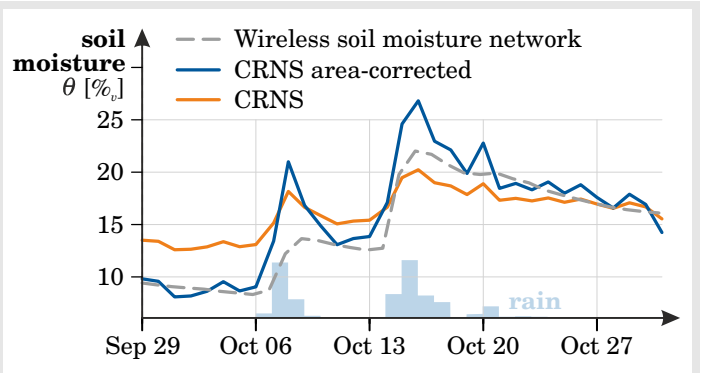

Fig. 4.6: Demonstrating the area correction approach (eq. 4.3) in the *Schmetterlingswiese*, which scales neutron signals depending on the fraction of non-paved area in the footprint.

Moreover, sprinkler experiments were conducted on the *Schmetterlingswiese* in $\approx 5\,\mathrm{m}$ distance from the sensors. Even four hours of irrigation with a small gardening sprinkler has not led to a clearly visible neutron response (not shown). With the help of eq. 4.2 the expected contribution of the sprinkled area can now be estimated, which is $n(5\,\mathrm{m}, 9\,\mathrm{m}, 25°) \approx 0.26\,\%$ and as such far below the statistical significance.

4.4. Conclusion & Outlook

The sensor-intercomparison approach provided a first impression of the uncertainties related to neutron count statistics. Although the detectors were located within a 15 m area at an average distance of 1.5 m, their signals exhibited significant differences in temporal variation and offset. By permutation of the sensor locations, individual local effects could be excluded from playing a major role in the game. In the course of this study the following insights were gained:

1. Calibration of detector-specific NPM parameters is essential to achieve comparable neutron counts and exclude otherwise noisy effects. It is thus recommended to adjust the pulse height spectra (PHS) consistently. After private communication with `Hydroinnova`, these findings then impacted the production line of CRNS detectors, which are now calibrated prior to shipping.
2. Individual *sensor efficiencies* were obtained and presented in the 4$^{\text{th}}$ COSMOS Workshop 2014 (not shown), an approach which has been adopted later on by Baatz et al. (2015). In the present work the *efficiency calibration* reduced the ensemble spread of all sensors.
3. If different CRNS detectors are required to deliver similar results under similar conditions, a minimum temporal resolution of $\approx$ 10 h was found to provide acceptable comparability.
4. Soil moisture dynamics inferred from CRNS observations in partly paved areas are significantly damped. An areal correction approach based on the sensitivity function W_r (Köhli et al. 2015) is presented, that scales the CRNS variability based on the fraction of non-paved areas in the footprint. This led to sufficient agreement with independently measured soil moisture profiles.
5. The potential of `URANOS` spatial simulations has been demonstrated to assess site-specific heterogeneity of neutrons that is unrelated to soil moisture. Together with mobile measurements in the urban area, a remarkable heterogeneity in the footprint has been revealed that contradicts the hitherto accepted "representativeness within 30 ha" associated with the CRNS method.

During periods of negligible changes of nearby water content, all the sensors still exhibited remarkable deviations. This raises the question whether the conventional correction parameters for air pressure, air humidity, and incoming radiation would need revision at this site. The next chapter acts on the suggestion to optimize those parameters by removing their correlation to the neutron count rate, hopefully reducing site-specific variability. Future studies should take the opportunity of such an arrangement presented here, to merge the individual count rates to a "super-detector". Thereby, extraordinarily high count rates could be achieved at a minimal statistical noise, opening the path for accurate identification of environmental factors.

As a consequence of the different variability of nearby CRNS sensors, as well as the significant neutron heterogeneity simulated and observed in the footprint, the question is immediately raised whether the accepted footprint radius of 300 m and the fairly smooth exponential sensitivity (Zreda et al. 2008; Desilets and Zreda 2013) are a valid representation of reality. Following these doubts, the footprint characteristics were further investigated experimentally (not shown) as well as theoretically (chapter 6), and published in Köhli et al. (2015).

Fig. 5:
Installation of the "cosmic buoy" at *Seelhauser See*, with the help of K. Rahn and M. Wieprecht (UFZ Magdeburg).

5.

Lake-side Neutron Trap

Monitoring incident cosmic rays with a buoy

The previous chapter revealed remarkable signal variability of nine cosmic-ray neutron sensors, even during periods of negligible hydrological changes. Together with other published datasets (e.g., Baatz et al. (2014), see Appendix C), the question is raised whether unrecognized meteorological effects or incoming radiation contribute to the signal at the surface.

As has been pointed out in chapter 3, the accepted temporal correction approaches underly various assumptions that might be inappropriate for the method of cosmic-ray neutron sensing (CRNS). For example, most publications in CRNS research made use of the *Jungfraujoch* neutron monitor (NM) in Switzerland, in order to correct their local data from Europe, USA, Australia, and beyond (see also section 2.2.4). In addition to that, neutron monitors preferably measure high-energy protons instead of low-energy neutrons.

This chapter hypothesizes that only a *nearby* neutron monitor with *similar* energy sensitivity is appropriate to reliably correct CRNS data. In order to exclude temporal hydrologic effects, a CRNS detector has been deployed on a lake to answer the raised questions. Moreover, unhindered correlation to air pressure and humidity offered a unique opportunity to revisit the corresponding correction parameters.

We hope for a good catch!

5.1. Introduction

Variable incoming cosmic-ray intensity can have many reasons from galactic and solar disturbances to atmospheric and meteorological changes (see also chapter 2). Most of these anomalies are expected to change proportionally in every domain of the neutron energy spectrum. As low-energy CRNS signals are typically corrected with high-energy neutron monitors (NM), their proportional variation would justify a simple relative correction factor (cmp. section 3.5). However, Kudela (2012) compared signals of five NMs at different locations on Earth and found that (1) solar *Forbush decrease* events (section 2.1.5) are better pronounced in monitors at low cutoff rigidities R_{cut} (cmp. contours in Fig. 5.1), (2) cosmic-ray intensity can decrease or increase depending on local magnetospheric transmissivity, and (3) depressions from severe solar storms are visible to some NMs, while completely absent to others. Additionally, Belov et al. (2005) revealed that local magnetospheric effects can significantly alter cosmic-ray variations on Earth by the order of $\approx 8\,\%$ for some individual neutron monitors, while they can be completely absent for others. Both these findings show that especially during short-term solar events (which can last for several days), the simple relative correction function is invalid and might depend on local geomagnetic conditions and the choice of the reference station.

The "viewing angle" of NMs plays an important role in that game. Due to the dipolar geomagnetic field and the rotation of the Earth, different locations at the surface receive cosmic rays from different directions (Herbst et al. 2013; Bütikofer et al. 2015). For example, NMs at the poles exhibit wider acceptance angles into the heliosphere and thus are exposed by different particles and energies. Fig. 5.1 illustrates those source directions for exemplary locations on Earth (X), where cosmic rays of high energy/rigidity entered the atmosphere (20 km altitude) close to X, while low-energy/rigidity particles originated far away from X. This simulation ultimately puts doubt on the convention to use the *Jungfraujoch* neutron monitor in Switzerland as a reference station for CRNS measurements all over the world. A similar picture has been published elsewhere by specifically addressing neutron monitor stations (Matthiä et al. 2009, Fig. 4).

Selection of adequate NM stations and correction factors should generally take the cutoff rigidity R_{cut} into account, as it describes the comparability of incident neutron energies. However, this approach cannot be reliable, because the change of the terrestrial magnetic dipole can introduce temporal variations of R_{cut} at the scale of 1–10^4 years (e.g., Guyodo and Valet 1996). While for example the NM in *Kiel* changed only marginally in the last century (2.64 $\rightarrow$ 2.52 GV), Herbst et al. (2013) revealed that other stations like *Mexico* changed more dramatically (11.38 $\rightarrow$ 8.21 GV). Temporally diverging trends observed with different neutron monitors confirm this long-term behavior (Oh et al. 2013), and may significantly bias CRNS corrections if no adaption is made. According to Oh, linear detrending approaches are appropriate to account for these effects.

A further criterion for selecting adequate neutron monitors should be its altitude. Although operators apply air pressure corrections to account for their specific altitude, differences might remain due to varying cosmic-ray energies (Sato 2015, Fig 11), wind effects (Bütikofer 1999; Abunin et al. 2016), or hydrological effects like snow (Tanskanen 1968; Korotkov et al. 2011; Dorman 2004). This already indicates

that high-energy neutron monitors like *Jungfraujoch* (4400 m a.m.s.l.) might not be a good estimator for fast neutrons at the sea level elsewhere. Moreover, Aplin et al. (2005) argues that the correction with surface air pressure does leave a significant residual dependency on pressure and temperature effects in the upper atmosphere. Tests at different latitudes suggest that high-energy cosmic rays are more affected by atmospheric disturbances than low-energy cosmic rays.

Besides those effects, even more factors prohibit comparability of neutron monitor data. For example, Krüger et al. (2008) observed device-based temperature effects on the performance of neutron monitors. Their suggested correction approach, however, is rarely applied by NM operators. And Chiba et al. (1975) revealed significant longitudinal discrepancies by comparing neutron monitors on three continents. For example, monitors KIEL and NEWK exhibit almost identical cutoff rigidities, but their location in Germany and USA may introduce significant differences (see also Appendix C).

Additionally, atmospheric stratification and clouds may influence the cosmic-ray particles in an unpredictable way (Kancírová and Kudela 2014; Ruffolo et al. 2016). Those effects can be accounted for using integral water vapor observations of microwave radiometers, for instance. Apart from that, individual changes of hydrogen, oxygen, ozon, nitrogen, or carbon may influence production rates of neutrons differently for CRNS energies compared to NM energies. In this regard, observations of atmosheric chemicals (e.g., Keeling and Shertz 1992) might help to explain differences of NM and CRNS incoming variations.

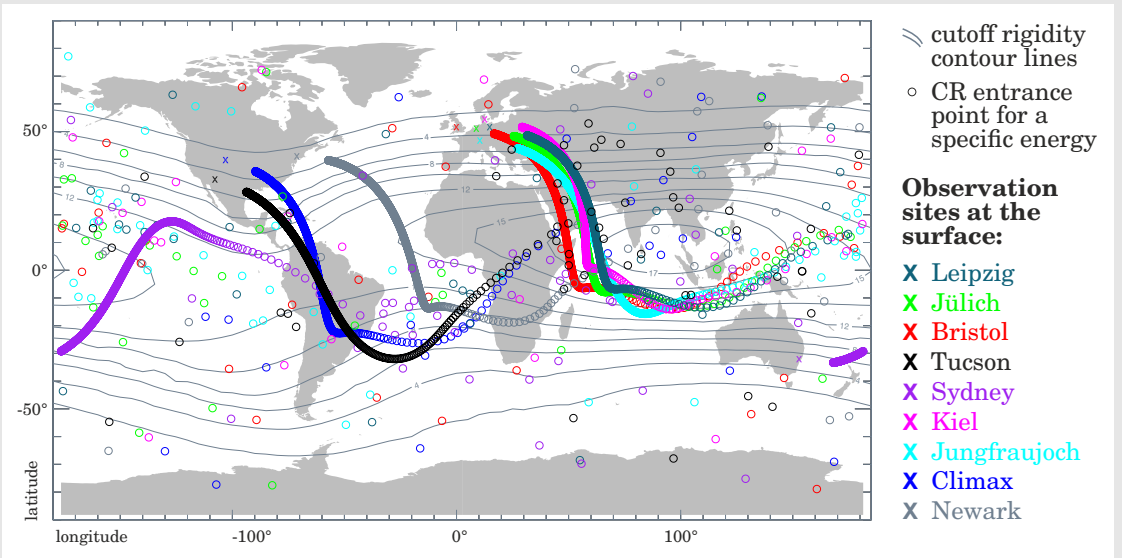

Fig. 5.1: A map of cutoff rigidities R_{cut} [GV] calculated for Jan 2016 (gray contours). Asymptotic viewing directions for incoming cosmic rays of selected locations on Earth (color), where circles represent rigidity levels between 0.6 and 100 GV. Signals of stations that are close together can have completely different origin, hence are prone to different geomagnetic variations. *Credit: simulated by* K. Herbst, *2016, using geomagnetic models from* Tsyganenko *(1998) and* Thébault *et al. (2015).*

The review represents the large number of unresolved issues in the research field of cosmic-ray neutron monitoring. The corresponding uncertainties directly propagate to the performance of CRNS for environmental research. Even the community of cosmogenic nuclide dating reported issues when using NMs as a proxy, due to disparate energy sensitivities (see Dorman 2004, p. 197).

As the demand for accurate observations and predictions is globally increasing, the correction for incoming radiation and meteorological effects should become a key challenge for the CRNS community. Correlations to those effects need to be removed entirely before data interpretation continues towards hydrological processes.

Naturally, removing correlations ρ does not equivalently remove features of correlating processes. For example, sometimes low pressure or high humidity correlate with precipitation and consequently with soil moisture. Then, minimizing ρ could also clear out the soil moisture signal. These issues are related to the popular *equifinality problem*, where different parameterizations may exist to explain a single observation (Beven and Freer 2001). For this reason, a CRNS detector was deployed on a lake, where effects from surface runoff and soil moisture are non-existent.

This configuration could then serve as a calibrator against the incoming variability. The advantage of water bodies beneath a neutron detector was also reported by Krüger and Moraal (2010), who performed intercalibration measurements of neutron monitors all over the world by placing a mini-NM over a small pool. First results of the buoy experiment were presented by Schrön et al. (2015), who found that the bouy time series deviated from three neutron monitors `JUNG`, `KIEL`, and `NEWK` by ≈ 1.4 standard deviations (see section 2.2.4 for a station overview).

5.2. Methods

5.2.1 Study site

The *Seelhausener See* is located at the border between Saxony and Saxony-Anhalt. As it has been previously used for mining activities, the lake is still not open for tourists and thus offers a perfect place to conduct research with sensible technology. The buoy detector was placed at coordinates `51.584139, 12.414150` (WGS84) or `4528812, 5716710` (Gauss-Krüger), where the distance from the shoreline was chosen to be ≈ 300 m. Preparatory analysis with the neutron transport model `URANOS` (Köhli et al. 2015) confirmed that this distance is sufficient, as only 2 % of the detected neutrons originated from an ideally dry shore (see Fig. 5.2).

5.2.2 The CRNS buoy detector

The buoy of `type 601 Profiler` from `IDRONAUT Profiling Systems` was provided by the `UFZ` Magdeburg, and has been successfully used in other studies on limnology. The moderated and the bare tube from a stationary CRNS were disassembled and integrated in a tailor-made aluminum lid, protruding upwards from the buoy (Fig. 5.3).

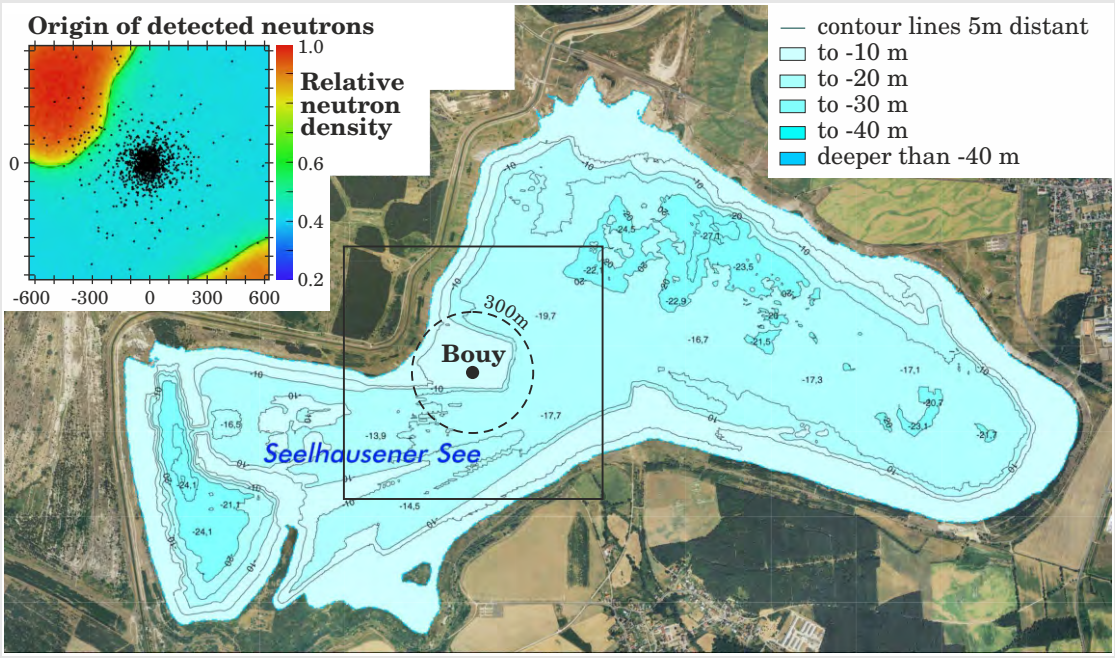

Fig. 5.2: Location of the CRNS buoy detector at lake *Seelhausener See*. The distance of 300 m from the shoreline was chosen such that more than 98 % of detected neutrons (black dots) had contact to water only (simulated with `URANOS` by M. Köhli). *Credit: Map adapted from LMBV*

The detectors were powered with eight batteries of type `Yuasa NPL`, 38 Ah, using lead-fleece technology to guarantee proper functioning under wobbling conditions. After installing on July 15th the batteries had to be recharged by the end of September as the power supply lasted 2.5 months. Finally, the buoy was retracted under frosty conditions on Dec, 2nd. An antenna regularly transmitted sensor data and GPS coordinates to an FTP server, in order to allow scientists to remotely keep track of the battery status, and for the sake of protection against theft and tempest.

5.2.3 Correction functions

Due to the unique setup of CRNS observations without any influence of soil or precipitation, the conditions were perfect for testing the accepted meteorological correction functions for air pressure p, air humidity h, and incoming radiation I (compare section 3.5).

$$\begin{aligned}
\text{air humidity correction:} \quad & C_h = 1 + \alpha\,(h - h_{\text{ref}}) \\
\text{atm. water correction:} \quad & C_{\text{IWC}} = 1 + \alpha_{\text{IWC}}\,\Delta\text{IWC} \\
\text{air pressure correction:} \quad & C_p = e^{\beta(p - p_{\text{ref}})} \\
\text{incoming rad. correction:} \quad & C_I = 1 + \gamma\,(I_{\text{ref}}/I - 1)
\end{aligned}$$

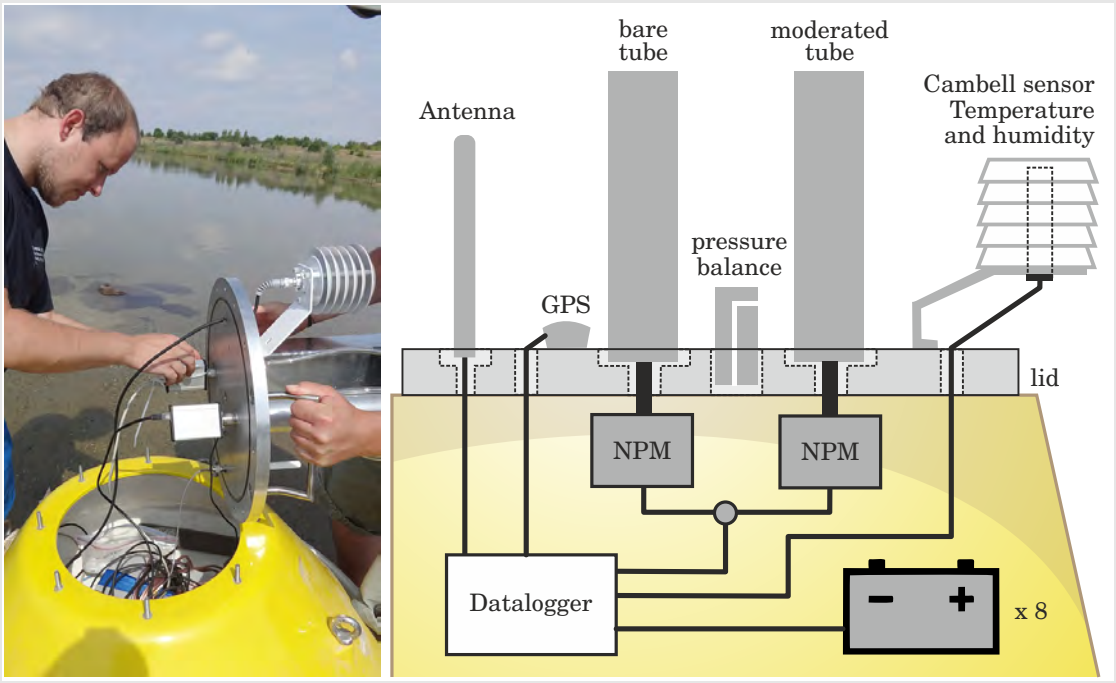

Fig. 5.3: Detector housing inside the tailor-made lid of the buoy, besides sensors for air humidity, temperature, GPS, and an antenna.

The parameters α and α_{IWC} account for water vapor in the near or total atmosphere, respectively. They were defined by Rosolem et al. (2013a) using neutron transport simulations, however systematic experimental validation has not been reported, yet. The *attenuation coefficient* $\beta \propto L^{-1}$ has been used for decades to process atmospheric correction of cosmic rays. It can be determined using different analytical relations (Clem et al. 1997; Dunai 2000; Desilets et al. 2006), by minimizing the correlation between incoming radiation and air pressure (Sapundjiev et al. 2014), or by comparing neutron time series with a reference station, where β is known (Paschalis et al. 2013). These various approaches show that β might be a complex variable that depends on several factors:

1. latitude, altitude, type and energy of incident particles (Dorman 2004; Clem and Dorman 2000, and references therein),
2. large variations during the solar cycle and during solar flare events (Dorman 2004; Kobelev et al. 2011),
3. properties and yield function of the detector device (Bütikofer 1999), which has never been identified for the CRNS technology.

The conventional approach to correct for incoming radiation uses $\gamma = 1$, but it still fails to remove all the incoming cosmic-ray variability (see Appendix C). Hawdon et al. (2014) presented a scaling concept to account for geomagnetic rigidity, $\gamma = 1 - 0.075(R_{\mathrm{cut}} - R_{\mathrm{cut}}^{\mathrm{ref}})$, however this approach has not led to convincing performance. Tests during the course of this study confirmed that it is generally a good idea to scale the anomaly of I to match the variability of N_{ph}. For example, peaks of

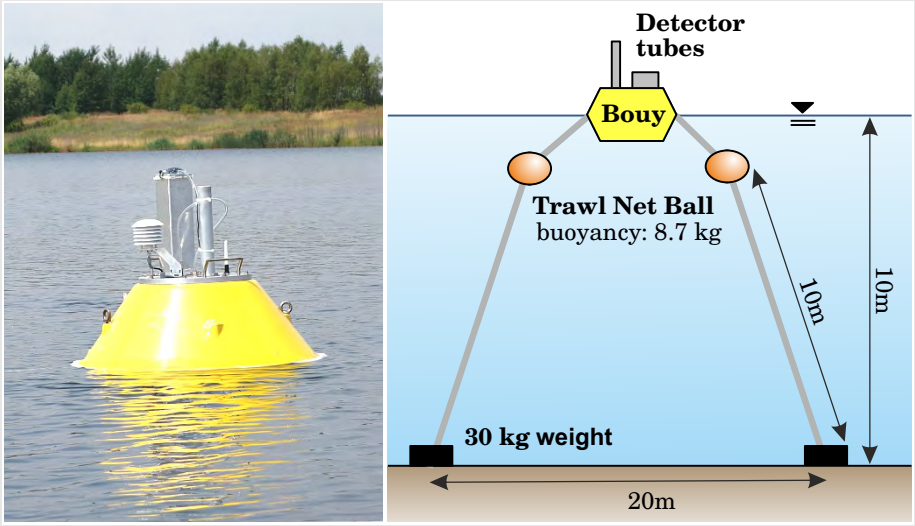

Fig. 5.4: Anchorage of the stationary buoy in the lake.

Forbush decreases (section 2.1.5) have been suggested as good candidates to measure the anomaly difference between two neutron monitors (Dorman 2004, page 189). However, the scaling factor γ may depend on many geomagnetic effects, as well as on differences in energy efficiency of CRNS and neutron monitors.

5.2.4 Parameter optimization

In order to find sufficient correction functions capable of removing the mentioned effects, the correlation ρ between neutron counts N and meteorological observations is to be minimized. For the optimization procedure, the following *objective function* is used:

$$\text{objective function:} \quad \min_{\alpha,\beta,\gamma} \rho_{phI} \rightarrow 0 \,,$$

$$\text{where} \quad \rho_{phI} = \left(\rho\left(N_{phI}\,, p\right)^6 + \rho\left(N_{phI}\,, h\right)^6 + \rho\left(N_{phI}\,, I\right)^6\right)^{\frac{1}{6}} \,, \tag{5.1}$$

$$N_{phI}(\alpha\,, \beta\,, \gamma) = N \cdot C_h(\alpha) \cdot C_p(\beta) \cdot C_I(\gamma) \,,$$

$$\rho(X, Y) = \left\langle (X - \langle X \rangle)(Y - \langle Y \rangle) \right\rangle / \epsilon_X \, \epsilon_Y \quad \text{(Pearson correlation)} \,.$$

In experimental environmental research, often the *Excel Solver Software* is used to optimize simple parameters relations (e.g., Heidbüchel et al. 2016). However, this study deals with highly uncertain data including statistical noise, and aims to optimize three parameters simultaneously. For these reasons, this study makes use of the *shuffled-complex-evolution* algorithm (SCE), which is a modern approach to find global minima in highly parameter-sensitive data (Duan et al. 1992), see also chapter 9.

During optimization, the *Pearson correlations* ρ of corrected neutron data to the meteorological effects were minimized, which is an accepted approach in experimental geophysics to identify unknown effects (e.g., Fu et al. 2015). However, if many factors could explain an observation, separate optimization may lead to false recognition

of coincidental effects. Therefore, this study uses semi-multiobjective parameter optimization that minimizes the correlation of N_{phI} to h, p, and I simultaneously. To achieve this, the correlations $\rho(N_{phI}, p)$, $\rho(N_{phI}, h)$, and $\rho(N_{phI}, I)$ were combined using the vector norm of $\epsilon^{p=6}$ (cmp. section 4.2.1), which has proven to equally improve the individual measures and robustly ignore outliers in hydrological research (Duckstein 1984). Moreover, equal objective weights were justified by assessing their impact in a separate study. On the other hand, purey multi-objective approaches exhibit several advantages (Mai et al. 2016) and may be worth investigating with regards to this dataset. Moreover, the *Kling-Gupta efficiency* (KGE) is applied to assess the quality of fit to other time series, because it accounts for mean, bias, and correlation simultaneously (Gupta et al. 2009).

5.3. Results & Discussion

By excluding any other sources of variability on the lake, the semi-corrected neutron signal correlates well to air pressure, humidity, and incoming radiation (Fig. 5.5). The goal of this research is to falsify the conventional correction approaches, which should remove the presented correlations completely. Although otherwise expected, further analysis of the time series indicated that rain drops do not have a major effect on the neutron signal during precipitation events, and particularly do not go in line with the residual effects observed after completed correction.

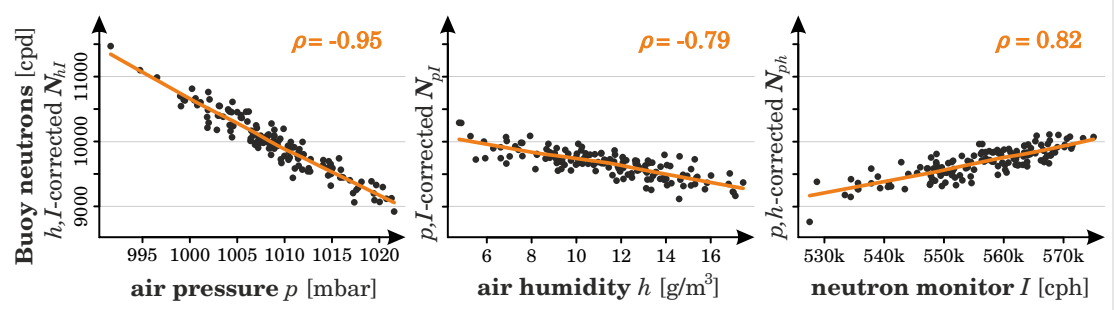

Fig. 5.5: Correlation of the daily aggregated and semi-corrected count rate from the buoy, N, to air pressure p, air humidity h, and incoming radiation I. *Credit: Figure adapted from Schrön et al. (2015)*

5.3.1 Correction for air humidity revisited

During an internal project-related study, Weimar (2015) correlated neutron counts from the buoy monitor with profiles of atmospheric water vapor. Integral water content (IWC) of the atmosphere can be measured up to various heights using the ≈ 22.2 GHz absorption line of H_2O in the microwave spectrum (Navas-Guzmán et al. 2014). The corresponding data was collected from a microwave radiometer operated by the TROPOS institute, Leipzig, Germany. The distance of ≈ 50 km to the lake, however, could weaken the comparability of those locations.

Previously, Rosolem et al. (2013a) hypothesized that CRNS detectors were insensitive to water vapor above 412 m, and elaborated correction functions for IWC and near-surface humidity h from neutron transport simulations. However, using the buoy detector in combination with the microwave radiometer, Weimar (2015) not only found residual correlation with IWC and h, but also significant influence of IWC above 412 m. The following revised correction functions removed the water vapor correlation $\rho(N_{pI}, h)$ to buoy neutrons:

$$C_h = 1 + \alpha\,(h - h_{\text{ref}})\,, \quad C_{\text{IWC}} = 1 + \alpha_{\text{IWC}}\,(\text{IWC} - \text{IWC}_{\text{ref}})\,,$$

Rosolem et al. (2013a): $\alpha = 0.0054\,, \quad \alpha_{\text{IWC}} = 0.0143\,,$ for IWC from 0 to 412 m,

Weimar (2015): $\alpha = 0.0076\,, \quad \alpha_{\text{IWC}} = 0.00235\,.$

Although the impact on the corrected neutron intensity is about 4–6 %, future studies need to test the performance on other stationary probes with regards to soil moisture prediction.

5.3.2 Optimization of correction parameters

The optimization strategy presented in the methods section led to significant deviation to the accepted parameters α, β, and γ, and further showed dependence on the chosen neutron monitor. As Table 5.1 shows, the correction with the JUNG neutron monitor leads to a remarkable agreement with Desilets et al. (2006) and Hawdon et al. (2014) for β and γ, respectively. The reason for this match might be that previous studies always used the *Jungfraujoch* monitor to verify their CRNS parameters. However, the result for α confirms that the humidity correction presented by Rosolem et al. (2013a) and discussed in the previous section is not appropriate for the actual atmospheric effects. Optimized parameters using monitors KIEL and NEWK deviate much from the accepted results, showing that local effects of the neutron monitors sites might influence their signal. Following this argumentation, different correction parameters are necessary for different neutron monitors.

Table 5.1: Meteorological correction parameters using accepted methods and the optimization method, both conditioned on the geomagnetic location of the buoy.

method	α [10^{-3}]	β^{-1} [mbar]	γ_{JUNG}	γ_{KIEL}	γ_{NEWK}
Rosolem et al. (2013a)	5.40				
Desilets et al. (2006)		131.60			
Hawdon et al. (2014)			1.111	0.951	0.954
conventional			1.000	1.000	1.000
min ρ_{ph}	4.28	141.38			
min ρ_{phI} using I_{JUNG}	6.39	131.51	1.095		
min ρ_{phI} using I_{KIEL}	5.83	142.76		1.042	
min ρ_{phI} using I_{NEWK}	4.74	135.48			1.094

This is further a call for operators of neutron monitors to correct for their local atmospheric and hydrological effects. Just recently, Ruffolo et al. (2016) confirmed this statement by concluding that correction for humidity could improve the explanatory power of neutron monitor observations.

5.3.3 The bouy as an alternative neutron monitor

Regarding the comparable energy window of the CRNS buoy with regards to CRNS stations, the detector on the lake might be a better alternative to neutron monitors when CRNS stations are corrected for incoming radiation. The hypothesis is tested by correcting the station data from CRS07 in *Großes Bruch*, were a network of soil moisture sensors can provide verification. The presented SoilNet data is spatially weighted following chapter 7 and Köhli et al. (2015).

Fig. 5.6 illustrates the performance of the buoy correction compared to the correction with the *Jungfraujoch* neutron monitor. While some features seem to improve during the precipitation event in late October or the Forbush decrease in mid September, significant gain is not evident from this picture.

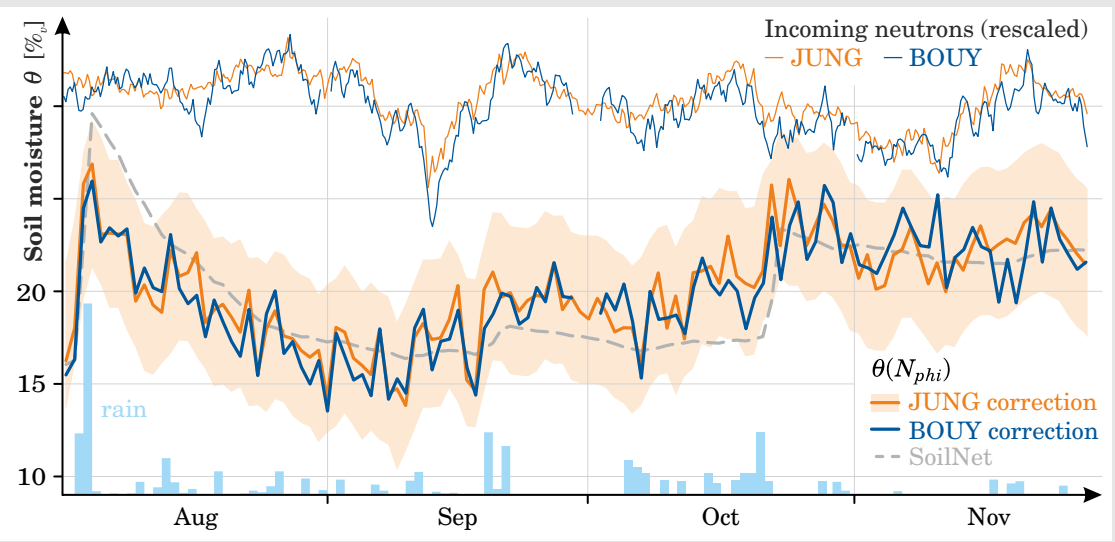

Fig. 5.6: Performance of the buoy incoming correction for soil moisture estimation in the TERENO study site *Großes Bruch* (see also chapters 7 and 8). The introduced discrepancies mostly stay within the error range of the CRNS.

In Table 5.2 the corresponding measures KGE and RMSE are presented in a daily and 3-daily mode. Such large integration intervals were necessary, because both stations exhibit tremendously low count rates. In fact, the overall improvement of the buoy correction from daily to 3-daily (while some NMs do not improve) shows that the main error comes from the low signal-to-noise ratio of the buoy detector. Although the improvements were not significant, the overall comparison with three other neutron monitors demonstrates the promising potential of the CRNS buoy as an alternative for neutron monitors.

Table 5.2: Performance of CRNS in *Großes Bruch* against the SoilNet using four different reference stations for incoming radiation. The buoy correction performs best in terms of KGE, and decent in terms of RMSE, for both, daily and 3-daily averaging windows.

neutron monitor	KGE_d	KGE_{3d}	$RMSE_d$	$RMSE_{3d}$
buoy	0.743	0.780	2.15 $\%_v$	1.71 $\%_v$
JUNG	0.703	0.717	2.12 $\%_v$	1.79 $\%_v$
KIEL	0.740	0.670	2.05 $\%_v$	1.68 $\%_v$
NEWK	0.699	0.738	2.34 $\%_v$	2.03 $\%_v$

5.4. Conclusion & Outlook

This study tested the concept of CRNS measurements on a lake, in order to access correlations to meteorological effects that are otherwise covered by predominant soil moisture dynamics. By analyzing the time series of five months in conjunction with neutron monitor data, the following conclusions were drawn:

1. Neutron monitor data should be treated carefully in the scope of CRNS research, as it depends on local weather conditions, geomagnetic location, and it is sensitive to different particles, directions, and energies. Special care should be taken during periods of turbulent solar activity.
2. A *buoy neutron monitor* is well able to record the incoming component of cosmic-ray neutrons, and to identify clear dependence on air pressure and humidity. Due to the low energy sensitivity of CRNS detectors, incoming corrections with the buoy led to slightly better – but statistically insignificant – performance for soil moisture prediction of a nearby stationary CRNS, compared to using conventional high-energy neutron monitors JUNG, KIEL, and NEWK (Table 5.2, Fig. 5.6).
3. Parameters β and γ depend on detector-specific and rigidity-dependent yield functions and efforts have been made to find their correspondent range for the CRNS technology (min ρ_{ph} in Table 5.1).
4. It has been further explained that parameters α, β, and γ may depend on geo-meteorological conditions. For example, α has been revised using water vapor measurements from a microwave radiometer (section 5.3.1). This chapter aimed to motivate researchers to apply sophisticated optimization techniques in order to find site-specific parameters for the CRNS correction functions.

Admittedly, this study exhibits two weak points that prohibit universal and accurate conclusions, and which should be addressed in future studies:

1. The buoy's count rate is very low (450 cph on average), consequently the results of the performance measures and parameter estimations were neither significant nor sufficiently robust. Future campaigns should apply larger CRNS detectors on a buoy, located at high altitudes, preferably near other neutron monitors (e.g., lake *Oeschinensee* near Jungfraujoch, 1500 m a.m.s.l.).

2. As correction parameters β and γ are site-specific, while α, β depend on atmospheric stratification, general conclusions can only be drawn if this concept is tested on other places on Earth.

Further research is necessary to understand the impact of different energy windows of CRNS and neutron monitors. In this regard, simulations of atmospheric particle cascades could reveal insights, e.g., using `PLANETOCOSMICS` (Desorgher et al. 2006) which is based on the Geant4 Monte-Carlo code (Apostolakis et al. 2009). The ideal goal would be to find a transfer function from high-energy neutron monitor data to low-energy CRNS corrections. Potential candidates will probably be dependent on the local rigidity R_{cut}, as it was found for mini-NMs by Krüger et al. (2008).

Experimental evaluation could be provided with neutron spectrometers, so-called *Bonner spheres*. Such a system is located at the *Schneefernerhaus* (Zugspitze, Germany), where the CRNS sensor `08` has been deployed in the last months of this research. Following the strategies from Pioch et al. (2010) who worked with neutron monitors, this could help to find the sensitive energy range of the CRNS detectors. Moreover, the influence of snow, weather, and solar flares on different energy regimes could be investigated thereby.

Fig. 6:
Thorough investigation of neutron physics, simulations, and tape rules led to new insights about the CRNS footprint (Köhli et al. 2015).

6.

Footprint Characteristics

Revised model assumptions reveal new insights

The search for the spatial sensitivity in the footprint started in early 2013, as its importance was indicated for geostatistical interpolation of mobile measurements and assimilation to hydrological models. The buoy experiment in chapter 5 has served as a perfect example to demonstrate the importance of knowing the sensor's footprint in advance to campaign planning. If the detector had been located closer to the shore, the significant contamination of soil neutrons would have superimposed the gentle effects of incoming radiation and humidity.

Investigations in an urban environment (chapter 4) have convincingly revealed a tremendous heterogeneity of neutrons in the footprint area. According to Desilets and Zreda (2013), the neutron response to small-scale soil water patterns should completely smooth out at the scale of 150 m. To resolve these contradictions, the spatial sensitivity of cosmic-ray neutron sensors (CRNS) has been revisited with additional measurement campaigns and thorough simulation efforts.

This chapter briefly summarizes methods and results from Köhli et al. (2015)[1] and puts our findings in context towards soil moisture estimation across scales.

[1] Köhli et al. (2015) is a journal publication written in the course of this PhD thesis. The 1st author (M. Köhli) and 2nd author (M. Schrön) contributed equally to the manuscript.

6.1. Introduction

An exact description of the instrumental sensitivity is important to understand, interpret, and validate measurement results. Consequently, the determination of sensor footprints has been first priority for ground-based sensors like TDR (Ferré et al. 1998), GPR (Huisman et al. 2003), GPS (Larson et al. 2008), gravimetry (Creutzfeldt et al. 2010), and even for satellite neutron sensors in space (Maurice et al. 2004; McKinney et al. 2006). Especially when the footprint is as large as ≈ 30 ha (Zreda et al. 2008; Desilets and Zreda 2013), insufficient knowledge about the spatial uncertainty and variability can be a decisive factor and critical issue for researchers as well as customers. Since the detector signal is prone to statistical uncertainty as well as to all kinds of hydrogen atoms in the environment, more and more problems have come up to sufficiently separate apparent noise from hydrological factors. Even detailed validation strategies with distributed sensor networks (SoilNets) did not adequately remove the discrepancies between cosmic-ray neutron sensing (CRNS) and area-average soil moisture (Franz et al. 2012a; Bogena et al. 2013; Coopersmith et al. 2014, among others). Moreover, conspicuous sensitivity of hydrogen sources very close to the sensor were reported by M. Zreda (unpublished), and have been confirmed also in the course of this dissertation by approaching lakes, rivers, and groups of people with the rover (e.g., chapter 8). Those findings have been contradictory to the results from Desilets and Zreda (2013) and finally led to the demand for an investigative revision.

6.2. Methods

The Monte Carlo approach is the only way to keep track of histories of millions of neutrons by simultaneously taking all relevant physical interactions into account. Although a large amount of particles are treated, the corresponding summary statistics can reveal insights into their collective effects and physical mechanisms. In this study, neutron transport simulations were performed with the Monte-Carlo code `URANOS` (section 3.8) which was specifically tailored to address the open questions of the CRNS community (Köhli et al. 2015) and proved to be reliable also in other research fields (Köhli et al. 2016).

The simulated neutrons were released in a domain shortly above the soil for the sake of computational efficiency. The according cosmic-ray neutron spectrum is the extracted component of only incident neutrons, which is based on modeled and experimentally verified results from Sato and Niita (2006) (see Fig. 3.1), and was also used by others to resolve long lasting issues (Lifton et al. 2014). One of the major differences to Desilets and Zreda (2013) is the low-energy contribution of incoming neutrons in this work, while the previous work assumed only high-energy neutrons from the atmosphere. While the incoming low-energy part is clearly verifiable (e.g., Schrön et al. 2015, Fig. 3), their potential to reach larger distances is lower and thus directly contributes to smaller footprint radii. Including this discrepancy, Table 6.1 summarizes all the major differences between the discussed models.

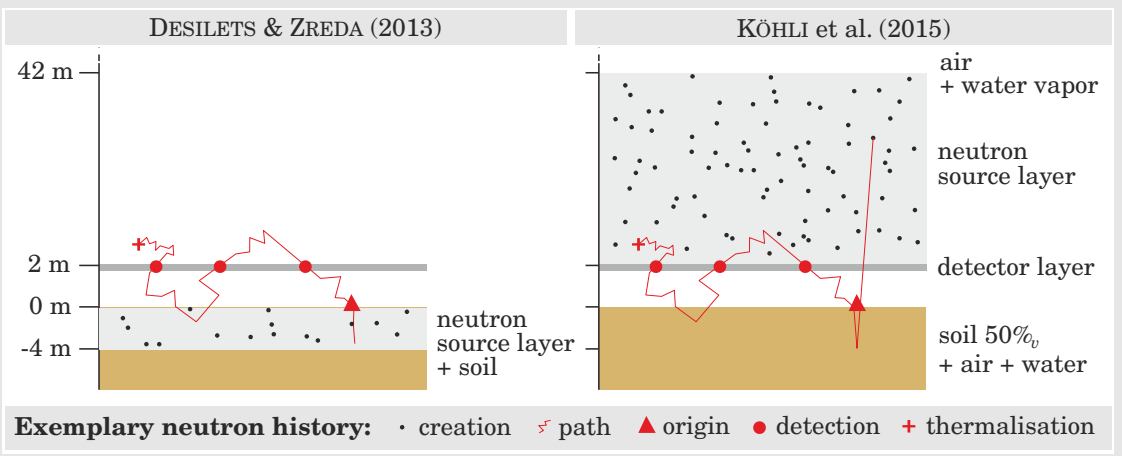

Fig. 6.1: Setup of the two models from Desilets and Zreda (2013) (left) and Köhli et al. (2015) (right). Neutrons were released in the *source layer* and their distance to the *origin* was tracked in the *detector layer*. Neutrons passing the detector are counted if they had preceding contact with the soil and are within the energy range of 10–10^3 eV.

Table 6.1: Major differences between the accepted and the revised neutron models.

	Desilets and Zreda (2013)	Köhli et al. (2015)
Model	Monte-Carlo code `MCNPX`.	Monte-Carlo code `URANOS`.
Physics	All particles, database `ENDF VII`.	Neutrons only, database `ENDF` and `JENDL-HE` (more precise models for high-energy neutrons), only relevant processes (e.g., no thermal).
Source location	Constant exponential distribution along a vertical line in the soil.	Layer from 2 to 42 m above ground.
Source spectrum	Constant $1/E$ evaporation spectrum (implicitly assuming only high-energy neutrons from top).	Incoming-only component of a verified model from Sato and Niita (2006).
Material	Soil: SiO_2, Air: N, O.	Soil: SiO_2, Al_2O_3, Air: N, O, Ar. (argon and oxygen exhibit considerable cross sections for neutrons).
Footprint determination	86 % of the integral of the exponential fit to dN/dr.	86 % of the integral of dN/dr.
Depth determination	Not provided (since source distribution was assumed constant).	86 % of the integral of dN/dd.

For every particle that passes the detector layer, the distance r to its origin is recorded. This leads to the elaboration of a so-called *ring intensity* or *radial sensitivity* $\mathrm{d}N/\mathrm{d}r$, which describes the number of neutrons that originated from a certain distance. The total number of detected neutrons in the whole domain then simply is the integration of all the ring sources over r:

$$N = \int_0^\infty \frac{\mathrm{d}N}{\mathrm{d}r} \cdot \mathrm{d}r \,, \quad \left[1/\mathrm{s}\right].$$

The footprint radius R_{86} is defined as the distance, from within which 86.5% of detected neutrons originated. It is obtained from solving the following equation for R numerically:

$$\int_0^R \frac{\mathrm{d}N}{\mathrm{d}r} = 0.865 \cdot N \,. \tag{6.1}$$

In the following, note that W_r denotes the analytical fit to $\mathrm{d}N/\mathrm{d}r$. Integrating a globally good fit, W_r, provides a good approximation to the actual footprint. In this regard, by integrating a partly good (but globally bad) fit, e.g., a simple exponential, will lead to something else than the footprint. This difference is considered as one of the major discrepancies between Desilets and Zreda (2013) and Köhli et al. (2015). *Penetration depth* D_{86} and vertical sensitivity W_d were obtained analogously.

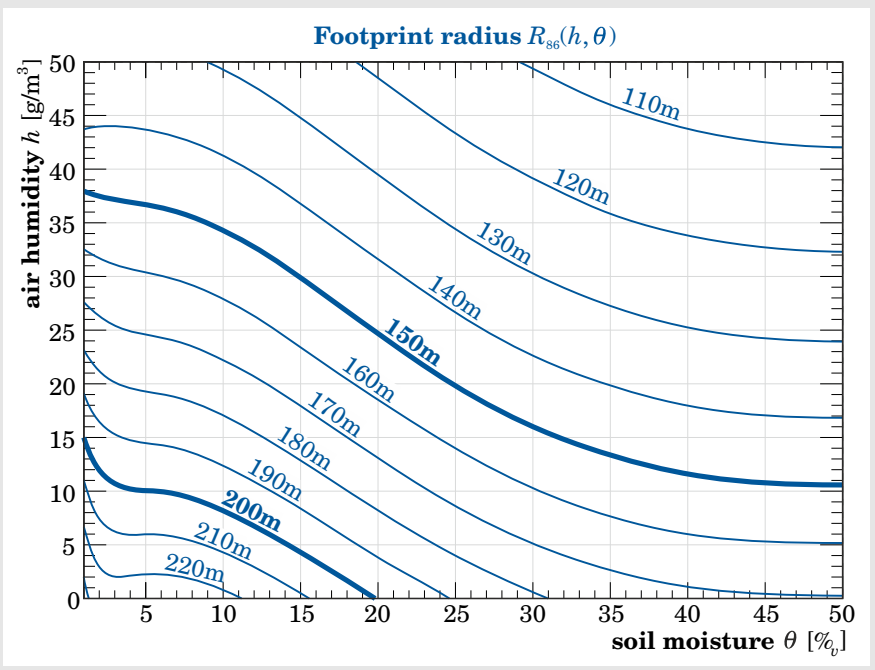

Fig. 6.2: Footprint radius R_{86} as a function of air humidity h and soil moisture θ. *Credit: Updated Figure from Köhli et al. (2015).*

6.3. Results

6.3.1 An analytical description of the radial sensitivity

The radial sensitivity $\mathrm{d}N/\mathrm{d}r$ of the detector exhibits a sharp peak within 0.5 m (because ring intensities vanish for $r = 0$) and decreases in a complex manner for higher radii (see Köhli et al. 2015, Fig. 3). The authors presented an analytical fit W_r to this decrease, that roughly indicates multi-diffusive regimes of short-range and long-range neutrons in the domain for $\theta \geq 2\ \%_v$:

$$W_r(h, \theta) \approx \begin{cases} F_1\, e^{-F_2 r} + F_3\, e^{-F_4 r}\,, & 0.5\,\mathrm{m} < r \leq 50\,\mathrm{m} \\ F_5\, e^{-F_6 r} + F_7\, e^{-F_8 r}\,, & 50\,\mathrm{m} < r < 600\,\mathrm{m} \end{cases} \tag{6.2}$$

The parameter functions $F_i(h, \theta)$ were provided by Köhli et al. (2015), Appendix A. Following eq. 6.1, the footprint is calculated and its dependency on air humidity and soil moisture is illustrated in Fig. 6.2. Additional sensitivity analysis for environmental parameters has been performed in order to obtain a practical and realistic description of the radial footprint that is subject to air pressure p and vegetation height H_{veg}:

$$\begin{aligned} R_{86}(h, \theta, p, H_{\mathrm{veg}}) &= f_p \cdot f_{\mathrm{veg}} \cdot R_{86}(h, \theta)\,, \\ \text{where} \quad f_p(p) &= \frac{0.5}{0.86 - e^{-p/p_0}} \approx p_0/p\,, \\ \text{and} \quad f_{\mathrm{veg}}(H_{\mathrm{veg}}, \theta) &= 1 - 0.17\left(1 - e^{-0.41 H_{\mathrm{veg}}}\right)\left(1 + e^{-7\theta}\right)\,. \end{aligned} \tag{6.3}$$

6.3.2 The penetration depth

The vertical sensitivity W_d has been identified to be almost exponential, and a relation is presented that also includes the penetration depth D_{86}:

$$\begin{aligned} W_d(r, \theta) &\propto e^{-2d/D_{86}(r,\theta)}\,, \\ \text{where} \quad D_{86}(r, \theta) &\approx \varrho_{\mathrm{bulk}}^{-1}\left(8.32 + 0.14\left(0.97 + e^{-r/100}\right)\frac{26.42 + \theta}{0.057 + \theta}\right)\,. \end{aligned} \tag{6.4}$$

6.3.3 Influence of complex terrain

The authors also investigated the influence of complex terrain to the footprint isotropy. Fig. 6.3 shows that roads, rivers, or hill slopes do not effect the direction and distance of neutrons. For the sake of visual interpretation, the 360° directions are discretized to 12° sectors. However, large water bodies (6.3a) or forests (not shown) may influence both, footprint and intensity from that direction. Furthermore, completely dry roads contribute to an intensity bias (red) of ≈ 20 % to the neutron signal.

6.4. Discussion

With regard to the methodological approach, the question was raised whether the choice of the source actually has an impact on the model results. Fig. 6.4 directly

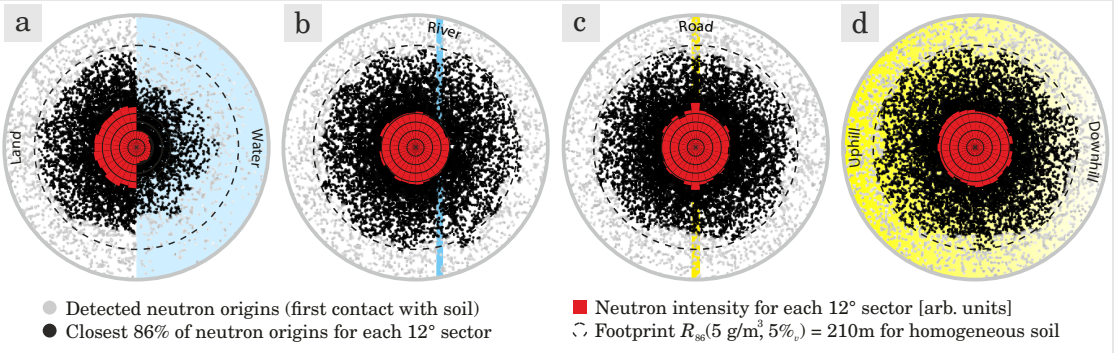

Fig. 6.3: Anisotropy of detected neutron origins (black) and neutron intensity (red) determined for every 12° sector of a circle around a centered detector. The displayed extent is 270 m in radius, whereas the dashed line represents the isotropic footprint with radius $R_{86}(h, \theta) \approx 210\,\text{m}$, considering $\theta = 5\,\%$ and $h = 5\,\text{g/m}^3$. The four exemplary cases illustrate bare soil (white) with (a) a coast line (blue), (b) a 10 m river at 50 m distance, (c) a 10 m concrete road (yellow) and (d) a 20° hill slope from the left down to the right. *Credit: Figure and caption from* Köhli *et al. (2015).*

addresses this discussion and presents results from URANOS with various sources. By taking their assumptions on source location and source energy into account, URANOS was able to reproduce the larger footprint reported by Desilets and Zreda (2013).

An important uncertainty in simulations for CRNS neutron detection is the energy sensitivity of the detector. The detection range from 10 to 10^3 eV has been recommended by Hydroinnova, however a weighted distribution is expected that can range down to the thermal regime (Desilets and Zreda 2008; McJannet et al. 2014).

Moreover, the footprint calculation takes only those neutrons into account which had prior contact with the soil. The detector, however, measures additional incident neutrons from the incoming variation. If the presented results are to be used to compare intensities (e.g., for water pool experiments), the ratio of incoming to reflected neutrons needs to be included (cmp. section 3.6).

6.5. Conclusion & Outlook

The work from Köhli et al. (2015) draws the following conclusions:

1. Neutron simulations are extremely sensitive to a few atoms of hydrogen, thus the conventional assumption of purely dry soil and air is not recommended for future studies.
2. The revised footprint radius $R_{86}(h, \theta, p, \text{veg})$ ranges from $130 \pm 4\,\%$ to $240 \pm 6\,\%$ depending on wetness conditions, and may increase with decreasing air pressure or decreasing vegetation height. Accordingly, a penetration depth $D_{86}(r, \theta)$ between 15 and 83 cm has been elaborated, which exhibits decreasing sensitivity with distance (see also Fig. 7).

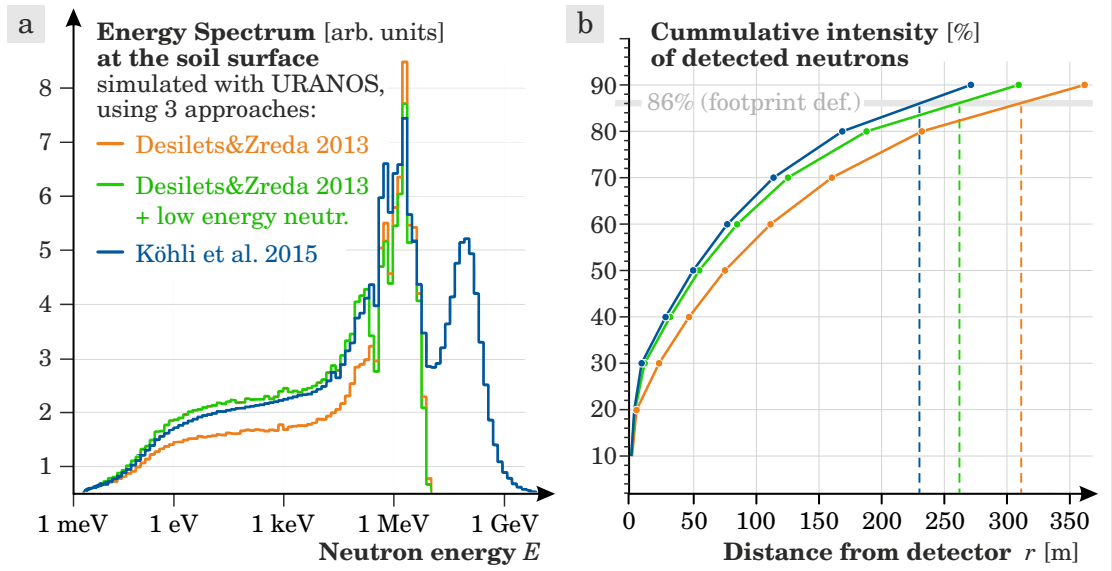

Fig. 6.4: The different approaches for the neutron input spectrum and their influence on the sensor footprint, calculated with URANOS (by M. Köhli). a Desilets and Zreda (2013) neglected incident high-energy neutrons and thus underestimated the contribution of low-energy neutrons. The addition of low-energy neutrons from top appears to be a major difference to Köhli et al. (2015). b Using the obsolete model assumptions, URANOS was able to accurately reproduce the footprint radius of ≈ 300 m obtained with MCNPX.

3. Depending on distance to the sensor, dry or wet spots contribute to the detected signal following the radial sensitivity function $W_r(h, \theta)$, which is extraordinarily steep in the first few meters. Accordingly, a vertical weighting $W_d(r, \theta)$ has been elaborated. Chapter 7 will demonstrate how these findings influence calibration and validation performance of cosmic-ray neutron sensors.
4. The detected signal is isotropic for most field applications covering rivers, roads, or hill slopes within the footprint. This opens the path to apply the sensor theory also for roving activities in even complex terrain. However, an intensity effect of roads remains remarkable and has been verified experimentally in chapter 8.
5. URANOS was able to reproduce transect experiments over rivers, oceans, and pools, which provide evidence for the new footprint theory.

From the modeler's point of view, the different results of both model approaches have their origin in the different model assumptions. The choice of the source location, as well as the incomplete exponential fit to the radial sensitivity dN/dr (Desilets and Zreda 2013) might have the largest impact to the model results. Preliminary simulations from Zreda et al. (2005) and Desilets et al. (2007) provided evidence that also the MCNPX model suggests smaller footprints if the assumptions were made differently to Desilets and Zreda (2013). The findings in both of their conference reports are much more in agreement with the results from Köhli et al. (2015) in terms of footprint radius, penetration depth, and soil moisture dependency.

Nevertheless, the CRNS method remains the only technology that is able close the gap between point and remote-sensing measurements, as it provides a representative average over tens of hectares and decimeters in depth. These findings will be particularly important when data is assimilated to gridded hydrological models, e.g., in chapter 9.

Following this new theory about the footprint characteristics, the next logical step is to quantify the impact to real world applications in the field. Chapter 7 aims to provide practical advice to calculate the weighted average of point measurements, and highlights the gain in CRNS performance for calibration and validation, when a proper weighing approach is used.

However, with regards to a practical understanding of the sensor footprint, there might be alternative definitions that offer a more intuitive approach compared to the 86 % cutoff. One could ask: At what distance to a remote field are changes of soil moisture still visible to the sensor? This question is addressed in Appendix E where a brief theory on the basis of the radial sensitivity W_r has been elaborated.

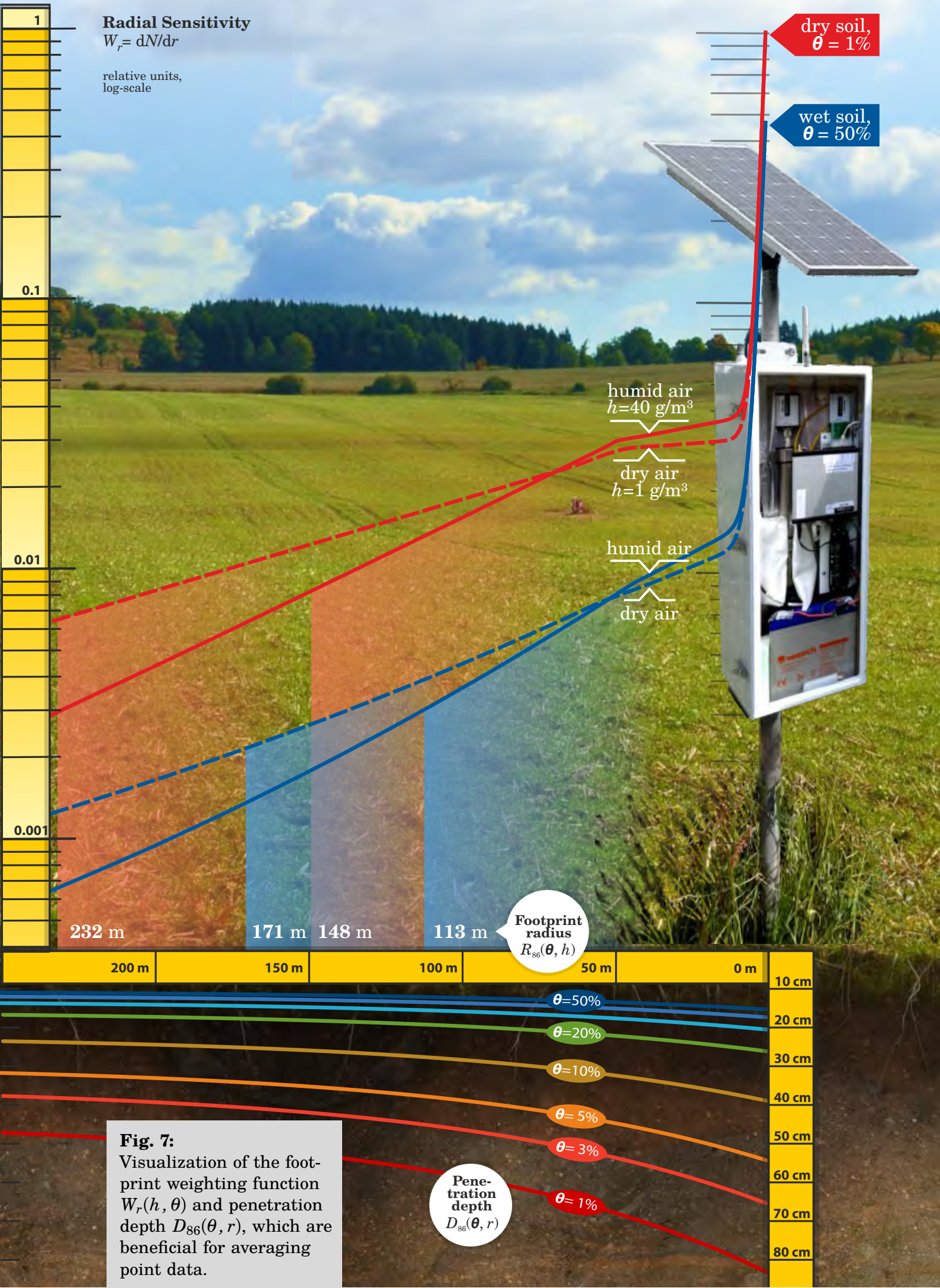

Fig. 7:
Visualization of the footprint weighting function $W_r(h, \theta)$ and penetration depth $D_{86}(\theta, r)$, which are beneficial for averaging point data.

7.

Give 'em weight!

Spatially weighted points improve performance

The theoretical determination of the radial sensitivity in the footprint was a necessary step towards reliable CRNS applications, and its transfer to practice will be another.

After the theoretical basis has been laid by Köhli et al. (2015), chapter 4 successfully isolated the detector response to relevant parts of the complex terrain around the sensors. Then, the sensitivity to distant shores was assessed in chapter 5 in order to keep the buoy detector insensitive to soil moisture changes. The present hypothesis expects considerable performance gain for CRNS validation and calibration, if proper weights are given to every measurement point/sample in the footprint.

This chapter makes use of the different accepted sensitivity functions to weight point data when averaged in the vertical and horizontal dimension. Thorough and systematic investigation is expedient to assess the different impact of those methods under various climatic conditions. While some datasets on homogeneous ground did not show significant change with the proposed weighting approach from chapter 6, most datasets improved robustly and even revealed new insights into hydrological processes.

7.1. Introduction

As soon as the characteristics of the CRNS footprint were elaborated, conclusions can be drawn for the contribution of distant areas to the signal. Since the first publication on cosmic-ray neutron sensing, outstanding features have been noticed in many datasets that could not be explained by the given theory and seemed to be unrelated to hydrological processes. Furthermore, many recent studies found deviations from neutron theory (eq. 3.7) when conventional averages were applied on point data, which led to recalibration of the according parameters $a_{0,1,2}$ (Rivera Villarreyes et al. 2011; Lv et al. 2014; Heidbüchel et al. 2016; Iwema et al. 2015). Therefore, a huge demand was raised to develop a proper weighting for vertical and horizontal distances to the CRNS detector.

Franz et al. (2012b) coupled the water transport model `HYDRUS-1D` with `MCNPX` simulations and found that wetting and drying cycles are non-uniquely represented by the CRNS method. Due to the integrative neutron signal, those hysteresis effects can be most significant when sharp wetting or drying fronts are shaping the soil water profile. As a consequence, Franz et al. (2012b) and Franz et al. (2013c) recommend vertical weighting of point measurements in the profile to account for these effects. On the other hand, `HYDRUS-1D` can also help to infer soil moisture profiles from CRNS observations using an inverse modeling approach (Rivera Villarreyes et al. 2014).

By simulating neutron detection over binary distributions of wet and dry fields, Franz et al. (2013c) showed that the estimation of soil moisture with neutrons is non-unique also in the horizontal space. Thus the sensor can underestimate the average soil moisture by up to 20 % depending on the individual distribution of water content in the footprint. For this reason, exact knowledge of the heterogeneity is a prerequisite for interpretation of single neutron count rates, and distance-weighting procedures are necessary to obtain sufficient performance during calibration and validation with point data.

In order to average calibration data horizontally, Franz et al. (2012a) adopted a sampling scheme from calculations by Zreda et al. (2008) to give every sample an equal weight. The resulting sensor locations at 25, 75, and 200 m correspond to an almost exponential horizontal weighting function. Bogena et al. (2013) were the first who applied this horizontal weighting to an irregularly distributed point sensor network, albeit indirectly by fitting the cumulative variant. Furthermore, scientists avoided horizontal weighting by re-locating their irregularly distributed point sensors in post-processing mode to the nearest radius of 25, 75, or 200 m (Franz et al. 2012a, among others).

The conventional sampling scheme was previously estimated on the basis of neutron simulations from Zreda et al. (2008) and Desilets and Zreda (2013), which have been revised and published in the course of the present work (Köhli et al. 2015). The results, also presented in chapter 6, significantly changed the shape of the weighting function, and moreover revealed remarkable dependence on wetness conditions of air and soil. The variable nature of the footprint is often considered as a downside, however the footprints of eddy covariance observations (to infer evapotranspiration) are much more prone to variable weather conditions due to wind direction and speed. The most prominent feature of the new weighting function $W_r(h, \theta)$ is the consideration of a huge contribution of the nearest area within a few

meters (see Figures 7 and 7.2). This chapter will demonstrate that better calibration and validation performance could have been obtained in many passed studies if a proper weighting approach was used.

7.2. Methods

This work is aimed to test weighting strategies that are both, based on different physical assumptions and frequently used by researchers in recognized publications. The following approaches were covered for vertical weighting in the soil profile:

1. equal average,
2. $1 - z/z^*$, based on MCNPX simulations from Zreda et al. (2008) and the linear assumption by Franz et al. (2012b), which became the accepted method in most studies.
3. $W_d(\theta, r)$, based on URANOS simulations and the analytical fit from Köhli et al. (2015), following recent insights about the physics of neutron transport and detection near the soil-atmosphere interface (cmp. eq. 6.4).

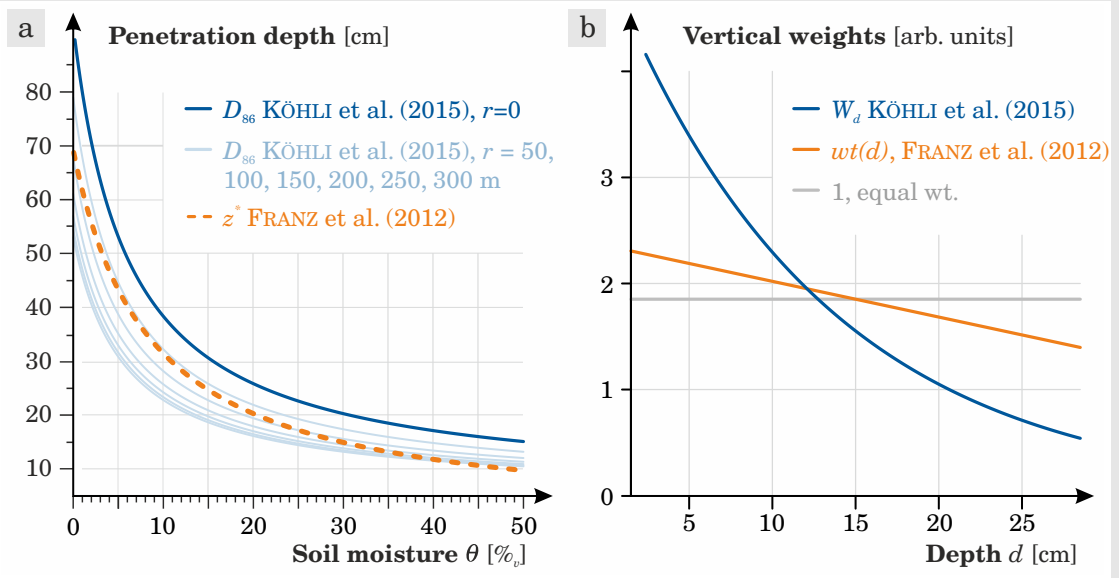

Fig. 7.1: Revised footprint depth and vertical weighting. a A comparison between $D_{86}(\theta, r)$ and $z^*(\theta)$ shows that Franz et al. (2012b) provide a decent estimation of the penetration depth. b On the other hand, the linear approach for vertical weighting highly underestimates the contribution from shallow water.

And for horizontal weighting in the footprint area:

1. equal average, which is usually applied for validation with soil moisture networks and remote sensing.

2. $e^{-r/127} \approx W_r^{\text{Bogena}}$, based on MCNPX simulations from Zreda et al. (2008) and fitted by Bogena et al. (2013), to which is implicitly referred when using the COSMOS standard sampling scheme, (25 m, 75 m, 200 m), presented by Franz et al. (2012a) and Zreda et al. (2012).
3. $W_r(h, \theta)$, based on URANOS simulations and analytical fits from Köhli et al. (2015), cmp eq. 6.2.

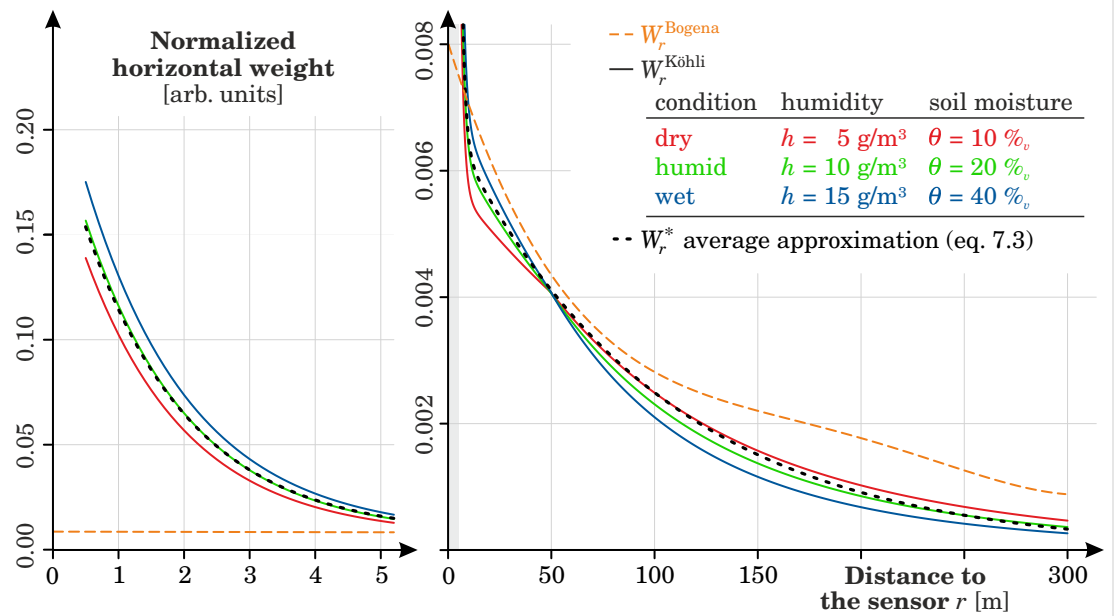

Fig. 7.2: Comparison of horizontal weighting functions, showing the conventional (almost exponential) approach W_r^{Bogena}, the curves W_r for three wetness conditions (Köhli et al. 2015), and the approximation W_r^* (eq. 7.2).

The conventional horizontal weighting function has never been published analytically. It is derived by taking the cumulative function, CFoC(r) from Bogena et al. (2013, eq. 13), who fitted data from Zreda et al. (2008, Fig. 3) in the domain of $r \leq 300$ m:

$$W_{r\leq 300}^{\text{Bogena}} = \partial_r \text{CFoC}(r) \propto 1 - a_1 r + a_2 r^2 - a_3 r^3 + a_4 r^4 \tag{7.1}$$
$$a_i = \left\{1.311 \cdot 10^{-2}, 9.423 \cdot 10^{-5}, 3.2 \cdot 10^{-7}, 3.95 \cdot 10^{-10}\right\}$$

To account for the remaining contribution beyond 300 m, the (usually few) data points were assigned the weight $W_{r>300}^{\text{Bogena}} = 0.1$.

7.2.1 Adaption of the weighting functions on air pressure and vegetation

Köhli et al. (2015) did not discuss in detail the dependencies of the weighting functions W_r and W_d on air pressure and vegetation, although they made clear that these quantities have significant influence on the footprint radius. For this reason

additional simulations with varying air pressure p and vegetation height H_{veg} were conducted, and a sufficient relation was found that does not further complexify the definitions of W_r and W_d. The weighting functions can easily adapt on variations of p (in mbar) and H_{veg} (in meter) by scaling their argument r with the scaling rules of the footprint radius R_{86} (eqs. 6.3):

$$W_r(h,\theta,p,H_{\text{veg}}) \equiv W_{r^*}^{\text{Köhli}}(h,\theta)\,, \quad \text{and} \quad W_d(\theta,r,p,H) \equiv W_d^{\text{Köhli}}(\theta,r^*)\,,$$
$$\text{where} \quad r^*(r,p,H_{\text{veg}},\theta) = r/\frac{0.4922}{0.86-e^{-p/p_0}}/\left(1-0.17\left(1-e^{-0.41H_{\text{veg}}}\right)\left(1+e^{-7\theta}\right)\right)\,. \tag{7.2}$$

Fig. 7.3 shows that this "workaround" performs well for various wetness conditions, as simulated curves and pressure-adapted curves are almost parallel (relative agreement is always sufficient for weighting functions).

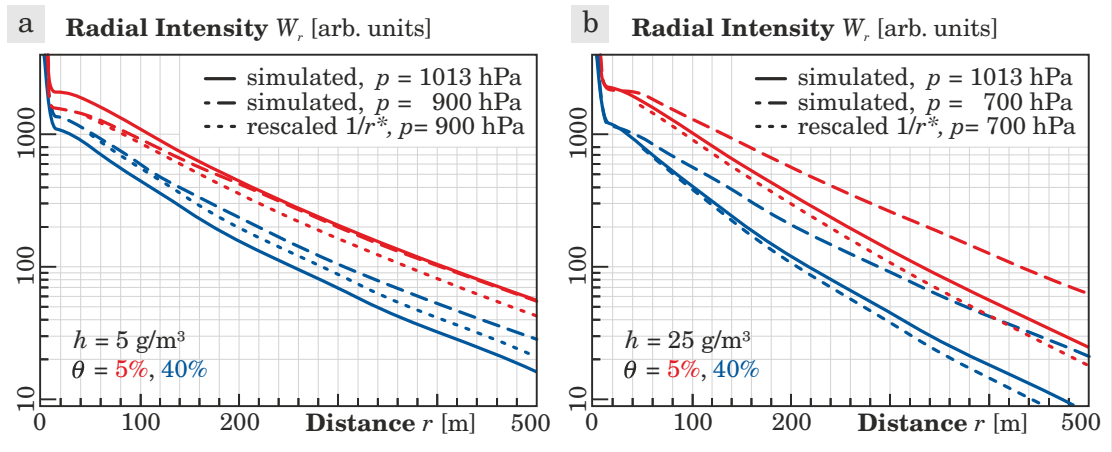

Fig. 7.3: Pressure dependence of the weighting function W_r demonstrated for two cases of air pressure and humidity. The rescaled p-adapted curves (dots, eq. 7.2) are almost parallel to the non-adapted curves (solid), indicating that the normlized weight leads to the same results. a dry midlands, b humid highlands.

7.2.2 The weighting procedure

Consider a number of soil profiles P at distance r_P from the CRNS. In each profile, point measurements of volumetric soil moisture $\theta_{P,L}$ are given at various layers L of depth d_L. Observations of air pressure p, air humidity h, and vegetation height H_{veg} are given at the time of interest, while estimations of soil bulk density ϱ_{bulk} exist for every profile. The general function for weighted averages is given as:

$$\text{wt}(\theta,w) = \frac{\sum_i w_i\,\theta_i}{\sum_i w_i}\,.$$

The procedure to obtain a soil moisture average $\langle\theta\rangle$ is described as follows:

1. Estimate an initial value $\langle\theta\rangle = \mathrm{wt}(\theta_{P,L}, 1) \equiv \langle\theta\rangle^{\mathrm{equal}}$ by an equally weighted average over all profiles P and layers L.
2. Calculate the penetration depth D_P for each profile P:

$$D_P^{\mathrm{Franz}} = z^*(\langle\theta\rangle) = \frac{5.8}{\langle\theta\rangle + 0.0829} ,$$

$$D_P^{\mathrm{Köhli}} = D_{86}(\langle\theta\rangle, r_P) = \varrho_{\mathrm{bulk}}^{-1}\left(8.321 + 0.1425\left(0.9666 + e^{-r_P^*/100}\right)\frac{26.42 + \langle\theta\rangle}{0.057 + \langle\theta\rangle}\right) .$$

3. Vertically average the values $\theta_{P,L}$ over layers L, to obtain a weighted average for each profile P:

$$\theta_P^{\mathrm{Franz}} = \mathrm{wt}(\theta_{P,L}, 1 - d_L/D_P) ,$$
$$\theta_P^{\mathrm{Köhli}} = \mathrm{wt}\left(\theta_{P,L}, e^{-2d_L/D_P}\right) .$$

4. Horizontally average the profiles θ_P:

$$\langle\theta\rangle^{\mathrm{Bogena}} = \mathrm{wt}\left(\theta_P, W_r^{\mathrm{Bogena}}\right) ,$$
$$\langle\theta\rangle^{\mathrm{Köhli}} = \mathrm{wt}\left(\theta_P, W_{r_P^*}^{\mathrm{Köhli}}(h, \langle\theta\rangle)\right) .$$

5. Use the new $\langle\theta\rangle$ to reiterate through 1.–5. until values converge.

The final product $\langle\theta\rangle$ is then compared with the volumetric water content, $\theta(N)/\varrho_{\mathrm{bulk}}$ derived from the CRNS using eq. 3.7. It is also thinkable to calculate gravimetric water content with local bulk densities before step 3, however, URANOS calculations of W_r and W_d have been conducted only for homogeneous soil and volumetric water content.

7.3. Results & Discussion

In order to provide a robust falsification of a potential benefit when using the revised weighted-averaging approach, a large number of own and published data sets have been consulted that offer comparison of the CRNS with independent soil moisture data under various climatic conditions. Fig. 7.4 shows three examples how properly weighted data could improve the explanatory power of the theoretical relation provided by Desilets et al. (2010). In the desert of Santa Rita (Arizona, US) (Franz et al. 2012a), the new vertical and horizontal weighting reduced the spread of data points in the wet regime, and reduced the bias visible in the dryer regime. Note that the theoretical line might be invalid around $\theta \approx 2\,\%_v$ as Desilets et al. (2010) have remarked. Calibration in the forested ecosystem has been difficult (Fig. 7.4b), as was noted by Heidbüchel et al. (2016). However, the re-weighting of their ten calibration campaigns improved the RMSE of neutron intensities by 16%. Those authors even calibrated the parameters a_i of eq. 3.7 and found the best overall performance using the same weighting approach as presented here.

At an irrigated agricultural site in northern Germany, Scheiffele (2015) tried to identify biomass growth in the cosmic-ray neutron signal using the accepted sampling scheme for three sensor calibrations. However, only when the soil samples

are properly weighted in post-processing mode, the signal from full-grown biomass is evident.

The pasture site *Großes Bruch* is a good example how an inappropriate averaging approach could hinder sufficient interpretation of time series data. Fig. 7.5a shows the soil moisture signal predicted from a stationary cosmic-ray neutron probe (CRS07, dashed) and the weighted SoilNet signal. Following the precipitation events in the second half of October, the shallow groundwater and loamy texture allowed large water ponds to reside permanently in the outer regions of the SoilNet. As distant areas contribute much less to the CRNS signal than closer ones, the proper weighting removed the saturated signal of those point sensors and nestled to the CRNS apparent signal. Additionally, beginning in the mid of September a significant amount of cows were present at this site, which led to large variations of the neutron signal and to an underestimation of the mean amount of soil moisture.

Using a relation between CRNS data and point measurements, residual information can be used to identify additional processes like biomass growth or rainfall interception (Baroni and Oswald 2015). With the help of the weighted averaging method presented in this work, these residuals have been identified to a much higher precision in an agricultural field (Fig. 7.4c) and in the *Wüstebach* forest (Fig. 7.5b). For the latter site, weighted averaging is performed based on the data presented in Bogena et al. (2013). The analysis shows three interesting effects on the resulting soil moisture signal in Fig. 7.5b. First, the W_r-weighted signal (blue) is wetter than the conventionally weighted (orange), which is reasonable due to the nearby river creek and the steep topographic gradient in the area. Second, the CRNS signal which was calibrated to the properly weighted soil moisture (light blue) outperforms the signal that was calibrated on the falsely weighted soil moisture (light orange). This performance gain is robust in terms of the four popular measures KGE, NSE, RMSE, and Pearson correlation, and even during exclusion of precipitation events (not shown). Third, interception and canopy water storage is much more prominent for the blue lines following huge precipitation events in May, July and October. The latter effect shows that proper weighting of calibration data is essential to identify residual hydrological effects which were otherwise lost by overfitting.

7.3.1 An invariant approximation to the revised weighting function

As the analysis above has shown, it is really important to use horizontal weighting functions because the conventional method can underrate soil moisture near the sensor by a factor up to 25. Furthermore, the variability of the weighting function can have influence on proper weighting where accuracy matters. On the other hand, private communications revealed that the exact formulation of $W_r(h, \theta)$ (eq. 6.2) turned out to appear too complicated to be applied by non-scientific users. If simplicity is a criterion, we propose an *approximated weighting function* W_r^* averaged from dry to wet conditions:

$$\langle W_r(h, \theta) \rangle_{h,\theta} \approx W_r^* = 30\, e^{-r/1.6} + e^{-r/100} \tag{7.3}$$

Figure 7.2 shows the decent compromise performed by this approximation for

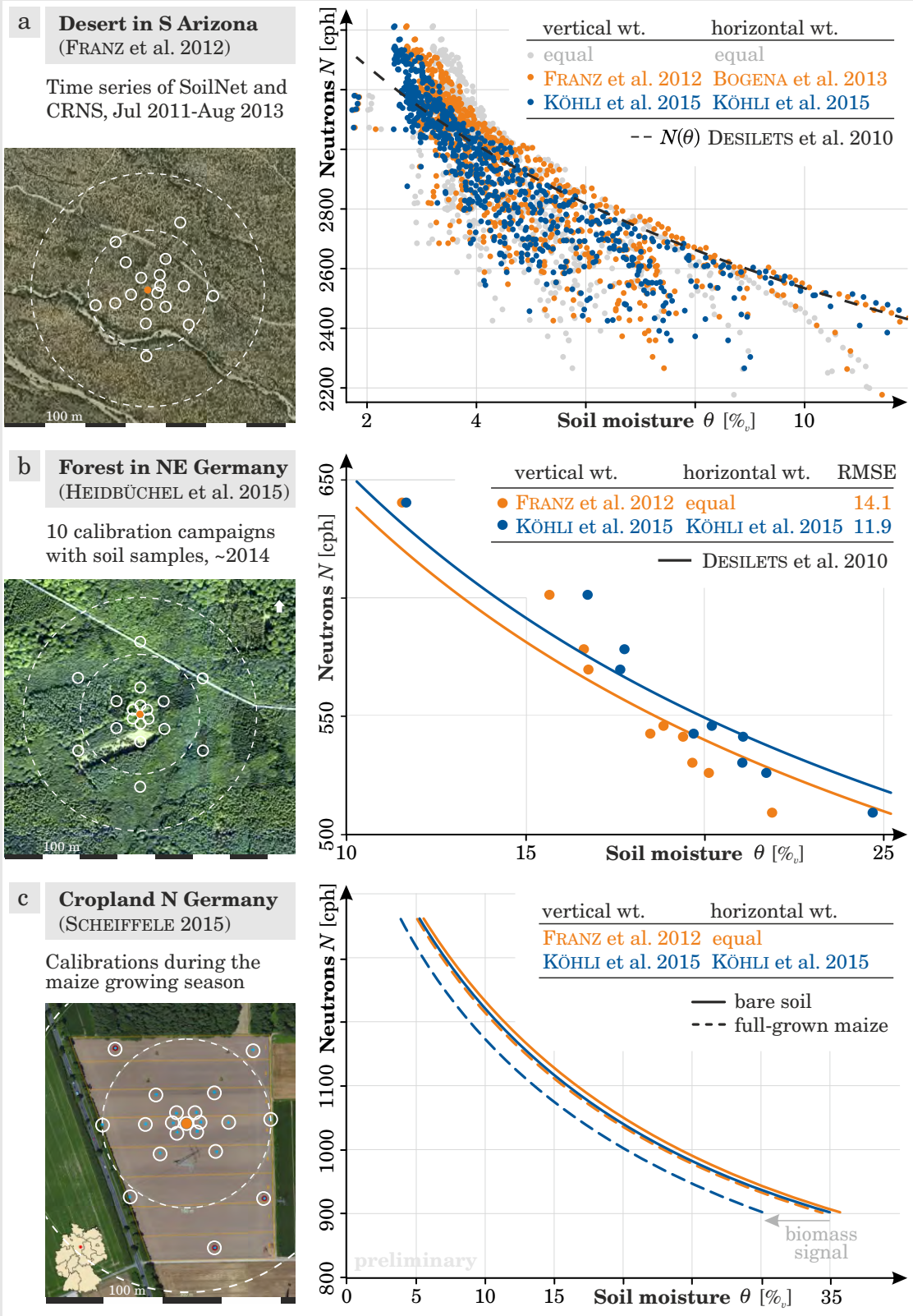

Fig. 7.4: Three example sites that demonstrate the importance of a proper horizontal and vertical point-weighting approach, which was calculated with the indicated methods. *Credit: Photos by Google Maps*

both, short-range and long-range neutrons. Tests in *Großes Bruch* and *Wüstebach* indicated that this approach deviates from the exactly weighted average not more than 1 $\%_v$ of converted soil moisture (not shown). However, the deviation varies with h and θ and thus can be an important source of error in temporal analysis.

Further studies will demonstrate whether eq. 7.3 is accurate enough to improve the CRNS performance under various wetness conditions and monitoring sites. If so, the reduction of computational effort will be valuable for regular analysis and end users.

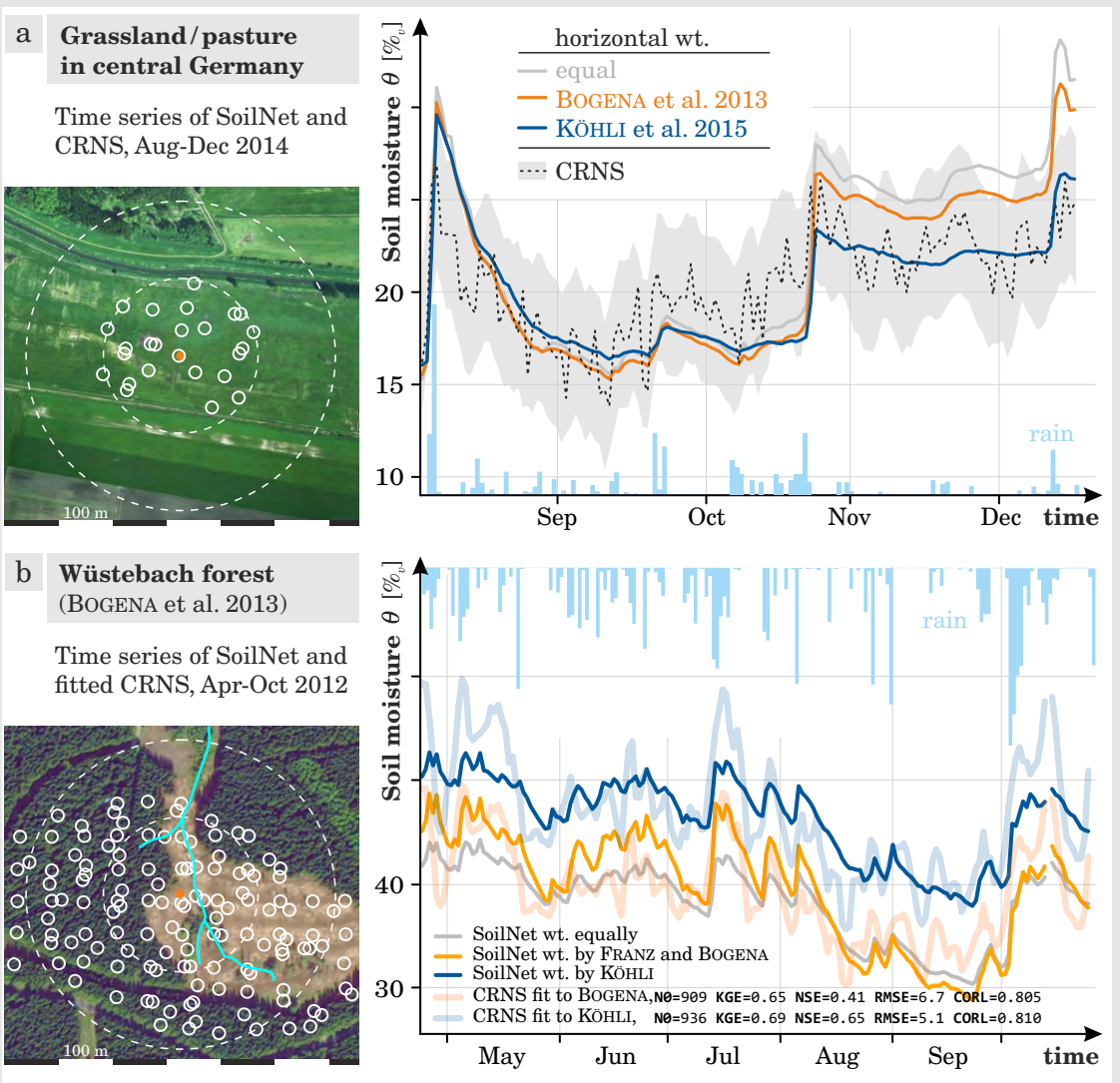

Fig. 7.5: a Time series of *Großes Bruch* showing the influence of cows to the CRNS variability in Sep–Oct, and the remote water ponds residing from Oct–Dec, biasing the falsely weighted SoilNet signal. b CRNS soil moisture in the *Wüstebach* forest, calibrated to fit the properly weighted (blue) and falsely weighted (orange) SoilNet data. Interception and canopy water is evident in May, July, and October.

7.3.2 Towards a revised sampling scheme

Based on Zreda et al. (2008), the conventional weighting function W_r^{Bogena} laid the basis for the COSMOS standard sampling scheme, $r_i = \{25\,\text{m}, 75\,\text{m}, 200\,\text{m}\}$ (Franz et al. 2012a). These radii were located in the 33 % quantiles of the footprint (compare also Bogena et al. 2013, Table 3):

$$\frac{1}{3} \approx \int_0^{59} W_r^{\text{Bogena}} \approx \int_{59}^{186} W_r^{\text{Bogena}} \approx \int_{186}^{\infty} W_r^{\text{Bogena}}\,. \tag{7.4}$$

As Köhli et al. (2015) introduced the new weighting function $W_r(h, \theta)$, the standard sampling scheme has become inappropriate for two reasons: the revised weights are more steep, and dynamically depend on wetness conditions. In particular, the horizontal weighting has been applied here to demonstrate its capability to significantly improve CRNS performance. While existing data from point sensor networks could be re-weighted, the question arises whether positioning schemes for upcoming soil moisture networks or calibration campaigns could adapt on the nature of neutron physics to maximize comparability.

Obviously, it is impossible to provide a new general position plan, due to the temporal variability of W_r and W_d, and the heterogeneity of local structures and conditions. Instead, selection of sampling locations should depend on (1) their representativeness for local features, and (2) their distance to the sensor. In general, it can be strongly recommended to select about half of available sampling points within the nearest 25 m, since the conventional sampling scheme from Franz et al. (2012a) does not account for 40–50 % of detected neutrons that originated in that area.

To give further advice on a reasonable distribution of points, Figure 7.6a illustrates five annuluses of the footprint area which equally contribute to the neutron signal. Since the signal contribution of an area between radii r_1 and r_2 can be calculated by integrating W_r (compare eq. 6.1), we find the five annuluses using the condition:

$$\text{Five annuluses:} \quad \int_{r_1}^{r_2} W_r(h, \theta)\,\mathrm{d}r \overset{!}{=} \frac{1}{5} \int_0^{\infty} W_r(h, \theta)\,\mathrm{d}r. \tag{7.5}$$

Therefore, an equal amount of locations is recommended in each annulus. For example, using the hitherto common amount of 18 locations under humid conditions, it is reasonable to select three locations within 1.4 m distance, another three within 12 m, and the remaining 3×4 locations distributed within 54, 129, and 230 m, respectively. In order to compare this approach with the conventional sampling scheme by Franz et al. (2012a), a 3-annulus scheme is adapted from eq. 7.5:

$$\begin{aligned}
\text{dry:} \quad & \frac{1}{3} \approx \int_0^{23} W_r^{\text{Köhli}} \approx \int_{23}^{114} W_r^{\text{Köhli}} \approx \int_{114}^{\infty} W_r^{\text{Köhli}}\,, \\
\text{wet:} \quad & \frac{1}{3} \approx \int_0^{3} W_r^{\text{Köhli}} \approx \int_{3}^{58} W_r^{\text{Köhli}} \approx \int_{58}^{\infty} W_r^{\text{Köhli}}\,.
\end{aligned}$$

Thus, if three radii are desired for the sampling scheme, a possible (but arbitrary) suggestion could be $r_i^{\text{dry}} \approx \{10\,\text{m}, 65\,\text{m}, 160\,\text{m}\}$ and $r_i^{\text{wet}} \approx \{1\,\text{m}, 25\,\text{m}, 85\,\text{m}\}$, as illustrated in Fig. 7.6b (compare also Heidbüchel et al. 2016, section 4.2).

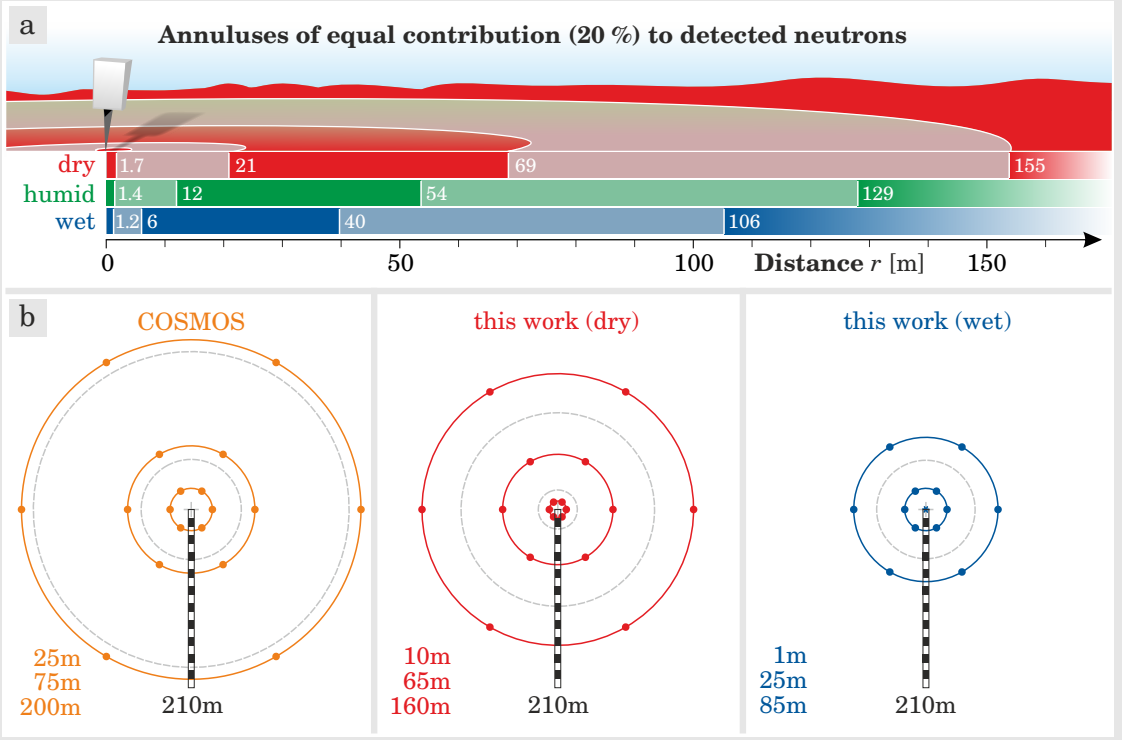

Fig. 7.6: a Illustration of regions of equal contribution (20 % quantiles) to the neutron signal for three climates. b The COSMOS standard sampling scheme based on W_r^{Bogena} compared to exemplary 3-radii-schemes based $W_r^{\text{Köhli}}$ for dry ($h = 1\,\text{g/m}^3, \theta = 1\,\%_v$) and wet ($h = 10\,\text{g/m}^3, \theta = 40\,\%_v$) conditions. Borders of 33 % quantiles are indicated grey and dashed.

This arrangement, however, should not relieve scientists of weighting their data in post-processing mode, because each annulus still exhibits a sensitivity gradient. But the 20 %-annulus method strongly concentrates locations within most relevant regions favored by detectable neutrons. It is also worth noting that locations need not to be equally distributed among the annuluses. The actual partitioning should rather be guided by expert knowledge about local correlation lengths of spatial soil moisture patterns. Given entirely homogeneous soil, for instance, a single location would do.

7.4. Conclusion & Outlook

In this chapter, a general concept and procedure for horizontal and vertical weighting has been presented, which are based on insights from neutron physics (chapter 6). The following conclusions were compiled:

1. The weighting functions W_r and W_d from Köhli et al. (2015) further scale with air pressure and vegetation height, using the rescaled distance r^* (eq. 7.2).
2. Proper weighted average improved correlation with data, reduced signal spread, and revealed otherwise invisible features.
3. The weighting procedure is described and a handy Excel sheet is provided in Appendix D for future CRNS calibration. More than one iteration step in the procedure is recommended but only slightly improves accuracy.
4. An approximated weighting function W_r^* has been developed which should be taken with care, for its adequate performance has not been sufficiently confirmed in this work.
5. Although existing data can be weighted in post-processing mode, missing locations close to the detector introduce significant uncertainty. Therefore, a new sampling scheme has been elaborated which is, however, dependent on wetness conditions.

As previous studies have shown the CRNS soil moisture signal could be calibrated to match the *equal* average of the areal soil moisture in the footprint. However, important hydrological features could have been missed thereby, like biomass, interception, snow, or nearby wet ponds.

The presented weighting approach gives best results if the sampling locations are distributed equally in rings of distinct distances r to the CRNS. Similar to the accepted sampling method from Franz et al. (2012a), those locations can be chosen based on equal contribution of their surrounding zones to the neutron signals. This zonation approach is geometrically point-symmetric and is comparable to *Voronoi cells*. The latter minimize the distance of each point to its cell border and has been applied for signal weighting by Coopersmith et al. (2014). More elaborated approaches make use of *fuzzy zonation*, which has been described by Paasche et al. (2006), for instance, and successfully applied to the *Schäfertal* catchment (Schröter et al. 2015). There exist also promising methods of Bayesian geostatistics that aim to find an *optimal sampling design* which minimizes the integrated variance (Nowak et al. 2010). The question where and how many point measurements should be distributed in a footprint is beyond the scope of this work, however, recent studies in this direction (e.g., Bramer et al. 2013) might be helpful for application to cosmic-ray neutron sensing. Often these methods require further knowledge of soil properties or structural parameters, which however can be iteratively improved in the process of optimization (Diggle and Lophaven 2006). This chapter focused on the theory and application of the averaging approach, while the performance of different interpolation strategies might depend on local soil patterns and deserves a study for its own. Most of these advanced strategies haven't been considered for CRNS sampling campaigns, but personal negotiations with the experts in that field gave a promising impression that CRNS calibration and validation campaigns could be improved in the future.

In this work many old and new datasets have been reanalysed to test the weighting approach. It is recommended to apply the procedure also to other studies, especially where the conventional approaches haven't led to the expected results. For example, Almeida et al. (2014) used sophisticated inference system methods in order to train a number of point measurements on fitting the CRNS data. Similar to the data presented here, their results in the $N(\theta)$ plot showed a different curvature than Desilets et al. (2010), and it would be interesting to revisit their analysis.

Moreover, independent measurements are not always available when CRNS technology is applied. It is then necessary to infer the footprint characteristics just from the available CRNS data. This would hypothesize that the determination of $\langle\theta\rangle$, R_{86}, and D_{86} can be inferred dynamically from rising or sinking neutron intensity. Although this should be the goal for CRNS applications, the question whether such approach leads to sufficient results is beyond the scope of this work, but can be smoothly accomplished in a future study based on the data presented here.

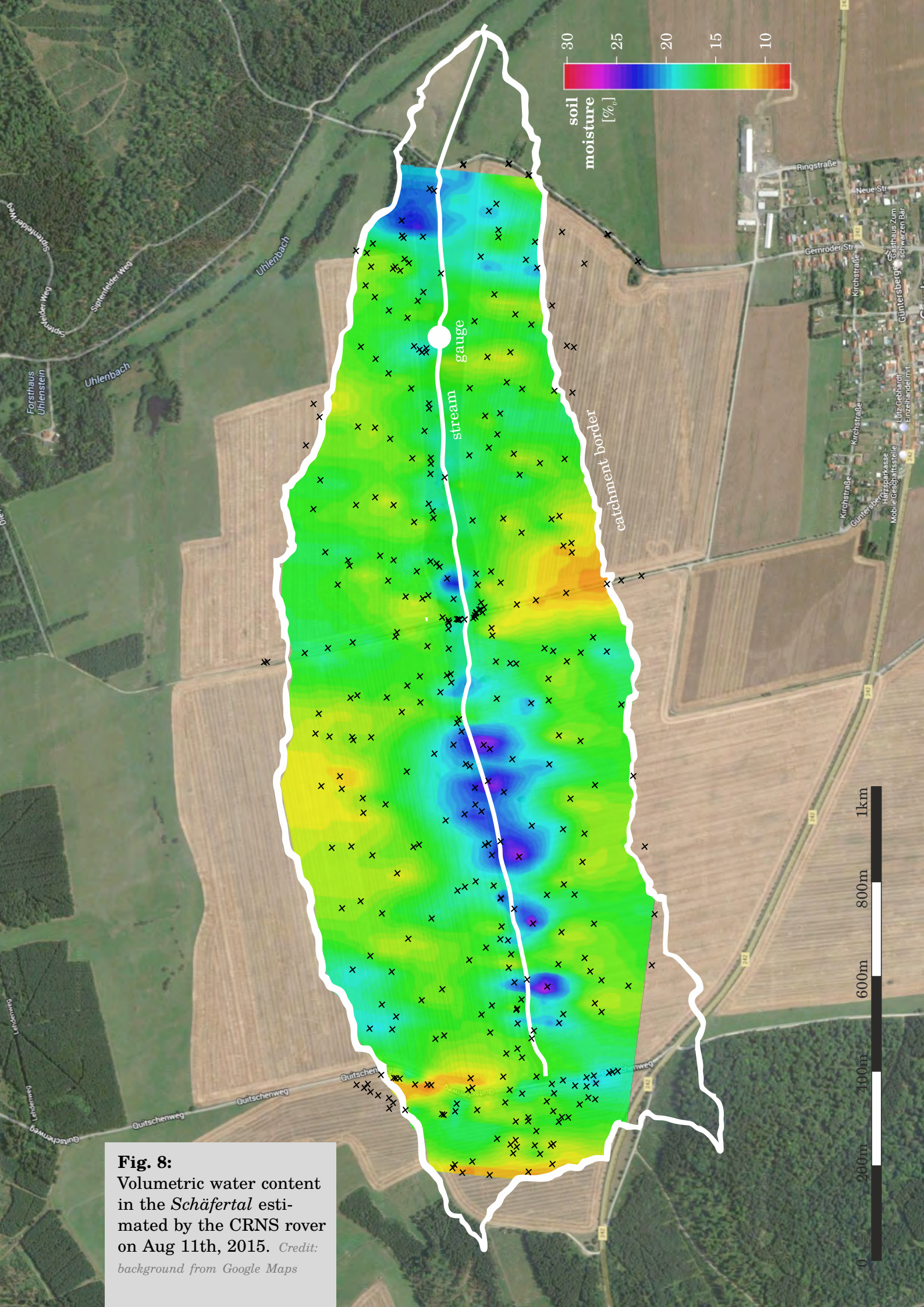

Fig. 8:
Volumetric water content in the *Schäfertal* estimated by the CRNS rover on Aug 11th, 2015. *Credit: background from Google Maps*

8.

Roving Across Scales

Spatial correction & validation of mobile CRNS

Now that chapters 6–7 have clarified the scales and uncertainties involved in CRNS measurements, mobile rover campaigns can be systematically planned and more precisely interpreted. In the further course of this work, the distance-weighting approaches were applied to calibrate and validate the rover with nearby TDR and SoilNet data points.

After the rover has been consulted in chapter 4 to survey small-scale heterogeneity in the CRNS footprint (0.12 km^2), campaigns in the present chapter continue to bridge the scale gap outlined in chapter 1. At first, spatial validation campaigns were conducted together with TDR instrumentation in the *Schäfertal* site (1.6 km^2). Then, novel spatial corrections for soil and vegetation were tested at the transect scale of 50 km length.

Soil moisture monitoring networks at three TERENO research sites confirmed the quality of large-scale rover measurements across various land use types. However, the spatial correction performance is prone to poor soil and land use data, while local effects from roads, cows, and scientists may introduce unrecognized variability.

8.1. Introduction

In order to perform multi-scale analysis of soil moisture patterns, a few stationary sensors cannot provide spatially representative data for entire catchments. For this reason, the CRNS method can be applied in a mobile mode with a neutron detector mounted on/in a car. This allows to further close the scale gap between conventional soil moisture observations (Robinson et al. 2008; Ochsner et al. 2013), and opens the path for validation of remote-sensing products, as conventional methods for upscaling point data are prone to large uncertainties (Crow et al. 2012). By 2016, the UFZ Leipzig owns the only so-called "CRNS rover" in Europe, which has been used so far for small-scale tomography in urban areas (chapter 4) or footprint validation experiments (chapter 6).

Desilets et al. (2010) proved the concept of mobile CRNS at the dry hills of Hawaii. Chrisman and Zreda (2013) then conducted monthly campaigns on the roads around Tuscon to compare the data with temporal SMOS products (Jackson et al. 2012). However, poor correlation was found, probably due to seasonal climatic variations, local effects on the rover, and different penetration depths of CRNS and SMOS. In the prairies of Oklahoma, Dong et al. (2014) calibrated rover measurements on shallow soil moisture observations (0–5 cm). McJannet et al. (2014) found that the standard approach from Desilets et al. (2010) performs better than the universal calibration function (Franz et al. 2013a) for rover campaigns, as data availability is the major obstacle to apply the latter. Recently, Franz et al. (2015) used a statistical approach to relate 3 stationary probes with 22 spatial rover surveys in order to predict soil moisture states of an agricultural site in Nebraska at scales of 1–12 km.

The short review shows that reasonable soil moisture estimates have been obtained for terrain that exhibited in the most part uniform land use and vegetation cover, where the assumption of spatially constant parameters (eq. 8.1) proved to be adequate. Little research has been done under humid climate conditions, where methodological advances for spatial corrections are necessary to account for spatially variable soil properties or for the variable amount of vegetation water in the surveyed area.

The goal of this chapter is to validate patterns of soil moisture measured by mobile CRNS at the scale of 1 km agricultural fields, and 50 km regional transects. Intensive TDR campaigns were conducted parallel to rover surveys in the *Schäfertal* catchment in order to capture typical spatial patterns. At the regional scale, three soil moisture monitoring networks (SoilNets) were used to judge the rover performance along steep gradients of topology and land use types. For the latter case, a spatial correction method was developed to translate rover results to volumetric soil moisture, θ_v, and to account for the large-scale heterogeneity of hydrogen sources (see Kasner 2016, for details).

8.2. Methods

The large mobile CRNS detector, described in section 3.4, was mounted in the trunk of a Defender/Landrover. As neutrons are almost exclusively sensitive to hydrogen, the material of the car appears almost transparent. The sensor integrates neutron counts over 1 minute, which implicitly stretches the otherwise circular footprint when

in motion. In contrast, the GPS positioning is read at the time of recording, so after the neutrons were integrated. To account for this artificial shift in post-processing mode, the UTM coordinates of each signal were back-projected to half of the distance covered within that minute.

8.2.1 Comparison of CRNS and TDR in the *Schäfertal*

The *Schäfertal* catchment is one of the TERENO intensive monitoring sites in central Germany (Zacharias et al. 2011). The site comprises five individual agricultural fields surrounding the small *Schäferbach* stream (white central line in Figures 8 and 8.1). It swells in the western part and runs through a tentative topological gradient towards the east, eventually merging into the *Selke* river and the subsequent *Bode* basin. The *Schäfertal* is instrumented since 2012 with four CRNS stations from the University of Potsdam, and an additional station from the UFZ installed late 2014.

Schröter et al. (2015) regularly performed TDR campaigns using ≈ 100 locations in an area of ≈ 1.6 km^2. During several campaigns from 2014–2015, the CRNS rover accompanied their team, but on most days the car was only allowed to access sandy roads that were crossing the agricultural fields and the stream. Shortly after harvest (usually in August) the fields were accessible with the car, such that the same locations could be sampled with the rover and the TDR team on the same campaign day.

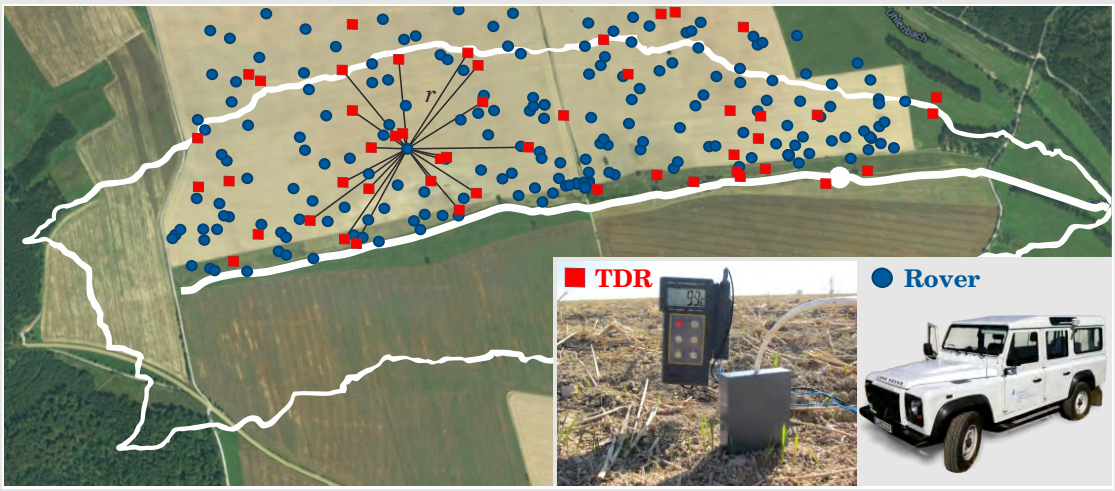

Fig. 8.1: Calibration of rover measurements (blue) using the weighted average of all TDR points (red) in the catchment. Weights are determined by the radial sensitivity function $W_{r^*}(h, \theta)$, eq. 7.2, depending on the distance r between TDR and rover position (exemplary black lines). *Credit: (top) Google Maps, (TDR) I. Schröter*

In order to convert neutrons to soil moisture, the assumption of constant soil and vegetation parameters was applied to eq. 3.7, which has been hitherto the accepted approach for CRNS surveys (Desilets et al. 2010; Dong et al. 2014, among others).

$$N_{\mathrm{St}}(\theta) = N_0 \cdot \left(\frac{0.0808}{\theta_v / \varrho_{\mathrm{bulk}} + \theta_{\mathrm{lw}} + 0.115} + 0.372 \right), \tag{8.1}$$

where for the *Schäfertal* we use $\varrho_{\text{bulk}} = 1.55\,\text{g/cm}^3$ (Borchardt 1982), and $\theta_{\text{lw}} = 2.3\,\%_g$ (see Table 8.1). The parameter N_0 has been determined by calibration with TDR measurements (0–10 cm), using the approach illustrated in Fig. 8.1. Since the sensitivity of the CRNS detector to distant areas has been elaborated in chapter 6, a weighted average can be applied to all TDR measurements to provide the apparent soil moisture value for the rover. By fitting eq. 8.1 to the obtained data $N(\theta_{\text{TDR}})$, the calibration parameter $N_0 = 10447\,\text{cph}$ has been elaborated for the whole *Schäfertal* catchment, including good agreement with data from the four CRNS stations (not shown). Due to the fact that the fields contained almost bare soil after harvest, this N_0 has further proven to be a great estimate also in other regions, e.g., Saxony, Rur-Eiffel, and Bavaria (not shown).

8.2.2 The spatial correction approach

From August to November 2015, eleven campaign days were invested to transect the *Bode* river catchment, including three soil moisture monitoring networks at the three TERENO research sites:

1. *Schäfertal* (agricultural fields, middle mountain region),
2. *Großes Bruch* (pasture grassland, flood plain), and
3. *Hohes Holz* (deciduous forest, low lands).

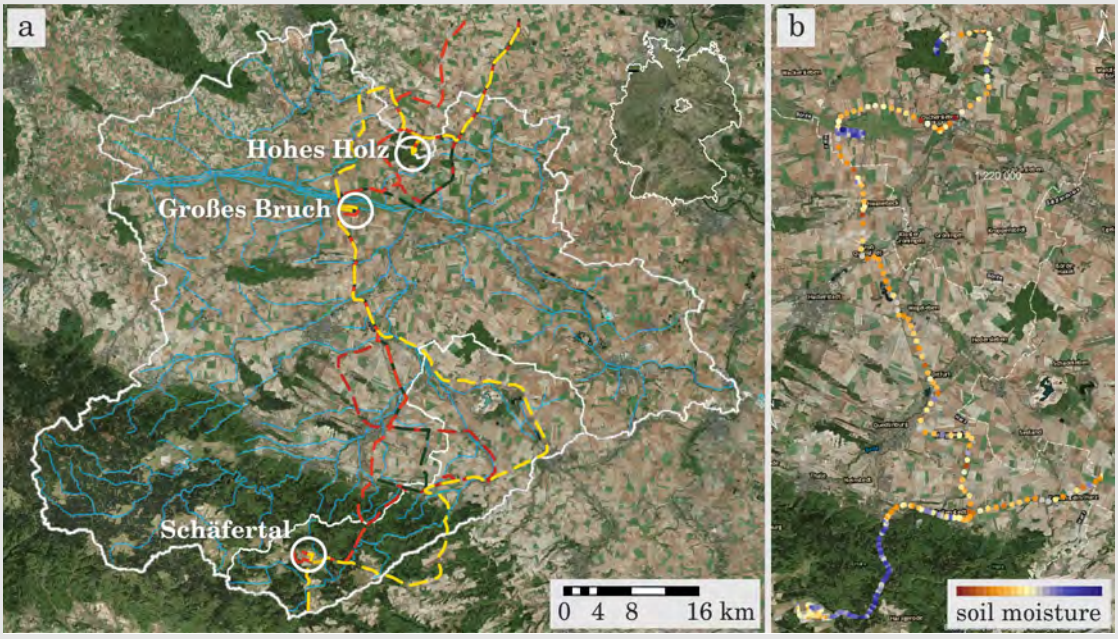

Fig. 8.2: Map of the great *Bode* and inner *Selke* river catchments in central Germany. a Four out of eleven rover campaigns indicated (color) between three TERENO intensive research sites. b Uncorrected soil moisture observation apparent to the rover, demonstrating a strong bias from vegetation.

Although paved roads are connecting the distant regions, the rover was halted at each site for 10–30 min. Depending on weather conditions, the detector has been deployed on a trolly during that period in order to approach the center of the soil moisture monitoring networks. These so-called SoilNets were established on all three validation sites at least 1 year in advance and provided a representative basis for soil moisture comparison. Similar to the TDR calibration in the *Schäfertal*, the same weighted averaging approach has been used.

Following eq. 8.1, gravimetric soil moisture θ_g is obtained from neutron counts N, however, in this case with spatially adapted parameters:

$$\theta_g + \theta_{\mathrm{lw}} = \frac{0.0808}{N_{\mathrm{Bode}}/N_0(\mathrm{BWE}) - 0.372} - 0.115$$

When the data is used for comparison with TDR, SoilNet, or hydrological models, it is necessary to convert θ_g to volumetric soil moisture using

$$\theta_v = \theta_g \cdot \varrho_{\mathrm{bulk}}(S_{\mathrm{type}}, S_{\mathrm{hum}}).$$

In order to develop a practicable procedure for the estimation of the involved parameters, this work makes use of freely and nationwide available soil and land use data. As explained by Kasner (2016) in more detail, the spatial distribution of bulk density has been determined as follows:

1. Determination of *soil types*, S_{type}, from the `BÜK1000` (Bodenübersichtskarte) following BGR (2007), Table 2.
2. Determination of *humus content*, S_{hum}, from the map "Gehalte an organischer Substanz in Oberböden Deutschlands", (BGR 2007, 1 : 1 000 000).
3. Determination of the bulk density, $\varrho_{\mathrm{bulk}}(S_{\mathrm{type}}, S_{\mathrm{hum}} < 1\,\%)_k$ for each soil class $k = 1, .., 5$, following Renger et al. (2008), Table 2. Depending on the humus content, ϱ_{bulk} is further reduced by $0.04\,\mathrm{g/cm^3}$ for $S_{\mathrm{hum}} = 1{-}6\,\%$, and $0.03\,\mathrm{g/cm^3}$ for $S_{\mathrm{hum}} > 6\,\%$.

The lattice water content in soils is very difficult to identify due to the lack of detailed information about the distribution of clay minerals. In this study, an assumption is made that the clay content, determined from the `BÜK1000`, is equal to the clay mineral content. The three most abundant clay minerals in the temporal climatic zone are *montmorillonit*, *illit*, and *vermiculit*. Following their individual chemical composition, those three contain an average mass percent of H_2O of $\approx 17.83\,\%_g$. The lattice water content can thus be obtained using a linear relation, an approach that has shown to be effective also in other regions (e.g., Greacen 1981):

$$\theta_{\mathrm{lw}} = \frac{\mathrm{clay}\,\%}{100} \cdot 0.1783\ [\mathrm{g/g}]\,.$$

From the German soil database (BGR 2007, 1 : 1 000 000) it is given that most regions of the transect are of soil type `Ut4` (strongly clayey silt), the forest *Hohes Holz* is of type `Ut3` (medium clayey silt), the *Schäfertal* catchment and surroundings are `Sl4` (strongly loamy sand), with little patches of `Lu` (silty loam) in between (see also Finnern et al. 1994). The lattice water content can change from $2\,\%_g$ in *Schäfertal* and *Hohes Holz* to $4\,\%_g$ in *Großes Bruch*, with plenty of fine structures in between.

Moreover, moisture in organic material, often denoted as θ_{SOC} or θ_{org} (eq. 3.8), is taken from humus information and corresponding map data (BGR 2007), and is further added to the lattice water quantitiy, θ_{lw}. Table 8.1 summarizes the most important features.

Table 8.1: Soil properties of the three soil moisture validation sites.

	Schäfertal	*Großes Bruch*	*Hohes Holz*
land use	hill slope, cultivated	grassland, pasture	mixed forest
altitude	393 m	84 m	168 m
soil type	`Sl4`	`Ut4`	`Ut3`
clay %	13 %	20 %	15 %
lattic water	2.5 $\%_g$	3.8 $\%_g$	2.6 $\%_g$
humus	no data	$2.0 \pm 0.5\ \%_g$	no data

Estimating soil moisture with CRNS in forests has been entitled the "worst case scenario" by Bogena et al. (2013), because organic material contributes additional hydrogen and shields neutrons from the soil. Just recently, Heidbüchel et al. (2016) confirmed that the calibration procedure in the forests is much more complicated compared to less complex terrain. Biomass water can be identified using the CRNS in conjunction with independent measurements (Baroni and Oswald 2015), however, SoilNet stations are only available at three sites along the transect. Baatz et al. (2015) and Franz et al. (2015) estimated *biomass water equivalent* (BWE) from samples and land use maps in the footprint of their sensors. They suggested a linear relation between BWE and the calibration parameter N_0, which is adopted in this work, as it has been successfully tested also in more recent studies (Avery et al. 2016):

$$N_0(\mathrm{BWE}) = N_0 - s \cdot \mathrm{BWE}\ ,$$

where $N_0 = 11447$ cph and the slope $s = 30.42$ are empirically calibrated to match the three SoilNet values as they were passed during the rover campaigns.

BWE highly depends on the dry standing biomass, B_{dry}, and comprises the actual fraction of water, f_{veg}, in the plant, as well as the fraction of water equivalent molecules, f_{mol}, of the organic material. The *vegetation moisture* content $f_{veg} = B_{wet}/B_{dry} - 1$ is assumed to be ≈ 0.19 for grass and crops (LfULG 2001). In contrast, values for typical tree species range from 0.72 to 1.15 and have been set accordingly (see e.g., Burmester 1987; Klaiber et al. 2002). The fraction of water H_2O in the tree, $f_{mol} \approx 0.58 \pm 0.03$, is calculated using the structure formula $C_6H_{10}O_5$ for cellulose and $C_{10}H_{12}O_3$ for lignin, in addition to further tree dependent data (König and Becker 1919). This value is in accordance with estimations from Nurmi (1999), Baatz et al. (2015), and others. Following Baatz et al. (2015), the biomass water

equivalent has been calculated as:

$$\begin{aligned} \mathrm{BWE} &= B_{\mathrm{wet}} - B_{\mathrm{dry}}\,(1 + f_{\mathrm{mol}}) \quad \left[\mathrm{kg/m^2}\right] \\ &= B_{\mathrm{dry}}\left(f_{\mathrm{veg}} + f_{\mathrm{mol}}\right) . \end{aligned} \tag{8.2}$$

The dry biomass weight B_{dry} was taken from detailed biotope data surveyed by Peterson and Langner (1992) using airborne infrared technology at 1 : 10 000 resolution. The data was categorized in forests, grove, herbaceous plants, water, bare soil, cultivated land, and urban area, which are in turn divided into sub-categories of primary and secondary land use types, morphology and structural information. For this work, the data has been reduced to the 30 most relevant biotopes in the study region. Dry biomass is then determined accordingly using various additional literature (see Kasner 2016, for details). BWE for cropland and grassland is in the range from 1–5 kg/m^2 and agrees well with estimations used by Baatz et al. (2015). These authors also emphasize large uncertainty of the linear regression method for small values and changes of biomass.

8.3. Results & Discussion

8.3.1 Small-scale patterns in the *Schäfertal*

Fig. 8.3a–d shows that in the summer of 2015 all the fields of the *Schäfertal* site were accessible with the car, however, TDR campaigns were incomplete due to technical reasons. In summer 2014, only the northern fields could be surveyed, but this time equal areal coverage has been obtained by TDR and the rover. All four campaign days demonstrate that both methods agree in representing the mean soil moisture. Besides the visual impression in columns 1 and 2, the probability density functions (column 3) of overlapping areas confirm emphatically that soil moisture patterns have been well captured by both methods. The fourth column maps the interpolated neutron pixels to the distance-weighted average of TDR points. Among various wetness conditions, the data points agree well with the theoretical line (eq. 8.1) with an acceptable spread, considering the fact that (1) the penetration depths of both methods were different (10 cm versus 30 cm), (2) TDR data was too sparse to justify *Kriging* interpolation, and (3) spatially invariant parameters have been used. Back in Fig. 8.3e–f, the effects of the road are clearly demonstrated, as the comparison with TDR measurements shifts the mean soil water content towards the dry end.

Rover measurements of campaign day Aug 11, 2015 (Fig. 8.3a) are also shown in Fig. 8 with a different color scale. The enlarged picture highlights three interesting features. First, contact springs can be identified in the western part close to the creek, where shallow groundwater permanently wettens the soil. This effect is especially prominent during dry periods (see Fig. 1) and has been found also by other researchers (Graeff et al. 2009; Schröter et al. 2015). The example shows that the rover can efficiently contribute to hydrological process understanding in small catchments. Second, the wet spot in the eastern corner overlays a small accumulation of trees, which were probably biasing the soil moisture estimation.

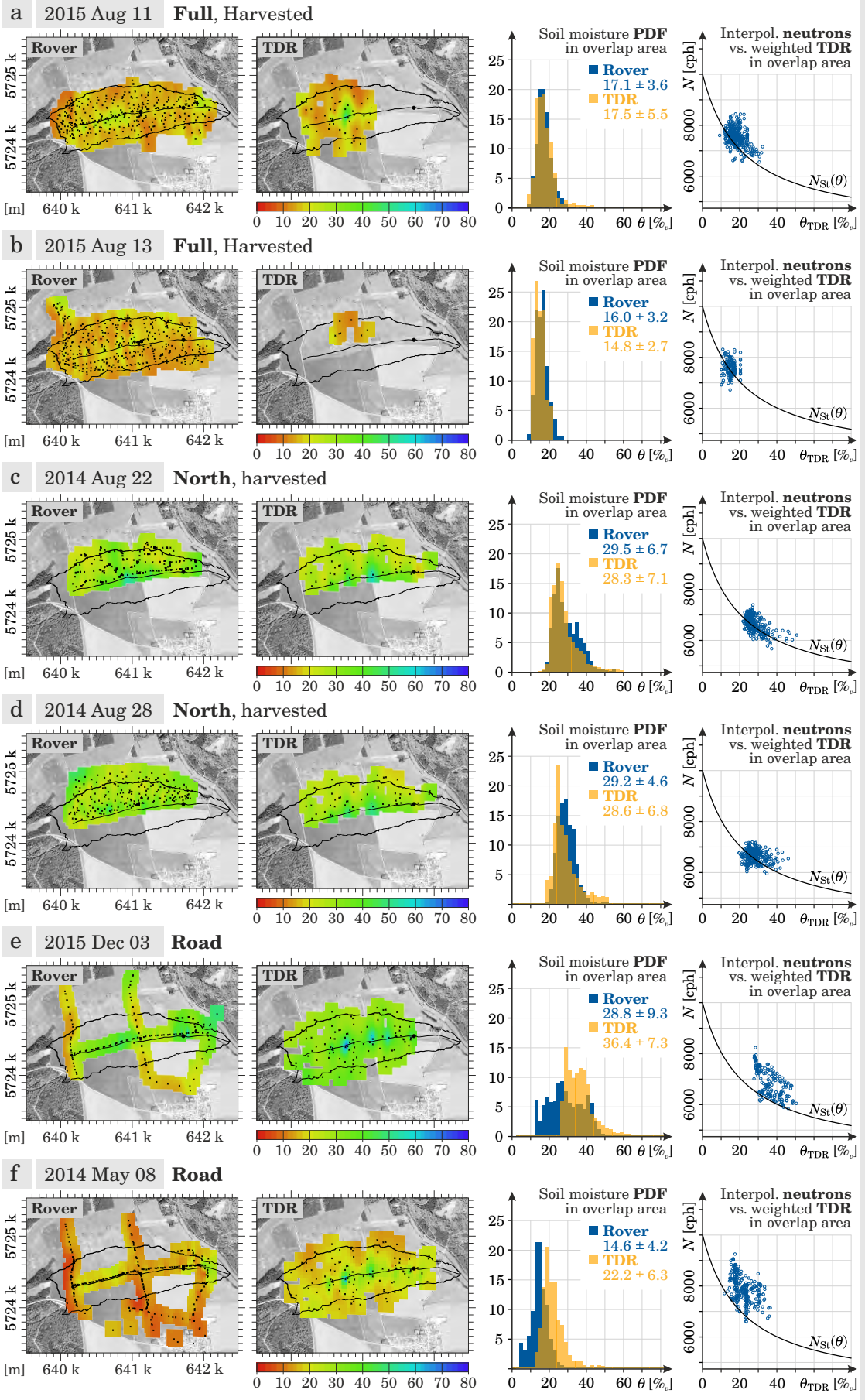

Fig. 8.3: Comparison of CRNS rover and TDR campaigns in the *Schäfertal* using interpolated data, probability density functions (PDF) and the $N_{St}(\theta)$ relation.

According to Lv et al. (2014), soil below trees can be dryer or wetter depending on the tree species and soil type. In their specific, case Lv found that the tree canopies prevented the soil from drying, which led to higher mean soil water content near the trees. Third, the effect of dry roads were most prominent at the path in the north-west corner, where no vegetation was present. In the southern part of the same road, wetter spots were visible in the interpolated map, because a dense hedge of shrubs accompanies the path.

8.3.2 Spatial correction across the *Bode* basin

The first part of this work imposingly showed that the assumption of spatially constant parameters is acceptable for almost homogeneous agricultural fields. However, Fig. 8 indicates that spatial correction for vegetation effects and soil properties might be important as soon as larger variability occurs. For this reason, large-scale transects through the *Bode* catchment were corrected for bulk density, lattice and humus water, and vegetation water. The approach was validated with three SoilNet installations along the path, and further supported by 11 repetitions between the dry summer and the wet winter of 2015.

Fig. 8.4 shows the time series of one of the campaign days with different correction steps in between. While the standard corrections for p, h, I (section 3.5), and θ_{lw} led to improved soil moisture estimations at all three validation sites, the most significant improvement was achieved by additionally including biomass information (BWE). The parts between these sites were predominantly covered by paved roads, which might bias the collected data towards the dry regime. The overall daily performance is illustrated in Fig. 8.5, where it should be noted that the error bars for SoilNet data can vary by up to 10 $\%_v$, because the TDT sensors used were partly unreliable.

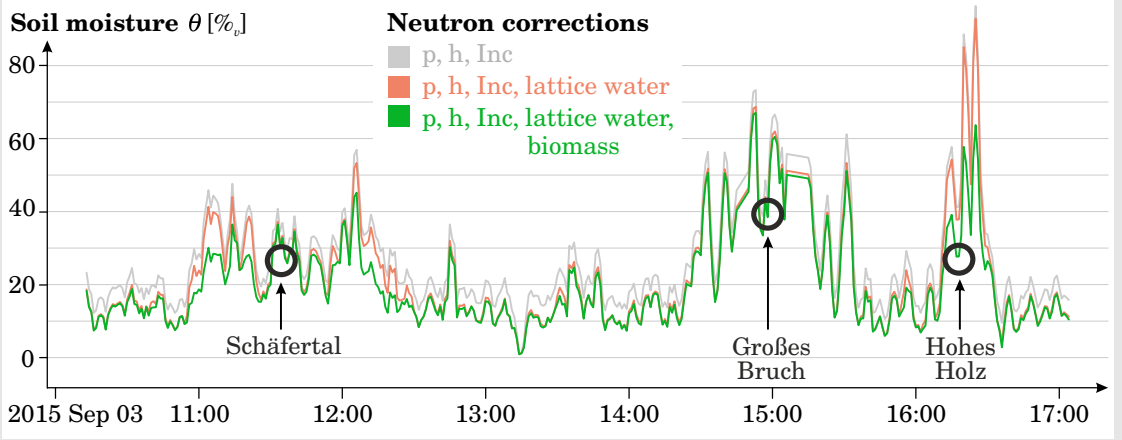

Fig. 8.4: Time series of an exemplary campaign day on Sep 03, 2015, where p, h, and I denote the meteorological standard corrections (section 3.5). While the three validation sites were passed, only the biomass-corrected rover signal represents local SoilNet observations. Along the track between the three field sites, soil moisture is probably underestimated due to road effects.

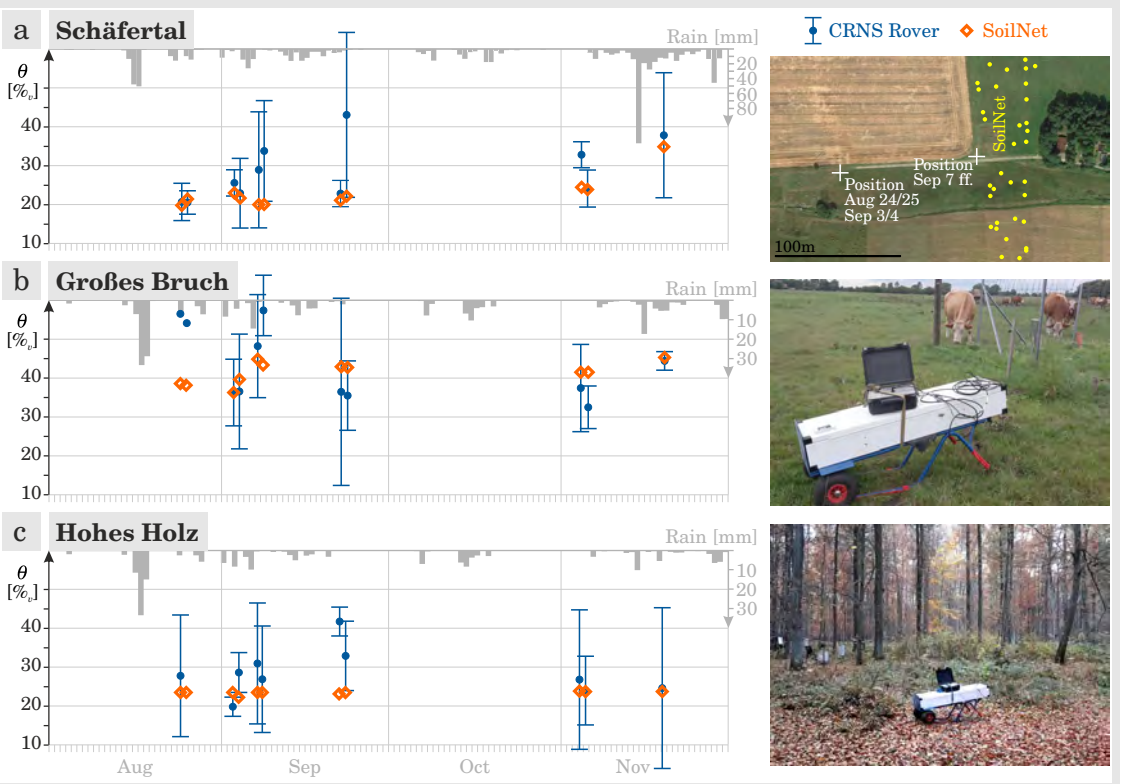

Fig. 8.5: Validation of fully corrected soil moisture estimates from the CRNS rover with three SoilNet sites of different land use. Deviations can be explained by interesting effects, such as presence of cows, interception, or dynamic biomass water. *Credit: Photos (a) Google Maps, (b,c) M. Kasner*

In the *Schäfertal*, the agreement between SoilNet and fully corrected CRNS soil moisture is remarkable in the first four campaign days. From Sep 7th on, the rover halted much closer to the SoilNet, but also closer to the small group of trees in the east (see also Fig. 8). Their response to precipitation events, as well as the fluctuating presence of scientists near the detector may explain the larger variation in the rover signal. This effect is also visible in *Großes Bruch*, were additionally the presence of cows interfered with the consistent execution of the measurement procedure. By the way, water content in scientists can be estimated to 40–50 % (Watson et al. 1980), while a significant amount of hydrogen, oxygen and carbon in the organic molecular structure further contributes to neutron moderation (Desilets et al. 2007). Thus, the use of the trolly at several days and stations, as well as the presence of cows, could significantly disturb the neutron signal and may explain the large variation in the individual measurement periods. However, detailed analysis of the campaign days reveal interesting features in *Großes Bruch*. In the two days of August, the grassland site was not accessible by the rover due to the presence of cows, thus the actual soil water content is overestimated. In Sep 7–8th (campaign days 5–6), flooding events led to water ponds in some parts of the footprint that were not captured by the SoilNet sensors. The campaigns in late September and early November were conducted under dry conditions and led to consistent underestimation of soil moisture, which can be

an indication for underestimated bulk density ϱ_{bulk} in the calculation. In fact, local soil samples confirmed that the pasture lands of *Großes Bruch* exhibited much higher bulk density than reported by BÜK1000, due to the perpetual compaction from cows. The performance in the forested ecosystem *Hohes Holz* highly depends on dynamic effects, like canopy interception water or seasonal variations of wet biomass. CRNS estimates of forest soil moisture agree well with the soil moisture network during periods of low water content in the trees, either due to drouht stress (summer), or preparation for hibernation (winter). In between, precipitation events, falling leaves, and water accumulation within the trees can lead to a decrease of neutrons.

Kasner (2016) thoroughly conducted sensitivity analysis with different correction parameters. As a result, the slope s of the correction function only has minor effect on the rover performance, compared to the other uncertainties involved. For example, static biomass estimates exhibit variations up to 50 % due to soil type and location (Röhrig and Ulrich 1991; Scarascia-Mugnozza et al. 2000), timber or natural forests (Ellenberg and Leuschner 2010), or individual tree species (Ellenberg et al. 1986; Hagemeier 2002). Besides standing biomass, its growth dynamics can significantly influence the CRNS signal (Rivera Villarreyes et al. 2011; Hornbuckle et al. 2012). Plants perform vertical redistribution of water on a daily basis which is also visible to CRNS (Baroni and Oswald 2015). Ideas exist to achieve temporal correction of biomass dynamics by infering the *Leaf Area Index* (LAI) from local LIDAR or NDVI remote-sensing products. However, other studies have shown that the correlation between LAI and the relevant quantity BWE is rather weak (Coopersmith et al. 2014; Baroni and Oswald 2015). The present study is further prone to uncertainty by excluding root-zone biomass from the analysis (cmp. also Baatz et al. 2015), which can have an effect on the neutron signal to higher (Franz et al. 2013b) or lesser degree (Bogena et al. 2013).

8.4. Conclusion & Outlook

The mobile cosmic-ray neutron sensor has been successfully applied to estimate soil moisture from the 1 km to 50 km scale. One of the most prominent insights from the dense network of measurements was the capability to capture small-scale patterns at resolutions of 10–100 m, depending on driving speed. This result opens the path for small-scale tomography of soil moisture patterns, while on the other hand sophisticated correction approaches become important to account for local effects of wet biomass and dry roads. The latter effect is presented here for the first time as the CRNS rover looses prediction capabilities in the *Schäfertal* on days when the field was not accessible.

Eleven rover campaigns have been conducted following large topographic gradients in the *Bode* river catchment. At this scale, correction for changing soil properties and biomass becomes important to account for the large fluctuations across the heterogeneous land. A well-performing relationship between rover data and soil moisture has been elaborated and validated using three distinct soil moisture monitoring networks. Results have shown that the simple conversion approach $\theta(N)$ from Desilets et al. (2010) is applicable if the parameters N_0(BWE), θ_{lw}, and ϱ_{bulk} are adapted on spatial data. The study provides considerable advance for the feasibility of CRNS rover measurements, as the presented parameterization appears to be

adequate for wet and dry conditions (compare e.g., separate approaches in Chrisman and Zreda (2013)).

Uncertainties of soil bulk density as well as spatial and temporal changes of biomass make up the most significant contribution to soil moisture estimates from CRNS roving. In order to quantify soil water content with an accuracy below 10–20 $\%_v$ it is strongly recommended to collect the corresponding biomass and soil data at the finest resolution possible (cmp. also Avery et al. 2016).

The spatial interpolation of TDR and CRNS data could be improved in order to adapt on proximal conditions. For example, Schröter et al. (2015) presented a fuzzy clustering approach to bring sparse TDR data into the whole area of the *Schäfertal*. Given the amount of CRNS measurements, ordinary Kriging might be a sufficient interpolation approach, however, promising geostatistical tools exist that can account for overlapping footprints and measurement uncertainty (e.g., Dietrich et al. 1998), by including the radial sensitivity function W_r (chapter 7).

The spatial data could then be upscaled to remote-sensing scales using sophisticated interpolation and Monte Carlo methods (Wang et al. 2014), under consideration of expert knowledge about the statistical properties of soil moisture patterns at various scales (Oldak et al. 2002). Nowadays remote-sensing techniques can provide forest soil moisture estimates, e.g., the SMOS $\tau\omega$-approach (Entekhabi et al. 2010). The rover could be one of few techniques able to evaluate these datasets at various spatial scales.

The spatial correction methods applied for the *Bode* transect are easily applicable to other regions where sufficient proximal data is available. Small-scale catchment hydrology in the *Schäfertal* might also benefit from this approach if optical information is included, for example from airborne hyper-spectral imaging. Freely available and coarse datasets of organic matter and soil properties (Shangguan et al. 2014; De Lannoy et al. 2014) allow the application of the presented method at the global scale (cmp. also Avery et al. 2016). Temporal changes of biomass water, for instance, could be addressed with regularly updated remote-sensing products.

In order to remove the dry road bias, neutron radiation could be shielded during road-only campaigns by adding extra moderators to the bottom of the trunk below the detector (e.g., polyethylene blocks or a Cadmium sheets). Following simulations from Köhli et al. (2015), a constant offset of 20–30 % of the neutron signal could be a reasonable post-processing approach (cmp. also Fig. 6.3). Simulations further showed that local effects more and more smooth out as the detector is lifted up (Fig. 10.4). Thus, detectors mounted on the roof of the car could diminish this effect, while airborne neutron detection above several meters height could serve as a promising alternative which is also unaffected by inaccessible terrain. Chapter 10 elaborates on this idea from a theoretical and experimental perspective.

The next chapter will investigate the potential of the spatial neutron data for the use in hydrological models. This application will be a good test whether the CRNS rover is capable to provide appropriate data in spite of the limits presented here.

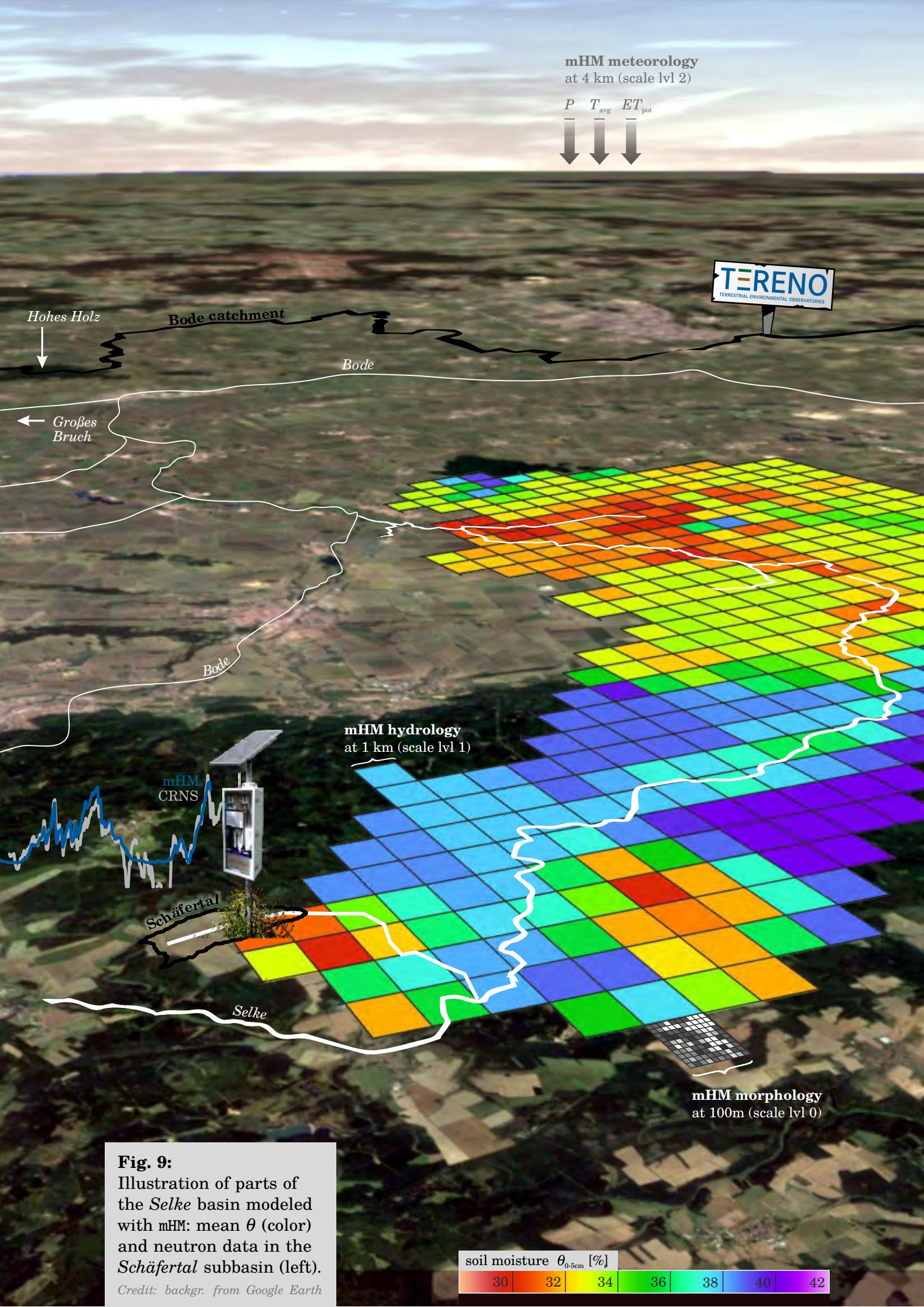

Fig. 9:
Illustration of parts of the *Selke* basin modeled with `mHM`: mean θ (color) and neutron data in the *Schäfertal* subbasin (left).

Credit: backgr. from Google Earth

9.

Hydrologic Modeling

Using CRNS data to evaluate model performance

In the previous chapters, the full spectrum of state-of-the-art soil moisture observations with CRNS has been utilized to provide temporal and spatial data at various scales. It is about time to get down to one of the major goals of CRNS research: to serve large-scale hydrological models as a constraint to close the water balance and to improve the modeled soil moisture state.

After thorough calibration of detector efficiency in chapter 4, CRNS stations in *Schäfertal*, *Großes Bruch* and *Hohes Holz* (chapters 5, 7, 8) may help to evaluate the performance of the model `mHM` at the temporal scale. With the transects conducted in the *Bode* catchment (chapter 8), the CRNS rover addresses the important challenge of improving the estimation of spatial patterns in distributed models. Moreover, insights in the CRNS footprint (chapters 6–7) have been particularly important to inform about the scale gap between observations and computational models. We can now better understand at which scale observations represent the value in a grid cell, for what choice of the cell size neutron data is beneficial, and the impacts of those decisions.

This chapter presents a framework to utilize CRNS data for evaluation and calibration of the hydrological model `mHM`. As a part of this framework, the forward model `COSMIC` has been implemented to enable `mHM` to predict neutron observations directly from modeled soil moisture profiles. These are exciting times, when dirty observations meet numerical bits, aiming to demonstrate their solidarity.

9.1. Introduction

Water scarcity, adaption on climate change, and flood risk assessment are critical topics in society and science these days. Accurate description of both, energy balance as well as water balance of river catchments are a prerequisite for reliable hydrological predictions, in which soil water storage plays a key role. The soil moisture state determines the efficiency of infiltration and percolation (e.g., groundwater recharge), evapotranspiration (i.e., feedback of water to the atmosphere), water availability for plants, and surface runoff.

However, chapter 1 reviewed that conventional measurement methods provide data at scales that are either not representative for areas larger than a few square meters, or fail to quantify the water storage below the surface layer. As regional hydrological and land-surface models typically run at intermediate resolutions from 100 m to kilometers, the lack of soil moisture observations at these scales is a serious problem. Consequently, validation or calibration of those models remain one of the key challenges in hydrology and climate science (Vereecken et al. 2007, 2008; Robinson et al. 2008). During the last decades two major strategies have been pursued to challenge the described problem:

1. Providing data at relevant scales, either by up- or downscaling or by choosing the right instrument (see also Fig. 1.2),
2. Selecting appropriate models that can deal with data at multiple scales.

The rescaling procedures often introduce huge uncertainties, for example when large-scale SMOS data is downscaled to 500 m (Ridler et al. 2014), or hydraulic parameters are upscaled (Vereecken et al. 2007). In this work, calibration and validation data is provided at the modeling scale using the technology of cosmic-ray neutron sensing (CRNS). Furthermore, the *mesoscale hydrological model* mHM is applied which takes care of flux conservation and parameter transferability to *any* scale.

The variety of hydrological models can be described as a manifold of intersecting categories. One of such classifications comprises (1) *reductionistic models* (low complexity, low uncertainty), and (2) *hyper-resolution models* (high complexity, high uncertainty). The modern approach of *multi-scale models* is a quantum state in between, offering high complexity at low uncertainty by process-orientated subgrid parameterization (Wood et al. 2011; Beven and Cloke 2012). To achieve this, *regionalization* techniques have been developed to infer scale-independent and transferable model parameters (see Gupta et al. 2014, for a review). These regionalized parameters could be used to parameterize pedo-transfer functions, for instance, to infer porosity from soil texture and bulk density data (Zacharias and Wessolek 2007). Although it is generally preferable to measure the quantities of interest directly (Vienken and Dietrich 2011), this is often prohibited for technically reasons or infeasible at large scales (e.g., for porosity and hydraulic conductivity).

Models of higher complexity often account for detailed physical processes at the micro-scale. The so-called *physical-based* models, e.g., HYDRUS (Šimunek et al. 2008), make use of Richards solvers and the conservation of mass, momentum and energy, in order to mimic the flow and transport of water through the micro-pore domain (section 1.4). The detailed formulation requires a huge amount of data to

constraint their parameters, and stable numerical solutions are often associated with high computational effort. Furthermore, those complex models do not guarantee to perform accurately. If the required information is not available, not representative, or even wrong, the results of complex models are often unusable. Apart from that, most of the corresponding equations loose validity beyond the scale of a few centimeters to meters, beyond which effective parameters are required to upscale processes that are only well understood at the micro scale (Blöschl and Sivapalan 1995; Vereecken et al. 2007).

In contrast to physical models, *lumped models* treat the whole watershed as a spatially homogeneous unit and rely on simple relations between precipitation and runoff. `METVER` is such a lumped model used by the Deutscher Wetterdienst (DWD) to estimate soil moisture at the plot-scale, which focuses on the agro-meteorological aspects of evapotranspiration (Müller and Müller 1988). As soon as spatially connected hydrological units are considered, processes and morphological properties might be too diverse throughout large catchments. In *semi-distributed* models, larger watersheds are divided in lumped sub-catchments in order to account for the coarse heterogeneity. The spatial discretization can also be performed in (regular or adaptive) grid cells, allowing to reach even higher spatial resolution and to distribute input data and parameters heterogeneously across the domain (see e.g., Carpenter and Georgakakos 2006). `mHM` is such a fully *distributed* model, but still conceptually lumped with regards to individual cells. Distributed models have increasingly gained popularity, especially since computational techniques have improved and highly resolved data became available, as was discussed in a special issue edited by Beven (1992).

The final goal of hydrological models is the proper prediction of fluxes (discharge, evaporation) and states (soil moisture, solute concentration). For example, Ceppi et al. (2014) were able to predict soil moisture more than a week in advance to support irrigation management. However, model results often exhibit significant uncertainty due to the lack and uncertainty of data, parameter uncertainty, or insufficient process conceptualization (Coron et al. 2014). In order to address the challenge of model validation and calibration, modelers should make use of the huge variety of measurements from all over the world. In this regard, data assimilation or calibration techniques are usually consulted to update model parameters, states, or fluxes, and to finally improve hydrologic predictions. For example, Renzullo et al. (2014) improved root-zone soil moisture by assimilating remote-sensing products, and validated with CRNS and in situ observations. Many efforts have been made recently to also assimilate CRNS data into *land-surface models*, which typically represent complex processes that are lumped at the plot-scale. Rosolem et al. (2014) performed the first assimilation of synthetic neutron data to the land-surface model `NOAH` and demonstrated the practicability of CRNS data to improve soil moisture profiles. Han et al. (2015) showed that neutron assimilation improves soil moisture predictions of a land-surface model in China by correcting for systematic biases that were inherited from uncertain soil maps.

The present study ventures the step towards neutron data integration into distributed, hydrological models, which typically aim to quantify river discharge, but are also more and more used to deliver soil moisture predictions (e.g., Zink et al. 2016). The hypothesis of this chapter is that the CRNS method could provide rep-

resentative data to accurately validate and calibrate the model mHM at appropriate scales. To achieve this, the performance of the model mHM is tested for the first time at resolutions of 20, 100, and 1000 m in the small catchment *Schäfertal*, where time series of neutron data will be used to validate and calibrate the model. Moreover, Haghnegahdar et al. (2015) argued that model performance can be different for calibration and validation runs, as calibration is prone to the "game" of equifinality. The authors concluded that only spatial validation is a sufficient test for distributed models. Following their argumentation, this chapter further aims to validate the modeled soil moisture patterns with CRNS rover surveys that have been evaluated in chapter 8.

9.2. Methods

9.2.1 The mesoscale hydrological model mHM

mHM is a state-of-the-art distributed hydrologic model that closes the catchment water balance by routing and conserving water fluxes throughout the river basin (Samaniego et al. 2010; Kumar et al. 2013a). The model conception is similar to the process-based model HBV (Bergstrom 1976), as the implementation of soil processes is conceptual, but the model parameters are physically motivated. Additionally, a regionalized set of global parameters γ promises the transferability of the model calibration across scales and locations. Currently, mHM represents the dominant hydrology on scales above 1 km and proved to perform well in hundreds of European catchments and beyond (e.g., Kumar et al. 2013b; Rakovec et al. 2016).

The most interesting feature of mHM is the *multiscale parameter regionalization* (MPR) technique, which requires calibration of global parameters (see also Pokhrel et al. 2008) in order to reduce the uncertainties that are typically related to up- or downscaling procedures. Conventional models use simple upscaling or downscaling strategies to bring the data (e.g., clay %) to the model grid, where scale-dependent parameters then deduce model variables (e.g., porosity Θ) that determine the fate of hydrological processes. However, those transfer functions (e.g., f : clay % $\mapsto \Theta$) are typically non-linear and therefore highly sensitive to the averaging sequence. The MPR method applies transfer functions to the data *before* rescaling, using the scale-independent parameters γ:

$$\text{conventional:} \quad y_1 = f(\langle x_0 \rangle, \gamma_1), \quad \text{MPR:} \quad y_1 = \langle f(x_0, \gamma) \rangle ,$$

where y_1 is the variable of interest at the modeling scale, x_0 is the available data at its specific scale, $f : x \mapsto y$ is an arbitrary transfer function, and $\langle \cdot \rangle$ is an averaging technique (e.g., the geometric mean). This procedure leads to a better representation of effective variables at the modeling scale and thus allows mHM to integrate data and operate efficiently across scales and locations (Samaniego et al. 2013; Kumar et al. 2013a,b; Rakovec et al. 2016).

The soil moisture domain of the model is discretized with a certain number of horizons (typically three at depths of 0–50, 50–250, and 250–2000 mm), while all soil layers are prone to root-water uptake and evapotranspiration processes. Excess

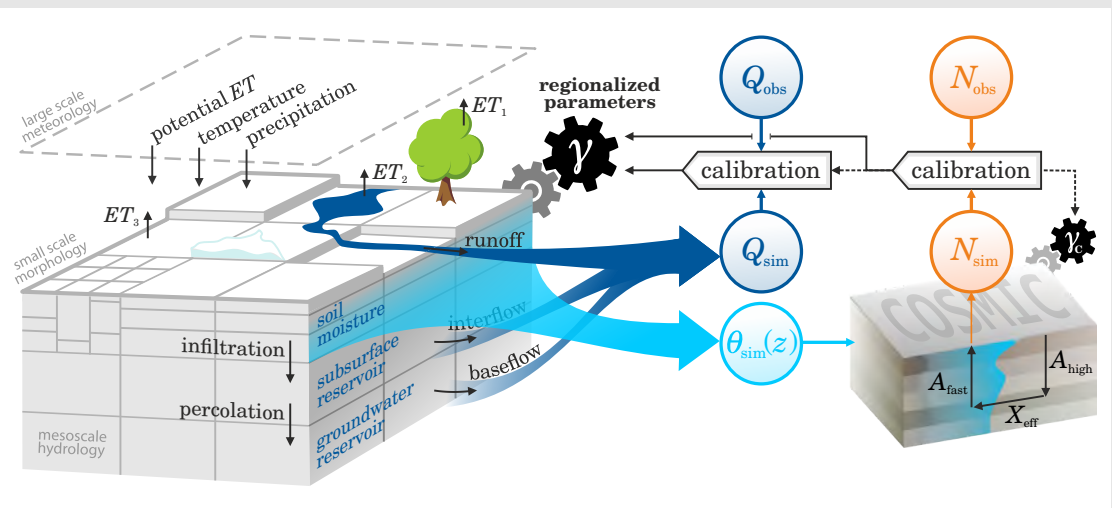

Fig. 9.1: Schematic of mHM processes and workflow in this study. The model generates direct discharge Q_{sim} from lateral cell outflows, while soil moisture layers $\theta_{\text{sim}}(z)$ are translated to neutrons N_{sim} by COSMIC. Both products can be used to calibrate the global parameter set γ against observations. Simultaneous calibration as well as calibration of γ_{COSMIC} are future projects (dashed).

water in the soil moisture layer is further redirected by surface runoff or infiltration (Fig. 9.1), while the exact partitioning is determined by the calibration parameters γ. This conceptualization is one of the reasons why validation of absolute modeled soil moisture often is not meaningful. Alternatively, anomalies, $(\theta - \langle\theta\rangle)/\epsilon(\theta)$, should be compared instead. For example, two different models can easily be calibrated to get the partitioning perfectly right, although their resulting soil moisture value can be totally different due to different data and parameters used to describe hydrological conductivity. On the other hand, Gao et al. (2015) recently found that also the use of anomalies as a measure for catchment wetness can be problematic.

As infiltrated water fills up the subsurface reservoir (see Fig. 9.1), slow interflow directly contributes to river discharge Q, and fast interflow is triggered if the filling level exceeds a certain threshold. The water is routed through the topographic gradients of the model domain by the *Muskingum-Cunge* flood routing algorithm (Todini 2007). During this process, fluxes (and thus masses) are conserved at any time by minimizing the flux difference at all scales: $|\Phi_i - \int_{j\in i} \phi_j| \rightarrow 0$, where Φ_i is the flux of an arbitrarily large group of cells, i, and ϕ_j are the fluxes of the subordinate cells j.

The mHM model further describes snow accumulation and melting based on the *improved degree-day* method, which generates snow from precipitation below a certain temperature threshold, and accounts for an increased snow melt during intensive rain events (Hundecha and Bárdossy 2004). Vegetation is implemented as a certain land use type that exhibits specific interception and permeability parameters, and which can be controlled dynamically with LAI time series data.

9.2.2 Implementation of the neutron forward models

Direct comparison of modeled soil moisture $\theta_{sim}(z)$ with CRNS observations θ_{obs} is difficult, because the latter instrument integrates over several decimeters in depth. Thus the CRNS method is unable to uniquely represent different soil moisture profiles $\theta(z)$ and thus the question, which soil horizon should be compared with θ_{obs}, cannot be answered. As Rivera Villarreyes et al. (2014) elaborated, inverse determination of soil water profiles from the integral CRNS signal is only feasible using independent measurements and a physical model like HYDRUS. Moreover, the penetration depth of neutrons is highly sensitive to θ (Köhli et al. 2015). In order to accommodate the changing nature of the effective depth, Shuttleworth et al. (2013) have decided to assimilate the actual measurement N_{obs}, rather than the soil moisture product. They developed an analytical model, COSMIC, which translates any modeled soil moisture profile into neutron counts above the surface. The conversion function has been validated with other accepted methods by Baatz et al. (2014) and was applied successfully for data assimilation in land-surface models by Rosolem et al. (2014) and Han et al. (2015).

The neutron forward operators were implemented in a dedicated module for mHM, featuring two different approaches to predict the neutron intensity at the surface:

1. N_0-method (Desilets et al. 2010) accounting for only the first horizon (compare section 3.6):
$$N_{sim} = N_0 \cdot \left(a_1 + \frac{a_0}{\theta(z_1) + a_2} \right) ,$$
2. COSMIC (Shuttleworth et al. 2013) accounting for all soil horizons z:
$$N_{sim} = N_{COSMIC} \cdot \sum_z A_{high}(z) \cdot X_{eff}(z) \cdot A_{fast}(z) .$$

The COSMIC function accounts for the downward attenuation A_{high} of incoming high-energy neutrons impinging the soil, their effectivity X_{eff} to create fast neutrons by interacting with the soil material, and finally the upward attenuation of isotropically propagating fast neutrons (see chapter 3 for details).

$$\text{High-energy neutron attenuation:} \quad A_{high}(z) = e^{-\Lambda_{high}(z)}$$
$$\text{Fast neutron attenuation:} \quad A_{fast}(z) = \frac{2}{\pi} \int_{\varphi=0}^{\pi/2} e^{-\Lambda_{fast}(z)/\cos\varphi} \mathrm{d}\varphi$$
$$\text{Neutron interaction depth:} \quad X_{eff}(z) = \alpha X_{soil} + X_{water}$$

The neutron interaction depth X is a virtual quantity depicting the fraction of fast neutrons that is created from high-energy neutrons interacting with the soil. It accounts for the density of water and soil (which is by a factor $\alpha \approx 0.24$ less effective in creating fast neutrons).

$$X_{soil}(z) = \Delta z \cdot \varrho_{bulk} , \qquad \Lambda_{high}(z) = \frac{X_{soil}(z)}{162.0} + \frac{X_{water}(z)}{129.1} ,$$
$$X_{water}(z) = \Delta z \cdot \varrho_{water} \cdot (\theta_z + \theta_{lw}) , \qquad \Lambda_{fast}(z) = \frac{X_{soil}(z)}{107.8} + \frac{X_{water}(z)}{3.2} .$$

The amount of water in each horizon, $X_{\text{water}}(z)$, is determined using the modeled soil water content SWC [mm] from mHM, $\theta(z) = \text{SWC}(z)/\Delta z$, the lattice water proportion, $\theta_{\text{lw}} = 7.5\,\%_v$, and the density of water, $\varrho_{\text{water}} = 1000\,\text{kg/m}^3$. The average density of the soil, ϱ_{bulk}, as well as θ_{lw} were kept constant in this study and will become variable in the next versions of the mHM neutron module.

Absolute calibration and validation of neutron counts is difficult, because both neutron models make use of arbitrary scaling factors N_0 and N_{COSIMC}. As a solution, the data has been first rescaled/normalized using the sensor-specific efficiency correction (chapter 4), then those scaling parameters have been adjusted to match CRNS station data in the *Schäfertal* catchment. Other sites might need variable scaling factors that depend, for instance, on latitude and altitude (cmp. chapter 5).

Two of the major hydrogen sources that were not accounted for in the presented neutron models are vegetation and snow. However, their implementation as additional layers is planned in the next versions of mHM, using relationships discussed in chapter 8 and section 3.6. Together with additional dependencies of COSMIC parameters like α (which is probably related to bulk density), a specific global parameter set for the neutron models, γ_N (or γ_{COSMIC}), will be added to mHM in order to regionalize the spatial transfer functions (see also section 9.4.3).

9.2.3 Study site

To test the hypothesis that neutron data can be beneficial for hydrological modeling, an ideal study site should be well monitored in terms of (1) discharge, meteorological and morphological data, and (2) cosmic-ray neutron data. The *Schäfertal* (1.6 km^2) is one of those intensive research sites in the scope of TERENO which was chosen for this study, where CRNS stations were installed between 2010 and 2013 by the University of Potsdam. According to Graeff et al. (2009) groundwater is the dominating process in the *Schäfertal* and bimodel runoff events occur regularly, however decreasingly since 1970 due to mining activities. The superior *Selke* basin (468 km^2) covers huge gradients of land use and topography from the forested *Harz* mountains in the south down into the agricultural low-lands in the north. To date, CRNS stations in the *Selke* were only located in the *Schäfertal* subbasin, however, statistical sensitivity analysis was consulted recently in order to plan optimal placement of additional stations.

Meteorological forcings for both basins were provided by the DWD and resolved as 4×4 km grid cells, while data from the local *Schäfertal* weather station has been incorporated when available. Morphology data like topography, geology, soil, etc., exhibited a 10 m resolution in the *Schäfertal* and 100 m in the *Selke* basin. Discharge data in the *Schäfertal* was made available for 1997–2007 by the Hochschule Magdeburg, who operate the river gauge in that catchment.

Neutron and discharge data have been assimilated at a daily basis, which is a decent compromise between favorable high-frequency data (Rosolem et al. 2014) and the typical measurement noise (see also chapter 4). Spatial neutron data from the CRNS rover has been equally averaged within each cell of mHM and also assimilated as a daily average.

9.2.4 Resolution study

One of the most impressive features of mHM is the ability to run at any scale, because the flux conservation condition between cells is an intrinsic feature of the model. From a naive perspective, lower cell size should then always lead to better spatial resolution and prediction performance. However, decreasing cell size s in the modeling domain reveals two major disadvantages:

- Small-scale processes are not implemented in mHM (e.g., lateral flows between cells, or Richard-like transport),
- Increase of memory usage and computational time by $\sim \mathcal{O}(s^{-2})$.

For the discharge quantity Q, the lack of small-scale processes might have negligible impact, because the catchment-integral property is able to average out slow-moving effects. Soil water storage can also be predicted satisfactorily if an integral catchment average was assessed (Rakovec et al. 2016), because mHM takes care of closing the global water balance. However, as soon as fluxes and storages of individual cells are evaluated, cell-to-cell related processes like lateral flow or sophisticated infiltration models will reveal their relevance.

These considerations have been taken into account for choosing the proper scale for mHM simulations, as it is important to select a proper cell size at which the observation is representative. In this case, the cell area should be covered by the CRNS footprint. The insights from chapter 6 can help here to investigate the contribution of measured neutrons within an imaginary cell of edge length s. By integrating the weighting function $W_r(h\,,\theta)$ (eq. 6.2), the contribution of neutrons to the detected signal in the cell center has been calculated and presented in Table 9.1.

Table 9.1: Contribution of neutrons within a rectangular cell of size s, as a fraction of total observed neutrons. W_r is integrated in a footprint circle of equivalent area for dry and wet conditions, h = 5–15 g/m^3, θ = 10–40 %$_v$.

cell area s^2	diameter $2s/\pi^{\frac{1}{2}}$	$N_{\text{cell}}/N_{\text{total}}$
20^2 m^2	22.6 m	35–45 %
100^2 m^2	112.8 m	55–67 %
250^2 m^2	282.1 m	78–86 %
1000^2 m^2	1128.5 m	99–100 %

The short analysis shows that neutron data from a cell at 20 m resolution could explain more than one third of the variability, while 100 m cells represent two thirds of the detected neutrons. At resolutions of 1 km all measured neutrons originated in that cell, however, still $\approx 61 \pm 6$ percent of the neutrons represent only 1 % of the total area. As a trade-off between computational efficiency and the lack of small-scale processes, 100 m resolution has been chosen for most simulations in the *Schäfertal* catchment, while the *Selke* has been set up at 1 km resolution.

Although multiple CRNS data points were usually available within 1 km^2 cells, special care should be taken during interpretation of CRNS data at this scale.

9.2.5 Parameter optimization

Parameter calibration is a complex field of research, covering the selection of informative parameters (Cuntz et al. 2015), the design of objective functions (Gan et al. 1997; Mai et al. 2016), the choice of adequate performance measures (Krause et al. 2005; Bennett et al. 2013), and the selection of a promising optimization algorithm (Zhang et al. 2009). If successfully applied, calibration results could narrow parameter ranges and minimize the uncertainty of model results (see e.g., Rosolem et al. 2013b).

To date, `mHM` gained capabilities to calibrate its parameter set γ against observations from discharge, basin-average and spatially distributed soil moisture, and total water storage. Popular efficiency measures in hydrology are the *Nash-Sutcliffe-efficiency* (NSE) (Nash and Sutcliffe 1970) and the more modern *Kling-Gupta-efficiency* (KGE) (Gupta et al. 2009). This study makes use of KGE for parameter calibration on neutrons, while for historical reasons robustness of model results have been indicated by both, NSE and KGE.

$$\mathrm{NSE} = 1 - \frac{\sum(\mathrm{sim} - \mathrm{obs})^2}{\sum(\mathrm{obs} - \langle \mathrm{obs} \rangle)^2}$$

$$\mathrm{KGE} = 1 - \left[\left(\rho(\mathrm{sim}, \mathrm{obs}) - 1 \right)^2 + \left(\frac{\epsilon_{\mathrm{sim}}}{\epsilon_{\mathrm{obs}}} - 1 \right)^2 + \left(\frac{\langle \mathrm{sim} \rangle}{\langle \mathrm{obs} \rangle} - 1 \right)^2 \right]^{\frac{1}{2}}$$

NSE normalizes the mean squared error by the observed variance, where the mean observed variable $\langle \mathrm{obs} \rangle$ is used as a baseline. Following this approach, site-specific variations could translate to biased estimation of model skills among different sites. On the other hand, the KGE measure is a revised version of NSE that accounts for correlation ρ, variance ϵ, and bias of simulated and observed variables (Gupta et al. 2009).

As an optimization strategy, the *shuffled-complex-evolution* (SCE) algorithm was selected, which is a state-of-the-art approach to find global minima in complex parameter domains (Duan et al. 1992). As the entire parameter space is randomly sampled and information between multiple local minima is shared/shuffled, the algorithm is slower but more reliable in finding global minima compared to other popular algorithms like the *Dynamically Dimensioned Search* algorithm (DDS) (Tolson and Shoemaker 2007).

In this work, simulated neutrons N_{sim} have been calibrated against observed data N_{obs} by maximizing the KGE of the catchment-averaged time series $\langle N \rangle \equiv \langle N \rangle(t)$:

$$\text{objective function:} \quad \max_{\gamma} \mathrm{KGE}\left(\langle N_{\mathrm{sim}} \rangle , \langle N_{\mathrm{obs}} \rangle \right) \rightarrow 1 \,. \tag{9.1}$$

As this objective function only calibrates the areal average, spatial patterns become almost invisible to the optimizer. Future studies are recommended to consider individual cells, e.g., by summing up $\mathrm{KGE}(N_{\mathrm{sim}}, N_{\mathrm{obs}})$ over all cells using the $p = 6$ vector norm (see also section 5.2.4).

The calibration process optimizes the global parameter set γ, while neutron model parameters (e.g., $\gamma_{\texttt{COSMIC}}$) have been excluded from automatic optimization in this work. Of course, parameter calibration in general is prone to the equifinality problem, that can lead to different solutions to match a single observation (Beven and Freer 2001). Especially when the real world is abstracted with large grid cells, the controlling parameters could be understood as *effective* parameters for a given averaging volume, and the identification of a *best* parameter set is not always possible (Wagener and Gupta 2005). With the help of multi-objective optimization strategies, future research aims to find parameter sets that can explain both, discharge and soil moisture dynamics, which will narrow the range of tolerance in the parameter space.

9.3. Results & Discussion

9.3.1 Small-scale performance in the *Schäfertal* catchment

The first tests with mHM at resolutions of 20 m and 100 m revealed equally good performance at the basin outlet. Model results for various parameter sets and soil horizons are presented in Fig. 9.2. Shallow soil layers (red) quickly saturate and thus contribute to early generation of interflow (and thus discharge). With increased soil water storage (orange), evaporation processes have access to more water and thus the subsurface reservoir contributes much less to river discharge. Upon calibration (blue), soil porosity, infiltration capacity, and the fast interflow threshold were adjusted to account for actual (and previously unknown) soil properties in the field. This experiment demonstrates that the model conceptualization is well able to catch small-scale discharge processes even in rather shallow slopes and short streams < 150 m.

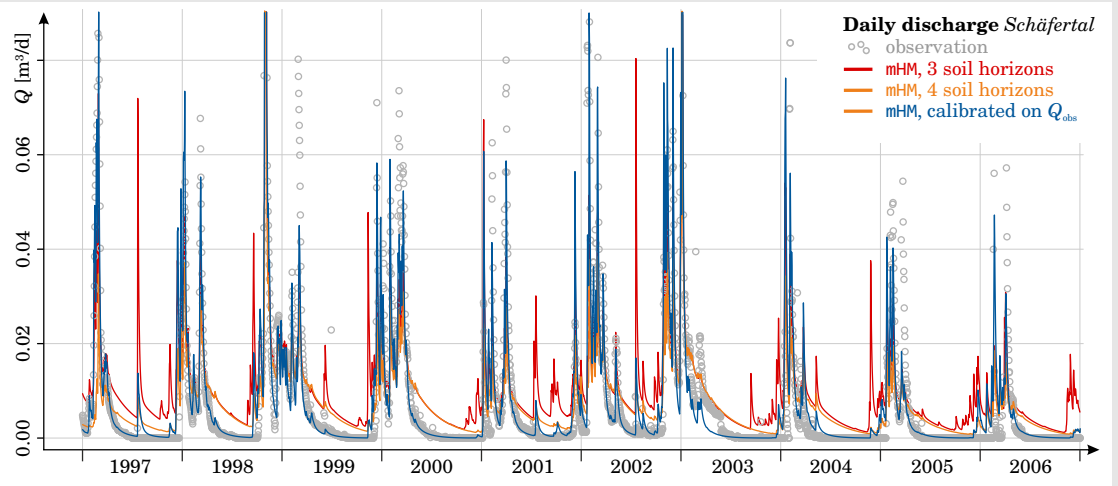

Fig. 9.2: Discharge in the *Schäfertal* catchment showing the effect of soil discretization as well as calibration on Q_{sim} (KGE = 0.91). Soil horizons were changed from (40, 80, 120) mm (red) to (40, 80, 600, 1000) mm (orange).

Following the German soil database (BGR 2007), soil properties in the *Schäfertal* were almost homogeneous. Under these conditions, mHM generated almost homogeneous soil moisture patterns that were only driven by topography and actual evapotranspiration (e.g., from slope exposition to the sun). For this reason, 29 soil cores were taken in the field up to 80 cm deep, and interpolated using the *random forest* approach (Breiman 2001; Wiesmeier et al. 2011) based on topography (M. Neubauer, 2014, unpubl.). Fig. 9.3a shows the resulting map of soil classes in the *Schäfertal*, which still exhibits only marginal variety with regards to existing diversity elsewhere (FitzPatrick 1980). Using constant bulk density estimates and homogeneous forcings, mHM has predicted soil moisture patterns for the *Schäfertal* (Fig. 9.3b) that are both, almost homogeneous (low spatial variability) and unrealistic compared to observations presented in Figures 8 and 8.3 (see also Schröter et al. 2015). This example shows that spatial soil moisture predictions highly rely on the quality of spatially distributed input data, and more sophisticated methods are required to interpolate soil properties, especially for small catchments.

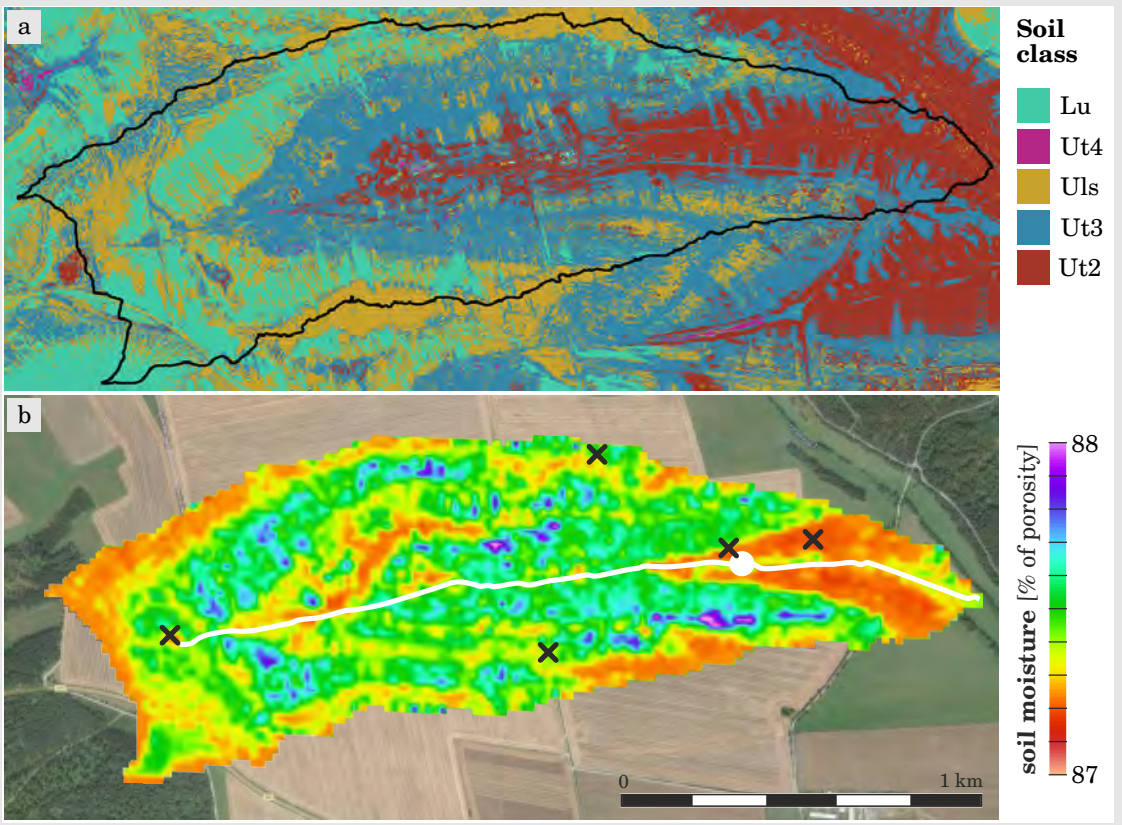

Fig. 9.3: a Soil classes in the *Schäfertal* estimated from soil cores and random forest interpolation based on topography (M. Neubauer 2014, unpubl.). b Spatial variability of soil moisture predicted by mHM at an exemplary day, showing unrealistic pattern and a diminutive range (compare Fig. 8). Black crosses indicate stationary CRNS probes, some of which were used for calibration in mHM.

The impact of the slope inclination and temporal *leaf area indexes* (LAI) have been investigated also in the course of this study, as their parameters determine actual evapotranspiration and thus soil moisture patterns. While LAI showed negligible influence on spatial soil moisture distribution for typical crops, the slope exposition provoked dryer south-facing slopes than north-facing slopes. Although the north-south effect is expected from solar radiation, independent observations with TDR and CRNS revealed opposing patterns (e.g., Schröter et al. 2015). Deactivation of the corresponding process in mHM has put the north-south gradient in a more realistic shape (not shown), and consequently questioned the concept of slope correction for small-scale applications.

One of the consequences from the homogeneous soil moisture product has been noticed during the comparison of absolute neutron counts for the different CRNS stations (crosses in Fig. 9.3b). Among these stations, the modeled count rates were almost identical, although remarkable differences have been identified in the observations (not shown). However, temporal dynamics (anomalies) of data from the SoilNet (not shown) and the CRNS stations were well captured by the hydrological model (partly evident from Fig. 9.4). In conclusion, this analysis indicates that the spatial heterogeneity of the total water storage (i.e., porosity or bulk density) is poorly represented by the given input data.

9.3.2 Mesoscale performance in the *Selke* basin

The *Schäfertal* has been modeled as a part of the superior *Selke* basin at 1 km resolution (see Fig. 9). The temporal variability of simulated neutrons was evaluated for a mHM cell that covered a representative area of the *Schäfertal*. Fig. 9.4a compares the observed neutron counts (averaged over four CRNS stations) with the model results, N_{sim}, and demonstrates acceptable agreement in relative and absolute terms. Only during winter periods N_{sim} refuses to change, because the neutron forward models only account for soil water, which is typically frozen and almost constant below the isolating snow cover. In contrast, neutron detectors are highly sensitive to snow (as a water phase) and thus exhibit vigorous variability.

Moreover, the two methods perform differently at different times of the year. Fig. 9.4a shows that COSMIC (orange) is well able to represent drying periods, while the N_0-method (red) demonstrates remarkable agreement with observations in autumn. However, it is suggested that the latter signal could be rescaled by a better choice of the parameter N_0, such that neutron counts are underestimated during autumn while remarkably matching during the other months. This underestimation could then be explained by the wet surface layer which neglects the dried soil horizons below. In turn, COSMIC accounts for exactly these stratified soil moisture profiles, but overstates the effect on simulated neutrons in autumn. On the other hand, COSMIC shows consistent overestimation of neutron counts between May and November, indicating uncared contribution of biomass water in nearby trees and crops.

Calibration of the model parameters γ against neutron observations led to slight improvement of the neutron prediction, although the objective function has not converged in the course of this study. However, the corresponding reduction of storage parameters and the fast interflow threshold impacted the discharge performance to a remarkable degree.

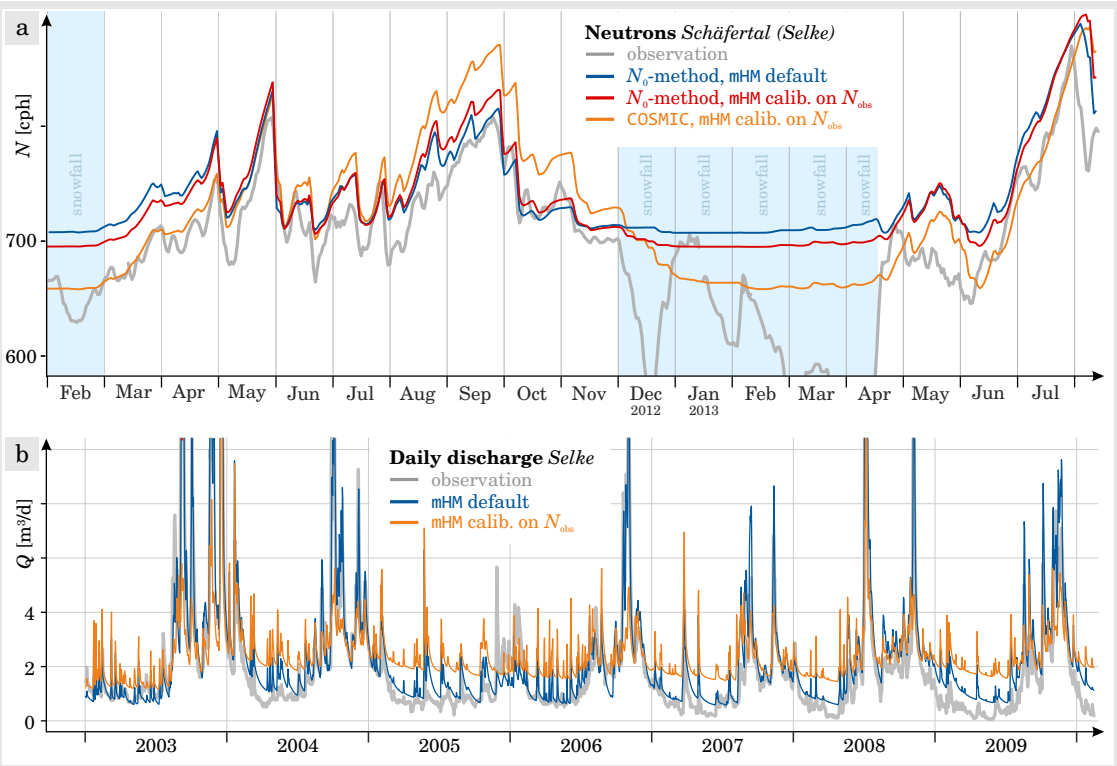

Fig. 9.4: Effect of neutron calibration in the *Selke* basin against time series data from the *Schäfertal* subbasin. a Absolute neutron counts were partly well matched by N_{sim}, while both methods show differences during wetting and drying periods. Snow and vegetation do not contribute to N_{sim}, however, they certainly do to N_{obs}. b Observed discharge Q_{obs} of the *Selke* river basin is well caught by Q_{sim} (blue) using mHM default parameters. Calibration on neutrons (orange) increases soil water storages and thus distorts the fit for discharge.

Table 9.2: Influence of the default and optimized parameter set γ on the discharge performance, KGE/NSE(Q_{sim}, Q_{obs}), where KGE was maximized for *Schäfertal* and NSE for *Selke*.

basin	measure	default γ	$\gamma \vert Q_{obs}$	$\gamma \vert N_{obs}$ (N_0)	$\gamma \vert N_{obs}$ (COSMIC)
Schäfertal	KGE	0.5	0.91	0.41	
	NSE	0.7	0.83	0.47	
Selke	KGE		0.76	0.33	0.38
	NSE	0.78	0.84	0.46	0.51

Figures 9.4a,b highlight that simultaneous calibration against neutrons and discharge is needed to avoid significant degradation of one of these variables.

9.3.3 Validation of spatial patterns with the CRNS rover

The spatial representation of soil moisture patterns in mHM is evaluated in the *Selke* river basin using CRNS rover surveys along roads on 11 days between August and November 2015 (see chapter 8 for details). As the previous section has elaborated, biomass correction is needed for proper assimilation of neutron data and was thus performed prior to the data analysis. Comparison of neutron counts in individual cells revealed patchy correlations ρ between 0.20 and 0.78 (Fig. 9.5). Although the overall gradient between the Harz mountains (brown) and the lowlands (green) was well captured by both methods, mHM predictions exhibit lower diversity among cells. However, as rover measurements were averaged within the covering cells, typically 1–2 data points were available in most of these 1 km^2 areas. It is thus expected that rover data was prone to local small-scale variability like roads, land use, or forests, which were not represented by the mHM cell average.

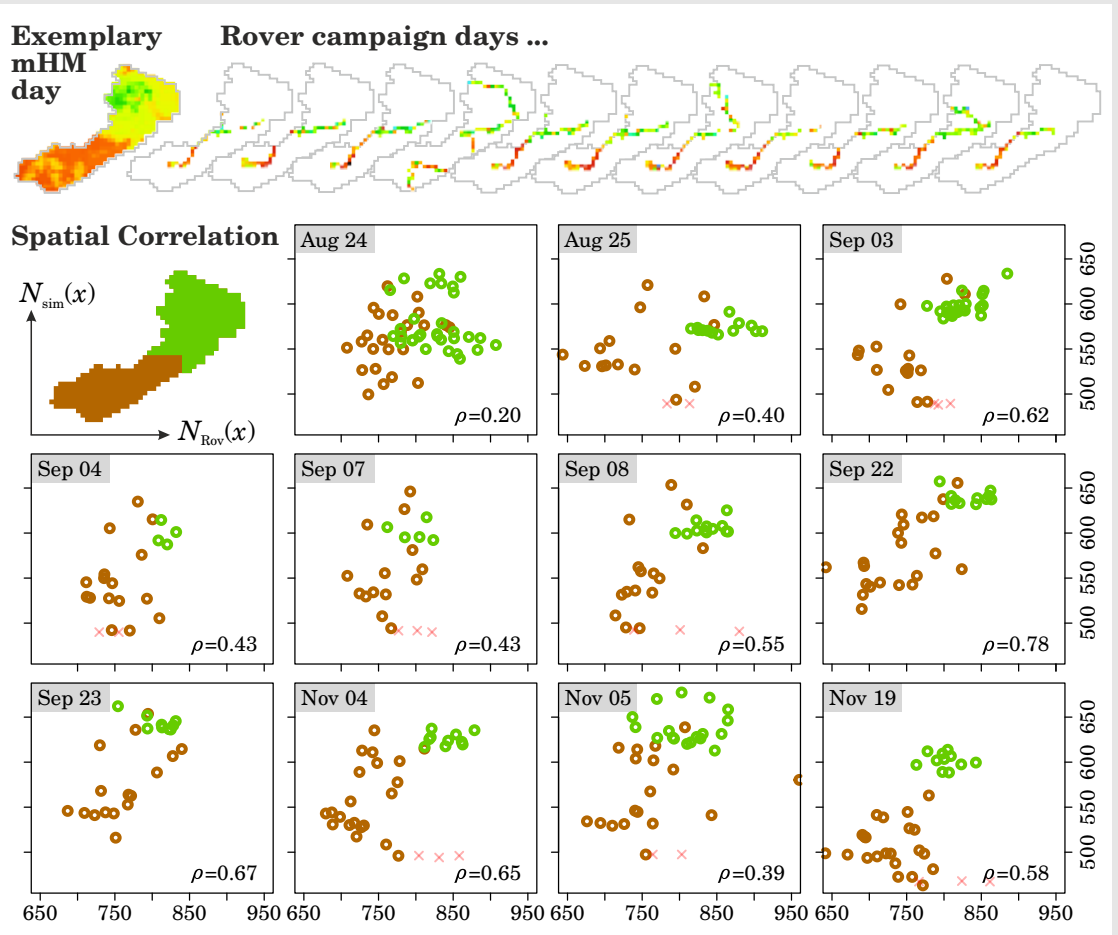

Fig. 9.5: Comparison of $N_{sim}(x)$ [cph] with spatial neutron data from the CRNS rover, $N_{Rov}(x)$ (corrected, rescaled) on 11 days along the *Selke* basin (see chapter 8). Correlations ρ are weakened by local effects (e.g., roads) and biomass representation in mHM (see Fig. 9.6). Three outlying pixels were removed from analysis (red crosses).

Furthermore, the theory of problematic vegetated regions can be supported by investigating the TERENO research sites *Großes Bruch* and *Hohes Holz*. Fig. 9.6 shows that mHM (orange) and CRNS (blue) perform well in pasture and grassland sites, while similar variations have been predicted at a forest site where actual soil moisture (gray) is driven by completely different processes. This analysis indicates that the modeled soil moisture is poorly represented in the *Hohes Holz*, which might be the case also in other forests of the *Selke* basin. Thus, it is not possible to find acceptable agreement between (biomass-corrected) rover observations and mHM, as long as the soil moisture model for forests has not been validated and the observation data exhibits significant uncertainty (see chapter 8).

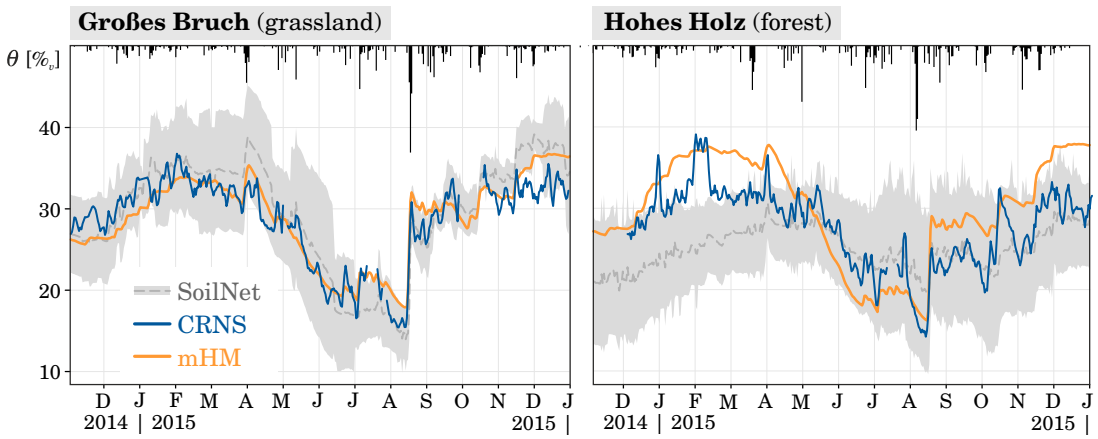

Fig. 9.6: Estimating soil moisture in the pasture site *Großes Bruch* and forest site *Hohes Holz* using SoilNet (grey), stationary CRNS (blue, not corrected for biomass), and mHM (orange). The poor representation of forest soil moisture in mHM might explain poor correlations to the CRNS rover (biomass-corrected) in Fig. 9.5.

9.4. Conclusion & Outlook

To this date, the mesoscale hydrological model mHM has been evaluated mainly on discharge performance, and little is known about the quality of its representation for spatio-temporal soil moisture patterns. This study uses mHM to simulate discharge and soil moisture in the *Schäfertal* catchment (1.6 km^2) and the superior *Selke* river basin (468 km^2), where meso-scale soil moisture data is available from cosmic-ray neutron sensors. Stationary and mobile CRNS data have been acquired to validate and calibrate both, temporal dynamics and spatial patterns of neutrons as a proxy for soil water content. The presented results demonstrate that:

1. mHM is able run at resolutions of 20–100 m in the *Schäfertal* catchment, where its calibrated discharge (Fig. 9.2) outperforms even physically based models like WASIM-ETH and HydroGeoSphere (not shown). However, separate calibration against neutron data (i.e., soil moisture) distorts the discharge dynamics (Fig. 9.4b).

2. Temporal dynamics and absolute soil moisture can be well represented at the mesoscale for non-forest sites (Figures 9.4a and 9.6).
3. Spatial patterns of modeled soil moisture do not sufficiently represent the heterogeneity in the *Schäfertal* (Fig. 9.3, compare also Figures 8 and 8.3), probably due to the lack of lateral flows and reliable soil data. Moreover, model comparison with biomass-corrected CRNS surveys in the *Selke* revealed patchy correlations (Fig. 9.5). As the measurements were conducted during a few hours per day and along official roads, they might under-represent the daily average in the 1 km^2 cells.
4. The neutron forward operators `COSMIC` and the N_0-method both show acceptable performance, depending on the homogeneousness of soil moisture profiles. As `COSMIC` implicitly performs a depth-weighted average, uncared features from biomass growth became more evident (Fig. 9.4a, see also chapter 7).

Further studies should focus on the impact of neutron data to the prediction uncertainty of discharge and soil moisture, for instance, as was done using soil moisture data in `mHM` (Samaniego et al. 2009) or land-surface models (Sutanudjaja et al. 2014). Especially the simultaneous, multi-objective calibration against neutrons N_{obs} and discharge Q_{obs} is a promising strategy to increase the overall performance of the hydrological model. Simultaneously conditioning on observed fluxes and states is a state-of-the-art approach, which is applied by Bergeron et al. (2016), for instance, using streamflow data combined with snow water equivalent.

9.4.1 Improvement of `mHM` and input data

Although `mHM` has proven to adequately predict discharge and soil moisture dynamics in meso- to large-scale catchments all over the world, the following improvements could be made in order to tune the capabilities for absolute soil moisture prediction:

1. tests of different conceptual and physical models for soil water partitioning,
2. implementation of lateral flows between cells for highly resolved regions < 1 km,
3. acquisition of high-resolution precipitation data and soil maps.

9.4.2 Improvement of `COSMIC`

As discussed in section 9.2.2, the `COSMIC` model only accounts for water content in the soil horizons, and is currently not adapted on other hydrogen pools. Further development with regards to hydrological applications should address:

1. Adaption of parameters to spatial data, e.g., θ_{lw}(clay %), $\varrho_{bulk}(\Theta)$, N_{COSMIC}(lat),
2. Implementation of additional water layers for vegetation, snow and their temporal dynamics, e.g., from `MODIS` data and the `mHM` snow model,
3. Improvement of neutron physics according to recent findings about low-energy contributions (chapter 6).

9.4.3 Parameter regionalization

The performance of the neutron prediction in mHM could be improved by regionalizing the parameters γ_N of the nested N_0-method or COSMIC:

$$N_{\text{sim}} = f(\theta_{\text{sim}}, \gamma_N).$$

Calibration of the parameter set γ_N could help to find globally valid correction functions for meteorology and biomass, as has been attempted in chapters 5 and 8, respectively. If the models were able to reliably predict spatial neutron density N_{sim} (validated with the CRNS rover and distributed stations), then these global parameters γ_N might work also in uncalibrated basins. As a consequence, campaign-based measurements of N_{obs} could be taken by the CRNS rover and translated to soil moisture without local calibration:

$$\theta_{\text{obs}} = f^{-1}(N_{\text{obs}}, \gamma_N),$$

given that sufficient land use and morphology data is available. One of the most direct impact will be on the determination of the parameter N_0 (Desilets et al. 2010), which is otherwise obtained only locally by exhaustive and expensive soil sampling campaigns.

This strategy would open the path for feasible on-demand applications of the CRNS rover everywhere on Earth, and simultaneously bridges the gap from local observations to regional predictions.

Fig. 10:
Gyrocopters carrying the double-tube CRS1000 neutron detector. *Credit: Photos by L. Bannehr. Second gyrocopter (sky) inserted by own montage.*

10.

Neutrons on the Fly

Airborne neutron detection with a gyrocopter

Cosmic-ray neutron detectors have been deployed so far on agricultural fields, lakes, towers, sleds, trolleys, and cars, while buried under snow or below ground in historical projects. Common to all approaches is the considerable sensitivity to nearby areas, which has been discovered in chapter 4 and exhaustively investigated in chapters 6–7. In fact, rover campaigns revealed an alarming effect of dry roads (chapter 8) and its impact on hydrological model applications was apparent (chapter 9).

If only CRNS technology could lift up from the ground, local effects would probably smooth out and the issue of inaccessible areas (e.g., during farming activities) might fade into the winds. Moreover, such a technology could further satisfy the hydrologist's thirst, as modelers are demanding large-scale soil moisture observations with deep penetration (see chapter 9) – a requirement that continues to challenge the community of optical remote-sensing. Apart from space satellite missions on other planets, airborne neutron detection for hydrological research has never been conceived.

This chapter ventures the applicability of neutron detection far above the surface. Theoretical investigations and first experiments provide evidence for sufficient sensitivity of airborne neutrons to (sub)surface water. This work opens the path towards further systematic assessment of airborne neutron sensing, which could become a valuable addition – or even an alternative – to conventional remote-sensing products.

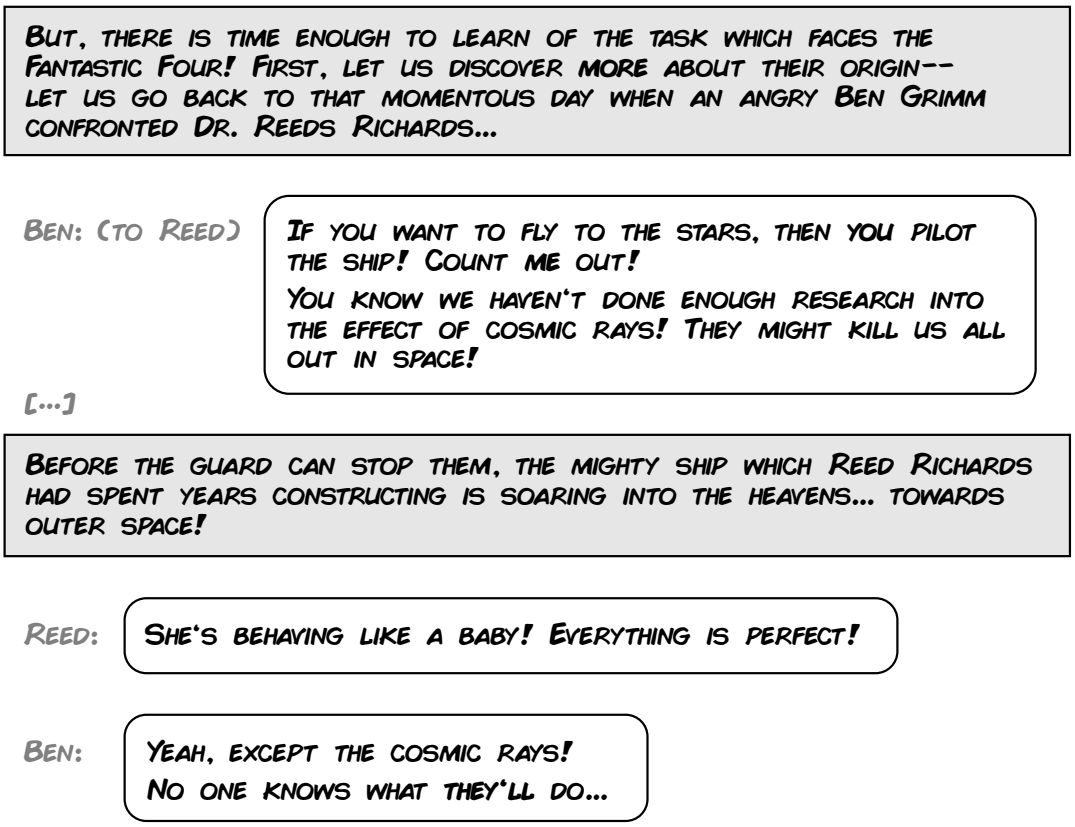

Fig. 10.1: The *Fantastic Four* came in contact with cosmic rays on their first space mission; quoted from "Fantastic Four" Vol. 1, by S. Lee, J. Kirby, G. Klein, and C. Rule (1961), ISSN: 0274-5291, Marvel Comics. (Lee et al. 1961).

10.1. Introduction

Spatial surveys of neutrons can be utilized to estimate small-scale and large-scale patterns of soil moisture (chapters 4, 8). This information is valuable for validation of remote-sensing pixels (Chrisman and Zreda 2013), model verification (chapter 9), hydrologial process understanding (chapter 8), or flood risk assessment. Furthermore, soil moisture information is also relevant for agricultural management. Accessing wet fields with agricultural vehicles can introduce irreversible compaction to the soil. In turn, compacted ground hampers soil aeration and drainage (DLG 2008) which may lead to decreased yield (Dürr et al. 1995). Recently, Zieger et al. (2015) introduced the ArcGIS package CCMOD2 to assess spatial trafficability on the basis of soil moisture estimates, however, validation data is required at all costs.

The major issues with mobile CRNS roving became obvious as rover surveys on roads were compared with TDR data in the field (Fig. 8.3e,f) or assimilated to the hydrological model mHM (chapter 9). The dry bias due to the presence of roads as well

as the problem of inaccessible areas raise the question whether alternatives exist to collect spatial neutron data with mobile aircrafts.

Airborne geophysics is a novel approach to quickly capture landscape structures and states. Siemon et al. (2015) apply gamma-ray surveys on a helicopter to estimate the spatial distribution of soil texture. Height-above-ground correction was applied by simultaneous surveys on the ground and by scanning of the vertical profile locally with the helicopter. Airborne estimation of soil moisture with gamma rays is a research field that has been exhaustively investigated, however, prior knowledge of soil texture is required (see e.g., Carroll 1981; Cline et al. 2009).

Cosmic-ray neutron measurements in the atmosphere have been performed already in early 1950s. Their characteristics in the first 350m above the Earths surface have been revealed for the first time by Hendrick and Edge (1966), using a television antenna tower. They considered soil moisture a nuisance for reliable interpretation of the cosmic neutron signal, but managed to estimate the theoretical characteristics of its influence. Further studies using airborne neutron detection were usually aimed to measure the incoming component of cosmic rays at higher altitudes. For example, Carmichael et al. (1969) carried mobile neutron monitors at heights beyond 3000 m, while Goldhagen et al. (2004) conducted surveys of neutron spectrometry on an air plane at various altitudes and latitudes.

Remotely sensed hydrogen content by reflected neutron radiation is a state-of-the-art technology in space and planetary sciences. While first evidence of water on Mars has been measured by neutron detectors on satellites (Mitrofanov et al. 2002), recent developments tend to improve the spatial resolution. The so-called *Neutron Fine Resolution Epithermal Neutron Detector* (FREND) is one of those new instruments that will measure neutron energies ranging from thermal up to 10 MeV. The detector is shielded to all sides with the exception of a thin opening angle in the nadir direction. Using this configuration, the instrument is able to observe Martian surface water down to 1 m depth at a horizontal resolution of ≈ 40 km (Mitrofanov et al. 2016). Moreover, remotely sensed thermal neutrons were also used to infer iron and carbon abundance in the first meters below Mercury's surface (Lawrence et al. 2010; Peplowski et al. 2016).

Back on Earth, ultra-lightweight air planes, so-called *gyrocopters*, have been applied recently to monitor plant activity (Calviño-Cancela et al. 2014) and atmospheric parameters, or to perform geographical imaging (Bannehr et al. 2015).

This chapter assesses the feasibility of airborne neutron detection as a proxy for (sub)surface water, by investigating the theoretical effects of altitude with the neutron transport code URANOS (see chapter 6). First experimental tests were conducted with a detector mounted in a gyrocopter in order to proof the concept of airborne neutron sensing.

10.2. Materials & Methods

Neutron transport simulations were performed with the URANOS software (Köhli et al. 2015), using detector layers at different heights above the ground. For the experimental verification a modified CRNS detector system is mounted inside a gyrocopter, which is applied and developed by the Hochschule Anhalt (Bannehr et al. 2015). These lightweight aircrafts make use of wind streams that are generated by a

small trailing propeller. This induces rotation of a larger propeller that requires a continuous airstrip during forward motion. The special technology of gyrocopters allows to conduct experiments at low fares, however, continuous motion and high operational altitude is required during the flight.

As weak signals from the soil were expected in 200 m height, two moderated tubes have been assembled from two CRNS probes (CRS09 and CRS04) in order to double the count rate of conventional stationary detectors. Together with a datalogger, T/RH measurement component, GPS, and a small battery, this mobile system is completely autonomous during flights. One of the major advantages of airborne neutron sensing, compared to other airborne sensors, is the arbitrary positioning of the system within the aircraft. No viewing angle or hole in the case is required, for neutrons are almost insensitive to anything but hydrogen.

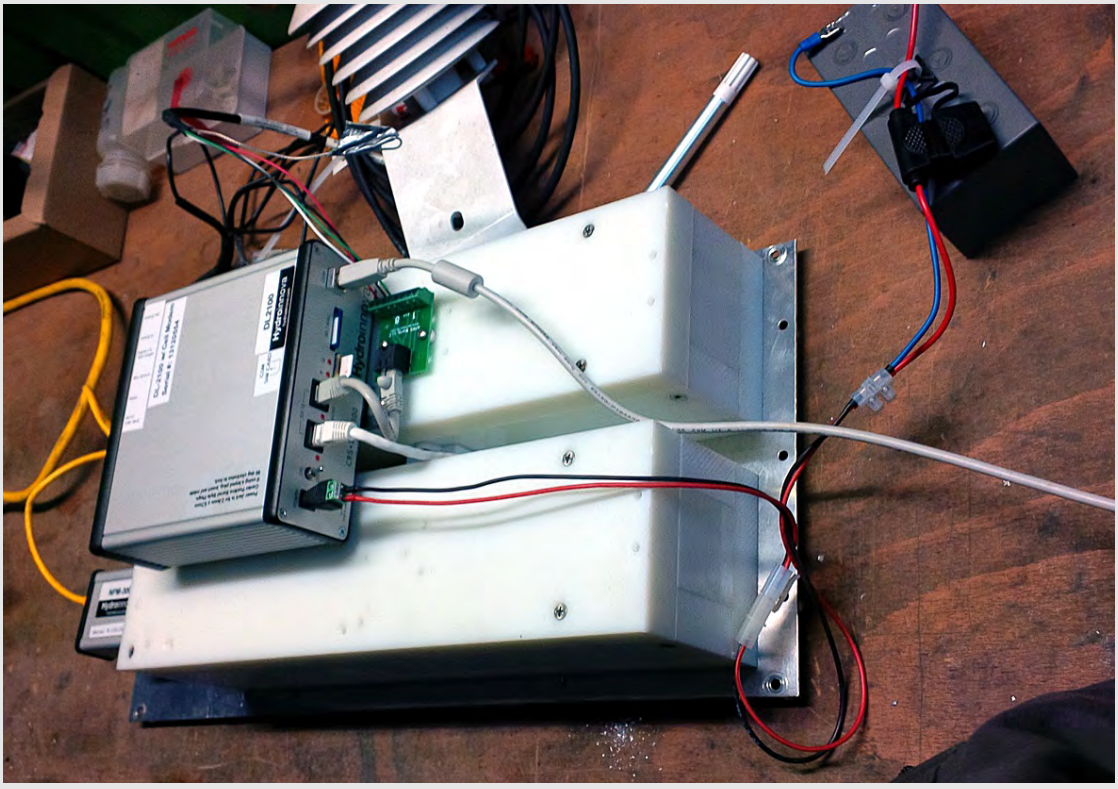

Fig. 10.2: Double-tube detector system assembled from two CRS1000.

The experimental site is the *Elbe* and *Mulde* river network around Dessau and Roßlau in central Germany. The flight path of the gyrocopter has been scheduled to visit eight parts of various land use types in the study area, while three parts were intensively observed by narrow circles over a 10-minutes period. During the 2-hour flight, ground-truth measurements were conducted with the CRNS rover in accessible areas of the city of Dessau, the *Elbe* flood plain, agricultural sites, and a forest. At three locations several TDR measurements were taken in the first 12 cm of the soil and averaged to a single value (see Fig. 10.7).

10.2.1 Correction for height above ground

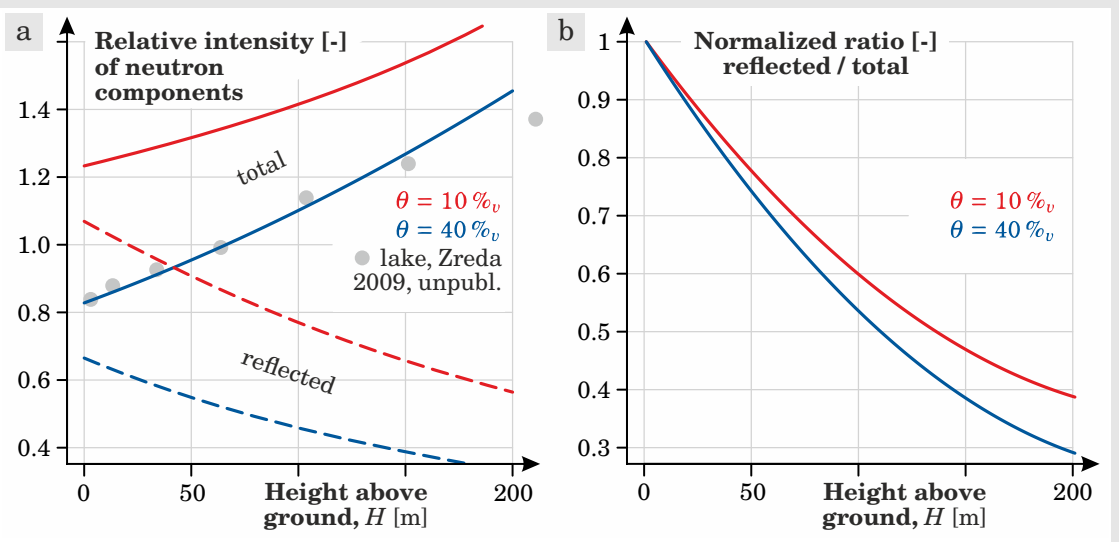

Fig. 10.3: Variation of neutron counts with height above ground H, simulated with URANOS (by M. Köhli). a While total neutron intensity increases, the number of ground reflected neutrons decreases relative to the ground. Measurements with a Helicopter over a lake agree well with simulations (Zreda et al., unpubl.). b The ratio of reflected over total neutrons, normalised to the ground ratio of 0.84 .

Consider the flying detector at one specific location with constant soil water content beneath. Neutron transport simulations show that the number of total neutrons N increases as the height above ground H increases (Fig. 10.3). Therefore, it is suggested to correct down the total count rate, $N_H = N \cdot C(H)$, with the height-dependent correction factor

$$C(H) = \left(1 + 0.002 \cdot H + 0.000004 \cdot H^2\right)^{-1}$$

This first-order approach was fitted against simulations for $\theta = 20\,\%_v$, however it supports two different observations. Firstly, the analytical prediction agrees well with data from Zreda et al. (unpubl.), who surveyed the height profile over Twin Lakes (CO) with a helicopter in August 2009 (Fig. 10.3a). Secondly, the count rate over *Gremminer See* during the airborne campaign was approximately 1158 cph at $H = 117\,\text{m}$. Using $N \cdot C(H = 117) \approx 899\,\text{cph}$, we arrive at a count rate which was typical for a CRNS campaign conducted with a buoy detector (single tube) on a neighboring lake (see chapter 5).

Conversion to soil moisture, $\theta(N_H)$, is beyond the scope of this work, because the corrected count rate N_H contains a different fraction of reflected neutrons compared to ground conditions. Thus, the ground-based relation $(N, N_0) \mapsto \theta$ from Desilets et al. (2010), which maps a given change of N to a change of θ, is not valid anymore. At larger heights H, a change of soil moisture would have much less impact on N_H compared to near-surface neutrons. Further research should investigate this behavior in detail and elaborate a new conversion function $\theta(N_H)$ for airborne neutron sensing.

N_H has been corrected by a simple approximation which cannot be applied accurately without prior knowledge of the soil moisture conditions. However, this first-order approach has proven to be beneficial for this work, as it helped to improve the interpretation of the first airborne neutron detection system.

10.3. Results & Discussion

Neutron simulations at various heights above ground provide evidence for increasing neutron intensity N. This is in perfect agreement with theoretical and experimental findings from various authors (Goldhagen et al. 2004; Kowatari et al. 2005; Sato 2015), and agrees well with CRNS measurements on a Helicopter above a lake (M. Zreda 2009, unpublished). However, Fig. 10.3 reveals a tremendous decrease of the soil-reflected component, N_{refl}, because the neutrons quickly thermalize on their way through the air. At heights of $H = 200$ m only 30–40 % of the total detected neutrons originated in the ground, where absolute variations of 30 $\%_v$ soil moisture translate to only 10 % variation of the neutron signal.

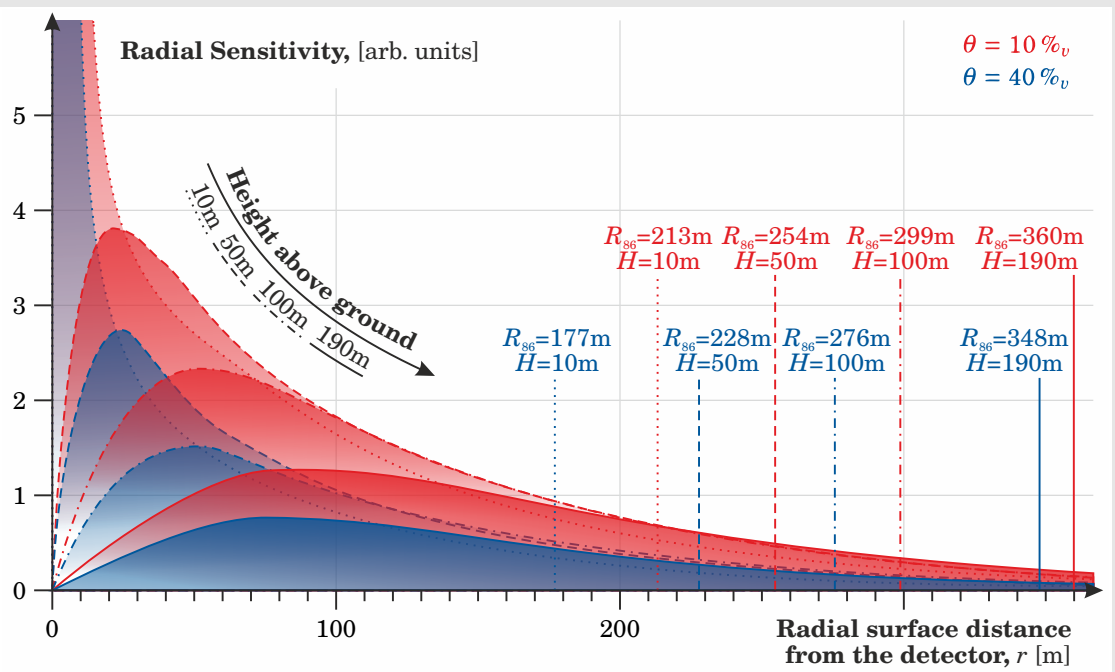

Fig. 10.4: Radial sensitivity dN/dr of the CRNS method over distance r to the sensor (compare Fig. 7.2), exemplary for two different soil moisture conditions θ, and four heights above ground H. With increasing altitude the area of highest sensitivity broadens tremendously and the footprint radius R_{86} increases. Simulations have been performed by M. Köhli using the URANOS Monte-Carlo code (section 3.8).

An interesting improvement, however, is revealed for the radial sensitivity function $W_r(h, \theta)$ at increasing altitudes. Fig. 10.4 indicates that the gigantic rise in $W_{r\to 0}$ is actually a peak that smoothes out and moves towards higher radii as H increases (compare also Fig. 7). Neutrons leaving the soil spread almost diffusively in air and can reach the aircraft at greater horizontal distances. As a consequence, ring sources at certain radii can dominate over both, small ring intensities ($r \to 0$) and long-distant neutrons ($r \to \infty$). This property further increases the integral sensor footprint, which almost doubles at $H = 200$ m under wet conditions.

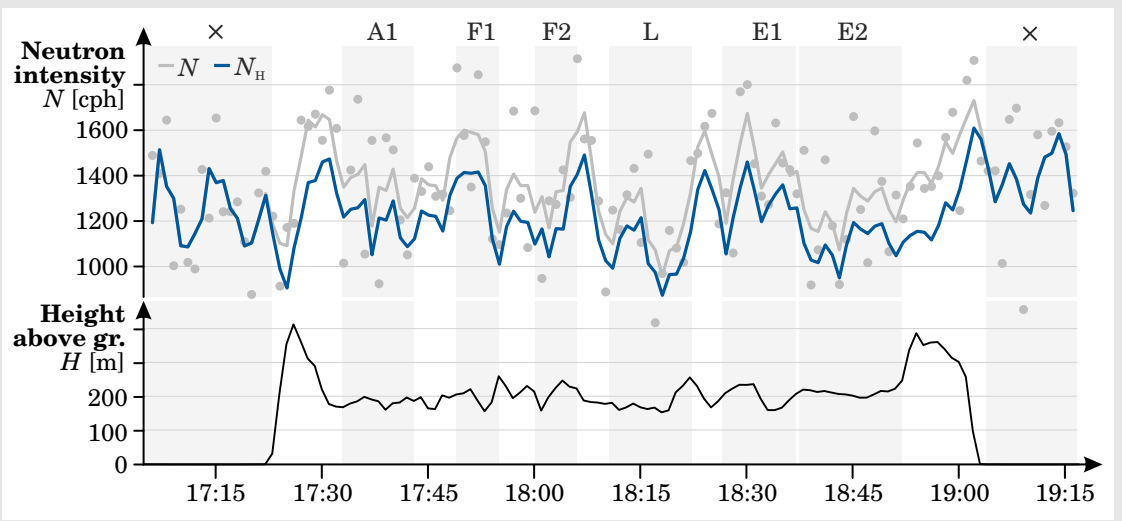

Fig. 10.5: Time series of the gyrocopter campaign, showing neutron counts as 1-min (points) and 3-min moving average (lines), conventionally corrected (grey) and height-corrected (blue), and the height above the ground surface (black). Highlighted are parts of the region which the aircraft passed or circled over. The statistical error is $\epsilon(N) = 30$–40 cph, fluctuations at the airport (×) result from fluctuating scientists, and the height correction is untrustworthy for $H > 200$ m.

10.3.1 Experimental evidence

The neutron count rate of the double-detector varies around $\approx$ 1300 cph, which corresponds to a statistical error of $\epsilon(N) \approx 36$ cph. Thus, the theoretically expected signal variation of 10 % (four standard deviations) between dry and wet soil should be well detectable by the airborne neutron sensor. Fluctuations at the airport may be due to the very close presence of scientists (Desilets et al. 2007) during mounting and unmounting of the devices.

Fig. 10.5 shows the time series of the gyrocopter campaign corrected for air pressure, air humidity, incoming radiation (grey), and additionally corrected for height above ground (blue) using the linear approximation of $C(H)$. While the signal drop over the lake (L) by $\approx$ 300 cph (25%) is significant, similar drops over land and remaining features of the altitude variations indicate room for improvement concerning the simple height correction approach, which is beyond the scope of this work.

The spatial distribution of measurements is illustrated in Fig. 10.7, showing TDR, rover, and gyrocopter observations across 8 parts of various land use. The most prominent feature is the low neutron count rate over the lake *Gremminer See*, where the gyrocopter circled for 10 minutes at a maximum distance of 250 m from the shoreline. Still, the 10 observations exhibited not entirely low count rates (blue) and rather fluctuate randomly up to even dryer values. This behavior can be explained by the larger footprint and the sensitivity maximum at about 80m (Fig. 10.4), such that the major part of neutrons did not originate from the zero nadir angle below the aircraft.

Comparison with the ground-truthing data demonstrates that the gyrocopter, rover, and TDR are able to capture the wet flood plains of the *Elbe* river. Interestingly, the forest appears rather dry for the TDR and the aircraft, although the rover signal is influenced by the wet biomass. This detail, together with evidence from neutron simulations (not shown) indicate that airborne detected neutrons may originate from deeper soil horizons and are less sensitive to biomass. The elevated height above ground could be an explanation for this effect, because detected neutrons require high initial energies to successfully pass the huge amount of air on their way to the aircraft. Neutrons of higher energy, however, were able to penetrate the soil deeper, and are less sensitive to hydrogen (see neutron cross sections, Fig. 3.2), particularly in the low-density domain above surface.

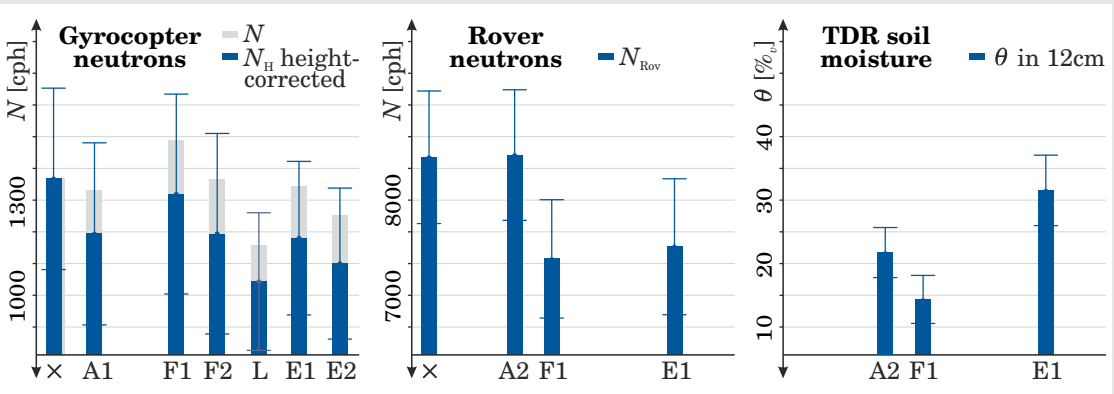

Fig. 10.6: Gyrocopter, rover, and TDR measurements compared for all 8 parts, averaged over the individual overflying periods (see shading in Fig. 10.5). According to TDR the forest F1 is dryer than the agricultural field A1. This relation is inverse for the rover neutrons due to the influence of the biomass. However, the gyrocopter confirms the TDR observation, indicating that biomass has less influence on flying detectors. This interpretation is also supported by the soil of the flood plain E1 which is wetter than the agricultural fields for all three methods.

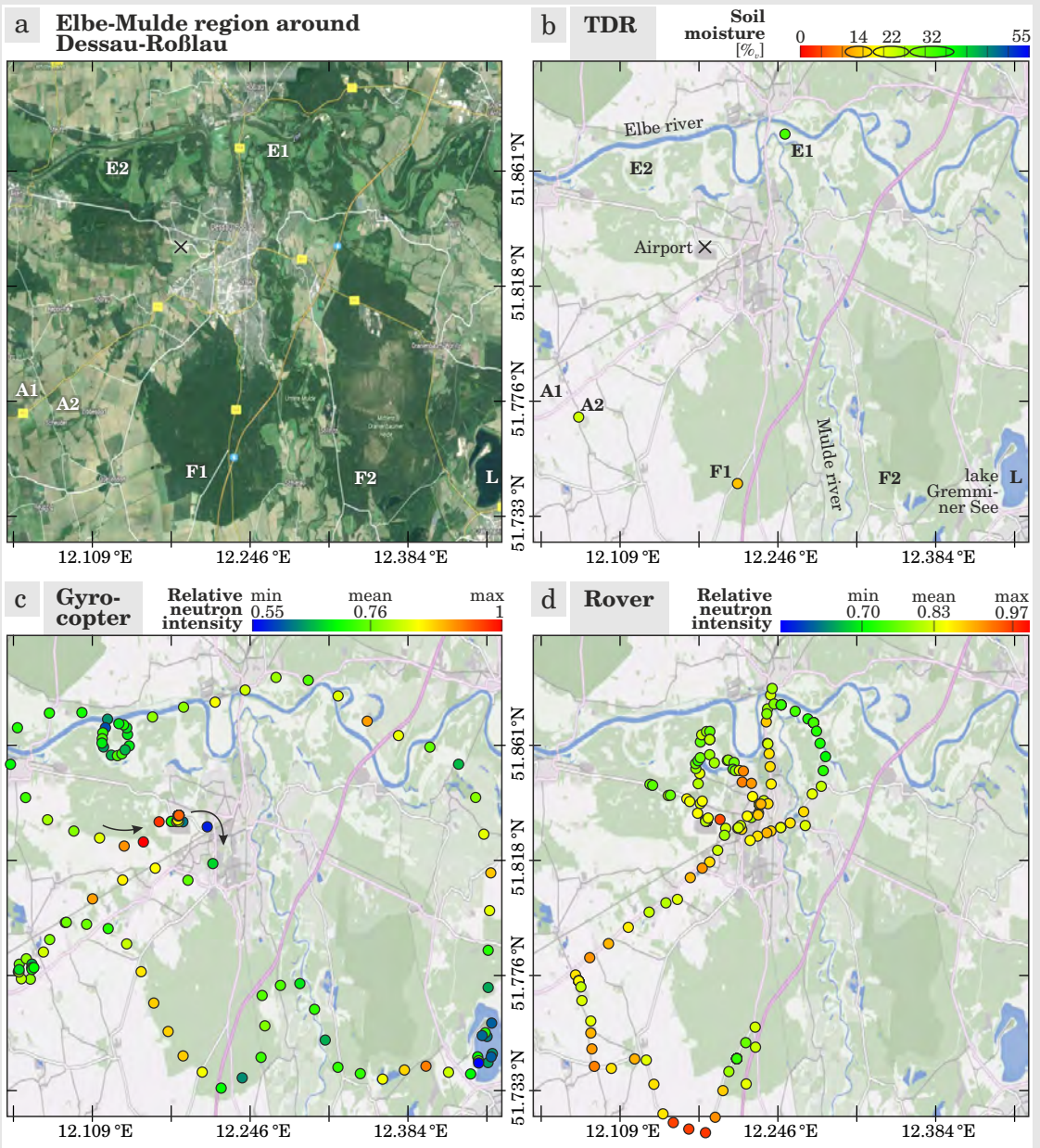

Fig. 10.7: Measurements in the *Elbe-Mulde* region. a Prominent parts contain agricultural fields, A, flood plains around the *Elbe*, E, forests F around the *Mulde* flood plain, and the lake *Gremminer See*, L. b TDR measurements taken near parts A2, F1, E1; each of which were averaged over 3–6 locations per part in the first 12 cm. c Height-corrected gyrocopter neutrons $N_H / \max(N_H)$, 3 min moving average, passing all prominent parts. d Rover neutrons $N_{\mathrm{Rov}}/10^4$, 3 min moving average, passing only parts E1, A2, F1. *Credit: Backgrounds by Google Maps*

10.3.2 Could rotor blades distort air pressure?

Air pressure measurements are important for the signal correction to properly account for the mass of the air column above the detector that attenuates neutrons (see 3.5.2). However, the datalogger samples air pressure inside the cabine, below the rotor screws. It is therefore advisable to estimate the impact of the *Bernoulli effect*, which describes local pressure reduction by fast moving air, as has been done in neutron monitor research (Bütikofer 1999; Abunin et al. 2016).

Assuming that the typical flight speed v varies between 20 and 30 m/s, and the mean air pressure at the day of the campaign was $\approx$ 990 hPa, then the potential variation of the count rate, δN, can be estimated from δv:

$$\begin{aligned} \delta v &= 20..30\,\mathrm{m/s} \\ \Rightarrow \delta p &= \frac{1}{2}\varrho_{\mathrm{air}} v^2 \Big|_{\delta v} \approx 3\,\mathrm{hPa}, \quad \text{(Bernoulli)} \\ \Rightarrow \delta N &= \langle N \rangle \cdot e^{\beta(p-p_{\mathrm{ref}})} \Big|_{\delta p} \approx 23\,\mathrm{cph}\,. \end{aligned}$$

The underestimation of air pressure by 3 hPa can lead to variations of N by 23 cph, which is below the average standard deviation $\sigma(N) \approx 34$ cph during the campaign. We therefore conclude that the *Bernoulli effect* in gyrocopters is probably a minor source of error for the analysis of airborne CRNS data.

10.3.3 Accuracy decreases with altitude

Figure 10.3b clearly illustrates that relative contribution of reflected neutrons N_{refl} (i.e., information from the soil) decreases rapidly with elevation. This leads to the question whether bigger detectors are needed to preserve the accuracy of neutron detection at the ground. As known from section 3.7, the relative error of counting measurements is $\sqrt{N}/N = 1/\sqrt{N}$. However, it is advisable to consider the actual component N_{refl} in this calculation in order to precisely address the error for the quantity of interest:

$$\epsilon_{\mathrm{rel}} = \frac{\sqrt{N}}{N_{\mathrm{refl}}} \approx \frac{\sqrt{N}}{0.84N} \approx 1.2\frac{1}{\sqrt{N}},$$

where on average $N_{\mathrm{refl}}/N \approx 84\,\%$ at the ground surface (Fig. 10.3). Normalized to this value, the relative error for altitudes $H = 200$ m can be estimated, using data from Fig. 10.3:

$$\begin{aligned} \text{wet:} \quad \epsilon_{\mathrm{rel}}(H = 200) &\approx \frac{\sqrt{1.74N}}{0.24N} \approx 4.4 \cdot \epsilon_{\mathrm{rel}}\,, \\ \text{dry:} \quad \epsilon_{\mathrm{rel}}(H = 200) &\approx \frac{\sqrt{1.4N}}{0.33N} \approx 3.1 \cdot \epsilon_{\mathrm{rel}}. \end{aligned}$$

In order to compensate for the increased relative error, the total counting rate N should increase by factors of $4.4^2 \approx 19.4$ and $3.1^2 \approx 9.6$. Following this rough calculation, the appropriate detector volume for 200 m altitude missions should be a factor of 19.4 larger than ground detectors if comparable accuracy is desired. We consider this a major challenge for future campaigns using airborne neutron sensing.

10.4. Conclusion & Outlook

This chapter has discussed the potential of airborne neutron detection for environmental research. In a theoretical study, evidence for an increased footprint and a more representative smoothing of the same has been gained. Thus, the method could circumvent major issues of ground-based mobile neutron sensing, e.g., inaccessible areas and the dry road bias. Those effects have shown to be problematic for interpretation, validation and assimilation to models (compare chapters 8 and 9).

First experiments with a gyrocopter aircraft were conducted to test the presented concept. The observed neutron intensities were sensitive to soil water content in various land use types, and showed reasonable agreement with ground-truth data. Further theoretical and experimental results indicated even deeper representation of soil horizons, and lower sensitivity to above-ground biomass.

Compared to the mobile CRNS rover (chapter 8), airborne CRNS is able to cover areas of much larger extent in a short period of time and could thus be valuable, for instance, to assess flood risk on-demand.

The major challenge of airborne neutron sensing is the decreasing intensity of the soil signal (Fig. 10.3). Further research is needed to better understand the altitude correction C_H and to ideally remove the incoming component from the signal. For example, by shielding neutrons from most directions, Mitrofanov et al. (2016) were able to filter out the incoming component and increased the spatial surface resolution of neutron sensors on planetary space missions. Generally, additional detectors (larger size, lower weight) are recommended for any airborne campaign to increase the count rate and decrease its uncertainty.

Technical disadvantages of the gyrocopter solution are the requirement for high velocities and high operating altitudes > 150 m due to safety reasons. Alternative aircraft systems may or may not serve as satisfactory candidates for future airborne CRNS missions:

1. **Helicopters:** low speed (even hold-up), low operating altitudes, very expensive fares, frequently used for airborne geophysics.
2. **Light planes:** much less prone to turbulence and vibration than gyrocopters, plastic bodywork could further contribute to neutron moderation, typical movement velocities of ≈ 2 km/min, often used for airborne remote-sensing.
3. **Balloons:** low speed and low operating altitudes, often used for high-altitude missions.
4. **Robotic drones:** agile carriers of small amount of load (maximum of 5 kg in Germany), probably not enough to carry neutron detectors of appropriate size.

Apart from the instrumental potential, improvement of data interpretation could be achieved with supporting instrumentation mounted on the same aircraft, e.g., optical DEM, LIDAR, or infrared methods. Detailed ground-truthing campaigns are further recommended, e.g., using the CRNS rover or *Wireless Sensor Networks* (Bumberger et al. 2015). The latter could be installed on-demand at meaningful spots within the survey area to measure soil moisture at various depths, and thus would be a valuable support for airborne CRNS missions.

Final Conclusion

The continual growth of the Earth's population entail an increased demand for food security and water availability, while the gradual changes of the climate involve the risk of water scarcity, floods and droughts. Therefore, the next years will bring immediate challenges for the society such as sustainable agricultural management, adaption on climate and land use change, and improved forecasting capabilities.

Chapter 1 has made the case for the requirement of representative soil moisture observations across scales to support model predictions, precision farming, and decision making. Cosmic-ray neutron sensing (CRNS) appeared to be one of the few methods that are capable of providing representative data at relevant horizontal and vertical scales. This dissertation explored the methodological background of the young research field of CRNS for environmental purposes, and ventured new steps towards hydrological modeling applications and airborne neutron sensing.

Chapter 2 has described the origin of the permanent and omnipresent cosmic radiation and has noted remarkable spatial variations, as well as temporal variations from hours to decades that need to be accounted for. The unique nature of neutrons has been presented in chapter 3, where it is further argued that the detection of the reflected component in air is indeed a promising strategy to infer water content of the soil, but special care should be taken of the influence of additional hydrogen sources in the environment.

In chapter 4 the sensor technology has been tested for the first time during a systematic intercomparison, where the need for an efficiency calibration has been revealed. These findings impacted the production lines of CRNS detectors, which are now calibrated prior to shipping. Moreover, unexplained temporal variations have raised the question whether the accepted correction functions for air pressure, air humidity, and incoming radiation are valid for all sites. These questions were addressed in chapter 5, where a neutron detector has been installed on a lake to reveal correlations to incoming variations without a soil moisture signal. And indeed, the analysis has indicated that conventional correction methods are deficient, while reference stations of neutron monitors should be selected carefully. Future studies are required to accurately quantify the corresponding impact on field applications.

Since small-scale variability within the conventional footprint of ~ 30 ha has been revealed in chapter 4, neutron transport simulations have been consulted to assess the footprint characteristics. By summarizing the published results from Köhli et al. (2015), chapter 6 showed that model assumptions of previous studies required significant revision, which resulted in a reduction of the footprint radius to 6–18 ha and revealed enormous sensitivity to the first meters around the sensor. These findings have been confirmed empirically, while their impact on sensor calibration, validation, and data interpretation was demonstrated in chapter 7.

The presented strategies to deal with the revised footprint characteristics opened the path for mobile applications. The CRNS rover has been applied in chapter 8 to estimate spatial soil moisture patterns in two catchments of 1.6 km^2 and 468 km^2 area. While the rover was able to reveal small-scale variability that could improve hydrological process understanding, special care should be taken of an enormous bias introduced by vegetation or dry roads. However, with the help of a proper spatial correction strategy presented here, the CRNS rover is able to deliver spatial soil moisture products across scales and land use types.

The integration of these spatial neutron surveys into the hydrological model `mHM` (chapter 9) demonstrated that the local effects in the data may indeed hinder appropriate representation of spatial soil moisture patterns at the 1 km^2 scale. Nevertheless, stationary neutron time series have shown remarkable agreement with `mHM` and thus can be beneficial to support hydrological models in the future.

Finally, chapter 10 has ventured the step towards airborne neutron sensing, which could solve the problem of local road effects, representative footprints, and inaccessible areas. While first studies with a gyrocopter provided a proof of concept, future studies will show whether soil moisture can be estimated to a sufficient accuracy by this method.

This dissertation revealed limitations and explored new potential of the CRNS method. For example, the analytical formulation of the footprint sensitivity adds certainty to the methodology, which is necessary for proper data interpretation, calibration, and validation. Furthermore, the added understanding of the detector sensitivity opens the path for improved and more accurate performance of the CRNS technology in the new field of hydrogeophysics. However, much is to be learned from related research fields like detector physics, particle physics, and remote-sensing, in order to fully understand and tailor the method to the needs of environmental applications. By bridging the gaps between scales and disciplines, cosmic-ray neutron sensing has been established as a unique technique that is employable for a wide range of applications. Finally there is hope that the intensive research of the last decade will pay off in the near future, so that the society can directly or indirectly benefit from this fascinating approach to monitor the hydrological cycle.

Fig. 11:
Surveying spatial patterns of neutrons (inside rover) and natural gamma rays (trailing sled) in the *Schäfertal*.

APPENDIX

A.

Decision between detector gases ^3He and BF_3

Table A.1: Confrontation between ^3He and BF_3, based on literature and specifications from Hydroinnova, collected in February 2014.

	Helium-3	Boron trifuoride
Cost	19–27 k$	15–22 k$
Delivery delay	6 months	2 months
Power consumption	≈ 100 mA, high voltage requirement	≈ 200 mA, slightly lower voltage requirement
Dimensions	80x30x20 cm, 15 kg	120x60x30 cm, 17 kg
Safety	harmless	toxic
Moisture protection	acceptable	much better
Neutron counts	100 %	75 %
Gamma discrimination	noise possible	almost perfect
Energy range	slightly larger than thermal	thermal only
Pulse height spectrum	broad peaks, eventually wall effects	narrow peaks
Extendible	yes	yes
Vibration	acceptable	slightly less sensitive
Lifetime near active radiators	$> 10^3$ years	≈ 20 years

Is BF_3 well suited for German safety regulations?

Although boron trifluoride is much cheaper than ^{3}He, it is a highly toxic gas and its concentration must not exceed a certain limit according to German safety regulations. With the help of some specifications from Hydroinnova, a rough calculation may help to estimate an approximate value for the BF_3 concentration.

Given a tube with diameter $d = 5.08\,\text{cm} \Rightarrow r = d/2 = 0.0254\,\text{m}$ and length is $L = 84.8\,\text{cm} \Rightarrow$ tube height $h = 0.848\,\text{m}$. Then,

$$\text{tube volume:} \quad V = \pi r^2 \cdot h = 0.00172\,\text{m}^3\,.$$

Gas pressure in the tube is $p = 0.6\,\text{atm}$ at $T = 25\,^\circ\text{C}$, where $1\,\text{atm} = 101325\,\text{Pa}$.

$$\text{pressure:} \quad p = 60795\,\text{Pa} \quad \text{at} \quad T = 298\,\text{K}\,.$$

Since pV/T is constant for an ideal gas, the *ideal gas law* provides a good approximation for the mass m of the detector gas:

$$\text{ideal gas law:} \quad \frac{p \cdot V}{T} = m \cdot R_s\,,$$

where $R_s = R/M$ is the specific gas constant, $M = 0.06782\,\text{kg/mol}$ is the molar mass of BF_3, and $R = 8.31446\,\text{J/mol/K}$. Deviations from the ideality may occur due to:

- 4% of the detector gas is actually $^{11}BF_3$, while 96% is $^{10}BF_3$,
- additional degrees of freedom of the 4-atomic molecule $\Rightarrow$ factor ≈ 2.

The absolute mass m of BF_3 contained in the tube then is (ideally):

$$m = \frac{p \cdot V}{T \cdot R} \cdot M\,, \quad \text{units:} \quad \left[\frac{\text{Pa} \cdot \text{m}^3}{\text{K} \cdot \text{J/mol/K}} \cdot \text{kg/mol}\right] = \left[\frac{\text{kg/m/s}^2 \cdot \text{m}^3}{\text{kg} \cdot \text{m}^2/\text{s}^2} \cdot \text{kg}\right] = [\text{kg}]$$

$$\Rightarrow \quad m \approx \frac{10^4 \cdot 10^{-3}}{10^2 \cdot 10^0} \cdot 10^{-2} = 10^{-3}\,\text{kg},$$

$$\text{or} \quad m = 2.86\,\text{g of } BF_3 \text{ in a single tube.} \tag{A.1}$$

Since the limit "maximum workplace concentration" by law in Germany was reported to be about $2.5\,\text{mg/m}^3$ in 2014, the exceeding factor is of the order of 10^3 if only one tube is used within a cubic meter (however, more are scheduled). Although, the boron gas is under low pressure and covered with stainless-steel and aluminum, serious security measures can be expected for the handling of these detectors (e.g., in terms of risk assessment and accident protection).

B.

Correction for load effects on pulse height spectra

A low-pass filter damps out full-load voltage

During operation of CRNS probes in *Schäfertal* several sensors produced unusual pulse height spectra (PHS). As a consequence, the count rates became dramatically excessive. The behaviour started at the day when the solar panel, charger, and battery were replaced by more powerful components. This "improvement" solved long lasting issues of power supply for those sensors, however, their count rate and PHS changed from that day on (see Fig. B.1a).

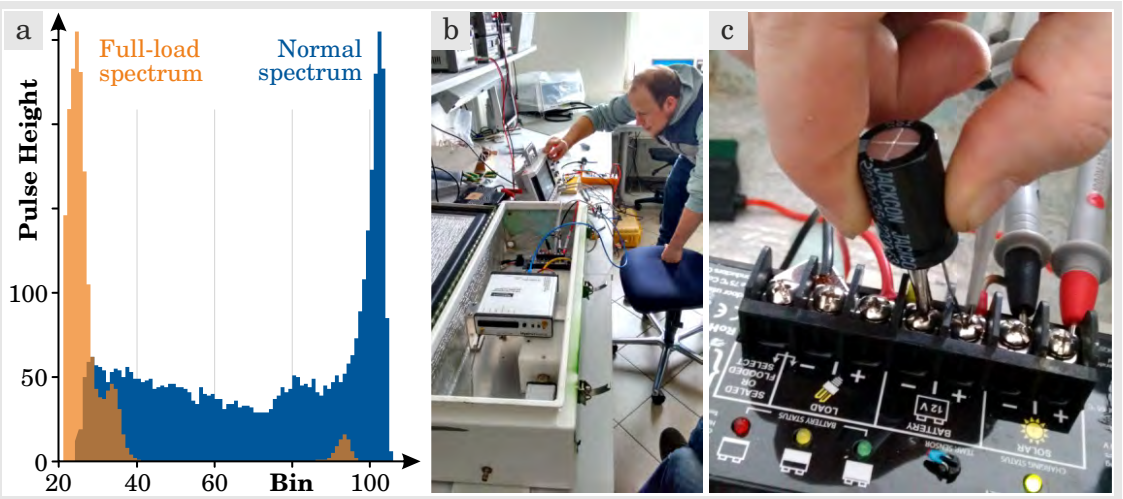

Fig. B.1: a A fully loaded battery produces abnormal pulse height spectra and thus pseudo-neutron counts. b Using an oscilloscope, high-voltage/high-frequency output from the solar charger has been identified as the error source. c First tests with a 2.2 mF resistance showed that the parasitic frequencies can be attenuated.

By default the battery supplies a voltage of 12–14 V to the data logger, which is then redirected to the neutron pulse module (NPM). However, under full-load conditions the excrescent solar energy is rejected by the charger, resulting in high-frequency ripples of the supply voltage with spikes up to 19–20 V at ≈ 300 Hz . Tests with different types of solar chargers confirmed that this behaviour is a general issue. Old NPMs which were shipped by `Hydroinnova` before 2012 cannot deal with these ripples and consequently produce abnormally high voltage spikes in the detector tube. As a consequence, the count rate gets abnormally high, the counter LED is permanently flashing, and a prominent peak in the PHS elaborates around bin #20.

The manufacturer of the NPMs, `Quaesta Instruments`, suggested to adjust the NPM parameters in order to deal with this abnormal voltage input (i.e., increasing high-voltage, command `HV1`, to 1100–1200, and decreasing gain, command `gain1`, to 1.5–2.5). This procedure requires in-situ communication with the datalogger while the *trial-and-error* approach is time consuming and highly uncertain.

As an alternative, a tailor-made low-pass filter has been developed in the course of this research project. Using two capacitors and a coil, the parasitic frequencies can be damped out completely as demonstrated in Fig. B.2, resulting in full restoration of the PHS. An additional suppressor diode avoids excess voltage above 22 V. The DC resistance for the coil has been chosen to be fairly high at 1.91 Ω in order to limit the charge rate of the capacitors. However, simulations showed that currents can generally be expected below 5 A, such that lower resistances could be sufficient, too. The supply voltage depends on the resistance ratio between coil and CRNS due to their serial connection, and thus varies slightly with changing power consumption. A minimal coil resistance is advantageous in this system and could potentially reduce the observed voltage drop of ≈ 0.2 ± 0.1 V (see Fig. B.2b).

Table B.1: Components selected for the CRNS low-pass filter.

component	type	specification
capacitors	`Würth`	25 V, 2.2 mF
coil	`Mundorf` MCoil Luftspule	1 mm, 10 mH, 1.91 Ω
diode	`TVS` suppressor diode	22 V

The second generation of the low-pass filter, which is currently under development, aims to reduce the voltage drop of 0.2 V by halving the coil resistance to ≈ 1 Ω. As a consequence of $U = R \cdot I$, the charging rate $\mathrm{d}I/\mathrm{d}t$ of the capacitors would increase, which can lead to an inductive excess voltage during startup following $U(t) = L \cdot \mathrm{d}I/\mathrm{d}t$. This effect can be compensated by halving the coil inductance L and duplicating the number of capacitors C, which simultaneously keeps the cutoff-frequency of the low-pass filter constant:

$$f_{\mathrm{cut}} = \frac{1}{2\pi\sqrt{L \cdot C}} \approx 24\,\mathrm{Hz}\,.$$

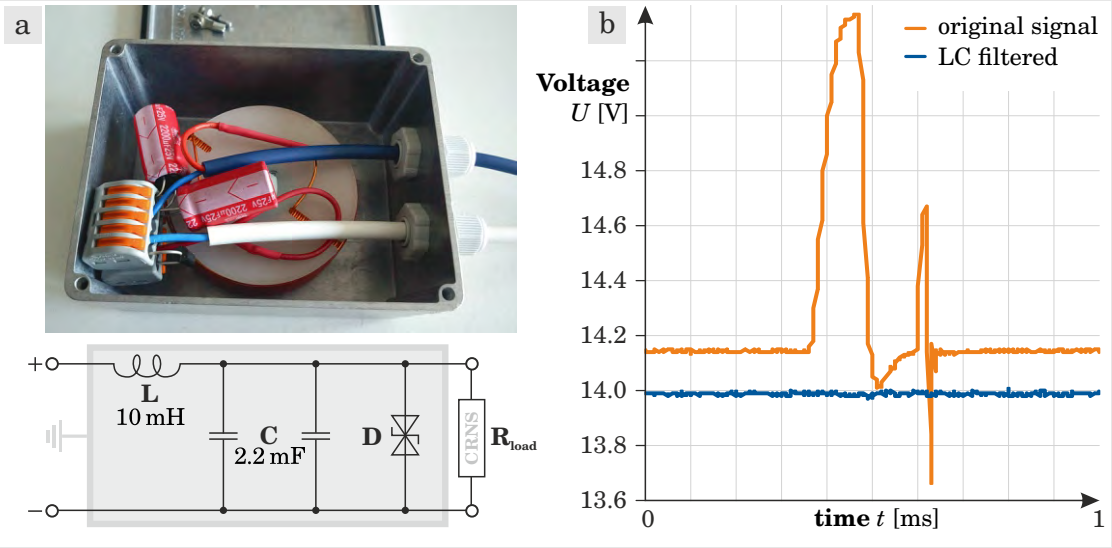

Fig. B.2: a Design of the low-pass filter between CRNS and battery. b High-voltage/high-frequency signal distortion with a period of 3.38 ms (≈ 300 Hz) under test conditions with ≈ 25 W (the solar panel could potentially serve 100 W). The filtered signal (blue) completely damps frequencies above 24 Hz at a cost of ≈ 0.2 V.

The component presented here can be added to the circuit without grave changes to the CRNS system and is thus a practical and distributable solution for NPM generations before 2012. We recommend this approach to Hydroinnova and other CRNS users to help avoiding long periods of false data, which are usually hard to identify just by looking at the count rate. This is exactly what happened to three probes of the CRNS network in the *Schäfertal* from May 2015 to Feb 2016.

Acknowledgements

S. Kögler deserves many thanks for the conception and technical implementation of the low-pass filter. The contributions from P. Biro, G. Womack, and D. Desilets to error diagnostics and experimentation is greatly acknowledged.

C.

Variations of incoming cosmic rays

The incoming radiation is an important factor for the performance of CRNS measurements, because this component needs to be removed entirely from the water-sensitive signal (see chapter 5). This chapter briefly summarizes the temporal variations of the incoming neutron radiation and emphasizes the necessity of further research on its influence on CRNS observations.

C.1. Period of uncertainty since 2011

The periodical increase of solar activity not only reduces the galactic cosmic-ray intensity on Earth, it also increases the frequency and amplitude of temporal cosmic-ray variations. These effects are influencing different energy bands and different locations on Earth differently. Since the current correction approach does not account for the corresponding complexity, those variations translate directly to significant uncertainty in CRNS measurements.

Fig. C.1 shows that cosmic-ray neutron intensity reached a new space age record in 2009 (Oh et al. 2013) and indicates that the measurement uncertainty has increased after Zreda et al. (2008) and Desilets et al. (2010) laid the foundation of cosmic-ray neutron sensing.

C.2. Local effects on neutron monitor intercomparison

Furthermore, the various neutron monitors on Earth show significant differences in terms amplitude, time lag, and important features, although their local cutoff rigidity is comparable. A clear indication is given in Fig. C.2 that neutron signals vary dramatically even on daily time scales. Geomagnetic variations or local weather

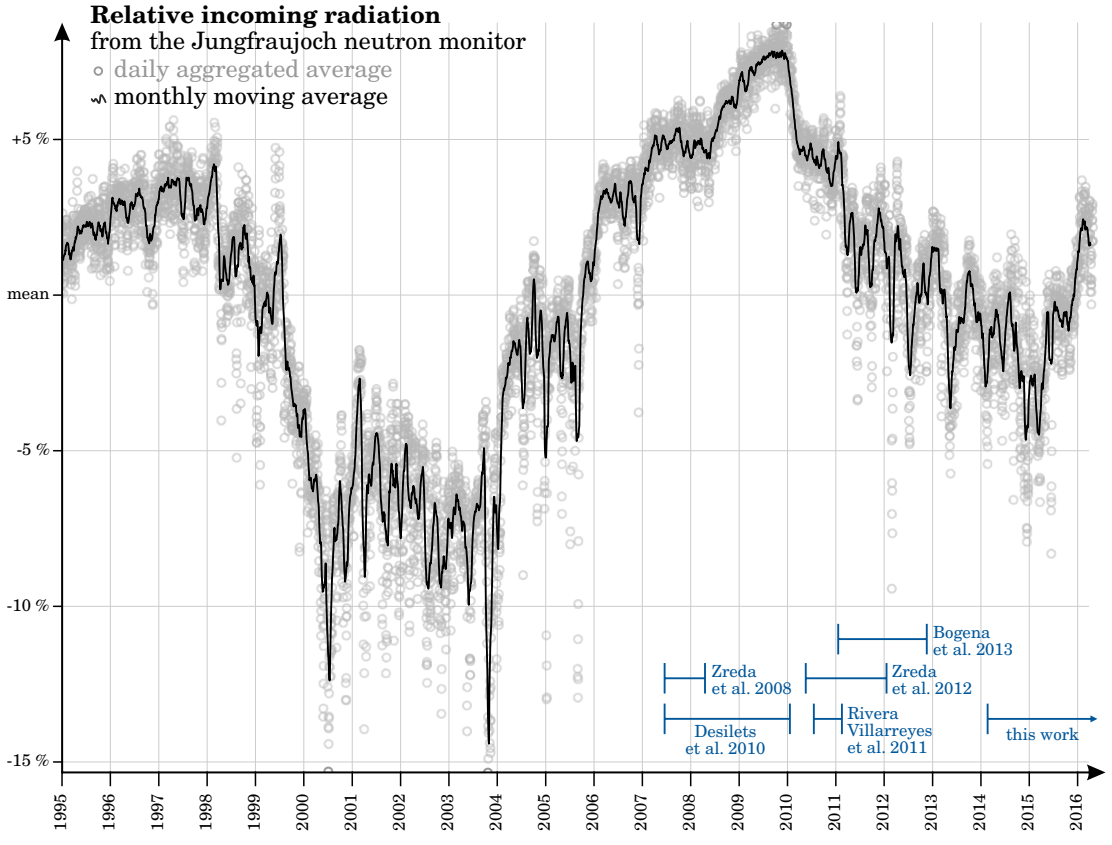

Fig. C.1: During periods of high solar activity the incoming cosmic-ray variation highly increases, thereby reducing the average count rate by 10–15 %, more than doubling its standard deviation, and introducing serious spikes of 1–8 %. The corresponding uncertainty propagates to the performance of CRNS observations, which is to some extend reflected in the published data (exemplary selection shown).

conditions might be reasonable explanations for those features (see e.g., Tsuchiya 2014, and references therein).

C.3. Remaining features in the corrected CRNS data

The correction of the CRNS signal with neutron monitor data assumes proportionality between their count rates (see section 3.5). Data from Rollesbroich 2012 (Fig. C.3) clearly shows residual features of the incoming radiation (orange) in the corrected signal (blue). Some of these problematic periods were replaced with gaps in Baatz et al. (2014), as their variations did not represent the soil moisture dynamics.

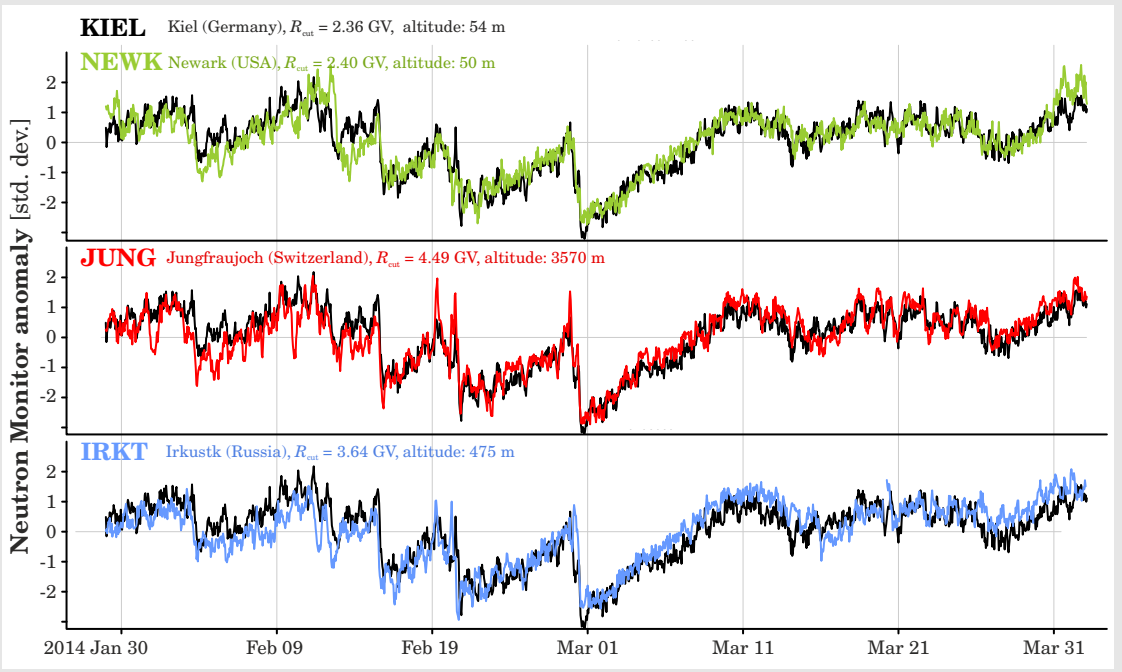

Fig. C.2: Comparison of four neutron monitors that could be a reasonable choice for central Germany, where $R_{\mathrm{cut}} \approx 3.06\,\mathrm{GV}$. Significant differences are visible in the daily count rate, e.g., opposing peaks or delayed decreases.

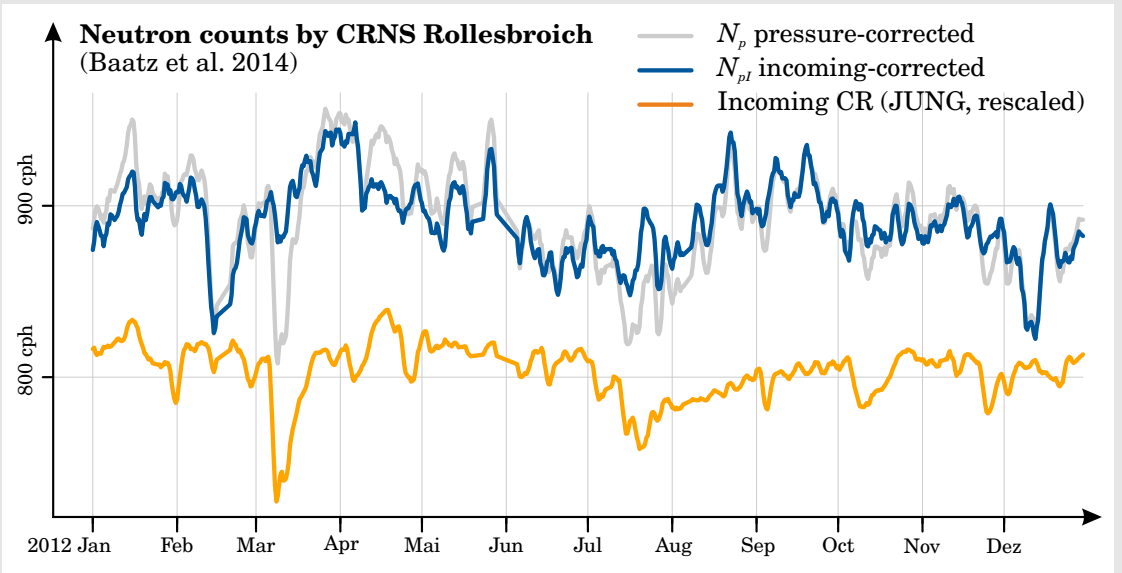

Fig. C.3: Remaining features in the data from Baatz et al. (2014) after conventional incoming correction.

D.

Excel toolbox for spatial weighting of point data

Proper horizontal and vertical weighting of point measurements is a prerequisite for proper validation and calibration of the CRNS method. Until the publication of Köhli et al. (2015) almost all users of CRNS probes avoided horizontal weighting. However, the revised neutron physics model reveals a highly non-linear shape of the detector's radial sensitivity (see chapters 6–7). The corresponding publication has been distributed with a rich supplement that provided the weighting functions W_r as ready-to-apply `Excel`, `R` and `MatLab` scripts. However, private communications revealed that the exact formulation of $W_r(h\,,\theta)$ appeared inapplicable for non-scientific users.

For this reason, an easy-to-use toolbox has been prepared in form of an Excel sheet to guide users through the weighting process. This sheet is able to take a snapshot of point data around the sensor and calculates the corresponding CRNS footprint R_{86}, the average penetration depth D_{86}, and the weighted average soil water content according to guidelines in chapter 7. Moreover, the toolbox encourages the user to iterate the obtained results.

The toolbox already covers very recent research about the weighting, e.g., to account for vegetation and air pressure (section 7.2.1). High usability is achieved by e.g., green cells for user input and orange cells for relevant output. Up to now, the toolbox was successfully applied by the University of Potsdam and the `IAEA`, Vienna.

Acknowledgement

J. Weimar set up a pre-version of this toolbox as a supplement for Köhli et al. (2015). Thanks also to G. Baroni for applying and testing the method.

1. CRNS Footprint Weighting

Average Environmental Conditions		
p=	1013,25	mbar, air pressure
Hveg=	0	m, tested for vegetation heights up to 2m
bd=	1,1	g/cm3, bulk density of the soil
h=	10	g/m3, air humidity tested from 0.1 to 50
SM=	0,24	m3/m3, soil moisture, tested from 0.02 to 50

1,000 footprint scaling
1,000 footprint scaling
0,909 depth scaling

Radial weighting function for horizontal averaging
in accordance to eq 4 from Köhli et.al. 2015, WRR

Distance r [m]	Horiz. weight
0	3,42E+05
0,1	3,22E+05
0,2	3,03E+05
0,3	2,85E+05
0,4	2,68E+05
0,5	2,52E+05
0,6	2,38E+05
0,7	2,24E+05
0,8	2,11E+05
0,9	1,99E+05
1	1,87E+05
1,1	1,76E+05
1,2	1,66E+05
1,3	1,57E+05
1,4	1,48E+05
1,5	1,39E+05
1,6	1,31E+05
1,7	1,24E+05
1,8	1,17E+05
1,9	1,11E+05
2	1,04E+05
2,1	9,87E+04
2,2	9,33E+04
2,3	8,82E+04
2,4	8,35E+04
2,5	7,90E+04
2,6	7,48E+04
2,7	7,09E+04
2,8	6,72E+04

	a00	8735	a01	17,1758	a02	11720	a03	0,00978	a04	7045	a05	0,003632
	a10	2,79E-02	a11	5,0399	a12	2,85E-02	a13	0,002455	a14	6,85E-05	a15	9,2926
	a20	247970	a21	17,63	a22	374655	a23	0,00191	a24	195725		
	a30	5,48E-02	a31	16,921	a32	0,6373	a33	5,99E-02	a34	5,43E-04		
	A0	10610,30257	A1	0,010053004	A2	331354,0694	A3	6,30E-01				

formulas

A0 = (a00*(1+a03*x)*exp(-a01*y)+a02*(1+a05*x)-a04*y);
A1 = ((-a10+a14*x)*exp(-a11*y/(1+a15*y))+a12)*(1+x*a13);
A2 = (a20*(1+a23*x)*exp(-a21*y)+a22-a24*y);
A3 = a30*exp(-a31*y)+a32-a33*y+a34*x;

WrA = A0*(exp(-A1*r))+A2*exp(-A3*r) radial weighting function for 0 ≤ r ≤ 50 m
Distance r is additionally scaled with air pressure and vegetation height (testing phase under current research)

b00	1383702	b01	4,156	b02	5325	b03	0,00238	b04
b10	6,03E-05	b11	98,5	b12	1,05E-03			
b20	11747	b21	41,66	b22	4521	b23	0,01998	b24
b30	1,54E-02	b31	10,06	b32	1,81E-02	b33	0,0011	b34
B0	3760,347408	B1	6,79E-03	B2	8609,512806	B3	0,016440603	

formulas

B0 = b00*(0.02-1/b05/(x-b05+b06*y))*(b04-y)*exp(-b01*(y-b04))+b02*(0.7-x*y*b03)
B1 = b10*(x+b11)+b12*y
B2 = (b20*(1-b26*x)*exp(-b21*y*(1-x*b24))+b22-b25*y)*(2+x*b23)
B3 = ((-b30+b34*x)*exp(-b31*y/(1+b35*x+b36*y))+b32)*(2+x*b33)

WrB = B0*(exp(-B1*r))+B2*exp(-B3*r) radial weighting function for 50.1 ≤ r ≤ 350 m
Distance r is additionally scaled with air pressure and vegetation height (testing phase under current research)

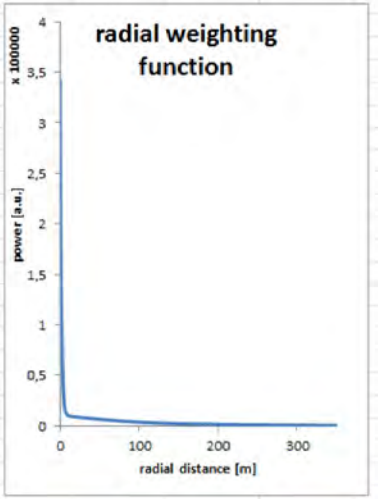

2.

Soil Moisture Samples for each depth (columns) for each profile (rows)

Distance r [m]	Depth [cm]										Profile avg SM	86% Penetration	Profile avg SM	Weights for each sample	
	5	10	15	20	25	30	35	40	45	50	equally weighted	Depth[cm]	depth-weighted	Expand this downwards a	
10	0,1	0,22	0,3	0,2	0,1	0	0	0	0	0,05	0,161666667	37,07309615	0,177126073	0,76358	0,583054
25	0,1	0,1	0,15	0,4	0,45	0,3	0,05	0,1	0,1	0,05	0,18	32,97134638	0,178225391	0,73838224	0,545208
50	0,4	0,2	0,4	0,02	0,4	0,4	0,5	0,2	0,1	0,05	0,267	24,36365392	0,308836897	0,66335336	0,440037
75	0,5	0,2	0,3	0,2	0,11	0,3	0,5	0,3	0,5	0,1	0,301	21,4878979	0,336432194	0,62789757	0,394255
100	0,5	0,3	0,12	0,4	0,22	0,15	0,05	0,1	0,1	0,05	0,199	25,55859859	0,319069505	0,67620584	0,457254
200	0,2	0,3	0,3	0,3	0,2	0,15	0,4	0,2	0,1	0,05	0,22	21,30610191	0,24867955	0,62540921	0,391136
300	0,1	0,4	0,3	0,2	0,1	0,2	0,3	0,1	0,4	0,05	0,215	20,47026518	0,219629843	0,61353777	0,376428

add more profiles here...

3.

Distance r	Profile avg SM	Horiz. Weight Wr	Horiz. weighted SM
10	0,177126073	10205,94745	0,051512415
25	0,178225391	8252,082888	0,041909188
50	0,308836897	6460,759751	0,056857645
75	0,336432194	4767,109413	0,045701322
100	0,319069505	3568,699065	0,032446759
200	0,24867955	1287,092665	0,009120654
300	0,219629843	551,5842945	0,003452068

CRNS apparent SM

24,1 %vol

Please update Conditions!G6 with this value
in order to iterate to a stable value

Avg Penetration Depth

26 cm

Footprint Radius

171 m

E.

Alternative definition of the footprint

Up to now the CRNS community has agreed on using the $1 - e^{-2} \approx 86\,\%$ quantile of detected neutrons to define the footprint area (Desilets and Zreda 2013). However, this approach involves three problems:

1. The shape of the revised weighting function, $W_r(h, \theta)$, is not a simple exponential anymore. Therefore, the $1 - e^{-2}$ limit is misleading when used to make conclusions about other features of the radial sensitivity.
2. Such a high-quantile value will always treat long-range neutrons with favor, regardless of how often they have scattered, i.e., probed the soil.
3. The quantity is not directly related to the actual question of interest: Is the sensor sensitive to remote soil moisture changes?

The following section proposes an alternative and more practical definition of the footprint size, by answering the following research question:

> “What maximum distance $R^*(\Delta\theta)$ from a remote field the detector should be located, such that a remote variation in soil moisture by $\Delta\theta = \theta_1 - \theta_2$ has significant contribution $\Delta N \geq \epsilon(N)$ to the detected neutron signal?”

The intensity distribution around the sensor, $W_r(h, \theta)$, weights different regions of the footprint highly unequal (see chapter 7 or Köhli et al. (2015)). Therefore, a new approach is suggested to interpret the footprint as the distance R^*, to which a remote change of soil moisture is still visible in the detector. We reject all neutron intensity changes below significance of the sensor, which is about $\epsilon(N) \approx 2\,\%$ (Zreda et al. 2012). It is further assumed that the interface between the region of θ_1 and θ_2 is a straight line as illustrated in Fig. E.1a.

By integration of W_r we find the intensity measured before the change of soil moisture:

$$N_1 = N(\theta_1) = \int_0^\infty W_r(h, \theta_1)\,\mathrm{d}r\,.$$

The contribution of the remote segment at a distance R^* then is

$$N_1^* = N(R^*, \theta_1) = \int_{R^*}^\infty W_r(h, \theta_1) \cdot \frac{1}{\pi} \arccos R^*/r \cdot \mathrm{d}r\,,$$

where the weighting function is geometrically reduced to the circular sector in which the segment lies. The following condition determines the distance R^*:

$$\frac{\Delta N^*}{N} = \frac{N_1^* - N_2^*}{N(\theta_1)} \stackrel{!}{=} 0.02\,. \tag{E.1}$$

This equation can be solved for R^* numerically, while an analytical formulation is not straight forward due to the complexity of W_r. Future calculations could show whether R^* could be expressed as a function of R_{86}, for instance. We strongly encourage researchers to perform experiments (e.g., strategic irrigation) that could appropriately falsify the elaborated theory.

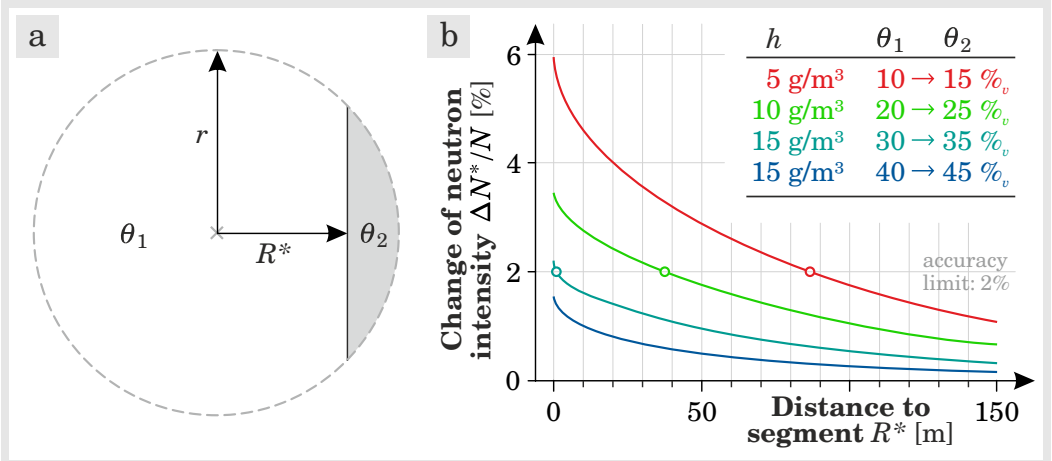

Fig. E.1: a Schematic illustration of the alternative footprint definition, considering a distance R^* at which a remote segment (grey) undergoes soil moisture changes from θ_1 to θ_2. b Eq. E.1 is evaluated for various wetness conditions from dry to humid climate: remote changes of $\Delta\theta = 5\,\%_v$ could be recognized if its distance is less than 87, 38, and 1 m. Additional wetting is insignificant in already wet soil for any distant segment.

Acknowledgements

M. Köhli is greatly acknowledged, who equally contributed to the development of this concept. We also thank S. Zacharias for fruitful discussions and criticism.

Acknowledgements

First and foremost, I would like to thank my supervisors, Steffen Zacharias, Luis Samaniego, Sascha Oswald, and Peter Dietrich for their endless confidence and patience, their visionary ideas, and serious interest in this new field of research.

This work largely profited from the inquisitive contributions from Markus Köhli. Thanks, Markus, for your curiosity and the endless discussions we had. I further like to emphasize the great and creative support from Simon Kögler, who turned all those technical ideas to reality and highly contributed to the success of the field work. Furthermore, I am grateful to my highly motivated students, Mandy Kasner and Jannis Weimar, with whom I enjoyed working every day. Special thanks goes to Sabine Attinger and Ute Wollschläger for their kind and faithful mentoring efforts.

I would also like to express my thanks to all members of the departments of Monitoring and Exploration Technologies, and Computational Hydrosystems. Particularly, thanks to Sophie Binder, Thomas Grau, Juliane Mai, Edna Rödig, Ingmar Schröter, and Matthias Zink for brightening the days at the UFZ.

Moreover, I heartily thank my family and parents for their motivation and reliable support during the last years. Completion of this thesis would not have been possible neither without the endless love and support of my wife, nor without the endless vitality of our two lovely children.

In the following pages, I'd like to thank and highlight all the contributions from my hardworking colleagues with regard to the individual chapters.

Ch. 4: *Intercomparison in an Urban Environment*

S. Zacharias and P. Dietrich contributed the ideas for sensor comparison and ranking statistics. G. Womack and D. Desilets provided support to change the detector parameters. A. Denk took independent soil moisture measurements during the sprinkler experiment. M. Kasner conducted the rover campaign in Fig. 4.5e and analysed soil samples in the laboratory. S. and A. Kathage helped to install the first sensors and provided technical assistance during the first months. H. Kotas and A. Schossland are thanked for their readiness to frequently assemble, disassemble, mount, and unmount the sensors. M. Köhli performed the spatial neutron simulation. P. Remmler installed the WSN system and converted the results under the coordination of J. Bumberger and H. Mollenhauer. S. Kögler permanently supplied valuable technical support and advice in all kinds of field work. U. Kappelmeyer provided meteorological data from a nearby UFZ owned weather station.

Ch. 5: *Lake-side Neutron Trap*

S. Kögler greatly supported the development of the buoy detector lid, took care about the electro-technical setup, and organized the lake campaigns while I was in parental leave. J. Weimar analyzed the buoy data with regards to independent measurements of atmospheric water vapor. K. Herbst conducted specific simulations to provide Fig. 5.1, and contributed to discussions about neutron monitors. J. Mai gave kind support for the development of the SCE optimizer. M. Köhli simulated the lake environment to assess the contribution from shore neutrons. The UFZ-limnology group, especially B. Böhrer and K. Rahn, kindly provided the buoy and technical support for its deployment. Permission to access the lake was kindly granted by D. Onnasch and P. Morszeck (LMBV). Particular thanks to B. Dannenberg for support and instructions at the lake site.

Ch. 6: *Footprint Characteristics*

Great thanks goes to M. Köhli who inquisitively jumped on the venture to develop the neutron model, performed the simulations, fitted the results, and discussed the involved aspects of particle physics. S. Zacharias, M. Zreda, and D. Desilets highly contributed with their doubts and open discussions to the refinement of this study. U. Schmidt and P. Dietrich are thanked for their constructive comments during the preparation of the manuscript.

Ch. 7: *Give 'em weight!*

S. Zacharias, M. Köhli contributed to the methodology and discussion. L. Scheiffele, G. Baroni, and S. Oswald provided data and analysis for the agricultural site near Braunschweig. H. Bogena provided *Wüstebach* data and contributed to its interpretation. C. Rebmann, J. Mai, M. Cuntz, S. Kögler, J. Weimar provided and prepared *Großes Bruch* SoilNet data. T. Franz provided data for the *Santa Rita* site.

Ch. 8: *Roving across scales*

M. Kasner conducted all 11 transects through the *Bode* catchment and performed most of the corresponding analysis and data collection in the scope of her Master thesis. Ideas and parts of the analysis were developed together and discussed with S. Zacharias. I. Schröter conducted the TDR campaigns in the *Schäfertal* and converted the signal to soil moisture. Thanks to S. Köhler, T. Grau, A. Schmidt, U. Wollschläger, and helpers for support during the campaigns. Stationary CRNS data, support, and advice were kindly provided by C. Rivera-Villarreyes, G. Baroni, and S. Oswald.

Ch. 9: *Hydrologic Modeling*

M. Zink laid the basis for reading spatial observations into `mHM`, prepared meteorological data, and ran `mHM` for *Großes Bruch* and *Hohes Holz*. D. Spieler prepared `mHM` for the *Selke* basin. M. Zink, M. Cuntz, R. Kumar, O. Rakovec, and S. Thober are thanked for kind support in all corners of `mHM`, `NetCDF` and `Python`. L. Samaniego and S. Zacharias constructively contributed ideas and conceptual strategies. R. Rosolem provided the standalone-version of the `COSMIC` model. J. Mai explained all the details around optimization strategies. M. Neubauer developed the soil texture map for *Schäfertal* and contributed model results from `HydroGeoSphere`. K. Mroos, G. Baroni and S. Oswald kindly provided data of the CRNS stations in *Schäfertal*. T. Grau and E. Martini provided SoilNet data for *Schäfertal*. F. Reinstorf provided discharge and weather data for *Schäfertal*, and simulations from `WASIM-ETH`. C. Rebmann and J. Mai provided SoilNet data for *Großes Bruch* and *Hohes Holz*. S. Attinger is thanked for frequent gatherings and discussions about the concepts and scaling in hydrological models.

Ch. 10: *Neutrons on the Fly*

L. Bannehr provided the gyrocopter technology and helped to mount the CRNS detector together with his team Ch. Ulrich and T. Kirschke, while L. Koppers aviated the aircraft. M. Kasner assisted during the ground-truthing campaign. M. Köhli performed simulations and supported discussions, the latter was further supported by S. Zacharias and P. Dietrich. S. Kögler and J. Weimar provided technical supports for constructing and mounting the CRNS to the gyrocopter. I finally thank P. Ziegler (FKIE) for initialising this idea and Prof. Bongartz and colleagues for their readiness to cooperate.


12194
DOUGLAS ADAMS
DAS LEBEN, DAS UNIVERSUM UND DER GANZE REST
1288
HEYNE
Lust an der Natur
NICHTLUSTIG ZEITMASCHINEN BEDIENUNGSANLEITUNG
GOLDMANN
Terry Pratchett Der Zeitdieb 45739
THE SLOWING DOWN AND THERMALIZATION OF NEUTRONS
DAS ELEGANTE UNIVERSUM
SIEDLER
BRIAN GREENE
Eiselt Fehlersuche in elektrischen Anlagen und Geräten
OXFORD
NEUTRON TRANSPORT THEORY
DAVISON
Eltern family
Ronja Räubertochter 1
SCHLAU IT! Englischwörterbuch für Kinder
1292
SACHSEN DICTIONARY
Astrid Lindgren · Ilon Wikland
Nein, ich will noch nicht ins Bett!
Oetinger
KNOLL
RADIATION DETECTION AND MEASUREMENT
SECOND EDITION
WILEY

Bibliography

A

Abramowski, A. et al. (2016). "Acceleration of petaelectronvolt protons in the Galactic Centre". In: *Nature*. DOI: 10.1038/nature17147 (cited on p. 41).

Abunin, A., P. Kobelev, M. Abunina, M. Preobragenskiy, D. Smirnov, and A. Lukovnikova (2016). "A wind effect of neutron component of cosmic rays at Antarctic station "Mirny"". In: *Solar-Terrestrial Physics (Solnechno-zemnaya fizika)* **2**:1, pp. 71–75. DOI: 10.12737/13505 (cited on pp. 84, 162).

Ackermann, M. et al. (2013). "Detection of the Characteristic Pion-Decay Signature in Supernova Remnants". In: *Science* **339**:6121, pp. 807–811. DOI: 10.1126/science.1231160 (cited on p. 41).

Alekseenko, V. V., Y. M. Gavrilyuk, D. M. Gromushkin, D. D. Dzhappuev, A. U. Kudzhaev, V. V. Kuzminov, O. I. Mikhailova, Y. V. Stenkin, and V. I. Stepanov (2009). "Correlation of variations in the thermal neutron flux from the Earth's crust with the Moon's phases and with seismic activity". In: *Izvestiya, Physics of the Solid Earth* **45**:8, pp. 709–718. DOI: 10.1134/S1069351309080102 (cited on p. 52).

Allen, R. G., L. S. Pereira, D. Raes, M. Smith, et al. (1998). "Crop evapotranspiration-Guidelines for computing crop water requirements-FAO Irrigation and drainage paper 56". In: *FAO, Rome* **300**:9, p. D05109 (cited on p. 29).

Almeida, A. C., R. Dutta, T. E. Franz, A. Terhorst, P. J. Smethurst, C. Baillie, and D. Worledge (2014). "Combining Cosmic-Ray Neutron and Capacitance Sensors and Fuzzy Inference to Spatially Quantify Soil Moisture Distribution". In: *IEEE Sensors Journal* **14**:10, pp. 3465–3472. DOI: 10.1109/JSEN.2014.2345376 (cited on p. 118).

Andreasen, M., K. H. Jensen, D. Desilets, M. Zreda, H. R. Bogena, and M. C. Looms (2017). "Cosmic-ray neutron transport at a forest field site: the sensitivity to various environmental conditions with focus on biomass and canopy

interception". In: *Hydrology and Earth System Sciences* **21**:4, pp. 1875–1894. DOI: 10.5194/hess-21-1875-2017 (cited on p. 55).

Aplin, K., R. Harrison, and A. Bennett (2005). "Effect of the troposphere on surface neutron counter measurements". In: *Advances in Space Research* **35**:8, pp. 1484 –1491. DOI: 10.1016/j.asr.2005.02.055 (cited on p. 85).

Apostolakis, J., M. Asai, A. G. Bogdanov, H. Burkhardt, G. Cosmo, S. Elles, G. Folger, V. M. Grichine, P. Gumplinger, and A. Heikkinen (2009). "Geometry and physics of the Geant4 toolkit for high and medium energy applications". In: *Radiation Physics and Chemistry* **78**:10, pp. 859–873 (cited on p. 94).

Astbury, A. (2005). *Cancer mortality, cosmic ray neutron dose, and summer solar UV-B flux share similar geographical distributions in the USA*. Tech. rep. Citeseer (cited on p. 46).

Atri, D. and A. L. Melott (2014). "Cosmic rays and terrestrial life: A brief review". In: *Astroparticle Physics* **53**: Centenary of cosmic ray discovery, pp. 186 –190. DOI: 10.1016/j.astropartphys.2013.03.001 (cited on p. 46).

Avery, W. A., C. Finkenbiner, T. E. Franz, T. Wang, A. L. Nguy-Robertson, A. Suyker, T. Arkebauer, and F. Muñoz-Arriola (2016). "Incorporation of globally available datasets into the roving cosmic-ray neutron probe method for estimating field-scale soil water content". In: *Hydrology and Earth System Sciences* **20**:9, p. 3859 (cited on pp. 126, 132).

B

Baatz, R., H. Bogena, H.-J. H. Franssen, J. Huisman, W. Qu, C. Montzka, and H. Vereecken (2014). "Calibration of a catchment scale cosmic-ray probe network: A comparison of three parameterization methods". In: *Journal of Hydrology* **516**:0, pp. 231 –244. DOI: 10.1016/j.jhydrol.2014.02.026 (cited on pp. 62, 83, 140, 178, 179).

Baatz, R., H. R. Bogena, H.-J. H. Franssen, J. A. Huisman, C. Montzka, and H. Vereecken (2015). "An empirical vegetation correction for soil water content quantification using cosmic ray probes". In: *Water Resources Research* **51**:4, pp. 2030–2046. DOI: 10.1002/2014wr016443 (cited on pp. 63, 70, 79, 126, 127, 131).

Bachelet, P., P. Balata, E. Dyring, and N. Iucci (1965). "The intercalibration of the cosmic-ray neutron monitors at 9 European sea-level stations and the deduction of a daily latitude effect in 1963". In: *Il Nuovo Cimento (1955-1965)* **36**:3, pp. 762–772 (cited on p. 70).

Balabin, Y. V., A. V. Germanenko, B. B. Gvozdevsky, and E. V. Vashenyuk (2013). "Variations of gamma radiation spectra during precipitations". In: *Journal of Physics: Conference Series* **409**:1, p. 012243 (cited on p. 57).

Bannehr, L., T. Kirschke, L. Koppers, and C. Ulrich (2015). "Possible Applications of a Gyrocopter in the Field of Environmental Research". In: *Peer Reviewed Proceedings of Digital Landscape Architecture 2015 at Anhalt University of Applied Sciences*. Ed. by E. Buhmann, S. M. Ervin, and M. Pietsch. Herbert Wichmann Verlag, VDE VERLAG GMBH, Berlin/Offenbach (cited on p. 155).

Barkov, L., V. Makarin, and K. Mukhin (1957). "Measurement of the slowing down of neutrons in the energy range 1.46-0.025 eV in water". In: *Journal of Nuclear Energy (1954)* **4**:1, pp. 94 –102. doi: 10.1016/0891-3919(57)90124-9 (cited on p. 55).

Baroni, G. and S. Oswald (2015). "A scaling approach for the assessment of biomass changes and rainfall interception using cosmic-ray neutron sensing". In: *Journal of Hydrology* **525**: pp. 264–276. doi: 10.1016/j.jhydrol.2015.03.053 (cited on pp. 36, 113, 126, 131).

Beane, S. R., E. Chang, S. Cohen, W. Detmold, H. W. Lin, K. Orginos, A. Parreño, M. J. Savage, B. C. Tiburzi, et al. (2014). "Magnetic moments of light nuclei from lattice quantum chromodynamics". In: *Physical review letters* **113**:25, p. 252001 (cited on p. 51).

Belov, A., L. Baisultanova, E. Eroshenko, H. Mavromichalaki, V. Yanke, V. Pchelkin, C. Plainaki, and G. Mariatos (2005). "Magnetospheric effects in cosmic rays during the unique magnetic storm on November 2003". In: *Journal of Geophysical Research: Space Physics* **110**:A9. A09S20. doi: 10.1029/2005JA011067 (cited on p. 84).

Belov, A. (2008). "Forbush effects and their connection with solar, interplanetary and geomagnetic phenomena". In: *Proceedings of the International Astronomical Union* **4**:S257, pp. 439–450 (cited on p. 43).

Bennett, N. D., B. F. Croke, G. Guariso, J. H. Guillaume, S. H. Hamilton, A. J. Jakeman, S. Marsili-Libelli, L. T. Newham, J. P. Norton, C. Perrin, S. A. Pierce, B. Robson, R. Seppelt, A. A. Voinov, B. D. Fath, and V. Andreassian (2013). "Characterising performance of environmental models". In: *Environmental Modelling & Software* **40**: pp. 1–20. doi: 10.1016/j.envsoft.2012.09.011 (cited on p. 143).

Bergeron, J. M., M. Trudel, and R. Leconte (2016). "Combined assimilation of streamflow and snow water equivalent for mid-term ensemble streamflow forecasts in snow-dominated regions". In: *Hydrology and Earth System Sciences* **20**:10, pp. 4375–4389. doi: 10.5194/hess-20-4375-2016 (cited on p. 150).

Bergstrom, S. (1976). *Development and application of a conceptual runoff model for Scandinavian catchments*. Tech. rep. (cited on p. 138).

Beven, K. (1992). "Editorial: Future of distributed modelling". In: *Hydrological Processes* **6**:3, pp. 253–254. doi: 10.1002/hyp.3360060302 (cited on p. 137).

Beven, K. and J. Freer (2001). "Equifinality, data assimilation, and uncertainty estimation in mechanistic modelling of complex environmental systems using the {GLUE} methodology". In: *Journal of Hydrology* **249**:1–4, pp. 11–29. doi: 10.1016/S0022-1694(01)00421-8 (cited on pp. 86, 144).

Beven, K. J. and H. L. Cloke (2012). "Comment on "Hyperresolution global land surface modeling: Meeting a grand challenge for monitoring Earth's terrestrial water" by Eric F. Wood et al." In: *Water Resources Research* **48**:1 (cited on pp. 26, 136).

BGR (2007). *Bodenübersichtskarte 1:1.000.000 (BÜK1000)*. url: http://www.bgr.bund.de/DE/Themen/Boden/Informationsgrundlagen/Bodenkundliche_Karten_Datenbanken/BUEK1000/buek1000_node.html (visited on 05/08/2016) (cited on pp. 125, 126, 145).

Blandford, R. D. and J. P. Ostriker (1978). "Particle acceleration by astrophysical shocks". In: *The Astrophysical Journal* **221**: p. L29. doi: 10.1086/182658 (cited on p. 41).

Blasi, P. (2013). "The origin of galactic cosmic rays". In: *The Astronomy and Astrophysics Review* **21**:1, pp. 1–73. doi: 10.1007/s00159-013-0070-7 (cited on p. 41).

Blöschl, G. and M. Sivapalan (1995). "Scale issues in hydrological modelling: a review". In: *Hydrological processes* **9**:3-4, pp. 251–290 (cited on p. 137).

Bogena, H. R., M. Herbst, J. A. Huisman, U. Rosenbaum, A. Weuthen, and H. Vereecken (2010). "Potential of wireless sensor networks for measuring soil water content variability". In: *Vadose Zone Journal* **9**:4, pp. 1002–1013 (cited on pp. 32, 33, 35).

Bogena, H. R., J. A. Huisman, R. Baatz, H.-J. Hendricks Franssen, and H. Vereecken (2013). "Accuracy of the cosmic-ray soil water content probe in humid forest ecosystems: The worst case scenario". In: *Water Resources Research* **49**:9, pp. 5778–5791. doi: 10.1002/wrcr.20463 (cited on pp. 62, 66, 75, 76, 98, 108, 110, 113, 116, 126, 131).

Borchardt, D. (1982). "Geoökologische Erkundung und hydrologische Analyse von Kleineinzugsgebieten des unteren Mittelgebirgsbereiches, dargestellt am Beispiel von Experimentalgebieten der oberen Selke/Harz". In: *Petermanns Geographische Mitteilungen* **4**:82, pp. 251–262 (cited on p. 124).

Brady, N. and R. Weil (1996). In: *The Nature and Properties of Soils*. 13th ed. Upper Saddle River, NJ: Prentice Hall, p. 960 (cited on pp. 30, 31).

Bramer, L. M., B. K. Hornbuckle, and P. C. Caragea (2013). "How many measurements of soil moisture within the footprint of a ground-based microwave radiometer are required to account for meter-scale spatial variability?" In: *Vadose Zone Journal* **12**:3 (cited on p. 118).

Breiman, L. (2001). "Random forests". In: *Machine learning* **45**:1, pp. 5–32 (cited on p. 145).

Breitschwerdt, D., V. A. Dogiel, and H. J. Völk (2002). "The gradient of diffuse γ-ray emission in the Galaxy". In: *Astronomy and Astrophysics* **385**:1, pp. 216–238. doi: 10.1051/0004-6361:20020152 (cited on p. 42).

Brocca, L., F. Melone, T. Moramarco, and R. Morbidelli (2010). "Spatial-temporal variability of soil moisture and its estimation across scales". In: *Water Resources Research* **46**:2. doi: 10.1029/2009WR008016 (cited on p. 50).

Brocca, L., T. Tullo, F. Melone, T. Moramarco, and R. Morbidelli (2012). "Catchment scale soil moisture spatial–temporal variability". In: *Journal of Hydrology* **422–423**: pp. 63–75. doi: 10.1016/j.jhydrol.2011.12.039 (cited on pp. 27, 50).

Brocca, L., T. Moramarco, F. Melone, and W. Wagner (2013). "A new method for rainfall estimation through soil moisture observations". In: *Geophysical Research Letters* **40**:5, pp. 853–858. doi: 10.1002/grl.50173 (cited on p. 29).

Brovelli, A. and G. Cassiani (2008). "Effective permittivity of porous media: A critical analysis of the complex refractive index model". In: *Geophysical Prospecting* **56**:5, pp. 715–727 (cited on p. 35).

Brutsaert, W. (2005). *Hydrology: an introduction*. Cambridge University Press (cited on p. 27).

Budds, J., J. Linton, and R. McDonnell (2014). "The hydrosocial cycle". In: *Geoforum* 57, pp. 167–169 (cited on p. 26).

Bumberger, J., H. Mollenhauer, P. Remmler, M. Schaedler, R. Schima, O. Mollenhauer, T. Hutschenreuther, H. Toepfer, and P. Dietrich (2015). "Adaptive Wireless Ad-hoc Sensor Networks for Long-term and Event-oriented Environmental Monitoring". In: *EGU General Assembly Conference Abstracts*. Vol. 17, p. 6248 (cited on pp. 35, 72, 163).

Burmester, A. (1987). "Einfluß von Extraktstoffänderungen auf den Feuchtigkeitsgehalt von Baumrinden". In: *Holz als Roh-und Werkstoff* **45**:1, pp. 11–13 (cited on p. 126).

Bütikofer, R., E. O. Flückiger, and L. Desorgher (2007). "Characteristics of near real-time cutoff calculations on a local and global scale". In: *30th International Cosmic Ray Conference, Mérida, México* (cited on p. 61).

Bütikofer, R. (1999). "Pressure correction of GLE measurements in turbulent winds". In: *International Cosmic Ray Conference*. Vol. 6, p. 395 (cited on pp. 60, 84, 88, 162).

Bütikofer, R., E. Flückiger, D. Galsdorf, B. Heber, K. Herbst, and C. Steigies (2015). "Rapid determination of cutoff rigidities and asymptotic directions using predetermined data from a database". In: *PoS* **ICRC2015**: p. 112. URL: http://pos.sissa.it/archive/conferences/236/112/ICRC2015_112.pdf (cited on p. 84).

C

Callegary, J. B., T. P. A. Ferré, and R. W. Groom (2007). "Vertical Spatial Sensitivity and Exploration Depth of Low-Induction-Number Electromagnetic-Induction Instruments". In: *Vadose Zone Journal* **6**:1, p. 158. DOI: 10.2136/vzj2006.0120 (cited on p. 34).

Calviño-Cancela, M., R. Méndez-Rial, J. Reguera-Salgado, and J. Martín-Herrero (2014). "Alien Plant Monitoring with Ultralight Airborne Imaging Spectroscopy". In: *PLoS ONE* **9**:7, pp. 1–9. DOI: 10.1371/journal.pone.0102381 (cited on p. 155).

Carmichael, H., M. A. Shea, and R. W. Peterson (1969). "III. Cosmic-ray latitude survey in Western USA and Hawaii in summer, 1966". In: *Canadian Journal of Physics* **47**:19, pp. 2057–2065. DOI: 10.1139/p69-259 (cited on p. 155).

Carpenter, T. M. and K. P. Georgakakos (2006). "Intercomparison of lumped versus distributed hydrologic model ensemble simulations on operational forecast scales". In: *Journal of Hydrology* **329**:1–2, pp. 174 –185. DOI: 10.1016/j.jhydrol.2006.02.013 (cited on p. 137).

Carroll, T. R. (1981). "Airborne Soil Moisture Measurement Using Natural Terrestrial Gamma Radiation". In: *Soil Science* **132**:5, pp. 358–366 (cited on p. 155).

Cassis, N. and A. Schreiner-McGraw (2014). *New soil moisture sensor tracks drought conditions in Arizona, Mexico*. URL: http://sese-archive.asu.edu/news/cosmic-ray-soil-moisture-sensor-deployed-urban-setting-phoenix (visited on 05/23/2016) (cited on p. 70).

Ceppi, A., G. Ravazzani, C. Corbari, R. Salerno, S. Meucci, and M. Mancini (2014). "Real-time drought forecasting system for irrigation management". In: *Hydrology and Earth System Sciences* **18**:9, pp. 3353–3366. doi: 10.5194/hess-18-3353-2014 (cited on pp. 27, 137).

Chadwick, M. et al. (2011). "ENDF/B-VII.1 Nuclear Data for Science and Technology: Cross Sections, Covariances, Fission Product Yields and Decay Data". In: *Nuclear Data Sheets* **112**:12, pp. 2887–2996. doi: 10.1016/j.nds.2011.11.002 (cited on p. 67).

Chandra, R., G. Davatz, and A. Howard (2010). "Gamma-insensitive fast neutron detector with spectral source identification potential". In: *Technologies for Homeland Security (HST), 2010 IEEE International Conference on*. IEEE, pp. 410–413 (cited on p. 57).

Chang, N.-B. and Y. Hong (2012). *Multiscale hydrologic remote sensing: Perspectives and applications*. CRC Press (cited on p. 33).

Chew, C., E. E. Small, and K. M. Larson (2016). "An algorithm for soil moisture estimation using GPS-interferometric reflectometry for bare and vegetated soil". In: *GPS Solutions* **20**:3, pp. 525–537. doi: 10.1007/s10291-015-0462-4 (cited on p. 34).

Chiba, T., H. Takahashi, and M. Kodama (1975). "Cosmic-ray neutron intensities observed during August 1970 - January 1975". In: *Annual Report* (cited on pp. 70, 85).

Chrisman, B. and M. Zreda (2013). "Quantifying mesoscale soil moisture with the cosmic-ray rover". In: *Hydrology and Earth System Sciences* **17**:12, pp. 5097–5108. doi: 10.5194/hess-17-5097-2013 (cited on pp. 33, 122, 132, 154).

Christensen, C. J., A. Nielsen, A. Bahnsen, W. K. Brown, and B. M. Rustad (1972). "Free-Neutron Beta-Decay Half-Life". In: *Phys. Rev. D* **5**: (7), pp. 1628–1640. doi: 10.1103/PhysRevD.5.1628 (cited on p. 50).

Clem, J. M., J. W. Bieber, P. Evenson, D. Hall, J. E. Humble, and M. Duldig (1997). "Contribution of obliquely incident particles to neutron monitor counting rate". In: *Journal of Geophysical Research: Space Physics* **102**:A12, pp. 26919–26926. doi: 10.1029/97JA02366 (cited on p. 88).

Clem, J. M. and L. I. Dorman (2000). "Neutron Monitor Response Functions". In: *Space Science Reviews* **93**:1, pp. 335–359. doi: 10.1023/A:1026508915269 (cited on p. 88).

Cline, D., S. Yueh, B. Chapman, B. Stankov, A. Gasiewski, D. Masters, K. Elder, R. Kelly, T. H. Painter, S. Miller, S. Katzberg, and L. Mahrt (2009). "NASA Cold Land Processes Experiment (CLPX 2002/03): Airborne Remote Sensing". In: *Journal of Hydrometeorology* **10**:1, pp. 338–346. doi: 10.1175/2008JHM883.1 (cited on p. 155).

Cooke, D. J., J. E. Humble, M. A. Shea, D. F. Smart, N. Lund, I. L. Rasmussen, B. Byrnak, P. Goret, and N. Petrou (1991). "On cosmic-ray cut-off terminology". In: *Il Nuovo Cimento C* **14**:3, pp. 213–234 (cited on p. 43).

Coopersmith, E. J., M. H. Cosh, and C. S. Daughtry (2014). "Field-scale moisture estimates using COSMOS sensors: A validation study with temporary networks and Leaf-Area-Indices". In: *Journal of Hydrology* **519, Part A**:0, pp. 637 –643. doi: 10.1016/j.jhydrol.2014.07.060 (cited on pp. 37, 98, 118, 131).

Coron, L., V. Andréassian, C. Perrin, M. Bourqui, and F. Hendrickx (2014). "On the lack of robustness of hydrologic models regarding water balance simulation: a diagnostic approach applied to three models of increasing complexity on 20 mountainous catchments". In: *Hydrology and Earth System Sciences* **18**:2, pp. 727–746. doi: 10.5194/hess-18-727-2014 (cited on pp. 29, 137).

Cosh, M. H. and W. Brutsaert (1999). "Aspects of soil moisture variability in the Washita '92 study region". In: *Journal of Geophysical Research: Atmospheres* **104**:D16, pp. 19751–19757. doi: 10.1029/1999JD900110 (cited on p. 29).

Crane, T. and M. Baker (1991). "Neutron detectors". In: *Passive Nondestructive Assay of Nuclear Materials*, pp. 379–406 (cited on p. 57).

Creutzfeldt, B., A. Güntner, S. Vorogushyn, and B. Merz (2010). "The benefits of gravimeter observations for modelling water storage changes at the field scale". In: *Hydrology and Earth System Sciences* **14**:9, pp. 1715–1730. doi: 10.5194/hess-14-1715-2010 (cited on pp. 33, 98).

Cronin, J. W., T. K. Gaisser, and S. P. Swordy (1997). "Cosmic Rays at the Energy Frontier". In: *Scientific American* **276**:1, pp. 44–49. doi: 10.1038/scientificamerican0197-44 (cited on p. 42).

Crow, W. T., A. A. Berg, M. H. Cosh, A. Loew, B. P. Mohanty, R. Panciera, P. de Rosnay, D. Ryu, and J. P. Walker (2012). "Upscaling sparse ground-based soil moisture observations for the validation of coarse-resolution satellite soil moisture products". In: *Reviews of Geophysics* **50**:2. doi: 10.1029/2011RG000372 (cited on p. 122).

Cuenca, R. H., Y. Hagimoto, and M. Moghaddam (2013). "Three-and-a-half decades of progress in monitoring soils and soil hydraulic properties". In: *Procedia Environmental Sciences* **19**: pp. 384–393 (cited on p. 33).

Cuntz, M., J. Mai, M. Zink, S. Thober, R. Kumar, D. Schäfer, M. Schrön, J. Craven, O. Rakovec, D. Spieler, V. Prykhodko, G. Dalmasso, J. Musuuza, B. Langenberg, S. Attinger, and L. Samaniego (2015). "Computationally inexpensive identification of noninformative model parameters by sequential screening". In: *Water Resources Research* **51**:8, pp. 6417–6441. doi: 10.1002/2015wr016907 (cited on p. 143).

D

De Lannoy, G. J. M., R. D. Koster, R. H. Reichle, S. P. P. Mahanama, and Q. Liu (2014). "An updated treatment of soil texture and associated hydraulic properties in a global land modeling system". In: *Journal of Advances in Modeling Earth Systems* **6**:4, pp. 957–979. doi: 10.1002/2014MS000330 (cited on p. 132).

Dengel, S., D. Aeby, and J. Grace (2009). "A relationship between galactic cosmic radiation and tree rings". In: *New Phytologist* **184**:3, pp. 545–551. doi: 10.1111/j.1469-8137.2009.03026.x (cited on p. 46).

Desilets, D. and M. Zreda (2013). "Footprint diameter for a cosmic-ray soil moisture probe: Theory and Monte Carlo simulations". In: *Water Resources Research* **49**:6, pp. 3566–3575. doi: 10.1002/wrcr.20187 (cited on pp. 54, 76, 80, 97–100, 102, 103, 108, 185).

Desilets, D., M. Zreda, and T. Ferré (2010). "Nature's neutron probe: Land surface hydrology at an elusive scale with cosmic rays". In: *Water Resources Research* **46**:11. doi: 10.1029/2009WR008726 (cited on pp. 61, 62, 112, 118, 122, 123, 131, 140, 151, 157, 177).

Desilets, D. and M. Zreda (2008). "Non-invasive method for measuring soil water content or snow water equivalent depth using cosmic-ray neutrons". Patent 0087837 (US) (cited on pp. 55, 102).

Desilets, D., M. Zreda, and T Prabu (2006). "Extended scaling factors for in situ cosmogenic nuclides: new measurements at low latitude". In: *Earth and Planetary Science Letters* **246**:3, pp. 265–276 (cited on pp. 60, 67, 88, 91).

Desilets, D., M. Zreda, and T. Ferré (2007). "Scientist water equivalent measured with cosmic rays at 2006 AGU Fall Meeting". In: *Eos, Transactions American Geophysical Union* **88**:48, pp. 521–522. doi: 10.1029/2007EO480001 (cited on pp. 36, 103, 130, 159).

Desorgher, L., E. O. Flückiger, and M. Gurtner (2006). "The planetocosmics Geant4 application". In: *36th COSPAR Scientific Assembly*. Vol. 36, p. 2361. url: http://cosray.unibe.ch/~laurent/planetocosmics/ (cited on p. 94).

Dietrich, P., T. Fechner, J. Whittaker, and G. Teutsch (1998). "An integrated hydrogeophysical approach to subsurface characterization". In: *IAHS Publication(International Association of Hydrological Sciences)* 250, pp. 513–519 (cited on p. 132).

Diggle, P. and S. Lophaven (2006). "Bayesian Geostatistical Design". In: *Scandinavian Journal of Statistics* **33**:1, pp. 53–64. doi: 10.1111/j.1467-9469.2005.00469.x (cited on p. 118).

DLG (2008). *Bodenschonender Einsatz von Landmaschinen. DLG-Merkbl. 344*. DLG e.V. url: http://www.lfl.bayern.de/mam/cms07/iab/dateien/boden_dlg_merkblatt.pdf (cited on p. 154).

Dobriyal, P., A. Qureshi, R. Badola, and S. A. Hussain (2012). "A review of the methods available for estimating soil moisture and its implications for water resource management". In: *Journal of Hydrology* **458–459**: pp. 110–117. doi: 10.1016/j.jhydrol.2012.06.021 (cited on p. 34).

Dobrzynski, L. and K. Blinowski (1994). *Neutrons and solid state physics*. Prentice Hall (cited on p. 53).

Doney, S. C., W. J. Jenkins, and J. L. Bullister (1997). "A comparison of ocean tracer dating techniques on a meridional section in the eastern North Atlantic". In: *Deep Sea Research Part I: Oceanographic Research Papers* **44**:4, pp. 603–626. doi: 10.1016/S0967-0637(96)00105-7 (cited on p. 45).

Dong, J., S. C. Steele-Dunne, T. E. Ochsner, and N. van de Giesen (2016). "Estimating soil moisture and soil thermal and hydraulic properties by assimilating soil temperatures using a particle batch smoother". In: *Advances in Water Resources* **91**: pp. 104 –116. doi: 10.1016/j.advwatres.2016.03.008 (cited on p. 32).

Dong, J., T. E. Ochsner, M. Zreda, M. H. Cosh, and C. B. Zou (2014). "Calibration and Validation of the COSMOS Rover for Surface Soil Moisture Measurement". In: *Vadose Zone Journal* **13**:4. doi: doi:10.2136/vzj2013.08.0148 (cited on pp. 122, 123).

Dorfi, E. A. and D. Breitschwerdt (2012). "Time-dependent galactic winds". In: *Astronomy & Astrophysics* **540**: A77. doi: 10.1051/0004-6361/201118082 (cited on p. 41).

Dorigo, W. A., W. Wagner, R. Hohensinn, S. Hahn, C. Paulik, A. Xaver, A. Gruber, M. Drusch, S. Mecklenburg, P. van Oevelen, A. Robock, and T. Jackson (2011). "The International Soil Moisture Network: a data hosting facility for global in situ soil moisture measurements". In: *Hydrology and Earth System Sciences* **15**:5, pp. 1675–1698. doi: 10.5194/hess-15-1675-2011 (cited on p. 27).

Dorman, I. and L. Dorman (2014). "How cosmic rays were discovered and why they received this misnomer". In: *Advances in Space Research* **53**:10, pp. 1388–1404. doi: 10.1016/j.asr.2013.04.022 (cited on p. 36).

Dorman, L. I., S. G. Fedchenko, L. V. Granitsky, and G. A. Rishe (1970). "Coupling and barometer coefficients for measurements of cosmic ray variations at altitudes of 260-400 mb". In: *International Cosmic Ray Conference* **2**: suppl. 2, p. 233 (cited on p. 44).

Dorman, L. I. (2004). *Cosmic Rays in the Earth's Atmosphere and Underground*. Springer Netherlands. doi: 10.1007/978-1-4020-2113-8 (cited on pp. 36, 43, 84, 86, 88, 89).

Duan, Q., S. Sorooshian, and V. Gupta (1992). "Effective and efficient global optimization for conceptual rainfall-runoff models". In: *Water Resources Research* **28**:4, pp. 1015–1031. doi: 10.1029/91WR02985 (cited on pp. 89, 143).

Duckstein, L. (1984). "Multiobjective optimization in structural design: The model choice problem". In: *New directions in optimum structural design*. Ed. by K. M. R. E. Atrek R. H. Gallagher and O. C. Zienkiewicz. Vol. 6. 2. Wiley-Blackwell, pp. 459–481. doi: 10.1002/oca.4660060212 (cited on p. 90).

Dunai, T. J. (2000). "Scaling factors for production rates of in situ produced cosmogenic nuclides: a critical reevaluation". In: *Earth and Planetary Science Letters* **176**:1, pp. 157–169 (cited on p. 88).

Dürr, H.-J., H. Petelkau, and C. Sommer (1995). "Literaturstudie Bodenverdichtung". In: *UBA-Texte* **55**:95, p. 203 (cited on p. 154).

E

Ellenberg, H. and C. Leuschner (2010). "Vegetation Mitteleuropas mit den Alpen: In ökologischer, dynamischer und historischer Sicht, 6., völlig überarb". In: *Aufl. ed. UTB, Stuttgart* (cited on p. 131).

Ellenberg, H., R. Mayer, and J. Schauermann (1986). *Oekosystemforschung. Ergebnis des Solling-Projekts: 1966-1986*. (Cited on p. 131).

Entekhabi, D., E. G. Njoku, P. Houser, M. Spencer, T. Doiron, Y. Kim, J. Smith, R. Girard, S. Belair, W. Crow, et al. (2004). "The hydrosphere state (Hydros) satellite mission: An earth system pathfinder for global mapping of soil moisture and land freeze/thaw". In: *IEEE Transactions on Geoscience and Remote Sensing* **42**:10, pp. 2184–2195 (cited on p. 33).

Entekhabi, D., E. G. Njoku, P. E. Neill, K. H. Kellogg, W. T. Crow, W. N. Edelstein, J. K. Entin, S. D. Goodman, T. J. Jackson, J. Johnson, et al. (2010). "The soil moisture active passive (SMAP) mission". In: *Proceedings of the IEEE* **98**:5, pp. 704–716 (cited on pp. 33, 132).

Erlykin, A. D. and A. W. Wolfendale (2010). "Long Term Time Variability of Cosmic Rays and Possible Relevance to the Development of Life on Earth". In: *Surveys in Geophysics* **31**:4, pp. 383–398. doi: 10.1007/s10712-010-9097-8 (cited on p. 46).

F

Famiglietti, J. S., D. Ryu, A. A. Berg, M. Rodell, and T. J. Jackson (2008). "Field observations of soil moisture variability across scales". In: *Water Resources Research* **44**:1. W01423. doi: 10.1029/2006WR005804 (cited on pp. 29, 31).

Fang, B. and V. Lakshmi (2014). "Soil moisture at watershed scale: Remote sensing techniques". In: *Journal of Hydrology* **516**: pp. 258–272 (cited on p. 31).

Federrath, C., M. Schrön, R. Banerjee, and R. S. Klessen (2014). "Modeling Jet And Outflow Feedback During Star Cluster Formation". In: *The Astrophysical Journal* **790**:2, p. 128. doi: 10.1088/0004-637x/790/2/128 (cited on p. 41).

Ferré, P. A., J. H. Knight, D. L. Rudolph, and R. G. Kachanoski (1998). "The sample areas of conventional and alternative time domain reflectometry probes". In: *Water Resources Research* **34**:11, pp. 2971–2979. doi: 10.1029/98WR02093. url: http://dx.doi.org/10.1029/98WR02093 (cited on p. 98).

Findell, K. L. and E. A. B. Eltahir (1997). "An analysis of the soil moisture-rainfall feedback, based on direct observations from Illinois". In: *Water Resources Research* **33**:4, pp. 725–735 (cited on p. 27).

Finnern, H., W. Grottenthaler, D. Kühn, W. Pälchen, W. G. Schraps, and H. Sponagel (1994). "Bodenkundliche Kartieranleitung, 4. Auflage". In: *Bundesanstalt für Geowissenschaften und Rohstoffe und den Geologischen Landesämtern in der Bundesrepublik Deutschland (in German), Hannover*, p. 392 (cited on p. 125).

FitzPatrick, E. A. et al. (1980). *Soils. Their formation, classification and distribution*. Longman. (cited on pp. 30, 145).

Ford, T. W., E. Harris, and S. M. Quiring (2014). "Estimating root zone soil moisture using near-surface observations from SMOS". In: *Hydrology and Earth System Sciences* **18**:1, pp. 139–154. doi: 10.5194/hess-18-139-2014 (cited on p. 33).

Franz, T., M. Zreda, R. Rosolem, and T. Ferré (2012a). "Field Validation of a Cosmic-Ray Neutron Sensor Using a Distributed Sensor Network". In: *Vadose Zone Journal* **11**:4. doi: 10.2136/vzj2012.0046 (cited on pp. 37, 98, 108, 110, 112, 116, 118).

Franz, T. E., M. Zreda, R. Rosolem, and T. P. A. Ferré (2013a). "A universal calibration function for determination of soil moisture with cosmic-ray neutrons". In: *Hydrology and Earth System Sciences* **17**:2, pp. 453–460. doi: 10.5194/hess-17-453-2013 (cited on pp. 62, 122).

Franz, T., M. Zreda, R. Rosolem, B. K. Hornbuckle, S. L. Irvin, H. Adams, T. E. Kolb, C. Zweck, and W. J. Shuttleworth (2013b). "Ecosystem-scale measurements of biomass water using cosmic ray neutrons". In: *Geophysical Research Letters* **40**:1936. doi: 10.1002/grl.50791 (cited on p. 131).

Franz, T., T. Wang, W. Avery, C. Finkenbiner, and L. Brocca (2015). "Combined analysis of soil moisture measurements from roving and fixed cosmic ray neutron probes for multiscale real-time monitoring". In: *Geophys. Res. Lett.* **42**:9, pp. 3389–3396. doi: 10.1002/2015gl063963 (cited on pp. 63, 122, 126).

Franz, T. E., M. Zreda, T. P. A. Ferré, R. Rosolem, C. Zweck, S. Stillman, X. Zeng, and W. J. Shuttleworth (2012b). "Measurement depth of the cosmic ray soil moisture probe affected by hydrogen from various sources". In: *Water Resources Research* **48**:8. doi: 10.1029/2012WR011871 (cited on pp. 108, 109).

Franz, T. E., M. Zreda, T. P. A. Ferré, and R. Rosolem (2013c). "An assessment of the effect of horizontal soil moisture heterogeneity on the area-average measurement of cosmic-ray neutrons". In: *Water Resources Research* **49**:10, pp. 6450–6458. doi: 10.1002/wrcr.20530 (cited on pp. 67, 108).

Franz, T. E., A. Wahbi, M. Vreugdenhil, G. Weltin, L. Heng, M. Oismueller, P. Strauss, G. Dercon, and D. Desilets (2016). "Using Cosmic-Ray Neutron Probes to Monitor Landscape Scale Soil Water Content in Mixed Land Use Agricultural Systems". In: *Applied and Environmental Soil Science* **2016**: (cited on p. 37).

Fry, M. J., J. Evans, H. Ward, J. Blake, L. Ball, and L. Doughty (2014). "The Provision Of Data From The COSMOS-UK Soil Moisture Monitoring Network". In: *International Conference on Hydroinformatics*, p. 56 (cited on p. 37).

Fu, C.-C., P.-K. Wang, L.-C. Lee, C.-H. Lin, W.-Y. Chang, G. Giuliani, and D. Ouzounov (2015). "Temporal variation of gamma rays as a possible precursor of earthquake in the Longitudinal Valley of eastern Taiwan". In: *Journal of Asian Earth Sciences* **114, Part 2**: Earthquake Precursory Studies, pp. 362–372. doi: 10.1016/j.jseaes.2015.04.035 (cited on p. 89).

G

Gan, T. Y., E. M. Dlamini, and G. F. Biftu (1997). "Effects of model complexity and structure, data quality, and objective functions on hydrologic modeling". In: *Journal of Hydrology* **192**:1, pp. 81–103. doi: 10.1016/S0022-1694(96)03114-9 (cited on p. 143).

Gao, X., X. Zhao, B. C. Si, L. Brocca, W. Hu, and P. Wu (2015). "Catchment-scale variability of absolute versus temporal anomaly soil moisture: Time-invariant part not always plays the leading role". In: *Journal of Hydrology* **529, Part 3**: pp. 1669–1678. doi: 10.1016/j.jhydrol.2015.08.020 (cited on p. 139).

Gaur, N. and B. P. Mohanty (2013). "Evolution of physical controls for soil moisture in humid and subhumid watersheds". In: *Water Resources Research* **49**:3, pp. 1244–1258 (cited on p. 29).

Glasstone, S. and M. C. Edlund (1952). *The elements of nuclear reactor theory.* New York: Van Nostrand, vii, 416 p. (Cited on p. 54).

Goldhagen, P., M. Reginatto, T. Kniss, J. W. Wilson, R. C. Singleterry, I. W. Jones, and W. van Steveninck (2002). "Measurement of the energy spectrum of cosmic-ray induced neutrons aboard an ER-2 high-altitude airplane". In: *Nuclear Instruments and Methods in Physics Research Section A: Accelerators, Spectrometers, Detectors and Associated Equipment* **476**:1–2, pp. 42–51. doi: 10.1016/S0168-9002(01)01386-9 (cited on p. 50).

Goldhagen, P., J. Clem, and J. Wilson (2004). "The energy spectrum of cosmic-ray induced neutrons measured on an airplane over a wide range of altitude and latitude". In: *Radiation Protection Dosimetry* **110**:1-4, pp. 387–392. doi: 10.1093/rpd/nch216 (cited on pp. 155, 158).

Graeff, T., E. Zehe, D. Reusser, E. Lück, B. Schröder, G. Wenk, H. John, and A. Bronstert (2009). "Process identification through rejection of model structures in a mid-mountainous rural catchment: observations of rainfall–runoff response, geophysical conditions and model inter-comparison". In: *Hydrological Processes* **23**:5, pp. 702–718. doi: 10.1002/hyp.7171 (cited on pp. 127, 141).

Grayson, R. B., A. W. Western, F. H. Chiew, and G. Blöschl (1997). "Preferred states in spatial soil moisture patterns: Local and nonlocal controls". In: *Water Resources Research* **33**:12, pp. 2897–2908 (cited on p. 29).

Greacen, E. L. (1981). *Soil water assessment by the neutron method*. Australia: CSIRO (cited on p. 125).

Gruber, A., W. A. Dorigo, S. Zwieback, A. Xaver, and W. Wagner (2013). "Characterizing coarse-scale representativeness of in situ soil moisture measurements from the International Soil Moisture Network". In: *Vadose Zone Journal* **12**:2 (cited on p. 27).

Gudima, K., S. Mashnik, and V. Toneev (1983). "Cascade-exciton model of nuclear reactions". In: *Nuclear Physics A* **401**:2, pp. 329–361. doi: 10.1016/0375-9474(83)90532-8 (cited on p. 51).

Gupta, H. V., C. Perrin, G. Blöschl, A. Montanari, R. Kumar, M. Clark, and V. Andréassian (2014). "Large-sample hydrology: a need to balance depth with breadth". In: *Hydrology and Earth System Sciences* **18**:2, pp. 463–477. doi: 10.5194/hess-18-463-2014 (cited on p. 136).

Gupta, H. V., H. Kling, K. K. Yilmaz, and G. F. Martinez (2009). "Decomposition of the mean squared error and NSE performance criteria: Implications for improving hydrological modelling". In: *Journal of Hydrology* **377**:1, pp. 80–91 (cited on pp. 90, 143).

Guyodo, Y. and J.-P. Valet (1996). "Relative variations in geomagnetic intensity from sedimentary records: the past 200,000 years". In: *Earth and Planetary Science Letters* **143**:1–4, pp. 23–36. doi: 10.1016/0012-821X(96)00121-5 (cited on p. 84).

H

Hagemeier, M. (2002). *Funktionale Kronenarchitektur mitteleuropäischer Baumarten - am Beispiel von Hängebirke, Waldkiefer, Traubeneiche, Hainbuche, Winterlinde und Rotbuche*. Schweizerbart'sche Verlagsbuchhandlung (cited on p. 131).

Haghnegahdar, A., B. A. Tolson, J. R. Craig, and K. T. Paya (2015). "Assessing the performance of a semi-distributed hydrological model under various watershed discretization schemes". In: *Hydrological Processes* **29**:18, pp. 4018–4031. doi: 10.1002/hyp.10550 (cited on p. 138).

Hall, S. A. (2013). "Characterization of fluid flow in a shear band in porous rock using neutron radiography". In: *Geophysical Research Letters* **40**:11, pp. 2613–2618. doi: 10.1002/grl.50528 (cited on p. 36).

Han, X., H.-J. H. Franssen, R. Rosolem, R. Jin, X. Li, and H. Vereecken (2015). "Correction of systematic model forcing bias of CLM using assimilation of cosmic-ray Neutrons and land surface temperature: a study in the Heihe Catchment, China". In: *Hydrology and Earth System Sciences* **19**:1, pp. 615–629 (cited on pp. 137, 140).

Hawdon, A., D. McJannet, and J. Wallace (2014). "Calibration and correction procedures for cosmic-ray neutron soil moisture probes located across Australia". In: *Water Resources Research* **50**:6, pp. 5029–5043. doi: 10.1002/2013WR015138 (cited on pp. 37, 88, 91).

Heidbüchel, I., A. Güntner, and T. Blume (2016). "Use of cosmic-ray neutron sensors for soil moisture monitoring in forests". In: *Hydrology and Earth System Sciences* **20**:3, pp. 1269–1288. doi: 10.5194/hess-20-1269-2016 (cited on pp. 61, 66, 89, 108, 112, 117, 126).

Hendrick, L. D. and R. D. Edge (1966). "Cosmic-Ray Neutrons near the Earth". In: *Phys. Rev.* **145**: (4), pp. 1023–1025. doi: 10.1103/PhysRev.145.1023 (cited on pp. 36, 155).

Herbst, K., A. Kopp, and B. Heber (2013). "Influence of the terrestrial magnetic field geometry on the cutoff rigidity of cosmic ray particles". In: *Annales Geophysicae*. Vol. 31. 10. Copernicus GmbH, pp. 1637–1643 (cited on p. 84).

Hess, W. N., E. H. Canfield, and R. E. Lingenfelter (1961). "Cosmic-ray neutron demography". In: *Journal of Geophysical Research* **66**:3, pp. 665–677. doi: 10.1029/JZ066i003p00665 (cited on p. 45).

Hignett, C. and S. R. Evett (2002). "Neutron thermalization". In: *Methods of soil analysis. Part* **4**: pp. 501–521 (cited on p. 36).

Hillas, A. M. (2005). "Can diffusive shock acceleration in supernova remnants account for high-energy galactic cosmic rays?" In: *Journal of Physics G: Nuclear and Particle Physics* **31**:5, R95 (cited on p. 41).

Hornbuckle, B., S. Irvin, T. Franz, R. Rosolem, and C. Zweck (2012). "The potential of the COSMOS network to be a source of new soil moisture information for SMOS and SMAP". In: *Geoscience and Remote Sensing Symposium (IGARSS), 2012 IEEE International*. IEEE, pp. 1243–1246 (cited on p. 131).

Hübner, C., R. Cardell-Oliver, R. Becker, K. Spohrer, K. Jotter, and T. Wagenknecht (2009). "Wireless soil moisture sensor networks for environmental monitoring and vineyard irrigation". In: *8th International Conference on Electromagnetic Wave Interaction with Water and Moist Substances (ISEMA 2009), Helsinki, Finland*, pp. 408–415 (cited on p. 35).

Huisman, J. A., S. S. Hubbard, J. D. Redman, and A. P. Annan (2003). "Measuring Soil Water Content with Ground Penetrating Radar: A Review". In: *Vadose Zone Journal* **2**:4, pp. 476–491. doi: 10.2113/2.4.476 (cited on pp. 34, 98).

Hundecha, Y. and A. Bárdossy (2004). "Modeling of the effect of land use changes on the runoff generation of a river basin through parameter regionalization of a watershed model". In: *Journal of Hydrology* **292**:1-4, pp. 281–295. doi: 10.1016/j.jhydrol.2004.01.002 (cited on p. 139).

I

IAEA (2008). *Field estimation of soil water content: A practical guide to methods, instrumentation and sensor technology*. Tech. rep. IAEA-TCS–30. International Atomic Energy Agency, Soil, Water Management, and Crop Nutrition Section Vienna (Austria), p. 141 (cited on p. 36).

Illston, B. G., J. B. Basara, C. A. Fiebrich, K. C. Crawford, E. Hunt, D. K. Fisher, R. Elliott, and K. Humes (2008). "Mesoscale monitoring of soil moisture across a statewide network". In: *Journal of Atmospheric and Oceanic Technology* **25**:2, pp. 167–182 (cited on p. 27).

Iskandar, D., H. Yamazawa, and T. Iida (2004). "Quantification of the dependency of radon emanation power on soil temperature". In: *Applied Radiation and Isotopes* **60**:6, pp. 971–973. doi: 10.1016/j.apradiso.2004.02.003 (cited on p. 26).

IUSS Working Group et al. (2014). "World reference base for soil resources 2014". In: *FAO, Rome* (cited on p. 30).

Iwema, J., R. Rosolem, R. Baatz, T. Wagener, and H. R. Bogena (2015). "Investigating temporal field sampling strategies for site-specific calibration of three soil moisture–neutron intensity parameterisation methods". In: *Hydrology and Earth System Sciences* **19**:7, pp. 3203–3216. doi: 10.5194/hess-19-3203-2015 (cited on pp. 61, 108).

J

Jacklyn, R. and A. Fenton (1957). "Changes in the high-latitude east-west asymmetry of cosmic rays". In: *Physical Review* **106**:4, p. 809 (cited on p. 43).

Jackson, T. J., R. Bindlish, M. H. Cosh, T. Zhao, P. J. Starks, D. D. Bosch, M. Seyfried, M. S. Moran, D. C. Goodrich, Y. H. Kerr, and D. Leroux (2012). "Validation of Soil Moisture and Ocean Salinity (SMOS) Soil Moisture Over Watershed Networks in the U.S." In: *IEEE Transactions on Geoscience and Remote Sensing* **50**:5, pp. 1530–1543. doi: 10.1109/TGRS.2011.2168533 (cited on pp. 33, 122).

Jawson, S. D. and J. D. Niemann (2007). "Spatial patterns from {EOF} analysis of soil moisture at a large scale and their dependence on soil, land-use, and topographic properties". In: *Advances in Water Resources* **30**:3, pp. 366 –381. doi: 10.1016/j.advwatres.2006.05.006 (cited on p. 29).

Jiang, D., J. Wang, Y. Huang, K. Zhou, X. Ding, and J. Fu (2014). "The review of GRACE data applications in terrestrial hydrology monitoring". In: *Advances in Meteorology* **2014**: (cited on p. 33).

Juckett, D. A. (2007). "Correlation of a 140-year global time signature in cancer mortality birth cohorts with galactic cosmic ray variation". In: *International Journal of Astrobiology* **6**: (04), pp. 307–319. doi: 10.1017/S1473550407003928 (cited on p. 46).

Jun, I., I. Mitrofanov, M. L. Litvak, A. B. Sanin, W. Kim, A. Behar, W. V. Boynton, L. DeFlores, F. Fedosov, D. Golovin, C. Hardgrove, K. Harshman, A. S. Kozyrev, R. O. Kuzmin, A. Malakhov, M. Mischna, J. Moersch, M. Mokrousov, S. Nikiforov, V. N. Shvetsov, C. Tate, V. I. Tret'yakov, and

A. Vostrukhin (2013). “Neutron background environment measured by the Mars Science Laboratory's Dynamic Albedo of Neutrons instrument during the first 100 sols”. In: *J. Geophys. Res. Planets* **118**:11, pp. 2400–2412. doi: 10.1002/2013je004510 (cited on p. 62).

Jung, M., M. Reichstein, P. Ciais, S. I. Seneviratne, J. Sheffield, M. L. Goulden, G. Bonan, A. Cescatti, J. Chen, R. De Jeu, et al. (2010). “Recent decline in the global land evapotranspiration trend due to limited moisture supply”. In: *Nature* **467**:7318, pp. 951–954 (cited on p. 27).

K

Kancírová, M. and K. Kudela (2014). “Cloud cover and cosmic ray variations at Lomnickỳ štít high altitude observing site”. In: *Atmospheric Research* **149**: pp. 166–173 (cited on p. 85).

Kasner, M. (2016). “Kalibrierung mobiler Cosmic-Ray-Neutronen-Messung in Bezug auf Vegetation und Bodeneigenschaften zur Abschätzung räumlicher Bodenfeuchte”. MA thesis. Halle (Saale), Germany: Martin-Luther-Universität Halle-Wittenberg (cited on pp. 122, 125, 127, 131).

Kazama, T. and S. Okubo (2009). “Hydrological modeling of groundwater disturbances to observed gravity: Theory and application to Asama Volcano, Central Japan”. In: *Journal of Geophysical Research: Solid Earth* **114**:B8. doi: 10.1029/2009JB006391 (cited on p. 33).

Keeling, R. F. and S. R. Shertz (1992). “Seasonal and interannual variations in atmospheric oxygen and implications for the global carbon cycle”. In: *Nature* **358**:6389, pp. 723–727 (cited on p. 85).

Kerr, Y. H. (2007). “Soil moisture from space: Where are we?” In: *Hydrogeology Journal* **15**:1, pp. 117–120. doi: 10.1007/s10040-006-0095-3 (cited on p. 33).

Kerr, Y. H., P. Waldteufel, J.-P. Wigneron, J.-M. Martinuzzi, J. Font, and M. Berger (2001). “Soil moisture retrieval from space: The Soil Moisture and Ocean Salinity (SMOS) mission”. In: *Geoscience and Remote Sensing, IEEE Transactions on* **39**:8, pp. 1729–1735 (cited on p. 33).

Klaiber, V., U. Seeling, and R. Mutz (2002). “Moisture content of stems of Norway spruce (Picea abies (L.) Karst.) after full tree storage in the stand”. In: *Schweizerische Zeitschrift fur Forstwesen* **153**:6, pp. 210–218 (cited on p. 126).

Klute, A., G. R. Blake, and K. H. Hartge (1986). “Bulk Density”. In: *SSSA Book Series*. Soil Science Society of America. doi: 10.2136/sssabookser5.1.2ed.c13 (cited on p. 30).

Kobelev, P., A. Belov, E. Mavromichalaki, M. Gerontidou, and V. Yanke (2011). “Variations of barometric coefficients of the neutron component in the 22-23 cycles of solar activity”. In: *CD Proc. 32nd ICRC, id0654, Beijing* (cited on p. 88).

Kodama, M. (1980). “Continuous monitoring of snow water equivalent using cosmic ray neutrons”. In: *Cold Regions Science and Technology* **3**:4, pp. 295–303. doi: 10.1016/0165-232x(80)90036-1 (cited on p. 36).

Kodama, M., S. Kudo, and T. Kosuge (1985). “Application of Atmospheric Neutrons to Soil Moisture Measurement”. In: *Soil science* **140**:4, pp. 237–242 (cited on p. 36).

Kögler, S., F. Schmidt, E. Martini, J. Bumberger, S. Zacharias, and U. Wollschläger (2013). "Comparison of two calibration approaches for low-cost soil moisture sensors". In: vol. 7, pp. 51–68 (cited on pp. 35, 70).

König, J. and E. Becker (1919). "Die Bestandteile des Holzes und ihre wirtschaftliche Verwertung". In: *Angewandte Chemie* **32**:40, pp. 155–160 (cited on p. 126).

Korotkov, V. K., M. D. Berkova, A. V. Belov, E. A. Eroshenko, P. G. Kobelev, and V. G. Yanke (2011). "Effect of snow in cosmic ray variations and methods for taking it into consideration". In: *Geomagnetism and Aeronomy* **51**:2, pp. 247–253. doi: 10.1134/S0016793211020095 (cited on p. 84).

Koster, R. D. et al. (2004). "Regions of Strong Coupling Between Soil Moisture and Precipitation". In: *Science* **305**:5687, pp. 1138–1140. doi: 10.1126/science.1100217 (cited on p. 27).

Kowatari, M., K. Nagaoka, S. Satoh, Y. Ohta, J. Abukawa, S. Tachimori, and T. Nakamura (2005). "Evaluation of the Altitude Variation of the Cosmic-ray Induced Environmental Neutrons in the Mt. Fuji Area". In: *Journal of Nuclear Science and Technology* **42**:6, pp. 495–502. doi: 10.1080/18811248.2004.9726416 (cited on p. 158).

Krause, P., D. P. Boyle, and F. Bäse (2005). "Comparison of different efficiency criteria for hydrological model assessment". In: *Advances in Geosciences* **5**: pp. 89–97. doi: 10.5194/adgeo-5-89-2005 (cited on p. 143).

Krüger, H. and H. Moraal (2010). "A calibration neutron monitor: Statistical accuracy and environmental sensitivity". In: *Advances in Space Research* **46**:11, pp. 1394 –1399. doi: 10.1016/j.asr.2010.07.008 (cited on p. 86).

Krüger, H., H. Moraal, J. W. Bieber, J. M. Clem, P. A. Evenson, K. R. Pyle, M. L. Duldig, and J. E. Humble (2008). "A calibration neutron monitor: Energy response and instrumental temperature sensitivity". In: *Journal of Geophysical Research: Space Physics* **113**:A8. A08101. doi: 10.1029/2008JA013229 (cited on pp. 44, 70, 85, 94).

Kudela, K. (2012). "Variability of Low Energy Cosmic Rays Near Earth". In: *Exploring the Solar Wind*. Ed. by M. Lazar. InTech. doi: 10.5772/37482 (cited on pp. 43, 84).

Kulmala, M., P. Hari, I. Riipinen, and V.-M. Kerminen (2009). "On the possible links between tree growth and galactic cosmic rays". In: *New Phytologist* **184**:3, pp. 511–513. doi: 10.1111/j.1469-8137.2009.03060.x (cited on p. 46).

Kumar, R., L. Samaniego, and S. Attinger (2013a). "Implications of distributed hydrologic model parameterization on water fluxes at multiple scales and locations". In: *Water Resources Research* **49**:1, pp. 360–379. doi: 10.1029/2012WR012195 (cited on p. 138).

Kumar, R., B. Livneh, and L. Samaniego (2013b). "Toward computationally efficient large-scale hydrologic predictions with a multiscale regionalization scheme". In: *Water Resources Research* **49**:9, pp. 5700–5714. doi: 10.1002/wrcr.20431 (cited on pp. 27, 138).

Köhli, M., M. Schrön, M. Zreda, U. Schmidt, P. Dietrich, and S. Zacharias (2015). "Footprint characteristics revised for field-scale soil moisture monitoring with cosmic-ray neutrons". In: *Water Resources Research* **51**:7. (M. Köhli and M. Schrön contributed equally to this work.), pp. 5772–5790. doi: 10.1002/

2015WR017169 (cited on pp. 14, 36, 50, 52, 55, 62, 63, 67, 76, 79, 80, 86, 92, 96–103, 107–110, 116, 118, 132, 140, 155, 166, 181, 185).

Köhli, M., F. Allmendinger, W. Häussler, T. Schröder, M. Klein, M. Meven, and U. Schmidt (2016). "Efficiency and spatial resolution of the CASCADE thermal neutron detector". In: *Nuclear Instruments and Methods in Physics Research Section A: Accelerators, Spectrometers, Detectors and Associated Equipment* **828**: pp. 242 –249. doi: 10.1016/j.nima.2016.05.014 (cited on pp. 67, 98).

L

Lacki, B. C., T. A. Thompson, and E. Quataert (2010). "The Physics of the Far-Infrared-Radio Correlation. I. Calorimetry, Conspiracy, and Implications". In: *The Astrophysical Journal* **717**:1, pp. 1–28. doi: 10.1088/0004-637x/717/1/1 (cited on p. 41).

Lal, D. (1991). "Cosmic ray labeling of erosion surfaces: in situ nuclide production rates and erosion models". In: *Earth and Planetary Science Letters* **104**:2, pp. 424–439. doi: 10.1016/0012-821X(91)90220-C (cited on p. 45).

Landau, L. D. and E. Lifshitz (1966). "Hydrodynamik". In: *Lehrbuch der theoretischen Physik, Berlin: Akademie-Verlag, 1966* **1**: (cited on p. 28).

Larson, K. M., E. E. Small, E. D. Gutmann, A. L. Bilich, J. J. Braun, and V. U. Zavorotny (2008). "Use of GPS receivers as a soil moisture network for water cycle studies". In: *Geophysical Research Letters* **35**:24. doi: 10.1029/2008GL036013 (cited on pp. 34, 98).

Lawrence, D. J., W. C. Feldman, J. O. Goldsten, T. J. McCoy, D. T. Blewett, W. V. Boynton, L. G. Evans, L. R. Nittler, E. A. Rhodes, and S. C. Solomon (2010). "Identification and measurement of neutron-absorbing elements on Mercury's surface". In: *Icarus* **209**:1. Mercury after Two MESSENGER Flybys, pp. 195 –209. doi: 10.1016/j.icarus.2010.04.005 (cited on p. 155).

Lee, S., J. Kirby, G. Klein, and C. Rule (1961). *Fantastic Four*. Vol. 1. ISSN: 0274-5291. Marvel Comics (cited on pp. 40, 154).

LfULG (2001). "Ermittlung von Erträgen auf dem Grünland." In: *Grünland "Aktuell"*. Fachmaterial (cited on p. 126).

Lifton, N., T. Sato, and T. J. Dunai (2014). "Scaling in situ cosmogenic nuclide production rates using analytical approximations to atmospheric cosmic-ray fluxes". In: *Earth and Planetary Science Letters* **386**:0, pp. 149 –160. doi: 10.1016/j.epsl.2013.10.052 (cited on p. 98).

Litvak, M. L. et al. (2014). "Local variations of bulk hydrogen and chlorine-equivalent neutron absorption content measured at the contact between the Sheepbed and Gillespie Lake units in Yellowknife Bay, Gale Crater, using the DAN instrument onboard Curiosity". In: *J. Geophys. Res. Planets* **119**:6, pp. 1259–1275. doi: 10.1002/2013je004556 (cited on pp. 52, 55).

Lv, L., T. E. Franz, D. A. Robinson, and S. B. Jones (2014). "Measured and Modeled Soil Moisture Compared with Cosmic-Ray Neutron Probe Estimates in a Mixed Forest". In: *Vadose Zone Journal* **13**:12, pp. – (cited on pp. 61, 108, 129).

M

Mai, J., M. Cuntz, M. Shafii, M. Zink, D. Schäfer, S. Thober, L. Samaniego, and B. Tolson (2016). "Multi-objective vs. single-objective calibration of a hydrologic model using single- and multi-objective screening". In: *EGU General Assembly Conference Abstracts*. Vol. 18, p. 8997 (cited on pp. 90, 143).

Malkov, M. A. and L. O. Drury (2001). "Nonlinear theory of diffusive acceleration of particles by shock waves". In: *Rep. Prog. Phys.* **64**:4, pp. 429–481. doi: 10.1088/0034-4885/64/4/201 (cited on p. 41).

Masarik, J. and J. Beer (2009). "An updated simulation of particle fluxes and cosmogenic nuclide production in the Earth's atmosphere". In: *Journal of Geophysical Research: Atmospheres* **114**:D11 (cited on p. 45).

Masoudi, S. F. and M. Ghashami (2014). "D–T neutron generators as a feasibility tool for landmine detection based on neutron backscattering method". In: *Annals of Nuclear Energy* **65**: pp. 441–445. doi: 10.1016/j.anucene.2013.11.030 (cited on p. 36).

Matthiä, D., B. Heber, G. Reitz, M. Meier, L. Sihver, T. Berger, and K. Herbst (2009). "Temporal and spatial evolution of the solar energetic particle event on 20 January 2005 and resulting radiation doses in aviation". In: *Journal of Geophysical Research: Space Physics* **114**:A8. A08104. doi: 10.1029/2009JA014125 (cited on p. 84).

Maurice, S., D. J. Lawrence, W. C. Feldman, R. C. Elphic, and O. Gasnault (2004). "Reduction of neutron data from Lunar Prospector". In: *Journal of Geophysical Research: Planets* **109**:E7. doi: 10.1029/2003JE002208 (cited on p. 98).

Mavromichalaki, H., P. Preka-Papadema, B. Petropoulos, I. Tsagouri, S. Georgakopoulos, and J. Polygiannakis (2003). "Low- and high-frequency spectral behavior of cosmic-ray intensity for the period 1953–1996". In: *Annales Geophysicae* **21**:8, pp. 1681–1689. doi: 10.5194/angeo-21-1681-2003 (cited on p. 43).

Mavromichalaki, H. et al. (2011). "Applications and usage of the real-time Neutron Monitor Database". In: *Advances in Space Research* **47**:12, pp. 2210 –2222. doi: 10.1016/j.asr.2010.02.019 (cited on p. 46).

McJannet, D., T. Franz, A. Hawdon, D. Boadle, B. Baker, A. Almeida, R. Silberstein, T. Lambert, and D. Desilets (2014). "Field testing of the universal calibration function for determination of soil moisture with cosmic-ray neutrons". In: *Water Resources Research* **50**:6, pp. 5235–5248. doi: 10.1002/2014WR015513 (cited on pp. 55, 62, 102, 122).

McKinney, G. W., D. J. Lawrence, T. H. Prettyman, R. C. Elphic, W. C. Feldman, and J. J. Hagerty (2006). "MCNPX benchmark for cosmic ray interactions with the Moon". In: *Journal of Geophysical Research: Planets* **111**:E6. doi: 10.1029/2005JE002551 (cited on p. 98).

Mekonnen, M. M. and A. Y. Hoekstra (2011). "The green, blue and grey water footprint of crops and derived crop products". In: *Hydrology and Earth System Sciences* **15**:5, pp. 1577–1600. doi: 10.5194/hess-15-1577-2011 (cited on p. 26).

Mercer, J. A., E. M. Hussein, and E. J. Waller (2007). "A non-intrusive neutron device for in situ detection of petroleum contamination in soil". In: *Nuclear Instruments and Methods in Physics Research Section B: Beam Interactions with*

Materials and Atoms **263**:1, pp. 217–220. DOI: 10.1016/j.nimb.2007.04.088 (cited on p. 36).

Mitrofanov, I., D. Anfimov, A. Kozyrev, M. Litvak, A. Sanin, V. Tret'yakov, A. Krylov, V. Shvetsov, W. Boynton, C. Shinohara, D. Hamara, and R. S. Saunders (2002). "Maps of Subsurface Hydrogen from the High Energy Neutron Detector, Mars Odyssey". In: *Science* **297**:5578, pp. 78–81. DOI: 10.1126/science.1073616 (cited on pp. 36, 155).

Mitrofanov, I. G., M. L. Litvak, A. B. Sanin, R. D. Starr, D. I. Lisov, R. O. Kuzmin, A. Behar, W. V. Boynton, C. Hardgrove, K. Harshman, I. Jun, R. E. Milliken, M. A. Mischna, J. E. M. ch, and C. G. Tate (2014). "Water and chlorine content in the Martian soil along the first 1900 m of the Curiosity rover traverse as estimated by the DAN instrument". In: *J. Geophys. Res. Planets* **119**:7, pp. 1579–1596. DOI: 10.1002/2013je004553 (cited on p. 52).

Mitrofanov, I., A. Malakhov, M. Mokrousov, D. Golovin, F. Fedosov, A. Kozyrev, D. Lisov, M. Litvak, S. Nikiforov, A. Sanin, V. Tret'yakov, and A. Vostrukhin (2016). "FREND neutron telescope for mapping the Martian water with fine spatial resolution". In: *EGU General Assembly Conference Abstracts*. Vol. 18, p. 16402 (cited on pp. 155, 163).

Mohanty, B. P., J. S. Famiglietti, and T. H. Skaggs (2000). "Evolution of soil moisture spatial structure in a mixed vegetation pixel during the Southern Great Plains 1997 (SGP97) Hydrology Experiment". In: *Water Resources Research* **36**:12, pp. 3675–3686. DOI: 10.1029/2000WR900258 (cited on p. 29).

Mollenhauer, H., R. Schima, P. Remmler, O. Mollenhauer, T. Hutschenreuther, H. Toepfer, P. Dietrich, and J. Bumberger (2015). "Mobile Wireless Sensor Networks for Advanced Soil Sensing and Ecosystem Monitoring". In: *EGU General Assembly Conference Abstracts*. Vol. 17, p. 6187 (cited on pp. 35, 72).

Moraal, H. and K. G. McCracken (2012). "The Time Structure of Ground Level Enhancements in Solar Cycle 23". In: *Space Science Reviews* **171**:1, pp. 85–95. DOI: 10.1007/s11214-011-9742-7 (cited on p. 43).

Moraal, H., A. Benadie, D. De Villiers, J. W. Bieber, J. M. Clem, P. E. Evenson, K. R. Pyle, L. Shulman, M. L. Duldig, and J. E. Humble (2001). "A mobile neutron monitor to intercalibrate the worldwide network". In: *International Cosmic Ray Conference*. Vol. 10, p. 4083 (cited on p. 70).

Moreira, A., G. Krieger, I. Hajnsek, K. Papathanassiou, M. Younis, P. Lopez-Dekker, S. Huber, M. Villano, M. Pardini, M. Eineder, F. D. Zan, and A. Parizzi (2015). "Tandem-L: A Highly Innovative Bistatic SAR Mission for Global Observation of Dynamic Processes on the Earth's Surface". In: *IEEE Geoscience and Remote Sensing Magazine* **3**:2, pp. 8–23. DOI: 10.1109/MGRS.2015.2437353 (cited on p. 33).

Mueller, B. and X. Zhang (2015). "Causes of drying trends in northern hemispheric land areas in reconstructed soil moisture data". In: *Climatic Change* **134**:1-2, pp. 255–267. DOI: 10.1007/s10584-015-1499-7 (cited on p. 26).

Müller, J. and G. Müller (1988). "Berechnung der Verdunstung landwirtschaftlicher Produktionsgebiete. I: Beschreibung des zur Bestimmung der aktuellen Evapotranspiration von Kulturpflanzenbeständen erarbeiteten Modells". In: *Zeitschrift für Meteorologie* **38**:5, pp. 332–337 (cited on p. 137).

N

Nash, J. E. and J. V. Sutcliffe (1970). "River flow forecasting through conceptual models part I—A discussion of principles". In: *Journal of hydrology* **10**:3, pp. 282–290 (cited on p. 143).

Navas-Guzmán, F., J. Fernández-Gálvez, M. J. Granados-Muñoz, J. L. Guerrero-Rascado, J. A. Bravo-Aranda, and L. Alados-Arboledas (2014). "Tropospheric water vapour and relative humidity profiles from lidar and microwave radiometry". In: *Atmospheric Measurement Techniques* **7**:5, pp. 1201–1211 (cited on p. 90).

Nikolić, S., G. van de Ven, K. Heng, D. Kupko, B. Husemann, J. C. Raymond, J. P. Hughes, and J. Falcon-Barroso (2013). "An Integral View of Fast Shocks Around Supernova 1006". In: *Science*. doi: 10.1126/science.1228297 (cited on p. 41).

Norbiato, D., M. Borga, S. Degli Esposti, E. Gaume, and S. Anquetin (2008). "Flash flood warning based on rainfall thresholds and soil moisture conditions: An assessment for gauged and ungauged basins". In: *Journal of Hydrology* **362**:3, pp. 274–290 (cited on p. 27).

Nowak, W., F. P. J. De Barros, and Y. Rubin (2010). "Bayesian geostatistical design: Task-driven optimal site investigation when the geostatistical model is uncertain". In: *Water Resources Research* **46**:3 (cited on p. 118).

Nurmi, J. (1999). "The storage of logging residue for fuel". In: *Biomass and Bioenergy* **17**:1, pp. 41–47. doi: 10.1016/S0961-9534(99)00023-9 (cited on p. 126).

O

Obhođaš, J., D. Sudac, K. Nađ, V. Valković, G. Nebbia, and G. Viesti (2004). "The soil moisture and its relevance to the landmine detection by neutron backscattering technique". In: *Nuclear Instruments and Methods in Physics Research Section B: Beam Interactions with Materials and Atoms* **213**: pp. 445–451 (cited on p. 36).

Ochsner, T. E., M. H. Cosh, R. H. Cuenca, W. A. Dorigo, C. S. Draper, Y. Hagimoto, Y. H. Kerr, E. G. Njoku, E. E. Small, and M. Zreda (2013). "State of the art in large-scale soil moisture monitoring". In: *Soil Science Society of America Journal* **77**:6, pp. 1888–1919 (cited on pp. 27, 122).

Oh, S., J. W. Bieber, P. Evenson, J. Clem, Y. Yi, and Y. Kim (2013). "Record neutron monitor counting rates from galactic cosmic rays". In: *J. Geophys. Res. Space Physics* **118**: pp. 5431–5436. doi: 10.1002/jgra.50544 (cited on pp. 70, 84, 177).

Oldak, A., Y. Pachepsky, T. J. Jackson, and W. J. Rawls (2002). "Statistical properties of soil moisture images revisited". In: *Journal of Hydrology* **255**: pp. 12–24. doi: 10.1016/S0022-1694(01)00507-8 (cited on p. 132).

Olive, K. A., Particle Data Group, et al. (2014). "Review of particle physics". In: *Chinese Physics C* **38**:9, p. 090001 (cited on p. 51).

Or, D., P. Lehmann, E. Shahraeeni, and N. Shokri (2013). "Advances in Soil Evaporation Physics—A Review". In: *Vadose Zone Journal* **12**:4, p. 0. doi: 10.2136/vzj2012.0163 (cited on pp. 28, 29).

Orford, K. J. (2000). "The analysis of cosmic ray data". In: *Journal of Physics G: Nuclear and Particle Physics* **26**:4, R1–R26. doi: 10.1088/0954-3899/26/4/201 (cited on p. 66).

Oswald, S. E., M. Menon, A. Carminati, P. Vontobel, E. Lehmann, and R. Schulin (2008). "Quantitative imaging of infiltration, root growth, and root water uptake via neutron radiography". In: *Vadose Zone Journal* **7**:3, pp. 1035–1047 (cited on p. 53).

P

Paasche, H., J. Tronicke, K. Holliger, A. G. Green, and H. Maurer (2006). "Integration of diverse physical-property models: Subsurface zonation and petrophysical parameter estimation based on fuzzy -means cluster analyses". In: *GEOPHYSICS* **71**:3, H33–H44. doi: 10.1190/1.2192927 (cited on p. 118).

Palmiotti, G., M. Salvatores, G. Aliberti, Nuclear Engineering Division, and CEA Cadarache (2007). "Validation of simulation codes for future systems: motivations, approach, and the role of nuclear data". In: *Proceedings of the Fourth Workshop on Neutron Measurements, Evaluations and Applications*. INL (cited on p. 52).

Pan, F. and C. D. Peters-Lidard (2008). "On the Relationship Between Mean and Variance of Soil Moisture Fields". In: *JAWRA Journal of the American Water Resources Association* **44**:1, pp. 235–242. doi: 10.1111/j.1752-1688.2007.00150.x (cited on p. 32).

Pang, Z., J. Cai, J. Fu, W. Song, and Y. Lu (2016). "Adaptability Analysis of Cosmic-Ray Neutron Method to Monitoring Soil Moisture in Desert Steppe". In: *Geo-Informatics in Resource Management and Sustainable Ecosystem*. Springer Science - Business Media, pp. 816–824. doi: 10.1007/978-3-662-49155-3_84 (cited on p. 37).

Paschalis, P., H. Mavromichalaki, V. Yanke, A. Belov, E. Eroshenko, M. Gerontidou, and I. Koutroumpi (2013). "Online application for the barometric coefficient calculation of the NMDB stations". In: *New Astronomy* **19**: pp. 10–18 (cited on p. 88).

Pazirandeh, A., M. Azizi, and S. F. Masoudi (2006). "Monte Carlo assessment of soil moisture effect on high-energy thermal neutron capture gamma-ray by 14N". In: *Applied Radiation and Isotopes* **64**:1, pp. 1 –6. doi: 10.1016/j.apradiso.2005.05.053 (cited on p. 36).

Pellegrin, S. M., C. Whitney, and C. G. Wilson (2010). "A Multichannel Nanoparticle Scintillation Microdevice With Integrated Waveguides for Alpha, Beta, Gamma, X-Ray, and Neutron Detection". In: *Journal of Microelectromechanical Systems* **19**:5, pp. 1207–1214. doi: 10.1109/JMEMS.2010.2067435 (cited on p. 56).

Pelowitz, D. B. et al. (2005). "MCNPX user's manual version 2.5. 0". In: *Los Alamos National Laboratory* **76**: (cited on p. 67).

Peplowski, P. N., R. L. Klima, D. J. Lawrence, C. M. Ernst, B. W. Denevi, E. A. Frank, J. O. Goldsten, S. L. Murchie, L. R. Nittler, and S. C. Solomon (2016). "Remote sensing evidence for an ancient carbon-bearing crust on Mercury". In: *Nature Geoscience* **9**:4, pp. 273–276. doi: 10.1038/ngeo2669 (cited on p. 155).

Peterson, J. and U. Langner (1992). *Katalog der Biotoptypen und Nutzungstypen für die CIR-luftbildgestützte Biotoptypen-und Nutzungstypenkartierung im Land Sachsen-Anhalt*. Landesamt für Umweltschutz Sachsen-Anhalt (cited on p. 127).

Petrow, T. and B. Merz (2009). "Trends in flood magnitude, frequency and seasonality in Germany in the period 1951–2002". In: *Journal of Hydrology* **371**:1–4, pp. 129–141. doi: 10.1016/j.jhydrol.2009.03.024 (cited on p. 26).

Pfotzer, G. (1936). "Dreifachkoinzidenzen der Ultrastrahlung aus vertikaler Richtung in der Stratosphäre". German. In: *Zeitschrift für Physik* **102**:1-2, pp. 41–58. doi: 10.1007/BF01336830 (cited on pp. 44, 45).

Phillips, F. M., D. C. Argento, G. Balco, M. W. Caffee, J. Clem, T. J. Dunai, R. Finkel, B. Goehring, J. C. Gosse, A. M. Hudson, A. T. Jull, M. A. Kelly, M. Kurz, D. Lal, N. Lifton, S. M. Marrero, K. Nishiizumi, R. C. Reedy, J. Schaefer, J. O. Stone, T. Swanson, and M. G. Zreda (2016). "The CRONUS-Earth Project: A synthesis". In: *Quaternary Geochronology* **31**: pp. 119–154. doi: 10.1016/j.quageo.2015.09.006 (cited on p. 45).

Pioch, C., V. Mares, and W. Rühm (2010). "Influence of Bonner sphere response functions above 20 MeV on unfolded neutron spectra and doses". In: *Radiation Measurements* **45**:10, pp. 1263 –1267. doi: 10.1016/j.radmeas.2010.05.007 (cited on p. 94).

Pokhrel, P., H. V. Gupta, and T. Wagener (2008). "A spatial regularization approach to parameter estimation for a distributed watershed model". In: *Water Resources Research* **44**:12 (cited on p. 138).

Postel, S. L., G. C. Daily, and P. R. Ehrlich (1996). "Human appropriation of renewable fresh water". In: *Science* **271**:5250, p. 785 (cited on p. 26).

Q

Qin, Y., X. Chen, K. Zhou, P. Klenk, K. Roth, and L. Sun (2013). "Ground-penetrating radar for monitoring the distribution of near-surface soil water content in the Gurbantünggüt Desert". In: *Environmental Earth Sciences* **70**:6, pp. 2883–2893. doi: 10.1007/s12665-013-2528-3 (cited on p. 34).

R

Rakovec, O., R. Kumar, J. Mai, M. Cuntz, S. Thober, M. Zink, S. Attinger, D. Schäfer, M. Schrön, and L. Samaniego (2016). "Multiscale and multivariate evaluation of water fluxes and states over European river basins". In: *J. Hydrometeor* **17**:1, pp. 287–307. doi: 10.1175/jhm-d-15-0054.1 (cited on pp. 138, 142).

Renger, M., K. Bohne, M. Facklam, T. Harrach, W. Riek, W. Schäfer, G. Wessolek, and S. Zacharias (2008). "Ergebnisse und Vorschläge der DBG-Arbeitsgruppe „Kennwerte des Bodengefüges "zur Schätzung bodenphysikalischer Kennwerte". In: *Schriftenreihe "Bodenökologie und Bodengenese"* 40 (cited on p. 125).

Renzullo, L. J., A. I.J. M. van Dijk, J.-M. Perraud, D. Collins, B. Henderson, H. Jin, A. B. Smith, and D. L. McJannet (2014). "Continental satellite soil moisture data assimilation improves root-zone moisture analysis for water resources assessment". In: *Journal of Hydrology* **519**: pp. 2747–2762 (cited on p. 137).

Richards, L. A. (1931). "Capillary conduction of liquids through porous mediums". In: *Journal of Applied Physics* **1**:5, pp. 318–333 (cited on p. 28).

Richardson, L. (1922). "Weather prediction by numerical process". In: (cited on p. 28).

Ridler, M.-E., H. Madsen, S. Stisen, S. Bircher, and R. Fensholt (2014). "Assimilation of SMOS-derived soil moisture in a fully integrated hydrological and soil-vegetation-atmosphere transfer model in Western Denmark". In: *Water Resources Research* **50**:11, pp. 8962–8981. doi: 10.1002/2014WR015392 (cited on p. 136).

Rivera Villarreyes, C. A., G. Baroni, and S. E. Oswald (2011). "Integral quantification of seasonal soil moisture changes in farmland by cosmic-ray neutrons". In: *Hydrology and Earth System Sciences* **15**:12, pp. 3843–3859. doi: 10.5194/hess-15-3843-2011 (cited on pp. 37, 61, 108, 131).

— (2014). "Inverse modelling of cosmic-ray soil moisture for field-scale soil hydraulic parameters". In: *European Journal of Soil Science* **65**:6, pp. 876–886. doi: 10.1111/ejss.12162 (cited on pp. 108, 140).

Robinson, D., C. Campbell, J. Hopmans, B. Hornbuckle, S. B. Jones, R Knight, F Ogden, J Selker, and O Wendroth (2008). "Soil moisture measurement for ecological and hydrological watershed-scale observatories: A review". In: *Vadose Zone Journal* **7**:1, pp. 358–389 (cited on pp. 31, 122, 136).

Röhrig, E., B. Ulrich, et al. (1991). *Ecosystems of the world 7. Temperate deciduous forests*. Elsevier Science Publishers BV (cited on p. 131).

Romano, N. (2014). "Soil moisture at local scale: Measurements and simulations". In: *Journal of Hydrology* **516**: Determination of soil moisture: Measurements and theoretical approaches, pp. 6–20. doi: 10.1016/j.jhydrol.2014.01.026 (cited on p. 34).

Rosolem, R., W. J. Shuttleworth, M. Zreda, T. E. Franz, X. Zeng, and S. a. Kurc (2013a). "The Effect of Atmospheric Water Vapor on Neutron Count in the Cosmic-Ray Soil Moisture Observing System". In: *Journal of Hydrometeorology* **14**:5, pp. 1659–1671. doi: 10.1175/JHM-D-12-0120.1 (cited on pp. 59, 60, 88, 91).

Rosolem, R., T. Hoar, A. Arellano, J. L. Anderson, W. J. Shuttleworth, X. Zeng, and T. E. Franz (2014). "Translating aboveground cosmic-ray neutron intensity to high-frequency soil moisture profiles at sub-kilometer scale". In: *Hydrology and Earth System Sciences* **18**:11, pp. 4363–4379. doi: 10.5194/hess-18-4363-2014 (cited on pp. 137, 140, 141).

Rosolem, R., H. V. Gupta, W. J. Shuttleworth, L. G. G. Gonçalves, and X. Zeng (2013b). "Towards a comprehensive approach to parameter estimation in land surface parameterization schemes". In: *Hydrological Processes* **27**:14, pp. 2075–2097 (cited on p. 143).

Roth, K., R. Schulin, H. Flühler, and W. Attinger (1990). "Calibration of time domain reflectometry for water content measurement using a composite dielectric approach". In: *Water Resources Research* **26**:10, pp. 2267–2273. doi: 10.1029/WR026i010p02267 (cited on p. 35).

Rudiyanto, M. Sakai, M. T. van Genuchten, A. A. Alazba, B. I. Setiawan, and B. Minasny (2015). "A complete soil hydraulic model accounting for capillary and adsorptive water retention, capillary and film conductivity, and hysteresis". In: *Water Resources Research* **51**:11, pp. 8757–8772. doi: 10.1002/2015WR017703 (cited on p. 28).

Ruffolo, D., A. Sáiz, P.-S. Mangeard, N. Kamyan, P. Muangha, T. Nutaro, S. Sumran, C. Chaiwattana, N. Gasiprong, C. Channok, C. Wuttiya, M. Rujiwarodom, P. Tooprakai, B. Asavapibhop, J. W. Bieber, J. Clem, P. Evenson, and K. Munakata (2016). "Monitoring Short-term Cosmic-ray Spectral Variations Using Neutron Monitor Time-delay Measurements". In: *The Astrophysical Journal* **817**:1, p. 38 (cited on pp. 85, 92).

Rühm, W., V. Mares, C. Pioch, E. Weitzenegger, R. Vockenroth, and H. G. Paretzke (2009). "Measurements of secondary neutrons from cosmic radiation with a Bonner sphere spectrometer at 79 N". In: *Radiation and environmental biophysics* **48**:2, pp. 125–133 (cited on p. 76).

Rühm, W., U. Ackermann, C. Pioch, and V. Mares (2012). "Spectral neutron flux oscillations of cosmic radiation on the Earth's surface". In: *Journal of Geophysical Research: Space Physics* **117**:A8. doi: 10.1029/2012JA017524 (cited on p. 43).

S

Salikhov, N. M., A. L. Shepetov, A. P. Chubenko, O. N. Kryakunova, and G. D. Pak (2013). "Observation of the prior earthquake effect on the flux of environmental neutrons, gamma-radiation, and on the local electric field in Tien Shan mountain". In: *ArXiv e-prints* (cited on p. 52).

Salvatores, M., Nuclear Energy Agency, and Organisation for Economic Co-Operation and Development (1994). "A first approach to data needs and target accuracies for hybrid systems". In: *Intermediate Energy Nuclear Data: Models and Codes*. Vol. 27, pp. 313–324 (cited on p. 52).

Samaniego, L. E., A. Bardossy, and R. Kumar (2009). "Conditioning of a mesoscale hydrologic model with proxy soil moisture fields". In: *AGU Fall Meeting Abstracts*. Vol. 1, p. 0959 (cited on p. 150).

Samaniego, L., R. Kumar, and S. Attinger (2010). "Multiscale parameter regionalization of a grid-based hydrologic model at the mesoscale". In: *Water Resources Research* **46**:5. doi: 10.1029/2008WR007327 (cited on pp. 28, 138).

Samaniego, L., R. Kumar, and M. Zink (2013). "Implications of Parameter Uncertainty on Soil Moisture Drought Analysis in Germany". In: *J. Hydrometeor* **14**:1, pp. 47–68. doi: 10.1175/jhm-d-12-075.1 (cited on pp. 26, 27, 138).

Sapundjiev, D., M. Nemry, S. Stankov, and J.-C. Jodogne (2014). "Data reduction and correction algorithm for digital real-time processing of cosmic ray measurements: NM64 monitoring at Dourbes". In: *Advances in Space Research* **53**:1, pp. 71–76 (cited on p. 88).

Sarazin, C. L. and R. Lieu (1998). "Extreme-Ultraviolet Emission from Clusters of Galaxies: Inverse Compton Radiation from a Relic Population of Cosmic-Ray Electrons?" In: *The Astrophysical Journal Letters* **494**:2, p. L177 (cited on p. 41).

Sato, T. and K. Niita (2006). "Analytical Functions to Predict Cosmic-Ray Neutron Spectra in the Atmosphere". In: *Radiation Research* **166**:3, pp. 544–555. doi: 10.1667/RR0610.1 (cited on pp. 50, 98, 99).

Sato, T. (2015). "Analytical Model for Estimating Terrestrial Cosmic Ray Fluxes Nearly Anytime and Anywhere in the World: Extension of PARMA/EXPACS". In: *PLoS ONE* **10**:12. Ed. by Q. Zhang, e0144679. doi: 10.1371/journal.pone.0144679 (cited on pp. 44, 84, 158).

Sax, K. (1963). "The stimulation of plant growth by ionizing radiation". In: *Radiation Botany* **3**:3, pp. 179 –186. doi: 10.1016/S0033-7560(63)80014-9 (cited on p. 46).

Scarascia-Mugnozza, G., H. Oswald, P. Piussi, and K. Radoglou (2000). "Forests of the Mediterranean region: gaps in knowledge and research needs". In: *Forest Ecology and Management* **132**:1, pp. 97–109 (cited on p. 131).

Scheiffele, L. M. (2015). "Assessment of soil moisture dynamics on an irrigated maize field using cosmic ray neutron sensing". MA thesis. Germany: University of Potsdam (cited on p. 112).

Schelle, H., W. Durner, S. Schlüter, H.-J. Vogel, and J. Vanderborght (2013). "Virtual soils: moisture measurements and their interpretation by inverse modeling". In: *Vadose Zone Journal* **12**:3 (cited on p. 31).

Schmelzbach, C., J. Tronicke, and P. Dietrich (2012). "High-resolution water content estimation from surface-based ground-penetrating radar reflection data by impedance inversion". In: *Water Resources Research* **48**:8 (cited on p. 35).

Schmugge, T. J., T. J. Jackson, and H. L. McKim (1980). "Survey of methods for soil moisture determination". In: *Water Resources Research* **16**:6, pp. 961–979 (cited on p. 34).

Schrön, M., S. Zacharias, M. Köhli, J. Weimar, and P. Dietrich (2015). "Monitoring Environmental Water with Ground Albedo Neutrons and Correction for Incoming Cosmic Rays with Neutron Monitor Data". In: *34th International Cosmic-Ray Conference (ICRC 2015)*. Proceedings of Science. url: http://pos.sissa.it/archive/conferences/236/231/ICRC2015_231.pdf (cited on pp. 61, 86, 90, 98).

Schröter, I., H. Paasche, P. Dietrich, and U. Wollschläger (2015). "Estimation of Catchment-Scale Soil Moisture Patterns Based on Terrain Data and Sparse TDR Measurements Using a Fuzzy C-Means Clustering Approach". In: *Vadose Zone Journal* **14**:11, p. 0. doi: 10.2136/vzj2015.01.0008 (cited on pp. 118, 123, 127, 132, 145, 146).

Shangguan, W., Y. Dai, Q. Duan, B. Liu, and H. Yuan (2014). "A global soil data set for earth system modeling". In: *Journal of Advances in Modeling Earth Systems* **6**:1, pp. 249–263. doi: 10.1002/2013MS000293 (cited on p. 132).

Sheffield, J. (2004). "A simulated soil moisture based drought analysis for the United States". In: *J. Geophys. Res.* **109**:D24. doi: 10.1029/2004jd005182 (cited on p. 27).

Shibata, K., O. Iwamoto, T. Nakagawa, N. Iwamoto, A. Ichihara, S. Kunieda, S. Chiba, K. Furutaka, N. Otuka, T. Ohasawa, T. Murata, H. Matsunobu, A. Zukeran, S. Kamanda, and J. Katakura (2011). "JENDL-4.0: A New Library for Nuclear Science and Engineering". In: *Journal of Nuclear Science and Technology* **48**:1, pp. 1–30. doi: 10.1080/18811248.2011.9711675 (cited on pp. 52, 67).

Shuttleworth, J., R. Rosolem, M. Zreda, and T. Franz (2013). "The COsmic-ray Soil Moisture Interaction Code (COSMIC) for use in data assimilation". In:

Hydrology and Earth System Sciences **17**:8, pp. 3205–3217. DOI: 10.5194/hess-17-3205-2013 (cited on pp. 62, 140).

Siemon, B., S. Costabel, W. Voss, U. Meyer, N. Deus, J. Elbracht, T. Günther, and H. Wiederhold (2015). "Airborne and ground geophysical mapping of coastal clays in Eastern Friesland, Germany". In: *Geophysics* **80**:3, WB21–WB34 (cited on p. 155).

Sigouin, M. J. P. and B. C. Si (2016). "Calibration of a non-invasive cosmic-ray probe for wide area snow water equivalent measurement". In: *The Cryosphere* **10**:3, pp. 1181–1190. DOI: 10.5194/tc-10-1181-2016 (cited on p. 63).

Šimunek, J., M. T. van Genuchten, and M. Šejna (2008). "Development and applications of the HYDRUS and STANMOD software packages and related codes". In: *Vadose Zone Journal* **7**:2, pp. 587–600 (cited on p. 136).

Small, E. E., K. M. Larson, C. C. Chew, J. Dong, and T. E. Ochsner (2016). "Validation of GPS-IR Soil Moisture Retrievals: Comparison of Different Algorithms to Remove Vegetation Effects". In: *IEEE Journal of Selected Topics in Applied Earth Observations and Remote Sensing* **PP**:99, pp. 1–12. DOI: 10.1109/JSTARS.2015.2504527 (cited on p. 34).

Smith, M., D. Kivumbi, and L. K. Heng (2002). *Use of the FAO CROPWAT model in deficit irrigation studies*. Food and Agriculture Organization of the United Nations (FAO): FAO (cited on pp. 26, 27).

Stacey, W. M. (2007). *Nuclear Reactor Physics*. 2nd ed. Wiley-VCH (cited on p. 53).

Steinhilber, F., J. A. Abreu, J. Beer, I. Brunner, M. Christl, H. Fischer, U. Heikkilä, P. W. Kubik, M. Mann, K. G. McCracken, et al. (2012). "9,400 years of cosmic radiation and solar activity from ice cores and tree rings". In: *Proceedings of the National Academy of Sciences* **109**:16, pp. 5967–5971 (cited on p. 45).

Strong, A. W., I. V. Moskalenko, and V. S. Ptuskin (2007). "Cosmic-Ray Propagation and Interactions in the Galaxy". In: *Annu. Rev. Nucl. Part. Sci.* **57**:1, pp. 285–327. DOI: 10.1146/annurev.nucl.57.090506.123011 (cited on p. 42).

Su, C.-H., D. Ryu, R. I. Young, A. W. Western, and W. Wagner (2013). "Inter-comparison of microwave satellite soil moisture retrievals over the Murrumbidgee Basin, southeast Australia". In: *Remote Sensing of Environment* **134**: pp. 1–11. DOI: 10.1016/j.rse.2013.02.016 (cited on p. 70).

Sutanudjaja, E. H., L. P. H. van Beek, S. M. de Jong, F. C. van Geer, and M. F. P. Bierkens (2014). "Calibrating a large-extent high-resolution coupled groundwater-land surface model using soil moisture and discharge data". In: *Water Resources Research* **50**:1, pp. 687–705. DOI: 10.1002/2013WR013807 (cited on p. 150).

T

Tabatabaeenejad, A., M. Burgin, X. Duan, and M. Moghaddam (2015). "P-Band Radar Retrieval of Subsurface Soil Moisture Profile as a Second-Order Polynomial: First AirMOSS Results". In: *IEEE Transactions on Geoscience and Remote Sensing* **53**:2, pp. 645–658. DOI: 10.1109/TGRS.2014.2326839 (cited on p. 33).

Tanskanen, P. J. (1968). "Influence of Snow on Neutron Monitor Intensity". In: *Nature* **219**:5157, pp. 926–927. DOI: 10.1038/219926a0 (cited on p. 84).

Taylor, C. M. (2015). "Detecting soil moisture impacts on convective initiation in Europe". In: *Geophysical Research Letters* **42**:11, pp. 4631–4638. doi: 10.1002/2015GL064030 (cited on p. 27).

Taylor, C. M., C. E. Birch, D. J. Parker, N. Dixon, F. Guichard, G. Nikulin, and G. M. S. Lister (2013). "Modeling soil moisture-precipitation feedback in the Sahel: Importance of spatial scale versus convective parameterization". In: *Geophysical Research Letters* **40**:23, pp. 6213–6218. doi: 10.1002/2013GL058511 (cited on p. 27).

Thébault, E., C. C. Finlay, C. D. Beggan, P. Alken, J. Aubert, O. Barrois, F. Bertrand, T. Bondar, A. Boness, L. Brocco, et al. (2015). "International geomagnetic reference field: the 12th generation". In: *Earth, Planets and Space* **67**:1, pp. 1–19 (cited on p. 85).

Todini, E. (2007). "A mass conservative and water storage consistent variable parameter Muskingum-Cunge approach". In: *Hydrology and Earth System Sciences* **11**:5, pp. 1645–1659. doi: 10.5194/hess-11-1645-2007 (cited on p. 139).

Tolson, B. A. and C. A. Shoemaker (2007). "Dynamically dimensioned search algorithm for computationally efficient watershed model calibration". In: *Water Resources Research* **43**:1 (cited on p. 143).

Topp, G. C., J. L. Davis, and A. P. Annan (1980). "Electromagnetic determination of soil water content: Measurements in coaxial transmission lines". In: *Water Resources Research* **16**:3, pp. 574–582. doi: 10.1029/WR016i003p00574 (cited on p. 34).

Troxler. *Troxler Model 3440. Surface Moisture-Density Gauge: Manual of operation and instructions*. Troxler Electronic Laboratories Inc., NC 27709, USA. url: http://www.troxlerlabs.com/downloads/pdfs/3440/3440manual.pdf (cited on p. 35).

Tsuchiya, H. (2014). "Surrounding material effect on measurement of thunderstorm-related neutrons". In: *Astroparticle Physics* **57–58**: pp. 33–38. doi: 10.1016/j.astropartphys.2014.03.009 (cited on p. 178).

Tsyganenko, N. A. (1998). "Modeling of twisted/warped magnetospheric configurations using the general deformation method". In: *Journal of Geophysical Research: Space Physics* **103**:A10, pp. 23551–23563. doi: 10.1029/98JA02292 (cited on p. 85).

Tuttle, S. and G. Salvucci (2016). "Empirical evidence of contrasting soil moisture–precipitation feedbacks across the United States". In: *Science* **352**:6287, pp. 825–828. doi: 10.1126/science.aaa7185 (cited on p. 27).

Tuttle, S. E. and G. D. Salvucci (2014). "A new approach for validating satellite estimates of soil moisture using large-scale precipitation: Comparing AMSR-E products". In: *Remote Sensing of Environment* **142**: pp. 207–222. doi: 10.1016/j.rse.2013.12.002 (cited on p. 33).

U

Usoskin, I. G., O. G. Gladysheva, P. Bobik, K. Kudela, and H. Kananen (1999). "Connections between neutron monitor count rate and solar modulation strength". In: *Czechoslovak Journal of Physics* **49**:12, pp. 1743–1749 (cited on p. 44).

V

Vereecken, H., R. Kasteel, J. Vanderborght, and T. Harter (2007). "Upscaling hydraulic properties and soil water flow processes in heterogeneous soils". In: *Vadose Zone Journal* **6**:1, pp. 1–28 (cited on pp. 27, 28, 136, 137).

Vereecken, H., J. A. Huisman, H. Bogena, J. Vanderborght, J. A. Vrugt, and J. W. Hopmans (2008). "On the value of soil moisture measurements in vadose zone hydrology: A review". In: *Water Resources Research* **44**:4. doi: 10.1029/2008WR006829 (cited on pp. 27, 136).

Vienken, T. and P. Dietrich (2011). "Field evaluation of methods for determining hydraulic conductivity from grain size data". In: *Journal of Hydrology* **400**:1, pp. 58–71 (cited on p. 136).

Vink, J., J. Bleeker, K. van der Heyden, A. Bykov, A. Bamba, and R. Yamazaki (2006). "The X-Ray Synchrotron Emission of RCW 86 and the Implications for Its Age". In: *The Astrophysical Journal* **648**:1, pp. L33–L37. doi: 10.1086/507628 (cited on p. 41).

W

Wagener, T. and H. V. Gupta (2005). "Model identification for hydrological forecasting under uncertainty". In: *Stochastic Environmental Research and Risk Assessment* **19**:6, pp. 378–387. doi: 10.1007/s00477-005-0006-5 (cited on p. 144).

Wagner, W., G. Blöschl, P. Pampaloni, J.-C. Calvet, B. Bizzarri, J.-P. Wigneron, and Y. Kerr (2007). "Operational readiness of microwave remote sensing of soil moisture for hydrologic applications". In: *Nordic Hydrology* **38**:1, pp. 1–20. doi: 10.2166/nh.2007.029 (cited on p. 33).

Walker, J. P., G. R. Willgoose, and J. D. Kalma (2004). "In situ measurement of soil moisture: a comparison of techniques". In: *Journal of Hydrology* **293**:1–4, pp. 85–99. doi: 10.1016/j.jhydrol.2004.01.008 (cited on p. 70).

Walsh, D. O., E. Grunewald, P. Turner, A. Hinnell, and P. Ferre (2011). "Practical limitations and applications of short dead time surface NMR". In: *Near Surface Geophysics* **9**:2, pp. 103–111 (cited on p. 34).

Walsh, D. O., P. Turner, E. Grunewald, H. Zhang, J. J. Butler, E. Reboulet, S. Knobbe, T. Christy, J. W. Lane, C. D. Johnson, et al. (2013). "A Small-Diameter NMR Logging Tool for Groundwater Investigations". In: *Groundwater* **51**:6, pp. 914–926 (cited on p. 34).

Wang, J., Y. Ge, Y. Song, and X. Li (2014). "A Geostatistical Approach to Upscale Soil Moisture With Unequal Precision Observations". In: *IEEE Geoscience and Remote Sensing Letters* **11**:12, pp. 2125–2129. doi: 10.1109/LGRS.2014.2321429 (cited on p. 132).

Watson, P. E., I. D. Watson, and R. D. Batt (1980). "Total body water volumes for adult males and females estimated from simple anthropometric measurements." In: *The American journal of clinical nutrition* **33**:1, pp. 27–39 (cited on p. 130).

Weimar, J. (2015). "Influence of the atmospheric water content on fast cosmic ray neutrons and its importance for the soil moisture retrieving CRNS technique". internal internship report. Dept. MET, UFZ Leipzig (cited on pp. 90, 91).

Western, A. W. and G. Blöschl (1999). "On the spatial scaling of soil moisture". In: *Journal of hydrology* **217**:3, pp. 203–224 (cited on p. 31).

Western, A. W., R. B. Grayson, and G. Blöschl (2002). "Scaling of soil moisture: A hydrologic perspective". In: *Annual Review of Earth and Planetary Sciences* **30**:1, pp. 149–180 (cited on p. 33).

Western, A. W., S.-L. Zhou, R. B. Grayson, T. A. McMahon, G. Blöschl, and D. J. Wilson (2004). "Spatial correlation of soil moisture in small catchments and its relationship to dominant spatial hydrological processes". In: *Journal of Hydrology* **286**:1–4, pp. 113 –134. doi: 10.1016/j.jhydrol.2003.09.014 (cited on pp. 29, 32).

Wiesmeier, M., F. Barthold, B. Blank, and I. Kögel-Knabner (2011). "Digital mapping of soil organic matter stocks using Random Forest modeling in a semi-arid steppe ecosystem". In: *Plant and Soil* **340**:1, pp. 7–24. doi: 10.1007/s11104-010-0425-z (cited on p. 145).

Williams, M. M. R. (1966). *The slowing down and thermalization of neutrons*. North-Holland Pub. Co. (cited on p. 54).

Wood, E. F., J. K. Roundy, T. J. Troy, L. van Beek, M. F. Bierkens, E. Blyth, A. de Roo, P. Döll, M. Ek, J. Famiglietti, et al. (2011). "Hyperresolution global land surface modeling: Meeting a grand challenge for monitoring Earth's terrestrial water". In: *Water Resources Research* **47**:5 (cited on pp. 26, 136).

World Economic Forum (2016). *The Global Risks Report, 11th Edition*. research report. Department of Computer Science, Humboldt University. url: http://www3.weforum.org/docs/GRR/WEF_GRR16.pdf (cited on p. 26).

Z

Zacharias, S. and G. Wessolek (2007). "Excluding organic matter content from pedotransfer predictors of soil water retention". In: *Soil Science Society of America Journal* **71**:1, pp. 43–50 (cited on p. 136).

Zacharias, S., H. Bogena, L. Samaniego, M. Mauder, R. Fuss, T. Pütz, M. Frenzel, M. Schwank, C. Baessler, K. Butterbach-Bahl, et al. (2011). "A Network of Terrestrial Environmental Observatories in Germany". In: *Vadose Zone Journal* **10**:3, pp. 955–973. doi: 10.2136/vzj2010.0139 (cited on pp. 27, 37, 123).

Zarrouk, N. and R. Bennaceur (2009). "A wavelet based analysis of cosmic rays modulation". In: *Acta Astronautica* **65**:1–2, pp. 262 –272. doi: 10.1016/j.actaastro.2009.01.020 (cited on p. 43).

Zhang, X., R. Srinivasan, K. Zhao, and M. V. Liew (2009). "Evaluation of global optimization algorithms for parameter calibration of a computationally intensive hydrologic model". In: *Hydrological Processes* **23**:3, pp. 430–441. doi: 10.1002/hyp.7152 (cited on p. 143).

Zieger, P., J. Biermann, and R. Hedel (2015). "Bewertung der Befahrbarkeit von Böden mit CCMod2 - ein Service auch für die Landwirtschaft". In: *Informatik in der Land-, Forst- und Ernährungswirtschaft, Fokus: Komplexität versus Bedien-*

barkeit / Mensch-Maschine-Schnittstellen, Referate der 35. GIL-Jahrestagung, 23.-24. Februar 2015, Geisenheim, Germany, pp. 205–208 (cited on p. 154).

Zink, M., L. Samaniego, R. Kumar, S. Thober, J. Mai, D. Schäfer, and A. Marx (2016). "The German drought monitor". In: *Environmental Research Letters* **11**:7, p. 074002 (cited on pp. 26, 27, 137).

Zreda, M., W. J. Shuttleworth, X. Zeng, C. Zweck, D. Desilets, T. Franz, and R. Rosolem (2012). "COSMOS: The COsmic-ray Soil Moisture Observing System". In: *Hydrology and Earth System Sciences* **16**:11, pp. 4079–4099. doi: 10.5194/hess-16-4079-2012 (cited on pp. 37, 53, 59–61, 110, 185).

Zreda, M., D. Desilets, and T. Ferré (2005). "Cosmic-ray neutron probe: non-invasive measurement of soil water content". In: *Measurement* **50**:75, p. 50 (cited on pp. 36, 103).

Zreda, M., D. Desilets, T. P. A. Ferré, and R. L. Scott (2008). "Measuring soil moisture content non-invasively at intermediate spatial scale using cosmic-ray neutrons". In: *Geophysical Research Letters* **35**:21. doi: 10.1029/2008GL035655 (cited on pp. 36, 67, 80, 98, 108–110, 116, 177).

Zweck, C., M. Zreda, and D. Desilets (2013). "Snow shielding factors for cosmogenic nuclide dating inferred from Monte Carlo neutron transport simulations". In: *Earth and Planetary Science Letters* **379**:0, pp. 64 –71. doi: 10.1016/j.epsl.2013.07.023 (cited on pp. 63, 67).

Zweibel, E. G. (2013). "The microphysics and macrophysics of cosmic rays". In: *Physics of Plasmas* **20**:5, p. 055501. doi: 10.1063/1.4807033 (cited on p. 42).

Author's declaration

I hereby declare that I am the sole author of this dissertation. The work is original except where indicated by special reference in the text and no part of the dissertation has been submitted for any other degree. This dissertation has not been presented to any other University for examination, neither in Germany nor in another country.

Martin Schrön
Potsdam, June 27th, 2016


HELMHOLTZ
CENTRE FOR
ENVIRONMENTAL
RESEARCH – UFZ
Universität
Potsdam